



Dresden Integrated Center for Applied Physics and Photonic Materials (IAPP)

Institut für Angewandte Physik

Fachrichtung Physik

Fakultät Mathematik und Naturwissenschaften

Photon Generation and Dissipation in Organic Light-Emitting Diodes

Dissertation

zur Erlangung des akademischen Grades

Doctor rerum naturalium

(Dr.rer.nat)

vorgelegt von

Yungui Li

geboren am 19.05.1990 in Hunan, P. R. China

Dresden 2019

1. Prof. Dr. Sebastian Reineke
2. Prof. Dr. Karl Leo
3. Prof. Dr. Guoli Tu

Eingereicht am 02.05.2019

Verteidigt am 09.07.2019

Abstract

By using phosphorescent and thermally activated delayed fluorescence emitters, the internal quantum efficiency of organic light-emitting diodes (OLEDs) can now reach 100%. However, a major fraction of generated photons is trapped inside the device, because of the intrinsic multi-layer device structure and the mismatch of refractive indices. This thesis comprises different approaches for the efficiency enhancement of planar OLEDs. In particular, outcoupling strategies to extract trapped photons to obtain highly efficient OLEDs are investigated.

The thin metal electrode MoO₃/Au/Ag has been used as an alternative electrode for bottom emitting OLEDs. In this thesis, the optical effect of the MoO₃ layer has been thoroughly investigated. It is shown that the MoO₃ layer can suppress the non-radiative surface plasmon polariton (SPP) modes at the interface between glass substrate and gold. Meanwhile, the reflectance and transmission of the electrode can be tuned by the thin MoO₃ layer, which can further modulate the cavity resonance of OLEDs. In presence of MoO₃ layer, white OLEDs based on Au/Ag electrode possess much higher efficiency (1.9 times) compared to the reference without MoO₃ layer, while similar electrical performance and better angular emission characteristics have been obtained.

Further, controllable nanostructures with directional randomness and dimensional order have been fabricated using reactive ion etching (RIE) on poly(dimethylsiloxane) (PDMS). It is possible to manipulate the size of these quasi-periodic nanostructures, by tuning the pretreatment condition of PDMS and the RIE recipe. An optical model is built to numerically simulate the optical effect of the nanostructure for white tandem OLEDs by simplifying the nanostructure into sinusoidal nanotextures. Considering the anisotropy factor, dipole positions on the corrugated surface, and the periodicity and depth of sinusoidal structures, the enhancement factor of white OLEDs can be simulated. Experimentally, the external quantum efficiency of an optimized white OLEDs can be enhanced by a factor of ~1.5, together with better angular color stability and homogeneous radiance distribution. The experimental result also demonstrate the rationality of the simulation model developed in this thesis, which can be applied for other new optoelectronic devices.

Kurzdarstellung

Durch den Einsatz von phosphoreszierenden und thermisch aktivierten verzögerten Fluoreszenzemittern kann die interne Quanteneffizienz von organischen Leuchtdioden (OLEDs) 100% erreichen. Aufgrund der intrinsischen Struktur der mehrschichtigen OLED und interner Totalreflexion bleibt jedoch ein großer Teil der erzeugten Photonen im Inneren der Struktur eingeschlossen. Diese Arbeit beinhaltet verschiedene Ansätze zur Effizienzsteigerung von planaren OLEDs. Insbesondere werden Auskoppelsstrategien untersucht, um eingeschlossene Photonen zu extrahieren und hocheffiziente OLEDs zu erhalten.

Eine dünne Metallelektrode bestehend aus $\text{MoO}_3/\text{Au}/\text{Ag}$ wurde als alternative Elektrode für die OLED verwendet. In dieser Arbeit wurde der optische Effekt der MoO_3 -Schicht ausführlich untersucht. Es zeigt sich, dass die MoO_3 -Schicht die nicht strahlenden Oberflächenplasmon-Polariton-Moden an der Grenzfläche zwischen Glassubstrat und Gold unterdrücken kann. Unterdessen können Reflexion und Transmission der Elektrode durch die dünne MoO_3 -Schicht gezielt eingestellt werden, um die Resonanz von OLEDs zu modulieren. In Gegenwart einer MoO_3 -Schicht besitzen weiße OLEDs auf der Basis einer Au/Ag -Elektrode im Vergleich zur Referenz ohne MoO_3 -Schicht eine viel höhere Effizienz (1,9-fach), während eine ähnliche elektrische Leistung und bessere winkelabhängige Abstrahlcharakteristik erzielt wurden.

Ferner wurden mittels reaktiven Ionenätzen (RIE) skalierbare Nanostrukturen mit zufälliger Ausrichtung und Dimensionierung auf Poly(dimethylsiloxan) (PDMS) hergestellt. Es ist möglich, die Größe dieser quasi-periodischen Nanostrukturen durch Einstellen der Vorbehandlungsbedingungen des PDMS und des RIE-Rezeptes zu beeinflussen. Ein optisches Modell dient zur numerischen Simulation des optischen Effekts der Nanostruktur für Weiße-Tandem-OLEDs, indem die Nanostruktur zu sinusförmigen Nanotexturen vereinfacht wird. In Anbetracht des Anisotropiefaktors, der Dipolpositionen auf der gewellten Oberfläche und der Periodizität und Tiefe kann die Effizienzsteigerung für weiße OLEDs simuliert werden. Experimentell kann die externe Quanteneffizienz von optimierten weißen OLEDs um einen Faktor $\sim 1,5$ erhöht werden, zusammen mit einer besseren Winkelfarbstabilität und einer homogenen Strahlungsverteilung. Das experimentelle Ergebnis zeigt auch die Leistungsfähigkeit des in dieser Arbeit aufgebauten Simulationsmodells, das für andere neue optoelektronische Bauelemente angewendet werden kann.

Table of Contents

Abstract.....	I
Kurzdarstellung.....	II
Publications.....	III
1 Introduction.....	1
2 Basics of organic semiconductors.....	5
2.1 Molecular orbitals.....	5
2.2 Optical properties.....	7
2.2.1 Absorption.....	8
2.2.2 Refractive index.....	8
2.2.3 Conventional fluorescent emitter.....	9
2.2.4 Phosphorescent emitter.....	11
2.2.5 Thermally activated delayed fluorescent emitter.....	13
2.2.6 Biluminescence and room-temperature phosphorescence.....	14
2.3 Intermolecular energy transfer.....	15
2.3.1 Reabsorption.....	15
2.3.2 Förster resonance energy transfer.....	16
2.3.3 Dexter energy transfer.....	17
2.4 Exciton diffusion.....	18
2.5 Charge carrier transport.....	20
2.6 Molecular doping.....	21
2.7 Thermal property.....	23
3 Basics of organic light-emitting diodes.....	27
3.1 Working principle and device structure.....	27
3.2 Device characterization.....	31
3.2.1 Internal and external quantum efficiency.....	31
3.2.2 Current efficiency.....	31
3.2.3 Luminous efficacy.....	31
3.2.4 Color quantification and quality.....	32
3.2.5 Angular dependent emission.....	33
3.2.6 Efficiency roll-off.....	34
3.3 Monochrome and white OLEDs.....	34

3.3.1	Monochrome OLEDs.....	34
3.3.2	White OLEDs	35
3.4	Charge-to-photon conversion	40
3.5	Photon dissipation	42
3.6	Photon trapping modes	45
3.7	Quantification of energy loss channels.....	49
3.8	Extraction efficiency	50
3.9	Enhancing photon extraction	51
3.9.1	External outcoupling.....	52
3.9.2	Internal outcoupling.....	59
3.9.3	Anisotropy factor	66
3.9.4	Cavity resonance.....	66
3.10	Micro/nano pattern fabrication	68
3.10.1	Photolithography and laser interference	68
3.10.2	Soft lithography	70
3.10.3	Stress release.....	72
3.11	Chapter summary.....	78
4	Experimental and methods	79
4.1	Materials.....	79
4.2	Nanostructure generation with PDMS.....	82
4.3	Thin metal electrode fabrication and characterization.....	82
4.4	Topography measurement	83
4.5	Device fabrication	83
4.6	XPS measurement	84
4.7	Dynamic mechanical analysis (DMA)	84
4.8	Device modeling.....	85
4.9	Photophysical properties measurement	86
5	Improved optics by ultrathin MoO ₃ layer for efficient OLEDs	87
5.1	Tandem white OLEDs.....	87
5.2	Enhancement mechanism investigation.....	90
5.2.1	Minor influence on the electrical efficiency	90
5.2.2	The suppression of SPP modes	91
5.2.3	Cavity resonance.....	92
5.2.4	Finite element analysis.....	96

5.3	Chapter summary.....	97
6	Tailor-made nanostructures for highly efficient white OLEDs	99
6.1	Nanostructure generation and control.....	100
6.1.1	Basic information of RIE induced nanostructures	100
6.1.2	Nanostructure uniformity.....	101
6.1.3	Nanostructure reproducibility	103
6.1.4	Nanostructure control	104
6.1.5	Mechanism of nanostructure control	107
6.2	Optical modeling of planar white OLEDs	110
6.3	Optical modeling of structured white OLEDs.....	112
6.4	White OLEDs with nanostructures.....	117
6.5	Complexity of experimental aspect ratio.....	121
6.6	Comparison with literatures.....	125
6.7	Chapter summary.....	126
7	Concluding remarks and outlook	127
7.1	Summary.....	127
7.2	Outlook.....	130
8	Appendix.....	131
8.1	Host influenced TADF	131
8.2	Photophysical properties of PO-T2T : P1 mixture	136
8.3	Monochrome OLEDs based on P1	139
8.4	Polychrome OLEDs with dual emission from P1 and CT-state	141
8.5	Summary.....	143
	References.....	144
	List of Abbreviations	173
	Acknowledgement	175
	Erklärung.....	177

Publications

Articles

1. Yungui Li, Zheng Tang, Christian Hännisch, Paul-Anton Will, Milan Kovačič, Ji-Ling Hou, Reinhard Scholz, Karl Leo, Simone Lenk, and Sebastian Reineke. Ultrathin MoO₃ Layers in Composite Metal Electrodes: Improved Optics Allow Highly Efficient Organic Light-Emitting Diodes. *Adv. Opt. Mater.* 1801262 (2018).
2. Yungui Li, Milan Kovačič, Jasper Westphalen, Steffen Oswald, Zaifei Ma, Christian Hännisch, Paul-Anton Will, Lihui Jiang, Manuela Junghaehnel, Reinhard Scholz, Simone Lenk, and Sebastian Reineke. Bridging Chaos and Order: Tailor-Made Nanostructures for Highly Efficient White Organic Light-Emitting Diodes. (submitted)
3. Yungui Li, Qiang Wei, Liang Cao, Felix Fries, Matteo Cucchi, Zhongbin Wu, Reinhard Scholz, Simone Lenk, Brigitte Voit, Ziyi Ge, and Sebastian Reineke. Organic light-emitting diodes based on conjugation-induced thermally activated delayed fluorescence polymers: Interplay between intra- and intermolecular charge transfer states. (in preparation)
4. Yungui Li, Lihui Jiang, Reinhard Scholz, Tian-yi Li, Max Gmelch, Felix Fries, Olaf Zeika, Simone Lenk, Karl Leo, and Sebastian Reineke. More Than Heavy Atom Effect: Achieving Ultralong Room-Temperature Phosphorescence by Suppressing the Intrinsic Non-radiative Loss. (in preparation)
5. Yungui Li, Lihui Jiang, Shunqi Xu, Matteo Cucchi, Tian-Yi Li, Olaf Zeika, Reinhard Scholz, Simone Lenk, Xinliang Feng, Karl Leo, and Sebastian Reineke. Molecular Packing Enhanced Photoluminescence in Organic Films. (in preparation)
6. Yungui Li, Milan Kovačič, Simone Lenk, and Sebastian Reineke. Modeling the Quasi-periodic Nanostructures as External Outcoupling Strategies for Organic Light-Emitting Diodes. (in preparation)

Conference contributions

1. Yungui Li, Toni Bärschneider, Paul-Anton Will, Yuan Liu, Simone Lenk, Karl Leo, and Sebastian Reineke. Ultrathin metal electrode for bottom-emitting OLEDs on buckled substrates. Deutsche Physikalische Gesellschaft (DPG), **2017**, HL 13.6, Dresden, Germany. (Oral presentation)
2. Yungui Li, Paul-Anton Will, Simone Lenk, and Sebastian Reineke. Controllable random nano-structures for organic light-emitting diodes. International Society for Optics and Photonics (SPIE), **2017**, San Diego, United States of America. (Poster)
3. Yungui Li, Paul-Anton Will, Simone Lenk, and Sebastian Reineke. Controllable buckling structures for flexible organic light-emitting diodes. European Conference on Molecular Electronics (ECME), **2017**, Dresden, Germany. (Poster)
4. Yuan Liu, Christian Hänisch, Yungui Li, Simone Lenk, Karl Leo, and Sebastian Reineke. Exciton control in exciplex-based white OLEDs: toward high efficiency and low efficiency roll-off. European Conference on Molecular Electronics (ECME), **2017**, Dresden, Germany. (Poster)

1 Introduction

Following the pioneering work by Tang and VanSlyke in 1987, organic light-emitting diodes (OLEDs) have attracted much interest from both academic and industry communities.[1] After decades of development, the technology is now matured to a level for applications in fields of display and special lighting. Display screens with OLED technology are now used in mobile phones from industry giants such as Apple, Samsung and Huawei, because of the merit of light weight, wide viewing angle, high color saturation and efficient luminous efficacy, as well as the possibility of flexible display and manufacture by inject printing.[2] When decreasing the pixel size of OLEDs down to several micrometers, it is possible to use micro-OLED screens for the near-eye display.[3] Moreover, monochrome OLEDs have also been used as light sources for automobiles.[4] On the other hand, white OLEDs can be a promising candidate for solid state lighting application.

Comparing to the existing light sources, such as incandescent bulbs, fluorescent tubes, or inorganic light-emitting diodes (LEDs), OLEDs possess the following advantages:

1. Cost effective. OLEDs mainly consist of organic materials, which can be made by economic effective processing techniques, such as inject printing, spin-coating and/or blade-coating.
2. High color rendering index (CRI). By using various organic emitters with different emissive colors, it is possible to achieve a wide spectrum covering the entire visible wavelength range.
3. Flexibility and light weight. When properly designed, OLEDs can be flexible and foldable with a very light weight and a thickness of several micrometers, showing the possibility for special applications and new design alternatives.
4. Face light source with a wide viewing angle, giving a pleasant light perception for human beings.

For both applications - display and lighting - the efficiency of OLEDs is one of the key factors, since it relates to power conversion from electricity to light. The internal quantum efficiency (IQE), which is defined as the yield of charge-to-photon conversion, has been reached unity (100%). However, only a small fraction of generated photons can escape the multilayer device structure of OLEDs. The external quantum efficiency (i.e. the yield of charges-to-emitting photons escaped to air zone, short as EQE) remains as low as 20 - 30% for a typical OLED, indicating that the majority of generated photons are trapped inside the device. The extraction for trapped photons is therefore important

for display and lighting applications. For display purposes at the specific luminance, the increase of outcoupled photons can extend the working time of the battery after one charge. On the other hand, reducing the energy loss for OLED light sources and improving the conversion of electrical charges into useful photons can directly decrease the energy consumption, which has great significance for energy saving and environment protection.

The photon trapping in OLEDs is a well-known phenomenon. Great efforts have been made to understand the photon trapping mechanism, and therefore further to design strategies to increase the device efficiency via extracting trapped photons. Different optical models have been built to describe the photon trapping mechanism and now it is possible to simulate the optical performance for a planar device by commercial software. Various strategies involving micro/nano structures have been introduced to reduce the photon trapping. However, new strategies generate micro/nano structures without photolithography processes may be needed, since the fabrication routine of micro/nano structures can also make substantial effect on the device fabrication process and also the device reliability. Hence, the enhancement of EQE is not enough from a practical point of view. The fabrication and implantation process, the device lifetime, should be taken into account when evaluating outcoupling strategies. On the other hand, in a scientific point of view, there is lack of physical model to numerically simulate the photon outcoupling from nanostructures with periodicity and depth distributions, which is potentially helpful for white OLEDs and new optoelectrical devices such as perovskite LEDs.

The work of this thesis is mainly focusing on photon generation and dissipation of OLEDs. Especially loss channels in OLEDs, like surface plasmon polariton and waveguide modes, but also the development of new techniques for outcoupling structures and optical modelling, are of interest. Furthermore, triplet harvesting for thermally activated delayed fluorescence (TADF) emitter is addressed based on a polymer emitter. Together with the introduction and an appendix chapter of TADF, the thesis consist of 8 chapters in total.

This introduction chapter is followed by chapter 2 to introduce the basic theory of organic semiconductors, including the fundamental properties of organic molecules, including molecular orbitals, photophysical, electrical and thermal properties. To be more specific, photophysical properties such as absorption, refractive index, photoluminescence quantum yield (PLQY), conventional fluorescent emission, phosphorescent emission, TADF, bioluminescence and room temperature phosphorescence are introduced. Intermolecular energy transfer mechanisms for organic emitters, charge transport and molecular doping is briefly introduced. In the end, the relation between the thermal properties and the chemical structures is discussed.

Chapter 3 focuses on the previous investigation on OLEDs. Firstly, the device working principle, representative device configurations and performance characteristics are introduced. This is followed by the introduction of monochrome and white OLEDs, physical processes of photon generation from injected charges, photon dissipation and trapping modes in OLEDs. After the summary of photon trapping mechanism in OLEDs, existing outcoupling strategies are summarized and compared. In the last section of chapter 3, the general methods to fabricate micro/nano structures for outcoupling purposes in OLEDs are introduced.

The experimental details are presented in Chapter 4, including the chemical structure of materials used in this thesis, sample preparation, device characterization and physical property measurements.

Chapter 5 summarizes results about optical effects of molybdenum trioxide (MoO_3) for OLEDs. It is noted that a thin MoO_3 layer has a vital influence on the device performance by introducing a synergistic effect of suppressing surface plasmon polariton (SPP) modes and decreasing the destructive resonance. The conclusion is drawn based on experimental results of device performance, physical property investigation of the thin film and optical simulations.

Chapter 6 describes the investigation on the fabrication of controllable quasi-periodic nanostructures and their application for extracting trapped photon in bottom white OLEDs. Firstly, the general information of these nanostructures is introduced, followed by a systematic research on the dimensional control and mechanism investigation. An optical model is built to numerically simulate the enhancement factor for OLEDs based on these structures. Finally, the device performance based on these nanostructures is presented and analyzed.

The major results of this thesis are summarized in Chapter 7, where outlook of this thesis is also presented there. The investigation on the interaction between host materials and a thermally activated delayed fluorescence polymer is presented as an appendix chapter after Chapter 7.

2 Basics of organic semiconductors

The following chapter discusses the fundamental properties of organic semiconductors, including the basic knowledge about molecular orbitals, optical, electrical and thermal properties. Optical properties of organic emitters including absorption, refractive index, photoluminescence quantum yield, the difference of conventional fluorescent emitter, phosphorescent emitter and thermally activated delayed fluorescent emitter and biluminescence from purely organic emitters are briefly introduced. This is followed by the introduction of intermolecular energy transfer mechanisms between organic emitters, charge carrier transport in organic semiconductors and thermal properties of organic materials.

Organic semiconductors possess unique and fascinating properties compared to inorganic semiconductors with main components of carbon, hydrogen and oxygen atoms. By means of versatile molecular design, they can be processed by approaches of spin-coating, blade-coating or thermal deposition. The basic units of an organic semiconductor are organic molecules bound by van der Waals forces. As the binding force is weaker compared to covalent or ion bonds in inorganic semiconductors, properties of organic semiconductors are primarily determined by the intrinsic optical, chemical and electrical properties of the single organic molecule. The fundamental knowledge about organic molecules then is of vital importance for further understanding physical phenomenon related to OLEDs.

2.1 Molecular orbitals

The organic molecules are formed by connection of atoms such as carbon, hydrogen and oxygen with different kinds of bond. The σ bond is very strong with a high binding energy, with two atoms sharing s orbital from each other, as shown in Figure 2.1. Carbon atom possesses six electrons in an electron configuration of $1s^2 2s^2 2p^2$, where the four electrons located in $2s$ and $2p$ orbitals are loosely bound to the nuclei. For a benzene molecule, strong σ bonds are formed between carbon-carbon and carbon-hydrogen atoms. The σ bonds formed between two carbon atoms by sharing sp^2 orbitals while the other σ bond between carbon and hydrogen atoms are resulting from sharing s orbitals of hydrogen atoms and sp^2 orbitals of carbon atoms. The parallel p_z orbitals are overlapping, perpendicular to the ring, forming an extended π system.

The electrons can flow through the extended π system, giving the possibility of electrical conductivity in organic semiconductors.

According to the theory of frontier orbitals of the molecule, orbitals of benzene with lower energy levels are occupied by electrons while orbitals with higher energy levels are empty, leading to the generation of an energy gap.[5] The most important states of an organic compound are the highest occupied molecule orbital (HOMO) and the lowest unoccupied molecular orbital (LUMO).[6] According to Koopmans' theorem, which ignores the reorganization energy of the molecule, the HOMO level of a molecule is equal to its ionization potential I_p and the LUMO level corresponds to the electron affinity E_a . [7] The energetic difference between the HOMO and LUMO defines the energy gap E_g for an organic molecule. It reads as:

$$E_g = E_{\text{LUMO}} - E_{\text{HOMO}} \quad (2.1)$$

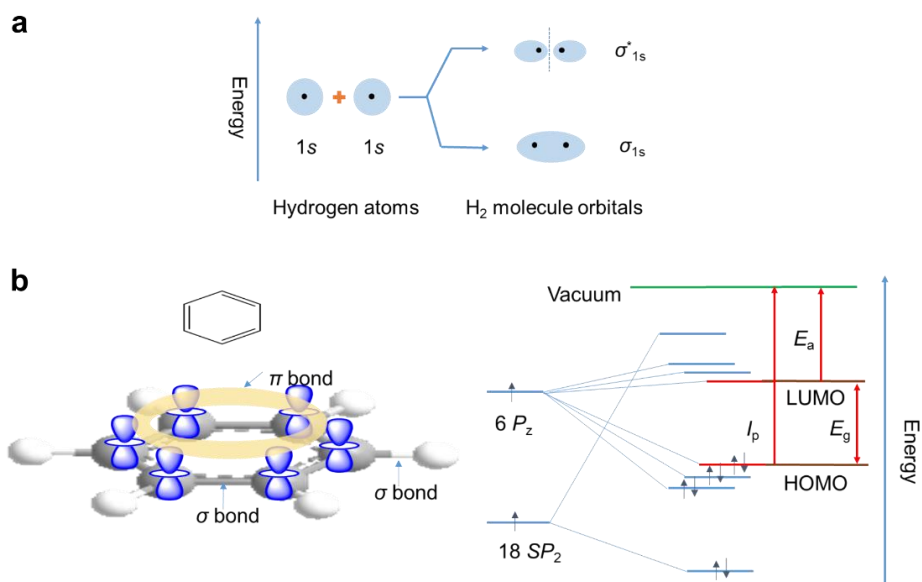


Figure 2.1. Schematics of orbitals, bonds and energy level relation for hydrogen and benzene molecules. (a) The formation of σ bonds in hydrogen molecule by sharing s orbitals from two hydrogen atoms. (b) The chemical structure, bonds and energy levels of a benzene molecule, representing the basic relation of different energy levels for organic molecules. Reproduced from reference [7].

The energy gap, one of the most important parameters for organic molecules, influences the electrical and optical properties of an organic molecule. Fortunately, the energy gap of organic molecules can be manipulated by incorporation of various atoms and fragments such as nitride, oxygen, sulfur, and numbers of aromatic rings with different electron withdrawing/donating abilities. The mature chemical synthesis technique allows a significant design freedom for organic molecules with energy gaps ranging from the ultraviolet to infrared region, giving the possibilities to obtain molecules which are suitable for different purposes, such as injection and transport materials in functional devices, emitters in OLEDs, absorbers in organic solar cells.

2.2 Optical properties

Since organic molecules in film states are bounded by weak van-der-Waals forces, without considering the effect from solvent molecules in solutions or aggregation in films, the optical properties including the absorption and emission behavior are similar to the single molecule in vacuum. The most important energy transitions following photon excitation of an organic molecule, are schematically depicted by the Jablonski diagram in Figure 2.2, including the absorption, internal conversion (IC), intersystem crossing (ISC), non-radiative relaxations, fluorescence and phosphorescence radiation.

The general discussion in the following sections is done without consideration of external environmental factors. However, it should be noted that for most organic emitters, the change of external conditions such as solvent polarity and viscosity, packing states in films and temperature can have considerable effects on the optical properties, such as the absorption and/or emission behavior. [8,9]

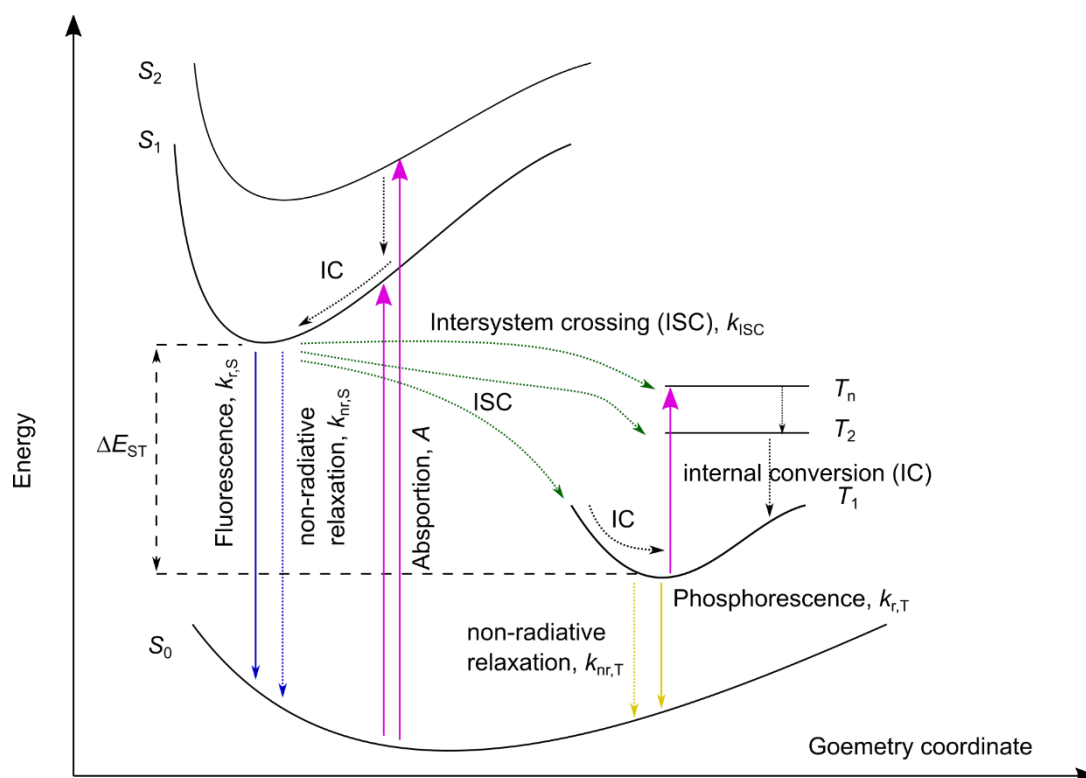


Figure 2.2. Jablonski diagram for a typical organic molecule, representing the most important energy transitions in an organic molecule: absorption, internal conversion, fluorescence, phosphorescence, non-radiative relaxations and intersystem crossing. The geometry coordinate indicates the subtle configuration change of the molecule. The straight solid arrows indicate radiative deactivation while the dashed lines represent non-radiative relaxations. When the single-triplet splitting ΔE_{ST} is small enough, the reverse intersystem crossing from T_1 to S_1 can also happen by harvesting the environmental thermal energy. The intersystem crossing can happen between singlet state S_1 to triplet states T_n with lower energy level compared to S_1 . Reproduced from reference [10].

2.2.1 Absorption

Upon absorption of light with energy higher than the energy gap ΔE , the molecule is excited from the ground state to a higher singlet state as an exciton with bound electron-hole pair. The energy of excitation photons determines which excited singlet states can be achieved. The molecule can also be excited to a higher energy level S_n by photon excitation. If the molecule is excited to the S_2 state, the molecule can lose energy to the S_1 state by the internal conversion (IC) and vibration relaxation in the time-scale of picosecond region.[10] Absorption can also take place from triplet state T_1 to a higher triplet level T_2 . However, the molecule has to be in T_1 state beforehand. Thus, the absorption from ground state directly to the triplet state T_1 or T_2 is forbidden.

The Lambert-Beer law describes the absorption A of the light at a single wavelength by an isotropic and homogeneous medium under low concentration:[11]

$$A = \log\left(\frac{I_0}{I}\right) = \epsilon dc \quad (2.2)$$

where I_0 is the intensity of the incident light beam, I is the light intensity through the medium with a thickness of d and extinction coefficient ϵ under the concentration of c . The extinction coefficient ϵ is a wavelength/frequency dependent parameter, which can be measured by means of UV-Vis absorption, determined by the intrinsic molecular chemical structure, solvent effects and/or packing states.[10]

For each excited state, there are many vibrational states, where the excited molecule can relax to the corresponding lowest excited state by internal conversion and then give emission, resulting from the fact that for the majority of organic complexes, the relaxation from higher excited states to the lowest excited state is faster than the following radiative processes. The vibrational relaxation and internal conversion can lose energy, leading to a red-shift of emission peak compared to the lowest absorption peak. This phenomenon, named as Stokes-shift, widely exists among organic molecules. The other possible processes after photon absorption shown in Figure 2.2 will be discussed in details in the following sections.

2.2.2 Refractive index

The refractive index n of a material is a dimensionless number, describing how light propagates through the medium. It is defined as

$$n = \frac{c}{v} \quad (2.3)$$

where c is the speed of light in vacuum, v is the phase velocity of light in the medium.

For a homogeneous medium, since the velocity of light in the medium is generally lower than the one in the vacuum, the refractive index can be regarded as the ability of decreasing the speed of light. According to Ewald–Oseen extinction theorem, the refraction can be further understood at the atomic scale, in a way that an electromagnetic wave's phase velocity is decreased in a medium because the electric field generates a disturbance towards the charges of atoms.[12] As the electromagnetic fields oscillate, the charges in the medium try to follow the electromagnetic field of the light. As a result, the charges radiate electromagnetic wave at the same frequency with a phase delay, since the charges may move out of phase. The light wave propagating in the medium is the sum of the original incident wave and the waves radiated by the entire moving charges of atoms.[12,13]

The refractive index is about 1.5 for the typical conventional glass and it is 1.7-1.8 for indium tin oxide (ITO) within the visible wavelength range. For organic materials, the refractive index is in range of 1.3-1.7 in the visible wavelength region.[14,15] Since most of organic materials consist of atoms like nitrogen, oxygen and carbon, the refractive index for most of homogeneous organic films is similar. However, the density and the microstructure of the organic films can influence the refractive index.[16] Even though the refractive index of organic materials makes a substantial influence on the light dissipation in the device, the design of materials with proper refractive indices for organic light-emitting diodes is challenging. The reason could be that electrical and optical properties should also be realized at the same time, when they are used as a functional material (see Section 3.1). It is possible to control the refractive index of to some extents, by means of using special components such as sulfur, phosphorus or halogen atoms and controlling the microstructure of the films.[17–22]

2.2.3 Conventional fluorescent emitter

After photon excitation, the organic molecule can deactivate through channels such as radiation, decomposition or thermal vibration, the quantum yield Φ is introduced to quantify the deactivation channels.[10] The differential definition for a certain deactivation process p reads:

$$\Phi_p = \frac{dn_p}{dn_a} \quad (2.4)$$

where n_p represents the number of excited states that undergo the process p and n_a is the total number of absorbed photons by the medium. For the specific case of radiative deactivation in absence of an optical cavity, the photoluminescence quantum yield

(PLQY) represents the emissive property of a given luminophore, defined as the ratio between the total number of photons emitted and the total number of photons absorbed, which is one of the most important parameters of organic emitters.

For a conventional fluorescent emitter, the competition between the rate of radiative deactivation and rates of non-radiative processes determines the PLQY:

$$\Phi_S = \frac{k_{r,S}}{k_{r,S} + k_{nr,S} + k_{ISC}} \quad (2.5)$$

Here, Φ_S denotes the PLQY of the conventional fluorescent emitter from singlet state to the ground state, $k_{r,S}$ denotes the radiative rate, $k_{nr,S}$ is the non-radiative decay rate, k_{ISC} represents the intersystem crossing (ISC) rates.

In general, these kinetic rates of a conventional fluorescent emitter is mainly determined by the intrinsic molecular structural and geometric configuration, which can be further modified by external surroundings including the solvent, packing modes in film state and temperature. The molecular rotation, vibration and stretching can contribute to the non-radiative losses, giving rise to a decrease of PLQY.[23]

The lifetime τ_S of singlet states is determined as:

$$\tau_S = \frac{1}{k_{r,S} + k_{nr,S} + k_{ISC}} \quad (2.6)$$

Since the relaxation from singlet state to the ground state is spin-allowed, the rates $k_{r,S}$ and $k_{nr,S}$ is high, giving the lifetime τ_S for conventional fluorescent organic emitters in the nanosecond regime.

It is well-known that for the conventional fluorescent aromatic components, the rate of non-radiative relaxation $k_{nr,S}$ is correlated to the energy gap E_g [10]:

$$k_{nr,S} = 10^{13} \cdot e^{-4.5E_g} \quad (2.7)$$

Thus, the non-radiative loss is more significant for emitters with a smaller energy gap. As a reason of that, there is a general trend for organic dyes that the PLQY for red emitters is generally lower compared to blue emitters.

In the early stage of OLEDs, the organic emitters are in general based on conventional fluorescent emitters, such as tris(8-hydroxyquinolinato)aluminium (Alq₃), dicyanomethylene-4H-pyran (DCM) and 4-(dicyanomethylene)-2-tert-butyl-6-(1,1,7,7-tetramethyljulolidin-4-yl-vinyl)-4H-pyran (DCJTb).[1,24] The conventional fluorescent emitters consisting of the aromatic fragments with a universal design freedom and high material stability in the device, are one of the most important kinds of material for OLEDs till today.[25]

Under photon excitation, the generation of triplets in conventional fluorescent emitters is via ISC as a non-radiative channel, as shown in Figure 2.2. However, the excitons formed in organic emitters by electrical excitation are statistically following the electron spin statistics, with the ratio of singlets to triplets as 1:3. Because the triplet state has a multiplicity of three, on average about 75% excitons are in forms of triplets under electrical excitation.[26] Since the relaxation from triplet states to the ground state for conventional organic emitters is spin-forbidden and non-radiative, the conventional fluorescent emitters give only a maximum of 25% internal quantum efficiency (IQE) in an electrical driven device, if no triplet harvesting strategy is applied. To solve the problem, phosphorescent emitter and thermally activated delayed fluorescent (TADF) emitter have been developed. The difference of conventional fluorescent emitter, phosphorescent emitter and TADF emitter under electrical excitation is schematically presented in Figure 2.3. The detailed mechanism for phosphorescent and TADF emitters are discussed in the following sections.

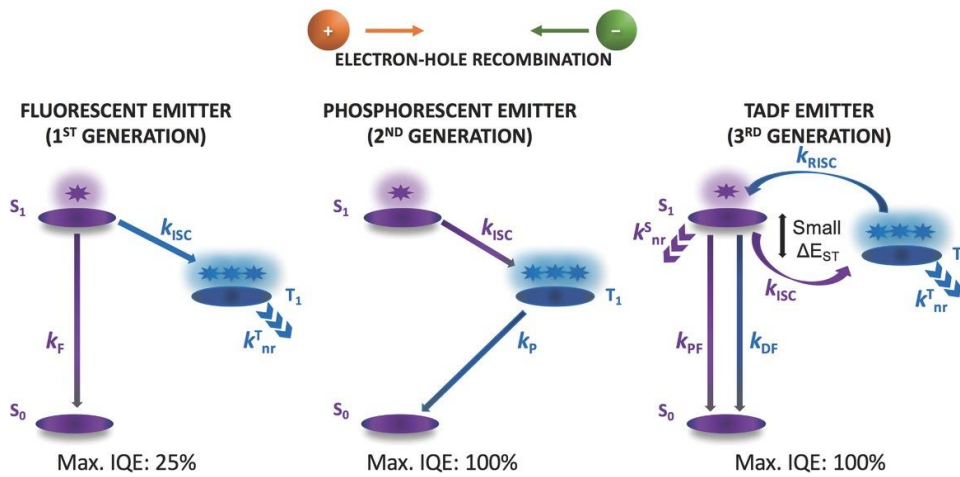


Figure 2.3. Emitting mechanism for different emitters in OLEDs under electrical excitation. Conventional fluorescent emitters without triplet harvesting gives only 25% IQE; phosphorescent emitters with triplet emission resulting from heavy atom effect and thermally activated delayed fluorescent emitters with small singlet-triplet splitting to harvest triplets to singlets via RISC by thermal energy. Reproduced from reference [38].

2.2.4 Phosphorescent emitter

Phosphorescent emission are theoretically resulting from the radiative relaxation from triplets to the ground state, as shown in Figure 2.2. In such a scenario, the PLQY Φ_T for phosphorescence emission can then be defined as:

$$\Phi_T = \frac{\Phi_{ISC} * k_{r,T}}{k_{r,T} + k_{nr,T}} \quad (2.8)$$

where Φ_{ISC} is the quantum yield for ISC, $k_{r,T}$ is the radiative rate of triplet emission and $k_{nr,T}$ is the non-radiative rate of triplets. The quantum yield Φ_{ISC} can be written as:

$$\Phi_{\text{ISC}} = \frac{k_{\text{ISC}}}{k_{r,S} + k_{nr,S} + k_{\text{ISC}}} \quad (2.9)$$

where the k_{ISC} is the ISC rate from the singlet state to triplets.

For an organic emitter under photon excitation, the rate $k_{\text{ISC},m}$ from S_1 to T_m state is dependent on the spin-orbital operator:[27,28]

$$k_{\text{ISC},m} = \frac{2\pi}{\hbar} \left\langle \Psi_1^{1(0)} | \mathcal{H}_{\text{SO}} | \Psi_m^{3(0)} \right\rangle^2 \times f \quad (2.10)$$

where the $\Psi_m^{3(0)}$ is the electronic wavefunction of the zeroth vibrational level of an m order triplet state (T_m), f is the Frank-Condon-weighted density for S_1 to T_m state non-radiative transition, while the spin-orbit Hamiltonian \mathcal{H}_{SO} can be written as: [27,28]

$$\mathcal{H}_{\text{SO}} = \alpha_{\text{F}}^2 \sum_{\mu}^N \sum_i^n \frac{Z_{\mu}}{r_{i\mu}^3} \vec{L}_i \cdot \vec{S}_i \quad (2.11)$$

where α_{F} denotes the fine-structure constant; Z represents the effective nuclear charge at nucleus μ ; S and L are the spin and orbital angular momenta of electron i , respectively.

According to Equation 2.11, the rate k_{ISC} and further Φ_{ISC} can be enhanced significantly when the atomic number and the proximity of atoms is increased. By using atoms with the large atomic weight, the spin-orbit coupling is strongly enhanced. For organometallic complexes with heavy metal components like platinum, iridium, osmium, or palladium as the molecule core, the rate of intersystem crossing is so significant that singlets can fully converted to triplets, followed by phosphorescence emission with the decay lifetime of τ_{T} . [29] Similar to the lifetime of singlets, the lifetime τ_{T} can be written as:

$$\tau_{\text{T}} = \frac{1}{k_{r,T} + k_{nr,T}} \quad (2.12)$$

where the $k_{nr,T}$ is the non-radiative rate of triplets.

Even though the selection rule for the previously spin-forbidden triplet emission is weakened with the heavy metallic atoms as the core of organometallic complexes, [28,30] the lifetime of triplets, in general, is still orders longer than the lifetime of singlets.[31] The first report on phosphorescent emitter for OLEDs was in 1998 by S. Forrest *et al.*, namely, 2,3,7,8,12,13,17,18-octaethyl-21H,23H-porphine platinum(II)

(PtOEP), with the triplet lifetime $\tau_T \sim 40 \mu\text{s}$ and phosphorescence quantum yield $\Phi_T \sim 50\%$.^[29] After this breakthrough, great efforts have been dedicated to achieve phosphorescent emitters with high PLQY and different emissive colors in the entire visible range.^[32] The development of phosphorescent materials makes it possible to obtain 100% IQE for OLEDs under electrical excitation. However, the intrinsic long-lived character of triplets leads to bimolecular processes in the device, giving rise to the efficiency roll-off under high current density, which will be explained in Section 3.2.6. As a consequence of that, the material design of phosphorescent emitters to obtain shorter triplet lifetime is very important for the entire field.^[31]

2.2.5 Thermally activated delayed fluorescent emitter

The utilization of heavy metallic atoms in phosphorescent emitters brings the drawbacks of toxicity and high cost. Apart from phosphorescence emission, another possible way to harvest triplet excitons is converting triplets to singlets by finely matching the triplet state and singlet state with a small singlet-triplet splitting ΔE_{ST} , as shown in Figure 2.2. The reverse intersystem crossing (RISC) from triplet states to singlet states can be realized by harvesting the environmental thermal energy, known as thermally activated delayed fluorescent (TADF) emitter.

The rate of RISC in TADF emitters is dependent on the ambient temperature T and the singlet-triplet splitting ΔE_{ST} :^[33]

$$k_{\text{RISC}} = k_{\text{ISC}} \cdot \exp\left(-\frac{\Delta E_{\text{ST}}}{k_{\text{B}}T}\right) \quad (2.13)$$

where k_{B} is the Boltzmann constant.

Fullerene and porphyrin derivatives are known to demonstrate TADF behavior but with very low PLQY.^[34,35] In 2011, the first purely organic, reliable TADF emitter 2-biphenyl-4,6-bis(12-phenylindolo[2,3-a] carbazole-11-yl)-1,3,5-triazine (PIC-TRZ) was reported by Adachi *et al.*, with a moderate PLQY of 39% and only 32% triplet utilization efficiency in the device.^[36] Later in 2012, the same group reported purely organic TADF emitters with almost 100% triplet harvesting efficiency.^[33] The key point of the TADF molecular design is the combination of a small ΔE_{ST} with a reasonable radiative decay rate to overcome the competitive non-radiative decay channels. Because the need of a small ΔE_{ST} and a reasonable radiative decay rate conflicts with each other, the overlap and the spatial separation of the HOMO and LUMO level needs to be carefully balanced.^[37]

According to Equation (2.13), the RISC rate for TADF emitters is exponentially dependent on ΔE_{ST} and linear with the k_{ISC} . However, in general, both k_{ISC} and k_{RISC} is

slower than the prompt fluorescence emission k_{PF} (10^9 s^{-1} range) from singlets, giving the harvested triplets to the singlet as a delayed fluorescence with a longer lifetime in the range of several microseconds to milliseconds. The exact value of k_{ISC} and k_{RISC} is dependent on the intrinsic chemical structures, molecular configuration and also the external environments.[38] After the first report of TADF emitters with high PLQY, intensive investigations have been made to obtain purely organic TADF emitters for different emissive colors.[38,39]

2.2.6 Biluminescence and room-temperature phosphorescence

Biluminescence, or dual emission, is the ability of a molecule to undergo radiative relaxation from singlet and triplet states. Some of organometallic complexes with heavy atoms, such as copper and osmium, show the dual emission behavior. In these emitters, the intersystem crossing and the spin-coupling effect is not effective enough to achieve the purely phosphorescent emission, leading to the emission from both singlet and triplet states. [40–42]

According to Equation (2.10) and (2.11), for purely organic materials, the rate of ISC can be facilitated with the presence of heavy atoms such as bromine and iodine. Other chemical strategies including resonance-activated spin-flipping, integrating aromatic carbonyl or/and heterocycle/heteroatom have also been applied to enhance the generation of triplets.[43–47]

The triplets can be quenched by oxygen and/or collisions from solvent molecules. It is therefore difficult to observe phosphorescence emission at room temperature, in solutions or amorphous films with the presence of oxygen.[48,49] The lifetime of triplets τ_T for room-temperature phosphorescence emitters is dependent on the quenching rate $k_{q,T}$:

$$\tau_T = \frac{1}{k_{r,T} + k_{nr,T} + k_{q,T}} \quad (2.14)$$

To achieve phosphorescent emission from purely organic materials, the exclusion of quenching channels is needed. The general way to measure the phosphorescent spectrum is cooling down the emitter (e.g. in liquid nitrogen) to reduce the non-radiative relaxation and protecting the triplets from oxygen at the same time. However, to achieve phosphorescent emission at room temperature from purely organic emitters, reducing the non-radiative losses of triplets in forms of molecular vibrations and rotations is of vital importance. When the intramolecular motion and the intermolecular collision are effectively suppressed, in cases when the emitter is mechanically fixed in a host matrix or packed in a crystal, phosphorescence emission at room temperature can be

realized.[50] Compared to the fast decay of fluorescent emission in nanoseconds region, the phosphorescence emission at room temperature from purely organic materials can extend to milliseconds or even minutes region, holding promising potential for sensors and data-safety applications.[50–53]

2.3 Intermolecular energy transfer

Highly efficient, multi-component luminescent systems are generally based on different energy transfer mechanisms from the donor molecule D to the acceptor molecule A . In the following discussion, their multiplicities are denoted with subscripts, i.e. 1 or 3 for the singlet and triplet. Asterisks represent excited states. The possible energy transfer mechanisms are summarized in Figure 2.4, including reabsorption, Förster resonance energy transfer (FRET) and Dexter energy transfer.

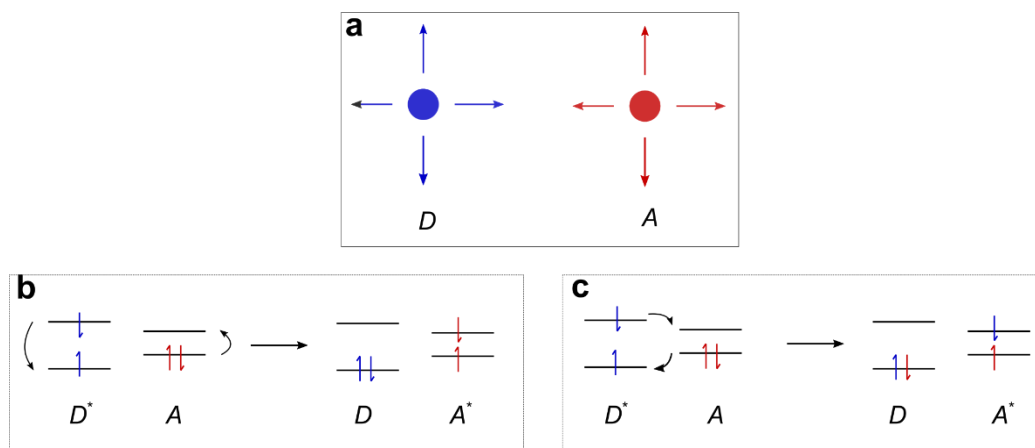


Figure 2.4. The possible energy transfer mechanisms for organic molecules. The donor is marked in blue, while the acceptor is red. (a) Reabsorption. The photon radiated from the donor molecule is absorbed by the acceptor; (b) FRET; The single-side arrow indicates the spin direction of the electron. The FRET happens in forms of non-radiative dipole-dipole interaction without exchange of the electron. The spin is conserved after the process. (c) Dexter energy transfer, where the electron of the donor molecule is exchanged with the electron of the acceptor molecule in the ground state.

2.3.1 Reabsorption

The simplest energy transfer can happen through a two-step process, involving the emission from the donor D and the absorption of a photon having a frequency ν by the acceptor A :



This energy transfer process is referred as reabsorption with a radiative and an absorption process. Because these two steps are completely separated and solely depend on the emission property of the donor and the absorption property of the acceptor, the process of FRET is not involving the spin of excitons. Since the acceptor can capture only small fraction of emitted photons in the device level, giving a quite low energy transfer efficiency, energy transfer in a form of reabsorption in OLEDs plays a minor role. Nevertheless, there are demonstrations in which utilizing the reabsorption process to make white emitting devices with the acceptor molecules as an external down-conversion layer.[54,55]

Non-radiative energy transfer processes are of vital importance in OLEDs, which in general can be divided into two distinctive transfer mechanisms, named as Förster and Dexter energy transfer, ascribing to Coulomb and exchange interaction, respectively. The following sections will give a detailed discussion for each mechanism.

2.3.2 Förster resonance energy transfer

The FRET happens in a form of dipole-dipole interaction between the donor molecule and the acceptor. The spectral overlap between the emission spectrum of the donor and the absorption of the acceptor is needed, which can be quantified in the spectral overlap integral J :

$$J = \int_0^{\infty} \bar{I}_D(\nu) \frac{\bar{\epsilon}_A(\nu)}{\nu^4} d\nu \quad (2.17)$$

where \bar{I}_D and $\bar{\epsilon}_A$ indicate normalized intensities with respect to the integrated band for the donor and the acceptor molecule, dependent on the frequency ν . As shown in Figure 2.4b, the FRET happens via dipole-dipole interaction through space. The radius (R_0) for this process is given by:[10]

$$R_0 = \sqrt[6]{\frac{9000c^4 \ln 10 \kappa^2 \Phi_D J}{128\pi^5 n^4 N_A}} \quad (2.18)$$

where c is the velocity of the light, κ is the orientation factor, n is the refractive index of the medium, N_A is the Avogadro constant, Φ_D is the PLQY of the donor molecule.

The FRET can efficiently happen in a distance up to 10 nm, which is much larger than the size of small molecules. The transfer efficiency E_F is determined by the molecular distance r between the donor and acceptor molecules:

$$E_F = \frac{1}{1 + \left(\frac{r}{R_0}\right)^6} \quad (2.19)$$

As shown in Figure 2.4, the total spin of each molecule is conserved after the energy transfer, leading to the following allowed energy transfer interactions:



It should be noted that a transfer from a triplet to a singlet state, i.e.



is forbidden, since it involves two simultaneous intersystem crossing steps. However, if a phosphorescent donor is used, the following transfers are possible because of the spin-orbit coupling and the intrinsic longer lifetime of triplet states of phosphorescent emitters:



2.3.3 Dexter energy transfer

In contrast, Dexter energy transfer is an energy transfer process involving the electron exchange between two neighboring molecules, which requires an orbital overlap between the donor and the acceptor molecules, as shown in Figure 2.4.

Dexter energy transfer obeys the Wigner–Witmer spin conservation rules, requiring the total spin of the spin configuration to be conserved during the transfer.[56] The following energy transfer reactions are allowed:



Since the singlet-singlet dipole interaction is a very efficient via FRET, it is rarely observed in a way of Dexter energy transfer (Equation (2.25)). The triplet energy

transfer from a triplet donor (either conventional fluorescent emitter, phosphorescent emitter or TADF emitter) to another acceptor in the ground state is allowed within the framework of Dexter energy transfer, as shown in Equation (2.26). Equation (2.27) represents the triplet-triplet annihilation. The annihilation process transfers two excitons to one, leading to the exciton quenching. It should be noted that the typical lifetime of triplet excitons are in the microseconds regime, which is long enough to introduce triplet-triplet, singlet-triplet or triplet-polaron annihilation under high exciton concentration.[57–60] These bimolecular quenching effect can decrease the PLQY for phosphorescent and TADF emitters, resulting in an efficiency roll-off under high current density, see details in Section 3.2.6. On the other hand, this additional singlet exciton generation can theoretically increase the IQE for devices based on conventional fluorescent emitters. However, the real efficiency is highly dependent on other bimolecular quenching processes.

In the case of Dexter energy transfer, the energy transfer rate is exponentially dependent on the intermolecular distance. As a reason of that, the Dexter energy transfer is a short distance interaction, with the typical energy transfer radius up to 1 nm.[10]

For OLEDs, photophysical properties of organic emitters are important to achieve a wide scope of emissive colors with high efficiency. On the other hand, charges should be injected and transported into organic emitters from external electrical sources. Thus, the charge transport and exciton diffusion of organic semiconductors and the injection from conductive electrode (metals or metal oxide) into organics are also of importance. In the following sections, electrical properties of organic semiconductors including exciton diffusion, charge transport and molecular doping will be introduced.

2.4 Exciton diffusion

The natural lifetime of an exciton can be defined by the mean time of a molecule remaining in the excited state. For simplification, assuming the molecule without competing non-radiative decay channels, the deactivation of an exciton can only occur by spontaneous emission. For an ensemble of molecules with an excited state density n , the spontaneous emission obeys the first order rate equation:

$$\frac{dn}{dt} = -k_r n \quad (2.28)$$

where k_r is the rate of emission from the excited states. The integration of the differential equation gives the time dependent exciton density with the initial density at n_0 :

$$n(t) = n_0 e^{-k_r t} \quad (2.29)$$

In real cases, there are various channels for deactivation from excited states, including the radiation, intersystem crossing with a rate of k_{ISC} or other non-radiative relaxations with a rate of k_{nr} , as shown in Figure 2.2. The final lifetime of an exciton is dependent on the sum of these rates, as discussed in details in Section 2.2.

There is a possibility for excitons to diffuse from the generation interface to areas with lower exciton concentration. The diffusion of excitons can be described by Fick's 2nd law. When neglecting higher order processes, the time dependent exciton density at position z reads:[61]

$$\frac{\partial n(z, t)}{\partial t} = G(z, t) - \frac{n(z, t)}{\tau} + D \frac{\partial^2 n(z, t)}{\partial z^2} \quad (2.30)$$

where G denotes the exciton generation, D is the diffusion constant and τ the lifetime of the exciton. When assuming the exciton generation as a delta-shaped profile:

$$G(z, t) = g\delta(z = 0, t) \quad (2.31)$$

the steady state solution ($\partial n(z, t)/\partial t = 0$) of Equation (2.30) reads:

$$n(z) = n_0 \cdot \exp\left(-\frac{z}{L}\right) \quad (2.32)$$

where L is the exciton diffusion length, described as:

$$L = \sqrt{D\tau} \quad (2.33)$$

A wide range of values has been reported for the diffusion length of organic semiconductors, highly dependent on the material and the excitation method. In general, the diffusion length for singlets is in the range of few nanometers.[62] The triplets are assumed to have a longer diffusion length, resulting from their longer lifetime, which can reach to regime of several micrometers in highly ordered systems.[63]

2.5 Charge carrier transport

As discussed in the previous sections, the HOMO level of organic semiconductors is occupied with electrons while the LUMO level is empty. Organic molecules can then be charged by either adding an additional electron in the LUMO as a negative charge, or removing the electron from the HOMO level as a positive particle. Since electrons and holes are strongly localized within organic molecules, a band transport like in inorganic semiconductors is not possible. The charge carrier transport under the driving voltage and/or the charge diffusion because of a difference of charge concentrations is determined by a series of hopping events of charge carriers between neighboring organic molecules. Charges are hopping from state to state, where the overall states are distributed energetically in a form of a Gaussian distribution.[64] Under an external electric field, a drift of the charge carriers is induced. The mobility μ can be technically defined as the ratio between the velocity v of the electrical charges and the amplitude of the applied electric field F :

$$\mu = \frac{v}{F} \quad (2.34)$$

At the interface of metallic electrode and the organic semiconductor, the energy barrier resulting from the difference between the work function of metals and the electron affinity ability or the ionization potential of organic semiconductors, sets the energy threshold for the excess energy required to inject the electrons from the metal to the semiconductor, or vice versa. In the case of Ohmic contact, where almost no resistance is in presence between the electrode and the organic semiconductor, the organic layer can be charged at the interface in the proximity of metals. The accumulation of charges at the interfaces generated an electric field can further hinder the charge transport, known as space-charge limited current (SCLC).[65] The current density j in a simple device architecture with an intrinsic semiconductor layer sandwiching between two metal electrodes under applied bias U for Ohmic injection in one-dimensional case can be described by the Mott-Gurney law:[66]

$$j = \frac{9}{8} \varepsilon_0 \varepsilon \mu \frac{U^2}{L^3} \quad (2.35)$$

where ε_0 denotes the permittivity constant, ε the permittivity of the organic material and L the thickness of the organic semiconductor.

The SCLC measurement can be used to determine the charge mobility of organic semiconductors, according to Equation (2.35). However, it should be noted that the

Mott-Gurney law is valid in the absence of traps at low electric fields without the consideration of diffusion contributions and temperature dependence.[66] The exclusion of background impurity induced traps, contaminations and/or oxidation on the surfaces is needed to obtain reproducible and reliable results, giving the measured mobility highly dependent on the sample preparation techniques. There are several other methods to measure the charge carrier mobility for organic semiconductor films, including the time-of-flight method, field-effect mobility measurements in unipolar devices, and field-effect transistor configuration.[66,67].

It should be noted that the charge mobility for holes and electrons can be different for one organic semiconductor. For typical intrinsic organic semiconductors as polycrystalline and amorphous state, the mobility of charge carriers is electrical field, temperature and concentration dependent, in the range of 10^{-8} to 10^{-2} cm^2/Vs , which is much lower than inorganic semiconductors.[68–70] As discussed in Section 2.1, since the electrical conductivity of organic semiconductor is resulting from the extended conjugation system, the enhancement of conjugation of organic compounds can potentially enhance the intrinsic conductivity for each molecule. In the film state, where the charge carrier transport is happening in forms of hopping, the packing can make a substantial effect on the charge carrier mobility.

2.6 Molecular doping

Similar to inorganic semiconductors, efficient doping of the charge transport layer can increase the density of free charge carriers, leading to a significant enhancement of conductivity in organic films by several orders of magnitude. The doping of carrier transport layers in OLEDs and other organic devices has been intensively explored and is still an important scientific research topic.[71–74] In 1998, Bharathan and Yang showed a reduced driving voltage for a polymer OLED device based on a structure of indium doped tin oxide (ITO)/3,4-polyethylenedioxythiophene-polystyrenesulfonate (PEDOT:PSS)/poly(2-methoxy-5-(2'-ethyl-hexyloxy-1,4-phenylene vinylene) (MEH-PPV)/Al with p-doped hole and n-doped electron transport layer.[75] They achieved the p-doping effect by modifying the ITO anode with a thin acid layer and n-doping effect with an active metal near the thick cathode Al on the top of the emission layer. The Fermi level is pinned to the electrodes, leading to a lower energy barrier for charge injection from ITO anode or Al cathode to MEH-PPV layer without matching of the work function of these electrodes. However, in this case, excitons generated in the MEH-PPV layer can also be quenched by dopant molecules near the emission layer, resulting in a low light intensity and efficiency.

The principle of organic p- and n-doping is schematically showed in Figure 2.5. For p-doping, the HOMO of the matrix gives an electron to the LUMO of the acceptor (dopant), leading to a higher hole density and thus higher conductivity in the doped layer. A similar working process is considered for n-doping, but here an electron is given from the HOMO of the dopant to the LUMO of the matrix. Since the doped layer shows orders of magnitudes higher conductivity compared to the intrinsic transport layer, the increase of thickness of the doped layer has little influence on the electrical property of OLEDs, but the cavity thickness can be gradually tuned.[76,77]

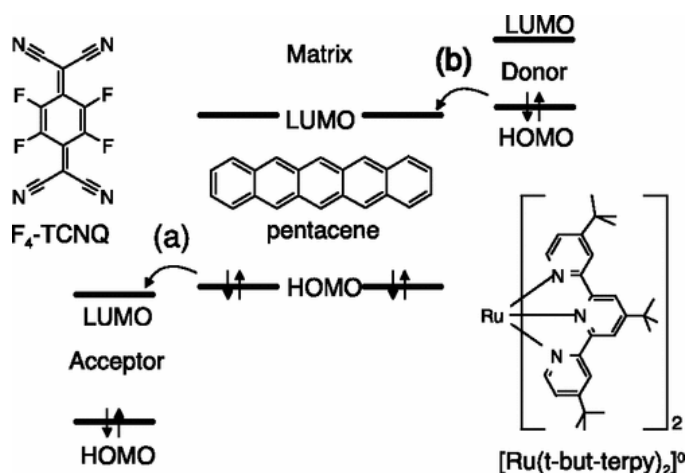


Figure 2.5. An example of the energy diagram of p-i-n doping concept. (a) Pentacene doped with F₄-TCNQ for p-doping and (b) n-doping with [Ru(t-but-terpy)₂]⁰. Reproduced from reference [261] with permission.

It should be noted that the p-dopant possesses usually a small energy bandgap, which can absorb the light emitted from the device, decreasing the OLEDs performance by absorption.[66] For n-dopants, since the HOMO level should be higher than the LUMO energy of the matrix. This requirement pushes the LUMO energy level of the n-dopant towards the vacuum energy. As a reason of that, the existing n-type dopants are highly reactive metals or salts, which are very sensitive to oxygen.[78,79] It is generally more difficult to find suitable n-dopants compared to p-dopants.

The second effect of organic doping is that effective doping can reduce the energy barrier between the conductor and organic materials, which actually might be even more important than the effect of increased charge motilities. The energetic alignment plays a crucial role when making Ohmic contacts between metals or conductive transparent oxides and organic materials. Theoretically, one would choose the contact materials such that the surface work function of the conductive oxides or metals aligns with the HOMO of organic materials at the hole injection side or with the LUMO level at the electron injection side. However, in real case, this is rarely possible because of the limited number of molecules meeting all desired properties. Due to the difference

in the work function of the metal and organic molecule, the energy level of the organic layer is depleted by doping at the interface, while the remaining dopant molecules generate a space charge zone. As shown in Figure 2.6, the organic doping leads to an energy level bending towards the Fermi energy E_F of the anode, increasing the tunneling probability of charges into the doped organic layers. The Ohmic injection is achieved without energy barrier and decreases the voltage drop at the interface, reducing the voltage losses in devices.

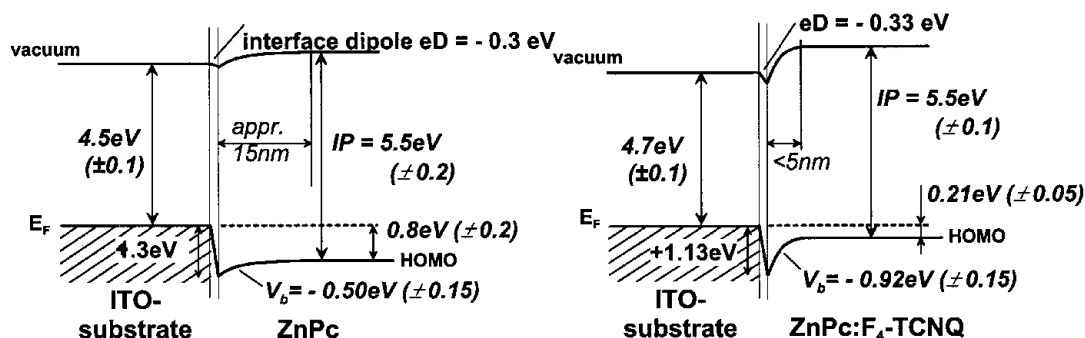


Figure 2.6. Energy level bending at the metal-organic interface by organic p-doping technique. Left: Intrinsic ZnPc layer without doping; right: doped with F₄-TCNQ. Reproduced from reference [262] with permission.

2.7 Thermal property

Organic materials can be deposited by means of thermal evaporation or spin-coating, giving the final composition in amorphous or crystalline state. Since the crystalline solids possess anisotropic optical, electrical or chemical properties, organic materials prepared as amorphous states are preferred over crystalline solids for OLEDs. On the other hand, organic semiconductors packed in a form of crystalline state can be beneficial for devices such as organic transistors where high charge mobility is needed.

Amorphous organic films consist of randomly orientated organic molecules bounded by weak intermolecular forces. Without introducing phase transition, the thermal energy can enhance the atomic vibrations, slowly ordering the molecular moieties to reduce the system energy. The glass transition of solid-state materials may occur from cooling the system, with significant change of heat capacity, viscosity or density, while no pronounced change in material structures. For polymers and small organic molecules, they can easily form glasses even upon very slow cooling or compression, since lack of a well-defined crystalline structure. Above the glass transition temperature (T_g), the movement of molecular groups is enhanced, while the

entire system keeps as a solid form below the melting temperature. However, it is possible to make the material decompose while further increasing the heating temperature.

The thermal property of materials is very important for organic semiconductors, since either a thermal evaporation or an annealing process can significantly affect the microscopic structure of the amorphous film. By finely tuning the processing temperature, films with higher density, different carrier mobility or anisotropic dipole orientation could potentially be achieved and lead to an enhancement of device performance in organic light-emitting diodes or organic solar cells.[80,81] The glass transition temperature of the materials used in OLEDs or solar cells may also relate to the device reliability, since the heat generated during operation could potentially warm up the device above T_g of some materials used in the device.[82,83]

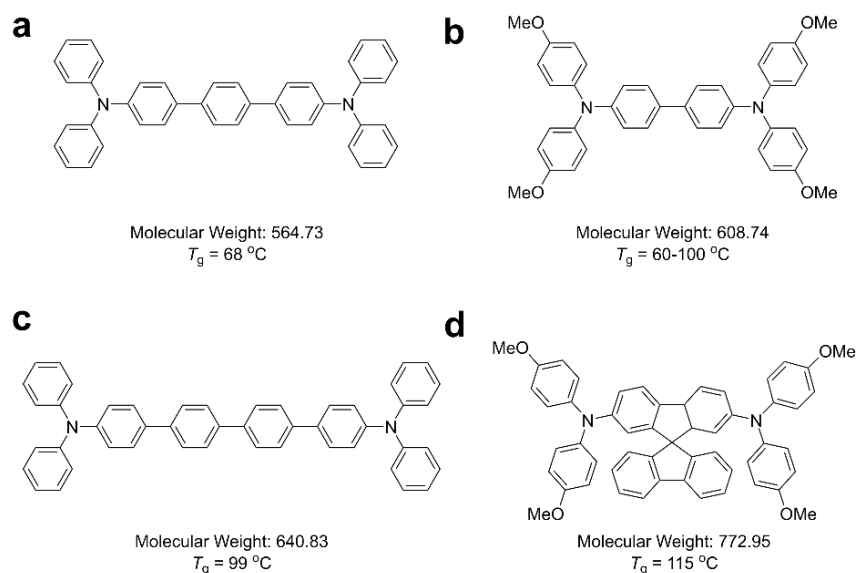


Figure 2.7. The relationship between the glass transition temperature and the chemical structure. For materials (a) with molecular weight of 564.7 g/mol, the T_g is 68 °C. For material (c) with one more benzene ring compared to (a), the T_g is 99 °C. For material (b), the molecular weight is 508.7 g/mol with T_g about 60-100 °C. The presence of twisted group in (d) gives a higher T_g at 115 °C.

Based on a pronounced change of energy absorbing or releasing rate when materials shift to the glass state, the differential scanning calorimetry (DSC) method is developed to determine T_g . The decomposition temperature, which indicates the highest temperature the materials can stand in the absence of oxygen, can be measured by thermogravimetric analysis (TGA), by tracking the weight loss in the route of increasing temperature in absence of oxygen.

The glass transition temperature of an organic material is highly dependent on its chemical structure. There is an empirical experience that the increase of the molecular weight, number of aromatic ring or the rigidity of molecular structure can gradually increase the T_g , as presented in Figure 2.7.

Previous investigations have revealed that the deposition substrate temperature of organic materials by thermal deposition can influence the photostability and emitting dipole orientation. [84,85] In cases when the substrate temperature during material deposition is in the range of 0.8 to 0.9 T_g of the emissive layer with low growth rates, the OLED efficiency can be enhanced with an extended lifetime.[86] The variation of substrate temperature can be easily achieved by external heating or cooling, which gives an additional pathway for device optimization.

3 Basics of organic light-emitting diodes

The chapter focuses on the fundamentals of organic light-emitting diodes. First, a brief introduction is given about the device working principle, the general device structure and performance parameters. In the following sections, methods to fabricate white OLEDs, the conversion of injected charges to photons, the photon dissipation and trapped modes in devices are summarized, followed by a summary of the existing outcoupling technologies. In the end, the typical methods to make micro/nano structures to outcouple trapped photons in OLEDs are reviewed.

3.1 Working principle and device structure

In the very early stage of the electroluminescence (EL) from organic semiconductors, hundreds of Volts were needed to observe light emission from anthracene crystals.[87] In 1987, C. W. Tang *et al.* reported the first thin film OLED working with a bias of less than 10 V, with two organic layers sandwiched between a bottom semi-transparent anode ITO and a top cathode (Mg: Ag alloy).[1] After decades of research, state-of-the-art OLEDs are in general thermally deposited with multiple functional layers based on small molecules and metal oxides. Various functional layers including the hole injection layer (HIL), hole transport layer (HTL), electron blocking layer (EBL), hole blocking layer (HBL), electron transport layers (ETL) and electron injection layer (EIL) have been introduced to achieve high device efficiency and lifetime, as well as to decrease the driving voltage. Figure 3.1 illustrates the energy diagram and working principle of a multilayer OLED.

First, under electrical operation with a typical driving voltage, electrical charges including holes and electrons are injected from the anode and cathode, respectively. Holes are injected from the anode with a high work function into the HOMO of the HIL and then hopping to the HTL. Meanwhile, electrons are injected from the cathode into the LUMO of the EIL and then into the ETL. Here, the injection layers are very important to decrease the energy barrier and the driving voltage, as discussed in Section 2.5 and 2.6. Second, charges go through the transport layers and the blocking layer before they recombine to form excitons in the emissive layer. The area where the exciton forms is generally named as the recombination zone. The functionality of blocking layers includes preventing the leakage of the opposite type of charge carrier, confining excitons within the recombination zone especially when their lifetime is long

and spatially separating excitons with dopants in doped transport layers.[88] In the end, excitons deactivate to the ground state by spontaneous radiation. Care must be taken to choose and optimize the thickness of these functional layers. The variation of the layer thickness of injection layers can affect the charge injection from the electrodes into the device and further the charge balance and the efficiency of exciton generation. The thickness of the ETL and/or HTL layer can substantially affect the cavity resonance, which will be discussed in detail in Section 3.9.4. Shift of the emissive color can be noted for many OLEDs when increasing the driving voltage, which can raise from many reasons, among which the change of the recombination zone is one of the possible and important reason. The blocking layers sandwiching the EML, possess the ability to confine the injected charges in the recombination zone by matching the HOMO and LUMO levels, as shown in Figure 3.1. For devices with phosphorescent and/or TADF emitters, the triplet energy of blocking layers should be higher than that of emitters, to avoid the reverse energy transfer from emitters to the blocking layer.

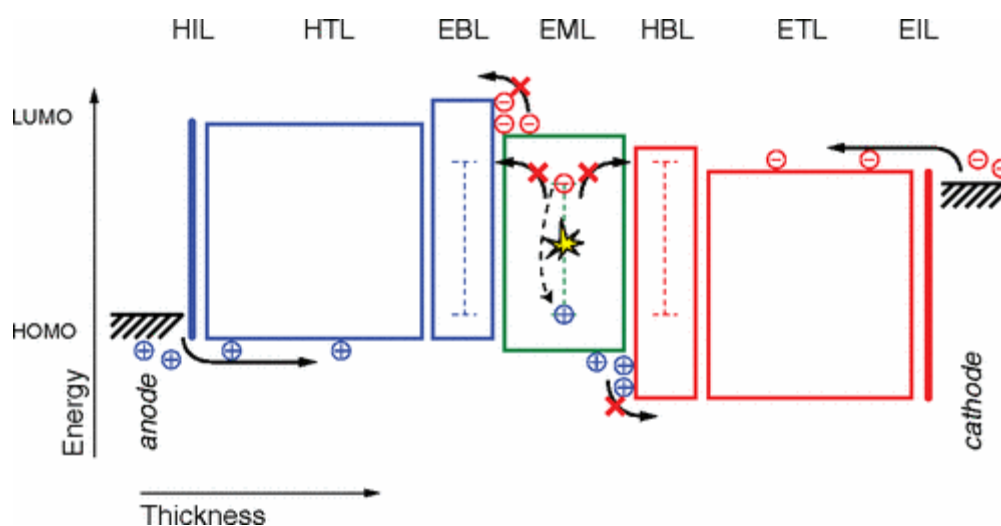


Figure 3.1. The energy diagram of a typical multilayer OLED. In some devices, different functions may be achieved by one layer. Reproduced from reference [88] with permission.

The representative architectures of OLEDs are summarized in Figure 3.2. The typical bottom emitting non-inverted device (Figure 3.2a) consists of a transparent anode on top of the substrate, followed by functional layers and capped with a highly reflective metallic cathode. In this configuration, photons generated in the EML go through the bottom transparent anode and then into the substrate and air zone. ITO is commercially available and widely used as the bottom transparent anode. However, the ITO anode has disadvantages including the utilization of indium, brittleness and the requirement of high temperature treatment to obtain high transmittance and low sheet resistance. Much research effort has been put in alternative electrodes.[89–92]

The typical device structure of top emitting OLEDs is shown in Figure 3.2b. In this configuration, the bottom anode is in general an opaque metallic electrode while the top cathode consists of a semi-transparent metallic layer. Since the sputtering of ITO can damage the deposited organic functional layers, a thermally deposited semi-transparent metal layer is used as the top electrode in top emitting OLEDs. The top emitting configuration is important for the display application, because the bottom metallic anode can be thermally deposited on the driving panel beneath.[93–95] It is worth noting that the top semi-transparent cathode plays a crucial role on the device performance. The microcavity formed between the top semi-transparent cathode and the bottom opaque anode can enhance the device efficiency by constructive resonance, while it may also introduce a serious angular dependent emission. The balance between the efficiency and angular dependent emission should be considered. With a capping layer on top of the cathode, the transmittance and the cavity resonance can be tuned, leading to comparable or even slightly higher efficiency of top monochrome OLEDs compared to the bottom counterpart.[96,97]

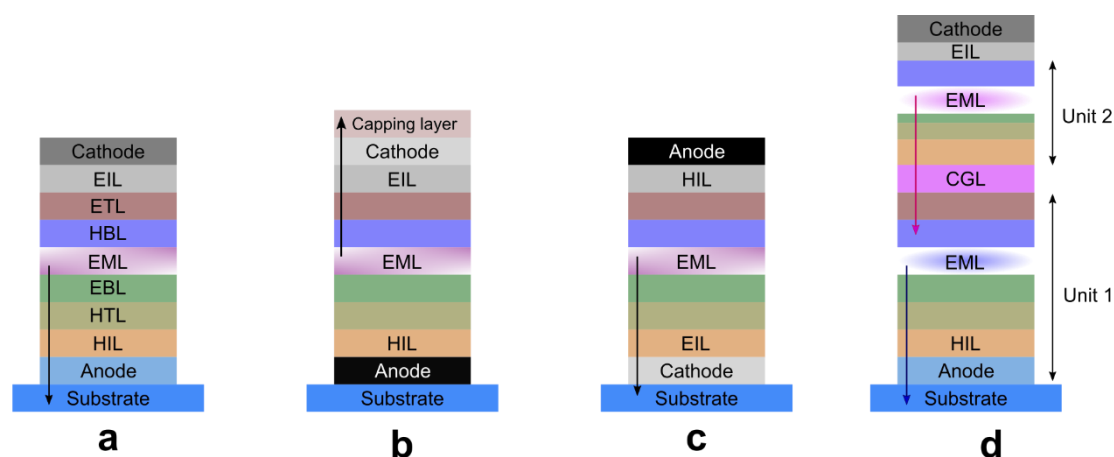


Figure 3.2. Representative device architectures for OLEDs. (a) Bottom emission. (b) Top emission. (c) Bottom inverted. (d) Two-unit bottom tandem configuration. For (b)-(d), some functional layers are omitted for presentation.

The device configuration of inverted bottom emitting OLEDs is, to some extent, similar with the non-inverted bottom OLEDs. As shown in Figure 3.2c, the cathode of inverted bottom emitting OLEDs is geometrically located on the substrate, while the top opaque metallic anode is located on top of the organic layers. A top emitting inverted OLED can also be realized, if the top anode is semi-transparent while the bottom cathode is opaque. [98,99]

The tandem device structure, as shown in Figure 3.2d, consist of several emissive units and each of them is connected by a charge generation layer (CGL). Each emissive unit can consist of multiple functional layers as in a typical single unit device, with ETL, HTL and blocking layers. Much research effort has been dedicated to investigate the working mechanism of CGL.[100,101] The intermediate CGL is in general comprised

of a p-type and another n-type layer. Under an applied voltage, electrons and holes are generated within the CGL and then injected into the neighboring injection layers. In principle, the EL intensity of the tandem OLED can linearly increase with the number of emissive units under the same current density. Hence, it is possible to obtain a comparable luminance with half of the driving current density compared to the single unit device. This fascinating feature can potentially give a longer device lifetime under high luminance intensity, which is of vital importance for display and solid-state lighting applications. When carefully tuning the emissive color from each unit, tandem white OLEDs can also be realized.[102,103]

Polymer based OLEDs are typically fabricated by spin-coating, spray-coating or ink-printing techniques, where solvents are removed by the following annealing process. The fact that organic solvents can harm the underlying layers makes it difficult to achieve complicated device structures. In order to get high performance for devices based on solution processing, tremendous efforts have been made on improving the fabrication techniques. Concepts including the application of crosslinking polymers to enable the spin-coating of the sequential layers, using orthogonal solvents to protect the layer underneath and cross-linking with direct photolithography to obtain patterned polymer layers have been introduced.[104–106]

According to the discussion above, it is possible to obtain transparent devices when both bottom and top electrodes are semi-transparent. This feature can be easily achieved by using a bottom transparent ITO or thin metal anode together with a top semi-transparent metallic cathode. When further replacing the brittle ITO with flexible electrodes such as metal nanowires, conductive polymer or graphene based electrodes, flexible and bendable OLEDs can be realized on a flexible substrate.[107,108] For a typical OLED device, the thickness of each functional layer is in a range of several nanometer to tens or hundreds of nanometer, giving the total device thickness as low as hundreds of nanometer to several micrometer. Hence, OLEDs possess the merits of light-weight, flexibility, tunable emissive color and transparency, making them a competitive technology for display and solid-state lighting applications.

3.2 Device characterization

3.2.1 Internal and external quantum efficiency

The internal quantum efficiency (IQE), is defined as the ratio of emissive excitons to injected charge pairs. However, there is only a fraction of emissive excitons that can spontaneously emit photons and subsequently escape from the multilayer structure. The external quantum efficiency (EQE) is defined as the ratio of the total number of escaping photons to the total number of injected charge pairs, which is one of the most important parameters to quantify the performance of an OLED. In the ideal case, all the injected charge couples form an exciton, which is radiatively deactivated and the photon is subsequently coupled from the device into the air zone. Factors which influence the IQE and EQE will be discussed in detail in the later sections.

3.2.2 Current efficiency

The current efficiency η_{CE} is defined as the luminance L divided by the injected current density j :

$$\eta_{CE} = \frac{L}{j} \text{ [cd/A]} \quad (3.1)$$

The current efficiency is widely used in the display industry.

3.2.3 Luminous efficacy

The luminous efficacy η_{LE} is defined as the ratio of the emitted luminous flux Φ to the consumed electrical power P externally to drive the device:

$$\eta_{LE} = \frac{\Phi}{P} = \frac{\Phi}{UI} \text{ [lm/W]} \quad (3.2)$$

where U represents the applied voltage.

The luminous efficacy is more related to the lighting field than the display application. Under the assumption of Lambertian distribution, for a device with an area of A , the luminous efficacy can be obtained with:

$$\eta_{LE} = \frac{\pi LA}{UI} \quad (3.3)$$

3.2.4 Color quantification and quality

To quantify the color, the human perception of light with different spectra should be taken into account. In 1931, the International Commission on Illumination (CIE) set up a standard color coordinate (CIE coordinate) to quantify the color in a form of XYZ color space. To eliminate the perception variation from different viewers, the CIE defined the standard observer to represent as the average chromatic response of human beings. The standard observer within the visible wavelength from 380 nm to 780 nm, is characterized by three color matching functions, as shown in Figure 3.3a. These color matching functions can be treated as the spectral sensitivity curves of three linear light detectors (human visibility), yielding the CIE tristimulus values of X , Y and Z , respectively.

In the emissive case, the CIE tristimulus values X , Y , Z can be obtained by:

$$X = \int_{\lambda} I(\lambda)x(\lambda)d\lambda, \quad Y = \int_{\lambda} I(\lambda)y(\lambda)d\lambda, \quad Z = \int_{\lambda} I(\lambda)z(\lambda)d\lambda \quad (3.4)$$

where the $I(\lambda)$ represents the spectral radiance of the light source.

The x , y , z coordinates in the CIE1931 color diagram then are given by:

$$x = \frac{X}{X + Y + Z}, \quad y = \frac{Y}{X + Y + Z}, \quad z = \frac{Z}{X + Y + Z} = 1 - x - y \quad (3.5)$$

The emitted color of OLEDs can be described by x and y in the two dimensional CIE1931 color diagram, as shown in Figure 3.3b. Typically, the spectrum with a color coordinate (0.447, 0.407) at point A is referred to as the warm white. Meanwhile, the coordinate (0.333, 0.333) at point E is defined as cold white.[88]

NTSC, named after the National Television System Committee in North America, is the most widely used color standard for the television color system. The original 1953 color NTSC standard, defined the colorimetric CIE coordinate values as follows: primary red R(0.67, 0.33), primary green G(0.21, 0.71) and primary blue B(0.14, 0.08). These typical points are also plotted in Figure 3.3b. In principle, with the primary blue, green and red, it is possible to obtain all other colors by mixing the primary colors with different ratios.[109]

For solid-state light sources, another important quality is the ability to reveal the color of various illuminated objects. The color rendering index (CRI) is defined as the performance of a light source on the color appearance of illuminated objects by comparison with their color appearance under a reference radiator.

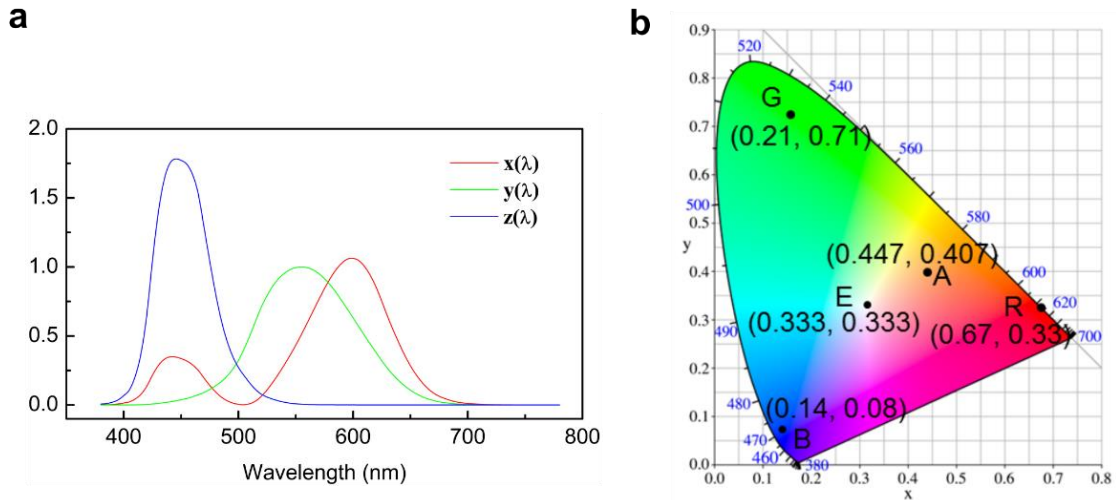


Figure 3.3. (a) Three color matching functions. (b) Two dimensional CIE1931 color diagram. The points B represents primary blue, G primary green and R primary red according to the NTSC standard. The CIE coordinates A is the warm white and E is the cold white color.

The CRI is defined in the range from 0 to 100. The higher the CRI value, the better the color rendition of the light source. By definition, an incandescent lamp has the highest CRI of 100. For a typical light source, a CRI value above 90 is very good at color rendering and it is still good between 80 and 90. For most of lighting applications, a CRI value between 60 and 80 would be sufficient. Generally, a minimum CRI of 75 is needed for the indoor solid-state lighting. Since the CRI is directly related to the emission spectrum of the light source, it is possible to obtain very good CRI values for white OLEDs by tuning the emission spectrum.

3.2.5 Angular dependent emission

As discussed in the Section 3.1, the basic structure of an OLED is like a sandwich, consisting of a bottom and top electrode forming a microcavity. The spectrum observed from different angles is dependent on the microcavity and the intrinsic emission of the emitter in free space. For general display and solid-state lighting applications, the color shift in different observing angles is unwanted. In very typical cases, the angular dependent emission behavior for OLEDs can be used to shape the radiated beam into a specific zone for some special applications.[110]

To quantify the angular dependent emission for an OLED, the change of the EL spectrum and the CIE color coordinate at different observing angles would be one possible way. Since the cavity leads to an inhomogeneous distribution of the electromagnetic energy radiated from OLEDs into the forward hemisphere, the distribution of radiance at different observation angles can be another parameter to describe the angular dependent emission for OLEDs.

3.2.6 Efficiency roll-off

The fact that the efficiency of OLEDs tends to decrease with increasing luminance or current density is referred to as efficiency roll-off, a universal phenomenon found in most of OLEDs known today.[57] Intensive research has been conducted to understand the cause of this roll-off. For OLEDs based on fluorescent emitters, factors including single-singlet, singlet-polariton, singlet-triplet annihilation and unbalanced charge carriers could contribute to the efficiency decrease when increasing the current density. Compared to the fluorescent counterpart, the roll-off is more pronounced for OLEDs based on phosphorescent and TADF emitters. Since the triplet contributes to the device efficiency with an intrinsic longer lifetime, additional processes such as triplet-triplet, singlet-triplet and triplet-polariton annihilations play important roles.[88] The roll-off can be improved by engineering the device architecture, such as using multiple emissive layers with different hosts to balance charge transport and graded doped emitters. Reducing the aggregation of emitters and decreasing the Förster radius could also improve the roll-off.[111] Since the intrinsic reason of roll-off is resulting from several orders higher lifetime of triplets compared to singlets, strategies to reduce the exciton lifetime are potentially helpful, but reasonable device efficiency should also be maintained at the same time.

3.3 Monochrome and white OLEDs

The emission color of OLEDs plays an important role, since both display and lighting applications are highly dependent on the color quality. It is then reasonable to briefly summarize the design principle to realize monochrome and white OLEDs.

3.3.1 Monochrome OLEDs

The monochrome OLEDs with a single emission color can be easily realized by using a single emitter based on the device structure introduced in Section 3.1. By using multiple functional layers together with proper emitters, efficient monochrome OLEDs with spectra from deep blue, sky blue, green, yellow, orange, to red and deep red can be realized. It should be noted that the microcavity formed between two electrodes can be used to enhance the color purity, where the detailed discussed will be done in Section 3.9.4. For display purposes, OLEDs with emission of the three primary colors (blue, green and red) have gained special attention, since the combination of these primary colors gives a variety of colors for display purposes. At this moment, the highest EQE of blue and green OLEDs has been reached with more than 30% by utilizing

phosphorescent and/or TADF emitters.[38] Meanwhile, the device lifetime for OLEDs based on blue phosphorescent or TADF emitters needs to be further improved. The highest reported lifetime T_{50} (luminance decreases to 50% of the initial luminance at 1000 cd/m^2) of blue OLEDs based on TADF emitters is ~ 450 h.[112] The lifetime T_{80} for OLEDs based on phosphorescent emitter is ~ 330 h with the same initial luminance at 1000 cd/m^2 .[60]

3.3.2 White OLEDs

Much research effort has been put in achieving highly efficient and color stable white OLEDs, since they can be used as solid-state light sources. Here, strategies to achieve white OLEDs are briefly summarized. White OLEDs based on solution-processing can be applied to precisely control the doping concentration in a single-EML structure, but the device efficiency and the reliability need to improve.[113,114] The summary here is focusing on OLEDs with small molecules fabricated by thermal deposition.

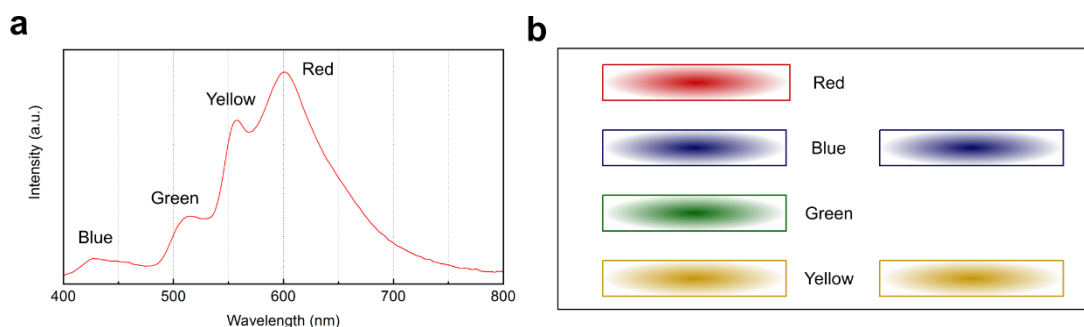


Figure 3.4. Color combination for white OLEDs. (a) A representative EL spectrum for white OLEDs with four color components: blue, green, yellow and red. (b) The possible emissive units combination in devices to achieve white emission. It is possible to have four color components from a single device. In other cases, three primary colors or the combination of blue and yellow emissive units can give white emission.

As shown in Figure 3.4, to achieve white emission, normally more than one emissive sources is needed. According to the difference of involved emitters described in Section 2.2.3 to 2.2.5, white OLEDs can be divided into three categories: 1. All fluorescence white OLEDs based on merely fluorescent emitters including the conventional fluorescence emitter and the TADF emitter. 2. Hybrid white OLEDs with fluorescent and phosphorescent emitters. 3. All phosphorescence OLEDs with phosphorescent emitters only.

In general, to achieve white OLEDs, the configuration of emissive layers (EMLs, Section 3.1) can be divided in three different cases according to the characteristic of the EML: 1. Bulk emission layers without doping, where the emission is coming from an intrinsic organic material.[115,116] 2. Host-guest systems where the emitters as guests

are dispersed into wide bandgap host materials.[117,118] There is an energy transfer process in the host-guest system, in forms of FRET (Section 2.3.2) and/or Dexter energy transfer (Section 2.3.3) between the host and guest materials. The host materials are used as the donor while the guest materials as the acceptor in the schemes of energy transfer. 3. The hybrid configuration where the host materials are fluorescent emitters while the guest molecules are phosphorescent emitters, where both the host fluorescent and guest phosphorescent emitters contribute to the white spectrum.[119–121]

3.3.2.1 All fluorescence white OLEDs

The IQE for OLEDs based on conventional fluorescent emitters is limited by the generation of non-radiative triplet excitons, as discussed in Section 2.2.3. Reports from [122] and [123] with EQE close to 5% represent the rule-of-thumb limit for white OLEDs based on fully conventional fluorescent emitters.

The white OLED with bulk emission layer is based on the non-doping technique, which has no need to precisely control the doping concentration. However, many emissive dyes suffer from aggregation caused quenching (ACQ), leading to an efficiency decrease in the neat film. To eliminate the concentration dependent fluorescence emission, emitters with aggregation enhanced emission (AEE) property have been developed.[9,23,124] For these emitters, the PLQY in solvent with a low concentration is lower compared to the one under high concentration or in solid neat film. For white OLEDs based on non-doping emissive layers, the thickness of these layers needs to be precisely controlled to reach a balanced white spectrum.

For all fluorescence white OLED based on the host-guest system, they are composed with doped emissive layers. In contrast to devices comprising TADF or phosphorescent emitters, the triplet energy levels for conventional fluorescent emitters have a minor influence on the device performance, since the triplet exciton is anyway non-radiative and the energy transfer from singlet to triplet excitons is quantum-mechanically forbidden (see Section 2.2.3).

In a single-EML device, the doping concentration of the dopant needs to be controlled to realize a balanced white spectrum with high color quality, as shown in Figure 3.5.[120] The application of multi-EML configuration or mixed host strategy can lead balanced charge injection and broaden the recombination zone, via the combination of different host materials with a preferred transporting mobility for holes or electrons, which facilitates to achieve stable EL spectra under different driving voltages.[117–119] Though the IQE for devices based on fluorescent emitters is limited by the generation of non-radiative triplet excitons, these strategies to obtain color stable white OLEDs do give insights for the development of white OLEDs based on TADF and phosphorescent emitters.

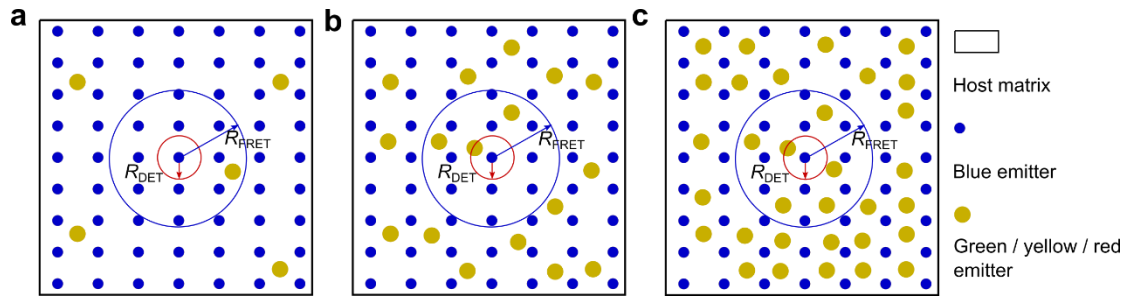


Figure 3.5. The concentration sensitivity of doped dyes for longer emissive wavelength in the host-guest system for white OLEDs with single-EML configuration. R_{FRET} : the radius of FRET; R_{DET} : the radius of Dexter energy transfer. (a) Low doping concentration. Since the doping concentration is so low, only part of the energy from blue emitters can transfer to doping molecules via the FRET. Energy transfer via Dexter energy transfer is impossible for the majority of blue emitters since the distance is much larger than R_{DET} . (b) Medium doping concentration. Both FRET and Dexter energy transfer is possible, but some triplets of blue emitter are still too far to show Dexter energy transfer. (c) High doping concentration. Both singlets and triplets of the blue emitter are quenched by the doped dyes with longer emissive wavelength. For these emitters, it could be conventional fluorescent, phosphorescent or TADF emitter.

The utilization of TADF emitters can harvest non-radiative triplets to emissive singlet excitons. Hence, it is then possible to obtain unity IQE by using TADF emitters in white OLEDs based on all fluorescence emitters.[125,126] Similar device concepts have been developed based on the investigation on conventional fluorescent emitters.[127] To avoid the ACQ and color shifting, the host-guest device system is widely used to construct efficient white OLEDs based on TADF emitters.[128,129] A blue TADF emitter is generally needed to realize 100% IQE for OLEDs based on fully fluorescent emitters. It is possible to construct a white OLED with a blue TADF emitter and either conventional fluorescent emitters or TADF emitters as longer wavelength dyes. For white OLEDs with blue TADF and conventional fluorescent guests, the energy transfer from the blue emitter to conventional fluorescent guest should go through FRET. Thus, the energy transfer should happen between singlet excitons from the blue TADF emitter to the conventional fluorescent emitter to reduce the triplet loss from the conventional fluorescent emitter. The triplet energy transfer via Dexter energy transfer to conventional fluorescent emitters would lead to a non-radiative energy loss. To realize the wanted FRET, the conventional fluorescent emitter should be doped in a low concentration, as shown in Figure 3.5, since the Dexter energy is a short distance energy transfer and can be easily blocked by reducing the doping concentration, as discussed in Section 2.3.3.[126] When all emitters show TADF, the Dexter energy transfer would have less impact on the IQE of white OLEDs. [130,131]

3.3.2.2 Hybrid white OLEDs

The hybrid white OLED is consisting of fluorescent and phosphorescent emitters to obtain a balanced white spectrum. Hybrid white OLEDs with stable blue conventional fluorescent emitters and highly efficient phosphorescent emitters as long wavelength dyes have been intensively studied during the last couple of years.

Hybrid white OLEDs can also be built with bulk emissive layers, single-EML or multi-EML structures with different emitting dopants. Here, the concentration of phosphorescent emitters in the single-EML device should be precisely controlled to obtain a white spectrum. The EL spectrum for these hybrid devices with single-EML is also sensitive to the driving voltage, since the exciton recombination zone can be shifted with different driving voltages.[121] When carefully tuning the material combinations and layer thickness, the multi-EML counterpart is more likely to show better color stability and/or less pronounced efficiency roll-off.

Even though it is possible to use the blue TADF emitter for achieving hybrid white OLEDs, a specific discussion in the following would focus on devices composite of conventional fluorescent blue emitters and phosphorescent emitters, since the conventional fluorescent blue emitter is in general, more stable than TADF emitter in the device.[112] In the single-EML cases, host materials contribute to the white spectrum with higher energy (blue part), while part of energy from host materials is transferred to the phosphorescent dopant with a lower energy level, to compensate the white spectrum in the longer wavelength range. As shown in Figure 3.5, the doping concentration of the guest emitter needs a precise control. In other words, the singlet energy transfer from the blue emitter to phosphorescent emitters is hindered, leading to the singlet emission from conventional fluorescent emitters and triplet emission from the phosphorescent emitters. For very low doping concentration, some of the host blue fluorescent emitter cannot find the doped phosphorescent emitter within the triplet diffusion length. In this case, a part of triplet energy cannot transfer to the phosphorescent emitter, leading to the decrease of device IQE through the non-radiative triplets in the conventional fluorescence emitter. When finely tuning the doping concentration of phosphorescent emitters, the proportion of the blue emission and the yellow/orange emission should be balanced to realize a high color quality white spectrum, together with nearly unity triplet harvesting efficiency. However, when further increasing the doping concentration of the phosphorescent emitter, both the singlet and triplet energy from the blue emitter can transfer to doped phosphorescent emitters, leading to a pure emission from the phosphorescent emitter, as shown in Figure 3.5c.[132]

Compared to the single-EML configuration, another way to harvest triplet excitons can be realized in a multi-EML structure by sequentially separating the blue emission layer and the doped phosphorescent emission layer. The triplet excitons of the blue emitter can transfer to the phosphorescent emitter within a long distance by diffusion. At the same time, the blue emission is coming from the relaxation of the singlets of the blue emitter. To make sure the triplet energy transfer is allowed, the triplet energy level of the phosphorescent emitter should be lower compared to that of the fluorescent emitter. As shown in Figure 3.6, the phosphorescent emitter is dispersed in an adjacent emissive layer close to the blue fluorescence layer. Since the singlet lifetime is shorter than the triplet lifetime, the diffusion length of singlets is shorter than the diffusion length of triplets. Hence, singlets will not reach the phosphorescent emitter when the recombination zone is carefully controlled. In this manner, the singlet transfer is hindered while the triplet transfer is realized by exciton diffusion. The IQE of the device is dependent on the fluorescent emitter, the phosphorescent emitters and the thickness of the emissive layers.[133,134] In the ideal case, all triplet excitons from the conventional blue fluorescent emitter will be transferred to phosphorescent emitters, giving the possibility to achieve unity of IQE in this device concept.

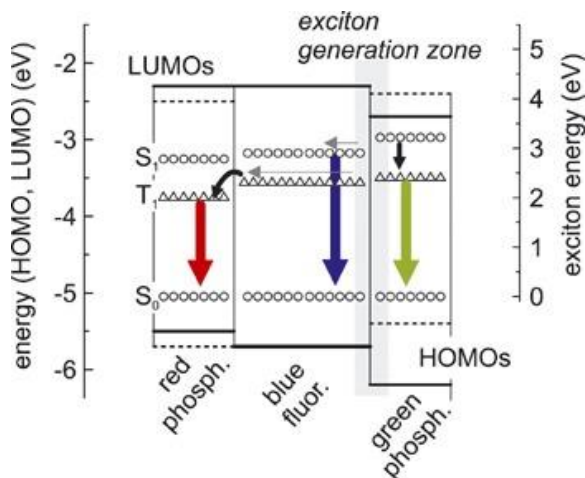


Figure 3.6. The mechanism of triplet harvesting from blue emitter by triplet diffusion to phosphorescent emitters with lower triplet energy level compared to the blue fluorescent emitter. In this scenario, the triplet level of the blue emitter is higher than the red phosphorescent emitter while lower than the green phosphorescent emitter. Reproduced from reference [133] with permission.

3.3.2.3 All phosphorescence white OLEDs

Phosphorescent materials are widely used to achieve highly efficient white OLEDs, since they can intrinsically realize 100% IQE. The device concepts for all phosphorescence white OLEDs are in principle the same as all fluorescence white OLEDs. Thus, configurations of both bulk emission layer and host-guest doping system

can be applied to achieve a balanced white spectrum. In the first case, non-doped intrinsic phosphorescent emitters can be deposited as ultrathin layers and separated by space layers.[135,136] Meanwhile, in host and guest doping systems, single-EML and multi-EML device configurations have been developed to achieve high efficiency, color quality and stability.[137,138] Here again, dopant concentrations and the recombination zone have to be optimized to obtain a white spectrum from a single-EML structure, as shown in Figure 3.5.[139,140] Compared to the single-EML device, the multi-EML configuration allows flexible control of each EML to broaden the exciton distribution, which can be used to obtain good device performance including high CRI, stable spectrum under different voltages and reduced efficiency roll-off.

Based on the tandem device structure, the combination of different emitting units can also give efficient white OLEDs. In the tandem configuration, it is flexible to choose different emitters to achieve 100% IQE and a balanced white spectrum, as shown in Figure 3.4. In general, the fabrication of white OLEDs is more complicated compared to monochrome OLEDs. Moreover, the color stability and roll-off under different luminance is very important for white OLEDs, since high luminance is normally needed for lighting applications. The management of singlet and triplet excitons, broadening the exciton recombination zone, decreasing the exciton lifetime and reducing the molecular aggregation could potentially improve the color stability and reduce the roll-off for white OLEDs.[141]

3.4 Charge-to-photon conversion

The following summary in Section 3.4 and 3.5 is based on the optical model presented by M. Furno *et al.*, which has been successfully applied to understand the optical property of planar OLEDs.[61]

In the presence of a microcavity in the device, the radiative rate of the excitons (either singlets or triplets) in free space k_r is modified as k_r^* , while the non-radiative rate k_{nr} remains the same. The effective radiative quantum yield of the exciton η_{rad}^* in OLEDs can be obtained via the formula:

$$\eta_{rad}^* = \frac{k_r^*}{k_r^* + k_{nr}} \quad (3.6)$$

The lifetime τ^* , similar to the one in free space stated in Section 2.2.3 and 2.2.4, can be determined by the radiative and non-radiative rate in the cavity:

$$\tau^* = \frac{1}{k_r^* + k_{nr}} \quad (3.7)$$

When considering the general case of a system characterized by a single exciton (either singlet or triplet), the exciton concentration per unit volume is a time (t) and position (z) dependent value, denoted as $n(z, t)$. Since the exciton concentration is related to the generation and exciton lifetime τ^* in the cavity, it reads:

$$\frac{\partial n(z, t)}{\partial t} = \xi G(z, t) - \frac{n(z, t)}{\tau^*(z)} - \frac{\partial n(z, t)}{\partial t} \Big|_{\text{losses}} \quad (3.8)$$

where G represents the exciton generation rate from the charge carrier recombination, ξ the generation fraction of the exciton species. The last term accounts for the exciton losses by exciton annihilation channels. Here, the exciton diffusion is not taken into account.

For low current, the exciton annihilation has little influence on exciton losses, the exciton concentration can be further simplified to:

$$\frac{\partial n(z, t)}{\partial t} = \xi G(z, t) - \frac{n(z, t)}{\tau^*(z)} \quad (3.9)$$

Solving Equation (3.9) gives the exciton concentration in the steady state:

$$n(z) = \xi G(z) \tau^*(z) \quad (3.10)$$

According to Equation (3.10), the exciton concentration in the steady state can be evaluated by the generation profile G and the effective lifetime of exciton τ^* in the given optical environment.

If further considering the case when the device is electrically driven with a current density j , the electrical efficiency γ of the device can be defined as a unitless ratio between the density of the decaying excitons and the density of injected electrical charges by the external voltage per unit area and unit time:

$$\gamma = \frac{e \int_z n(z) / \tau^*(z) dz}{j} \quad (3.11)$$

where e denotes the elementary charge.

When excitons are generated within a thin zone in a well-designed device, the generation region can be described by the δ distribution:

$$G(z) = g \delta(z - z_0) \quad (3.12)$$

where $z = z_0$ represents the generic position within the emitting layer. The relation

between the factor g and the generation rate G reads:

$$g = \int_z G(z) dz \quad (3.13)$$

The substitution of Equation (3.11) with (3.12) and (3.13) gives the final form of the electrical efficiency:

$$\gamma = \frac{e\xi g}{j} \quad (3.14)$$

It is noted that the electrical efficiency γ is dependent on the exciton generation in the device, but it is independent on the radiative rate of excitons. The fraction of the singlet and triplet excitons can influence the efficiency, since the triplets of the conventional fluorescent emitter are non-radiative, giving rise to a pronounced decrease of the electrical efficiency in these devices.

The final EQE of the device η_{ext} can be described as:

$$\eta_{\text{ext}} = \gamma \eta_{\text{rad}}^* \eta_{\text{out}} \quad (3.15)$$

where η_{out} denotes the outcoupling efficiency of generated photons from multilayered structures into the far field. Hence, the final EQE is determined by the electrical efficiency of charge carrier conversion to excitons, effective radiative efficiency of the excitons in the optical environment and the outcoupling efficiency of generated photons from the multilayered device.

3.5 Photon dissipation

The radiative decay of excitons and the outcoupling of the generated photons can be treated as classical electrical dipole antennas radiating electromagnetic power with a spectrum. The total radiated power $F(\lambda)$, also known as Purcell factor, normalized to the power in free space, can be obtained according to:

$$F(\lambda) = \int_0^\infty K(\lambda, u) du^2 = 2 \int_0^\infty K(\lambda, u) du \quad (3.16)$$

Here, u represents the normalized transverse wave vector and is defined as $u = k_x/k$, with k the total wave vector at the emitter location and k_x the wave vector in the plane of the emitting source. K is the total spectral power, which is a wavelength dependent parameter.

The dipole orientation of these emitters can also affect the total radiated power. For an emitter with an anisotropic factor a , the total spectral power K per unit normalized in-plane wave vector reads:

$$K = aK_{\text{TM}_v} + (1 - a)K_{\text{TM}_h} + (1 - a)K_{\text{TE}_h} \quad (3.17)$$

where K_{TM_v} denotes the transverse magnetic (TM) mode from vertical dipoles, K_{TM_h} is the TM mode from horizontal dipoles, K_{TE_h} represents the transverse electric (TE) mode from the horizontal dipole. The total spectral power $F(\lambda)$ radiated by the emitter at the wavelength λ reads:

$$F(\lambda) = 2 \int_0^\infty [aK_{\text{TM}_v}(\lambda, u) + (1 - a)K_{\text{TM}_h}(\lambda, u) + (1 - a)K_{\text{TE}_h}(\lambda, u)] du \quad (3.18)$$

The outcoupled power $U(\lambda)$ at wavelength λ is calculated by integrating the spectrum of externally radiated power $K_{\text{out}}(\lambda, u)$ per unit normalized in-plane wave vector :

$$U(\lambda) = 2 \int_0^{u_{\text{crit}}(\lambda)} u K_{\text{out}}(\lambda, u) du \quad (3.19)$$

The upper integration limit $u_{\text{crit}}(\lambda)$ is the maximum value of the in-plane wave vector allowing the generated photons for far-field propagation. By using the Snell's law, with refractive index $n_e(\lambda)$ of the light generation medium and the refractive index $n_o(\lambda)$ of medium in the far-field, the $u_{\text{crit}}(\lambda)$ is obtained as:

$$u_{\text{crit}}(\lambda) = \frac{n_o(\lambda)}{n_e(\lambda)} \quad (3.20)$$

The outcoupling efficiency of a planar organic light-emitting diodes reads:

$$\eta_{\text{out}} = \int_\lambda \frac{U(\lambda)}{F(\lambda)} d\lambda \quad (3.21)$$

For a molecular emitter, the radiative decay rate is k_r in free-space, the effective radiative decay rate k_r^* in the optical microcavity within the device is wavelength dependent. It reads:

$$k_r^*(\lambda) = F(\lambda)k_r(\lambda) \quad (3.22)$$

The effective total decay rate reads

$$k^*(\lambda) = F(\lambda)k_r(\lambda) + k_{nr} \quad (3.23)$$

Accordingly, the radiative decay rate of an emitting molecule in an optical cavity is proportional to the Purcell factor, but the non-radiative decay rate keeps unmodified. Due to a variation of radiative decay rate within the device, the effective radiative efficiency of the emitting molecule varies with the change of the optical cavity. The final effective radiative quantum yield in the cavity is obtained as a ratio between the effective radiative decay rate and the total decay rate:

$$\eta_{\text{rad}}^*(\lambda) = \frac{k_r^*(\lambda)}{k_r^*(\lambda) + k_{nr}} = \frac{F(\lambda)\eta_{\text{rad}}}{1 - \eta_{\text{rad}} + F(\lambda)\eta_{\text{rad}}} \quad (3.24)$$

Summarizing the detailed expression for effective radiative efficiency and outcoupling efficiency for OLEDs, the final EQE for an OLED reads:

$$\eta_{\text{ext}} = \xi\gamma \int_{\lambda} S_{\text{el}}(\lambda) \frac{F(\lambda)\eta_{\text{rad}}}{1 - \eta_{\text{rad}} + F(\lambda)\eta_{\text{rad}}} \frac{U(\lambda)}{F(\lambda)} d\lambda \quad (3.25)$$

where $S_{\text{el}}(\lambda)$ is the normalized luminescence spectrum of the emitter.

The EQE η_{ext} is dependent on the electrical efficiency, effective radiative efficiency and the outcoupling efficiency. The electrical efficiency is solely determined by the electrical properties of the device through the number of useful charge carrier recombination events. The effective radiative efficiency is influenced by the intrinsic radiative quantum yield and the optical environment. The cavity resonance formed by the metallic electrode within the device can induce constructive or destructive interference, giving rise to the opportunity to modify the EQE by tuning the Purcell factor. The outcoupling efficiency is determined by factors such as the anisotropy factor, the refractive index of each functional layer and the device geometry, further discussion about outcoupling efficiency is given in the following sections.

3.6 Photon trapping modes

As shown in Figure 3.2, the typical device architecture for a conventional bottom emitting OLED is based on glass substrates with a layer of ITO anode. Photons generated from organic materials with the typical refractive index n of 1.7-1.8, are propagating to the air zone ($n = 1.0$) via the glass substrate ($n = 1.5$). As shown in Figure 3.7, total internal reflection (TIR) can happen when the light beam is propagating from a medium with a higher refractive index to the other medium with a lower refractive index. The waveguide modes denote photons waveguided in organic layer/ITO anode, while the substrate modes represent the photons trapped in the substrate. These two loss channels are resulting from the gradual change from the high refractive index organic materials, ITO anode to the glass and air with a lower refractive index. In a simple ray-tracing picture and assuming that the light beam initially emits isotropically in all directions within the emissive layer, one can estimate the outcoupling efficiency $\eta_{\text{out}} \approx 1/(2n^2)$, where n is the refractive index of the emissive materials.[142] However, this approximation is oversimplified, since there is a lack of consideration of the anisotropic factor of emitter molecules, the optical cavity thickness and the interaction between photons and free electrons in the conductive metals.

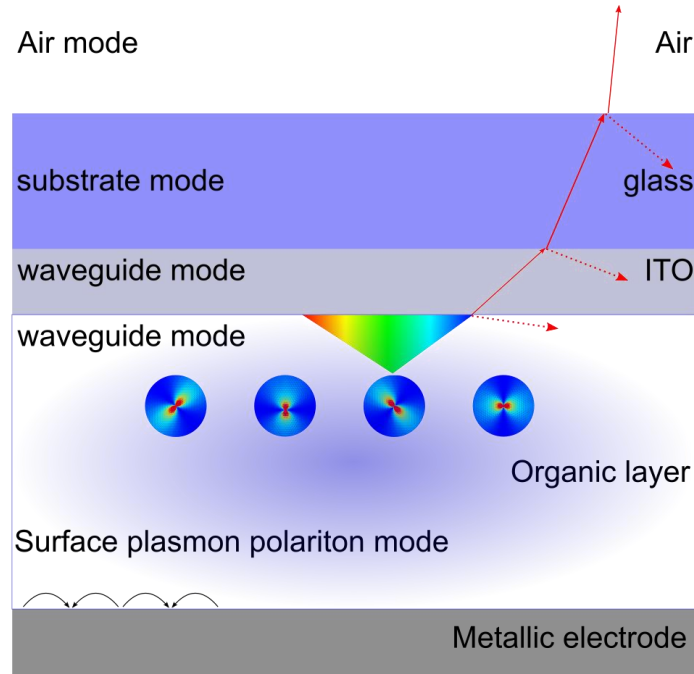


Figure 3.7. Energy trapping mechanism in OLEDs, including refractive indices mismatching induced air mode, substrate mode and waveguide mode and the excitation of SPP modes at the interface between the organic layer and the conductive metallic electrode.

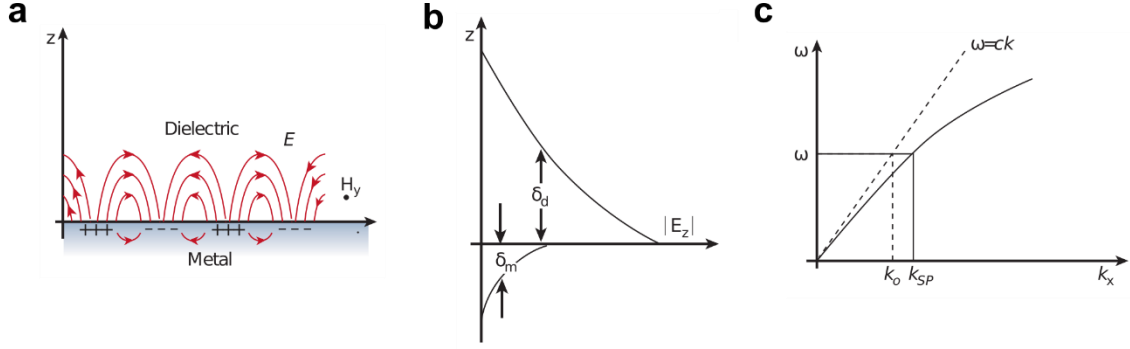


Figure 3.8. Surface plasmon polariton modes. SPP modes at the interface between a metal and a dielectric medium have a combined electromagnetic wave and surface charge character as shown in (a) the electromagnetic field of SPP modes propagating on the surface in the x direction. H_y shows the magnetic field in the y direction of the shown p-polarized wave. (b) The combined character also leads to the field component E_z being enhanced near the surface and exponentially decaying with the distance away from the surface. δ_d is the decay length of the field into the dielectric medium, while δ_m is the decay length into the metal. (c) The dispersion relation for a SPP mode shows the momentum mismatch between the light in free space and SPP mode. The momentum of the SPP mode is larger than the light in free space, indicating the bound, non-radiative nature of SPP mode. The energy is trapped within the surface and evanesces. Reproduced from reference [213] with permission.

The interaction between electromagnetic waves and free electrons in metals can excite surface plasmon polariton (SPP) modes. The SPP modes have been intensively investigated after the pioneering work of Ritchie in the 1957.[143] For short, SPP modes are electromagnetic waves that propagate along the surface of a conductor, usually a metal with free electrons. The electron charges on a metal surface can perform coherent fluctuations along the surface, which are denoted as surface plasma oscillations, demonstrated by electron energy-loss experiments in 1960, as shown in Figure 3.8a.[143,144] The frequency ω of these oscillations is bounded to the in-plane wave vector k_x by a dispersion relation $\omega(k_x)$. These charge oscillations are localized in the z direction (perpendicular to the planar surface), accompanying by a mixture of transversal and longitudinal electromagnetic field components. The intensity of electric field E can be described as:[145]

$$E = E_0^\pm \exp[+i(k_x x \pm k_z z - \omega t)] \quad (3.26)$$

where E_0 is the intensity at the surface, $+$ represents for $z \geq 0$, $-$ for $z \leq 0$, k_z is the wave vector perpendicular to the surface. The field intensity E is exponentially decaying along the perpendicular direction (imaginary k_z). The in-plane wave vector k_x is parallel to the x direction with a relation of $k_x = 2\pi/\lambda_p$, where λ_p is the plasma oscillation wavelength.

According to Maxwell's equation, the dispersion relation can be obtained for a semi-infinite metal system with a planar surface, adjacent to a dielectric medium with dielectric ϵ_{diel} :

$$D_0 = \frac{k_{z1}}{\varepsilon_{\text{met}}} + \frac{k_{z2}}{\varepsilon_{\text{diel}}} = 0 \quad (3.27)$$

$$\varepsilon_{\text{met}} \left(\frac{\omega}{c}\right)^2 = k_x^2 + k_{z,\text{met}}^2 \quad (3.28)$$

$$\varepsilon_{\text{diel}} \left(\frac{\omega}{c}\right)^2 = k_x^2 + k_{z,\text{diel}}^2 \quad (3.29)$$

The dispersion relation can then be written as:

$$k_x^2 = \left(\frac{\omega}{c}\right)^2 \frac{\varepsilon_{\text{met}}\varepsilon_{\text{diel}}}{\varepsilon_{\text{met}} + \varepsilon_{\text{diel}}} \quad (3.30)$$

According to the Drude model, the dielectric function of metal reads:

$$\varepsilon_{\text{met}} = \varepsilon'_{\text{met}} + i\varepsilon''_{\text{met}} \quad (3.31)$$

where $\varepsilon'_{\text{met}}$ is the real part and $\varepsilon''_{\text{met}}$ is the imaginary part of the permittivity. For metals, the real part is negative and the imaginary part positive.[146]

For $\varepsilon''_{\text{met}} < |\varepsilon'_{\text{met}}|$, the real part of the SPP in-plane wave vector k_x can be written in the following way:

$$k'_x = \left(\frac{\omega}{c}\right) \sqrt{\frac{\varepsilon'_{\text{met}}\varepsilon_{\text{diel}}}{\varepsilon'_{\text{met}} + \varepsilon_{\text{diel}}}} \quad (3.32)$$

$$k''_x = \left(\frac{\omega}{c}\right) \left(\frac{\varepsilon'_{\text{met}}\varepsilon_{\text{diel}}}{\varepsilon'_{\text{met}} + \varepsilon_{\text{diel}}}\right)^{\frac{3}{2}} \frac{\varepsilon''_{\text{met}}}{2(\varepsilon'_{\text{met}})^2} \quad (3.33)$$

Since $\varepsilon'_{\text{met}}$ is negative and $\varepsilon_{\text{diel}}$ is positive, the SPP dispersion k'_x can only exist when the absolute value of $\varepsilon'_{\text{met}}$ is larger than $\varepsilon_{\text{diel}}$. In this case, a SPP is excited when light is propagating between the metal and the dielectric medium. k''_x represents the internal absorption of metals. Because k'_x denotes the propagation property of SPP modes, in the following discussion, k_{spp} is presented rather than k'_x .

According to the dispersion relation of SPP modes, the momentum of SPP modes approaches the light line $\sqrt{\varepsilon_{\text{diel}}}\omega/c$, but it is always larger than $\sqrt{\varepsilon_{\text{diel}}}\omega/c$, as shown in Figure 3.8c. The mismatch of momentum makes SPP modes intrinsically non-radiative. Thus, whenever the SPP modes are excited at the planar surface, this part of electromagnetic energy is trapped as SPP mode at the region between the metal

conductor and the dielectric medium. The SPP mode can propagate along with a flat metal surface, but it will gradually attenuate because of the absorption in the metal. The intensity of SPP modes in the plane direction is dependent on the k_x'' , with a relation of:

$$E_x = E_0 \exp[-2(k_x''x - \omega t)] \quad (3.34)$$

The propagation length $L_{\text{spp},x}$ along the planar surface is defined as the distance where the intensity of the electric field has dropped to 1/e of its initial value. Then the propagation length $L_{\text{spp},x}$ is given by:

$$L_{\text{spp},x} = (2k_x'')^{-1} \quad (3.35)$$

The decay length of SPP modes into the metal δ_m and the dielectric medium δ_d , can be defined as the depth when the field intensity decreases to 1/e, as shown in Figure 3.8b. In the metal, the depth reads:

$$\delta_m \approx \frac{\lambda}{2\pi} \left[\frac{\epsilon_{\text{met}} + \epsilon_{\text{diel}}}{(\epsilon'_{\text{met}})^2} \right]^{\frac{1}{2}} \approx \frac{\lambda}{2\pi} \left(\frac{|\epsilon'_{\text{met}} + \epsilon_{\text{diel}}|}{|\epsilon'_{\text{met}}|} \right) \quad (3.36)$$

In the dielectric medium, the depth reads:

$$\delta_d \approx \frac{\lambda}{2\pi} \left(\frac{\epsilon_{\text{met}} + \epsilon_{\text{diel}}}{\epsilon_{\text{diel}}^2} \right)^{\frac{1}{2}} \approx \frac{\lambda}{2\pi} \left(\frac{|\epsilon'_{\text{met}} + \epsilon_{\text{diel}}|}{\epsilon_{\text{diel}}} \right) \quad (3.37)$$

To give an impression about the respective lengths for SPP modes at the interface between silver and organic materials ($n = 1.7$), for light at wavelength of 600 nm, one can obtain δ_m of 784 Å and δ_d of 4359 Å. It indicates that the field penetrate into the metal side is much shallower than in the organic material. Whenever the silver layer is thinner than this value (784 Å), SPP modes at each side of Ag layer can couple with each other, giving more complex SPP modes. The long distance of SPP modes coupling through an opaque thick metal film shows potential application in special cases, as the distance is much longer compared to FRET or Dexter energy transfer.[147–149] The propagation length $L_{\text{spp},x}$ along with the surface can also be calculated according to Equation (3.35), which is as high as 129 μm. Thus, when the SPP mode of silver is excited by 600 nm of light, the delocalized SPP mode can propagate for a long distance before its intensity decreases to 1/e.

Because of the fascinating properties of SPP modes, it has been used in fields such as optics communication, surface science and photocatalysis.[150] However, the excitation of SPP modes in OLEDs represents an energy loss channel. The electromagnetic waves are oscillating in resonance with the electrons in metallic electrons, propagating along the interface between the dielectric medium and the metal electrode. To achieve higher device performance, one should reduce the fraction of photons trapped as SPP modes in OLEDs.

3.7 Quantification of energy loss channels

For state-of-the-art OLEDs, the IQE can reach unity, when 100% of injected charges are converted to photons. Because of loss channels including substrate modes, waveguide modes, SPP modes and absorption, the major part of generated photons is trapped inside the multilayered device. Before increasing the efficiency of OLEDs by reducing and/or extracting the trapped photons, quantification for each energy loss channel is needed.

The fraction of trapped photons in bottom OLEDs is different from those in top emitting OLEDs. For the former, loss channels are substrate modes, waveguide modes, SPP modes, absorption and non-radiative losses. However, for the top emitting OLEDs, there is no substrate mode since the light directly penetrates from the device to air zone. When varying the thickness of the ETL and HTL, the fraction of each mode is changed. However, it should be noted that, when intrinsic organic material is used as transport layers, the electrical properties of the devices can also be altered by changing the recombination zone and the electrical efficiency, as stated in the Section 3.1. In a case like that, the change of the device performance is not solely resulting from the optical effect, but also from the change of electrical efficiency, as described by Equation (3.25).

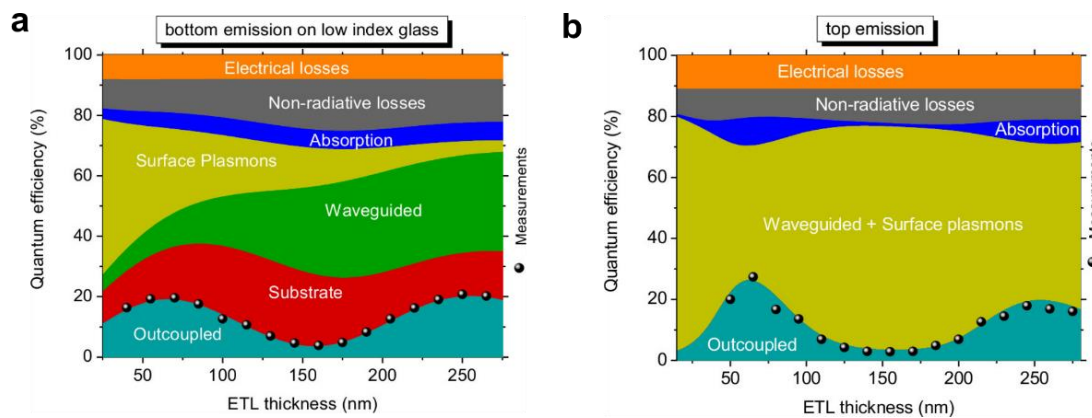


Figure 3.9. Quantification of different loss channels for (a) red bottom emitting OLEDs with a change of n-doped ETL thickness and (b) red top-emitting OLEDs with different n-doped ETL thickness. The simulation is based on the electromagnetic model summarized in Section 3.5. The solid dots are experimental EQE for these two kinds of OLEDs. Reproduced from reference [263] with permission.

As discussed in Section 2.6, by using the highly efficient organic doped system, the mobility of the transport layer can be increased by several orders. The charge carrier balanced or the recombination for OLEDs is not influenced when tuning the thickness of doped transport layers, giving the possibility to maintain the electrical property while optimizing the optical microcavity of devices.[76,78]As a reason of that, the change of the device performance results solely from the optical effect, the impact of the electrical efficiency variation can be ruled out.

The contribution of each mode to the entire trapping losses is device dependent. Here, state-of-the-art red phosphorescent bottom and top emitting OLEDs are applied to make a detailed discussion on the quantification for each loss channel. As shown in Figure 3.9a, the maximum EQE for bottom emitting red OLEDs is about 20%. The substrate modes account for about 10-20%, depending on the ETL thickness. It should be noted that SPP modes and waveguide modes are more sensitive to the change of ETL thickness. The increase of the ETL thickness will raise the proportion of waveguide modes and decrease SPP modes. Waveguide modes account for about only 5% at low ETL thickness and further increase to more than 30% with thick ETL layer. Meanwhile, more than 30% of the photons are trapped as SPP modes when the ETL thickness is low and it drops to less than 5% when ETL thickness is increased to the second maximum of EQE (with ETL thickness about 250 nm). The non-radiative loss is slightly varied when changing the ETL thickness, which accounts for about 10% of the total energy loss in this case.

As for the top emitting red OLEDs shown in Figure 3.9b, the maximum EQE can reach more than 20% at the maximum position, which is slightly higher compared to the bottom one. In the top configuration, the majority of photons are trapped as waveguide modes and SPP modes. The total proportion of these two modes account for 40-70% of the quantum efficiency. Since the performance for top emitting OLEDs is sensitive to the cavity length, the change of ETL thickness can significantly vary the resonance behavior, the Purcell factor and outcoupling efficiency. For devices at the minimum position, a very low EQE about 5% can be obtained where 70% of energy are trapped as waveguide and SPP modes.

3.8 Extraction efficiency

As discussed in previous sections, the outcoupling efficiency is not only dependent on the ETL thickness, but also the dipole orientation (anisotropy factor), the emission wavelength and the device architecture. Also, the fraction of each loss channel is varies for different devices. It is then reasonable to define a value to evaluate the performance of different outcoupling strategies, since the enhancement factor may be misleading,

especially in cases the reference sample is off the position of maximum EQE. The extraction efficiency η_{EE} , can be defined as a ratio between the extracted photons $n_{\text{ext.ph.}}$ and the trapped photons $n_{\text{tra.ph.}}$:

$$\eta_{EE} = \frac{n_{\text{ext.ph.}}}{n_{\text{tra.ph.}}} \quad (3.38)$$

Since the trapped photons are simulated and represented as percentage of quantum efficiency, the extraction efficiency can also be calculated as: [151]

$$\eta_{EE} = \frac{\text{EQE}_{w/} - \text{EQE}_{w/o}}{\chi_{\text{SUB}} + \chi_{\text{WG}} + \chi_{\text{SPP}}} \quad (3.39)$$

where the $\text{EQE}_{w/}$ is the EQE with outcoupling structures, $\text{EQE}_{w/o}$ the EQE of reference device without extraction strategy, χ_{SUB} the quantum efficiency of substrate modes, χ_{WG} quantum efficiency of the waveguide modes, χ_{SPP} the quantum efficiency of SPP modes. For top emitting OLEDs, there is no substrate mode, i.e. $\chi_{\text{SUB}} = 0$. The calculation of extraction efficiency for OLEDs should be based on the device performance where triplet-triplet annihilation or leakage current have minor influence. Since the enhancement factor is normally calculated at a typical luminance or current density for the specific reference device, the extraction efficiency can be meaningful in terms of comparing the efficiency of light outcoupling structures from different reports.

3.9 Enhancing photon extraction

As the energy loss mechanism is varied with different modes, the outcoupling strategy is therefore also targeting at different loss channels. From a theoretical point of view, it is meaningful to sort the outcoupling strategies according to the targeted loss channel. For some cases, photons can be extracted from more than one loss mode at the same time. The discussion about different outcoupling strategies in the following part, is then sorted by the targeted mode. The discussion in this section is focusing on the performance enhancement and the outcoupling mechanism. The fabrication processes are mentioned, but a more detailed summary is given in a later section. The advantages and disadvantages for different outcoupling strategies are discussed. Since the dipole orientation can significantly influence the outcoupling efficiency, the management method for tuning the anisotropy factor is also briefly summarized.

3.9.1 External outcoupling

According to the analysis in section 3.6, losses from substrate modes are resulting from TIR when light is propagating from the substrate medium ($n \approx 1.5 - 1.8$) to air ($n = 1.0$). The critical angle θ for TIR can be calculated according to the Snell's law (Equation (3.20)). For normal glasses ($n = 1.5$), the incident light with angles higher than $\arcsin(1/1.5)$ (41.8°) would be reflected at the glass/air interface. As a reason of that, methods reducing the TIR at the interface can be used to extract substrate modes.

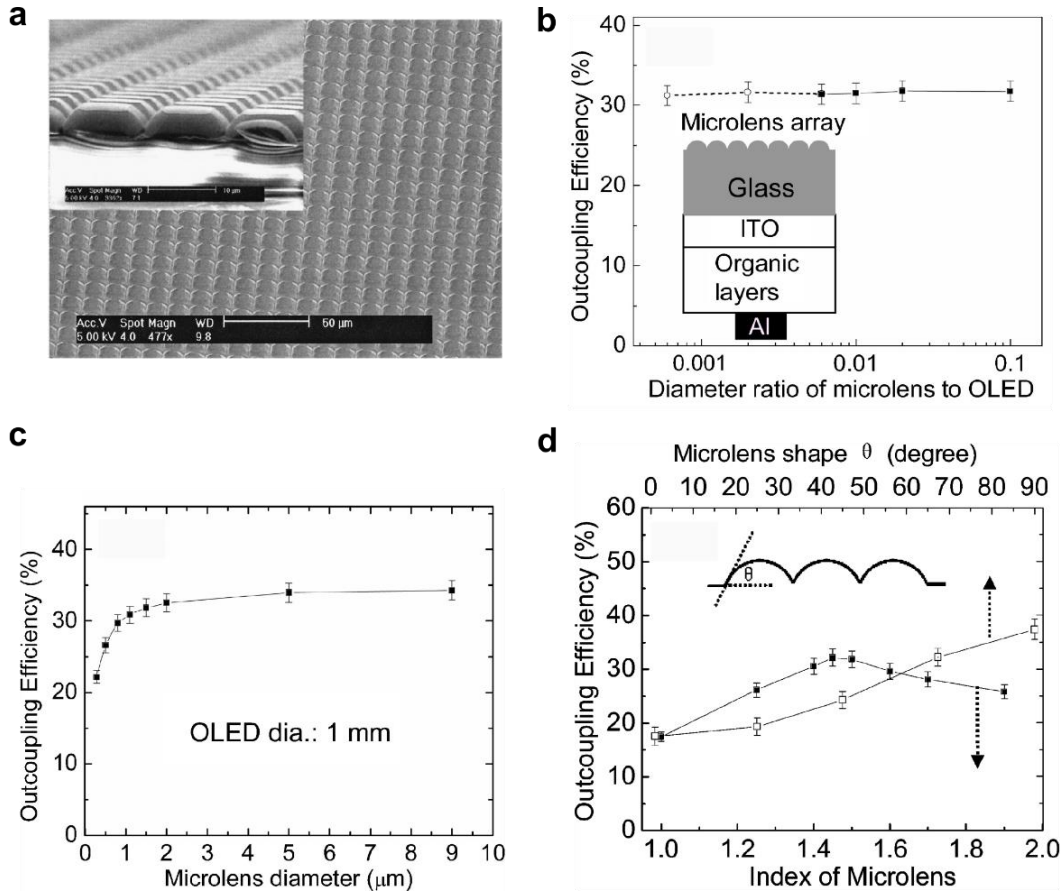


Figure 3.10. Microlens arrays used as external outcoupling strategies for bottom emitting OLEDs. (a) SEM of a microlens array with detailed side view of the lens as an inset. (b) The outcoupling efficiency vs the ratio of microlens to OLED diameter, calculated by 3D Monte Carlo simulations based on hexagonal microlens arrays, in which the refractive indices of the microlens and glass substrate is 1.45 and the corresponding microlens contact angle θ is 70° . The open circles and dashed lines indicate that the ray-tracing may not be accurate enough when the microlens diameters reaching the emissive wavelength. Inset: the OLED structure with the PMMA microlens array incorporated on the glass substrate. (c) The outcoupling efficiency vs the microlens diameter, assuming the OLED emitting at 550 nm with a diameter of 1 mm and calculated via finite difference time domain method. (d) The outcoupling efficiency estimated as a function of the refractive index of microlens (solid squares) with a contact angle θ of 70° ; and a function of microlens shape θ from the flat case ($\theta = 0^\circ$) to the half-spherical case ($\theta = 90^\circ$). Inset: the contact angle θ of the microlens to the substrate. (a) reproduced from references [153] and (b)-(d) reproduced from [154] with permission.

One of the general ideas to reduce the TIR at the substrate/air interface of bottom emitting OLEDs is using external curved structures to change the incident angle of light beam from the substrate to the air zone. The application of a half-sphere lens with larger size than the OLED pixel would easily increase the EQE by a factor of two for conventional device layouts (OLEDs based on standard glass substrates without other optical enhancements).[152] However, the application of larger area of half-sphere macroextractors could suffer from being too bulky in case of a large area OLEDs.

In 2002, S. Möller *et al.* demonstrated that ordered polydimethylsiloxane (PDMS) microlens arrays with a size of 10 μm attached to normal glass substrates can enhance the EQE of green OLEDs by a factor of 1.5 over flat substrates, as shown in Figure 3.10a.[153] They showed that the EQE increased from 9.5% to 14.5% at a current density of 0.1 mA/cm^2 . No EL spectrum change was observed at different observation angles.

Later in 2006, detailed studies have been conducted by the same group to investigate the influence of the size ratio of the microlens diameter to the OLED pixel, the refractive index of microlens, the shape of the microlens and the thickness of glass substrates.[154] As shown in Figure 3.10b and c, simulation results based on the Monte Carlo method showed that the enhancement is insensitive to the diameter of microlens when it is much smaller than the OLED pixel diameter, but larger than the emitted light wavelength, while the refractive index and the shape of microlens were held constant. When the diameter of the lens increases to a level which is comparable to, or bigger than the OLED, the EQE depends on the relative position of the microlens and the OLED pixel. Simulations also indicate that in a case of the worst misalignment of the OLED from the lens center, corresponding to the edge of the lens bisecting the OLED can reduce the EQE. However, the ray-tracing simulation is not accurate enough whenever the size of the lens decreases to the emissive wavelength range. The wave optics finite difference time domain simulation was conducted to estimate the EQE in the case when the diameter is comparable to the emissive wavelength. It was shown that the EQE of OLEDs based on these structures decreases rapidly when the diameter of lens reaches the emission wavelength. When increasing the refractive index of the microlens, the total reflection between the glass/microlens is decreased, but the loss between the microlens/air interface is increased, leading to a decrease of the EQE to the air zone. Based on these simulation results, they demonstrated a hybrid white OLED with a maximum EQE of $14.3 \pm 0.3\%$ at $900 \text{ cd}/\text{m}^2$ and luminous efficacy of $21.6 \pm 0.5 \text{ lm}/\text{W}$ at $220 \text{ cd}/\text{m}^2$ with hexagonal polymethylmethacrylate microlens arrays. An enhancement factor for EQE of about 50% was achieved with the angular independent emission and high CRI of 85 at the same time.

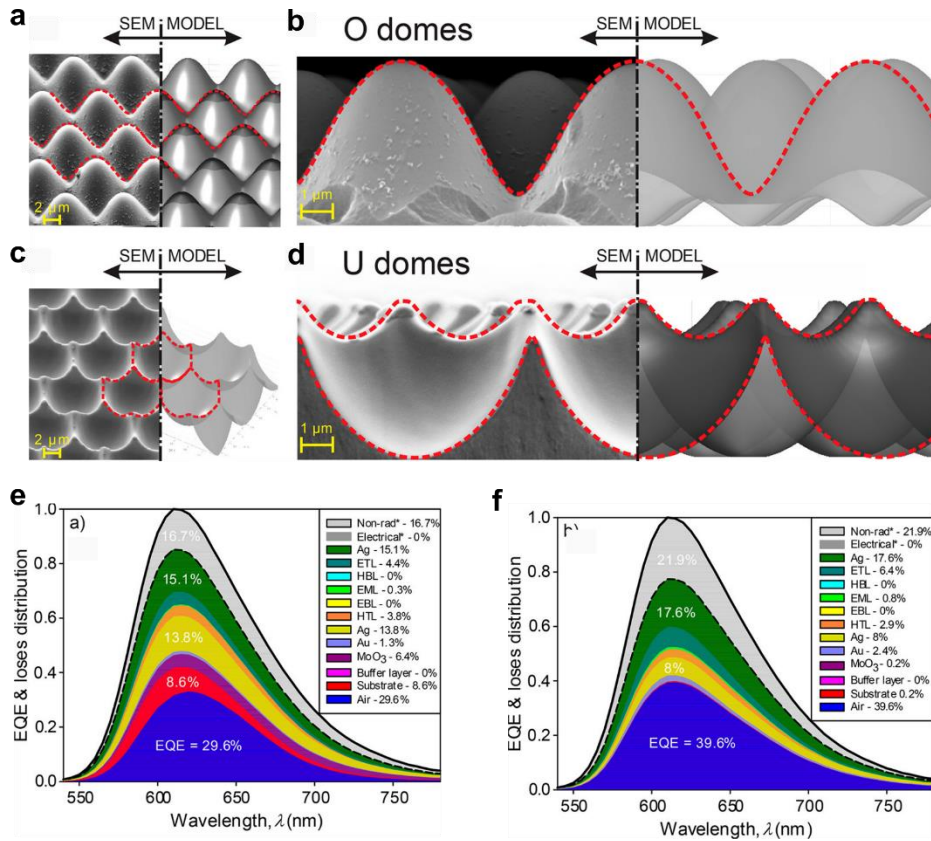


Figure 3.11. (a) SEM images of positive (O (a, b)) and negative shaped domes (U (c, d)) replicas with period of about $7.37 \mu\text{m}$ and height of about $5.5 \mu\text{m}$ in experiments (a, c) and matched textures used in simulation models (c, d), represented at viewing angles of 45° (a, c) and 90° (b, d). The EQE and energy losses in different layers for OLEDs with optimized structure for (e) flat device without any textures and (f) devices with O domes texture. Reproduced from reference [155] with permission.

The picture is slightly different whenever the bottom emitting OLEDs is based on thin metal electrodes with a much stronger cavity. Recently, M. Kovačić *et al.* reported an external outcoupling strategy on periodically positive and negative hexagonal dome-shaped structures, to extract the trapped photons as substrate modes in bottom red OLEDs based on MoO₃ (2 nm)/Au (2 nm)/Ag (6 nm) composite electrode.[155] As shown in Figure 3.11, when using the positive (O dome) and negative dome-shape (U dome) textures to extract trapped photons in the optimized bottom red OLEDs, the EQE can be improved from 29.6% to 30.3% with O dome texture and up to 31.4% with U dome texture. However, if the device was further optimized for devices with outcoupling textures, significant improvement of EQE to 39.4% and 39.6% can be obtained for the O and U dome textures, respectively. Hence, the optimized device for flat substrates was not the optimized configuration for devices with external outcoupling textures. In the end, an OLED with 50.5% light extraction efficiency and improved angular intensity distribution was obtained with O dome structures

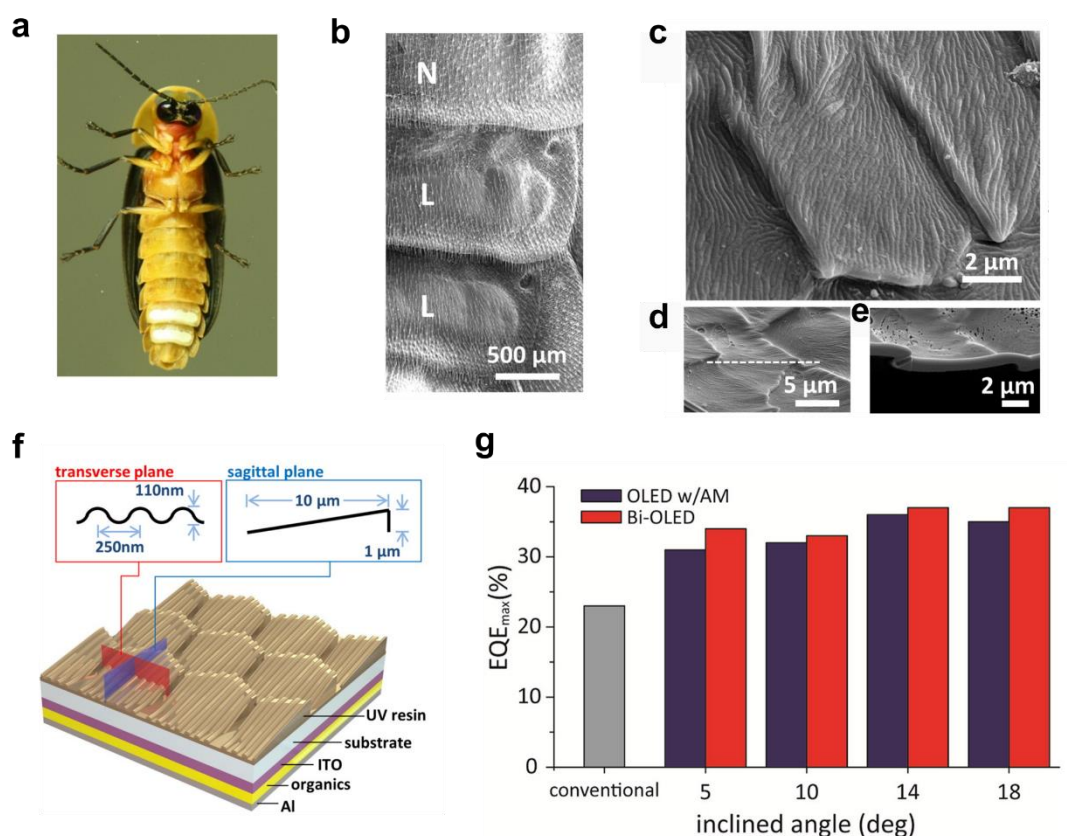


Figure 3.12. Bioinspired OLEDs on hierarchical structures of a firefly. (a) An image of a male firefly (*Pyrocoelia rufa*). (b) SEM image of abdominal segments of a male firefly with normal (N) and lantern (L) cuticles. (c) SEM picture of the lantern cuticle in a larger magnification. Longitudinal nanostructures are located on asymmetric structures in a micrometer size. (d) The direction of the focused ion beam (FIB) section is along the white dash line. (e) A longitudinal cross-section of the lantern cuticle. (f) The biologically inspired OLED panel with an aluminum layer, organic functional layers and an optical layer with hierarchical structures on a glass substrate. (g) Maximum EQE of an OLED panel vs the device with a smooth surface, asymmetric microstructures and hierarchical ultrastructures at different inclined angles (5, 10, 14 and 18°). Reproduced from reference [158] with permission.

Since the outcoupling of substrate modes is based on the principle of decreasing the incident angle between glass substrates and air cone, nanostructures with proper aspect ratio between the height and the periodicity could potentially enhance the EQE for bottom OLEDs. There is no need of precise control of the height and periodicity. Corrugations with wide distribution of periodicity and height could enhance the EQE.[156,157] Bioinspired nanostructures with different periodicities and heights can also extract the photons trapped in substrate modes. In 2016, J. Kim *et al.* reported the unique optical functions of hierarchical ultrastructures in a firefly and the applications to build highly efficient OLEDs.[158] As shown in Figure 3.12, the hierarchical ultrastructure was comprised of longitudinal nanostructures and asymmetric microstructures (AM), which was replicated by using geometry-guided resist reflow, replica molding and PDMS oxidation. To mimic the hierarchical structure from the firefly, predefined thermoset microstructures with different inclined angles were

achieved by using two steps of patterning by photolithography with accurate alignment and then replicated by the PDMS precursor. The cured PDMS replica was then unidirectionally stretched and oxidized by oxygen plasma treatment to form wrinkle nanostructures perpendicular along the stretching direction. The inclined angle of the microstructures can slightly influence the outcoupling efficiency. For green OLEDs based on bis(2-phenylpyridine)iridium(III)-acetylacetonate ($\text{Ir}(\text{ppy})_2\text{acac}$) emitter in an exciplex host of 4,4'-Bis(N-carbazolyl)-1,1'-biphenyl (CBP) and bis-4,6-(3,5-di-3-pyridylphenyl)-2-methylpyrimidine (B3PYMPM), the EQE was enhanced by up to 61% compared to the one on the flat glass substrate with an inclined angle of 18° . As shown in Figure 3.12g, the enhancement is comparably lower for devices with only the asymmetric microstructures than the Bi-OLEDs with hierarchical ultrastructures.

It should be noted that the external outcoupling structures discussed above were fabricated by complicated lithography, etching and nanoimprinting processes, which arises the concern of high costs and environmental hazards. Some facile, low-cost and controllable methods to generate micro/nano patterns have been developed for the outcoupling of substrate modes. Remarkable EQE enhancement was obtained when applying wrinkle patterns formed by UV radiation on polymers[159], nanopatterns spontaneously generated by O_2 plasma treatment on flexible PET substrates[160] and crystallization-assisted nanolens array[161] to the glass substrate of bottom emitting OLEDs. By using glass substrates with sand-blasted edges and back-side, a 20% improvement of current efficiency has been demonstrated for green OLEDs.[162] By wet-etching polymeric micro/nano particles, quasi-periodic structures can also be applied as external outcoupling strategies.[98] The fabrication approaches for micro- and nanopatterns will be discussed in Section 3.10.

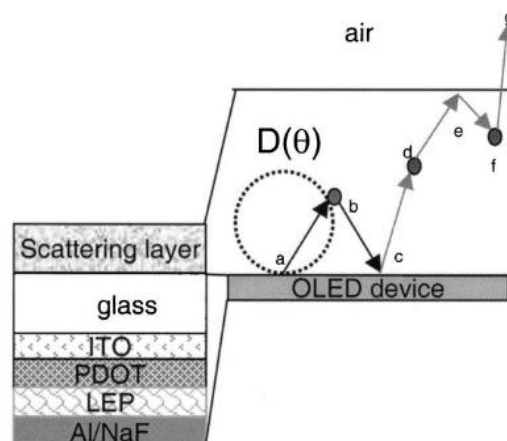


Figure 3.13. A schematic illustration of outcoupling trapped photons with external scattering films with micro/nano particles. $D(\theta)$: internal angular distribution of light. The line denotes the trace of a single prototypical ray interacting with the medium and scattering nanoparticles (sites a - g). Reproduced from reference [264] with permission.

The discussion of external outcoupling strategies above is based on the idea to tune the incident angle at the substrate/air interface, in which the light propagation inside the substrate is not disturbed. Meanwhile, it is also possible to tune the light propagation direction by scattering before it hits the substrate-air interface. In this manner, rays are transmitted into the substrate as usual, while the propagation is scattered by micro/nano particles with a different refractive index compared to the substrate. The addition of particles into the substrate is a relatively simple and cost-effective method. By tailoring their distribution, the refractive index and the size of particles, the scattering effect can be tuned for outcoupling trapped photons as substrate modes.

As shown in Figure 3.13, particles buried inside the scattering films can modulate the light beam propagation direction by a couple of times. In the end, both forward scattering and back scattering have to be taken into account. The scattering efficiency and backward scattering efficiency can be calculated according to Mie theory.[163] The refractive indices of the doped particles and the medium, the doping concentration and the size of particles can significantly affect the scattering efficiency and the backward scattering efficiency.[164]

In work by L. Li *et al.*, nanoparticles of barium strontium titanate (BST) with a refractive index of 2.6 (measured at 512 nm) and size of 200 nm were dispersed within a polymer poly(diacrylate) substrate to enhance light extraction efficiency of green polymer OLEDs and white OLEDs. The nanocomposite electrode consisted of a layer of single-walled carbon nanotubes (SWNT) and silver nanowires (AgNWs) which were embedded in the surface of the nanoparticle-polymer composite substrate, giving the average roughness R_a of the SWNT/AgNW-nanocomposite substrate of only 1.51 nm. For green OLEDs based on SWNT/AgNW-nanocomposite substrate, a maximum EQE of 38.9% was achieved, which was about 1.8 times higher compared to the device based on SWNT/AgNW without BST nanoparticles. For white OLEDs based on SWNT/AgNW-nanocomposite substrate, maximum EQE of 30.5% was obtained, with an enhancement factor of about 1.6 compared to the reference OLED with SWNT/AgNWs electrode on polymer substrate without BST nanoparticle.

It should be noted that the scattering can also happen whenever the buried particle has a lower refractive index than the medium. In recent work by T. Koh *et al.*, a thin light scattering layer with air voids as low-index scattering centers buried in a high-index polyimide matrix was developed, as shown in Figure 3.14.[165] These porous polyimide scattering layers with air voids were made through a scalable fabrication technique by immersion precipitation relying on the interaction between a solution and an anti-solvent for precursors of polyimide. An average haze factor of 77% in the visible wavelength range was obtained for the scattering film. When externally attaching 2 μm scattering films on the glass substrate of a green OLED stack, they showed an

enhancement factor of 65% for the EQE and 77% for the luminous efficacy. Furthermore, when integrating the scattering film to an all phosphorescent single unit white OLED, the EQE increased from 11.9% for the reference device at 3 mA/cm^2 , to 19.0% for devices with the porous polyimide scattering layer at the same current, corresponding to an enhancement factor of 1.6. The angular radiant intensity was initially broader than Lambertian for the reference white OLED and was similar to the Lambertian distribution with the scattering film. The spectral stability was also improved considerably across the observation angle range. The CIE coordinate shifted from (0.505, 0.439) at 0° to (0.477, 0.437) at 60° , with a $|\Delta(x, y)|$ of (0.028, 0.002) for the reference device. Meanwhile, the CIE was (0.462, 0.448) at 0° and it shifted to (0.461, 0.448) at 60° without big change of CIE the device with the scattering layer.

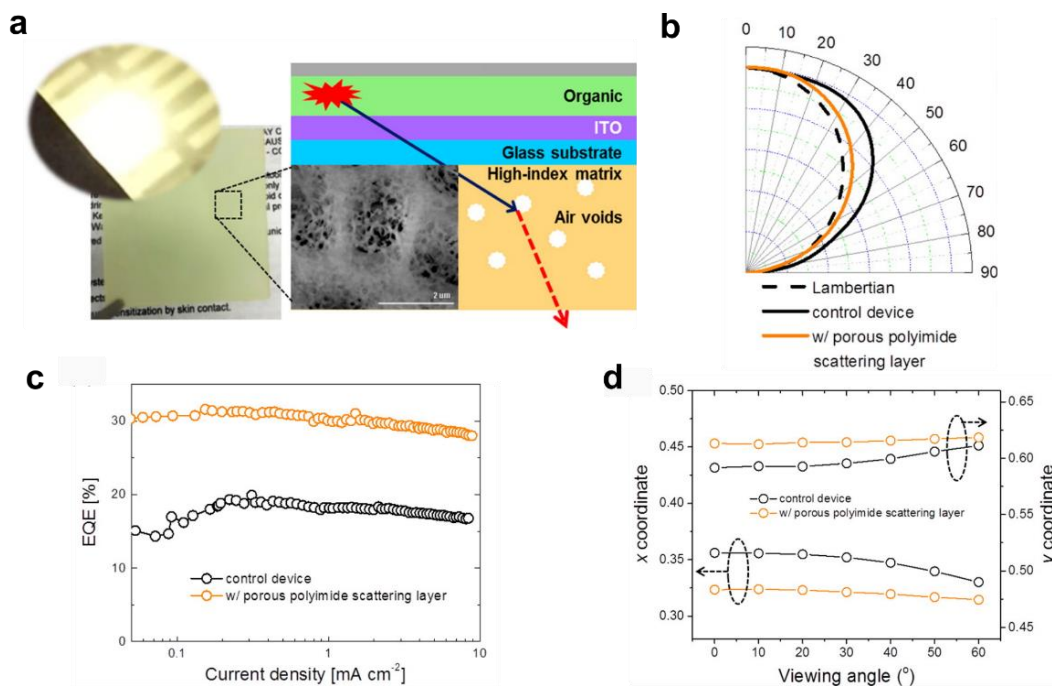


Figure 3.14. External outcoupling of photons in OLEDs by a high index contrast scattering layer with air voids. (a) A schematic illustration of the light scattering film with air voids buried in high-index polyimide flexible films for outcoupling substrate modes. (b) EQE-current density curves for white OLEDs with or without the light scattering film. (c) The angular radiant intensity for white OLEDs with or without the scattering film. (d) The CIE coordinate change for white OLEDs with or without the scattering film. Reproduced from reference [165] with permission.

Scattering can also be achieved by the crystallization of organic molecules,[161] utilizing the refractive index difference between glass fabrics and polymers [166] and dry etching the Si_3N_4 layer to form vacuum nanohole arrays.[167] It should be noted that the aggregation of micro/nano particles in the scattering scheme may make a detrimental effect on the efficiency. It is also possible to combine micro/nano patterns and particles to bring a synergetic effect. Both the geometry change and the buried particles can enhance the device performance. Since substrate modes are only relevant

for bottom emitting OLEDs, the outcoupling techniques are usually applied inside the substrate or attached externally on the back side of the substrate, without the disadvantage of influencing the electrical property of OLEDs.

Even though it is possible to obtain quite high enhancement factors with different external outcoupling strategies to extract trapped photons as substrate modes, reports with merely enhancement factor is not ideal. Since the enhancement factor is dependent on the performance of the reference device, there is a lack of comparison for different strategies. The extraction efficiency (see Section 3.8) is needed to quantitatively compare the ability of outcoupling efficiency of strategies showed previously.

3.9.2 Internal outcoupling

The excitation of waveguide modes is resulting from the higher refractive index of organic layers/ITO anode ($n = 1.7-1.8$) compared to the conventional glass substrate ($n = 1.5$) within the visible wavelength range. A facile method is applying substrates with comparable refractive index compared to the ITO anode. As reported by Rosenow *et al.* [168] and Reineke *et al.* [152], highly efficient white OLEDs have been obtained based on high refractive index glass substrates. However, substrates are doped with toxic ingredient to realize high refractive, raising concerns of environmental compatibility and high costs for the mass production. It is also possible to use less toxic polymer layers with high refractive index to reduce the TIR between the ITO/substrate interface.[169] However, since the refractive index of the polymer films cannot fully cover the entire visible range, there are still trapped photons as waveguide modes.

Micro/nano patterns with periodic, quasi-periodic or random structures can be applied to extract waveguide modes and/or SPP modes in OLEDs. An appropriate periodicity is mandatory to efficiently waveguide light into the substrate to meet the Bragg scattering condition.[170,171] It is the same for extracting SPP modes by integrating corrugated structures into the device, to reduce the momentum of SPP mode by shifting them to emissive modes. Since the Bragg-scattering is wavelength and angular dependent, structures with a broad distribution of periodicity would be beneficial for white OLEDs, to achieve a wavelength and angular independent emission behavior for lighting applications. Besides the periodicity of grating structures, the amplitude is also an important factor to influence the light extraction efficiency. Because the deposition of functional materials would somehow smooth the structure and change the electrical property of OLEDs, these effects should be excluded before analyzing the optical effect from micro/nano patterns. [170]

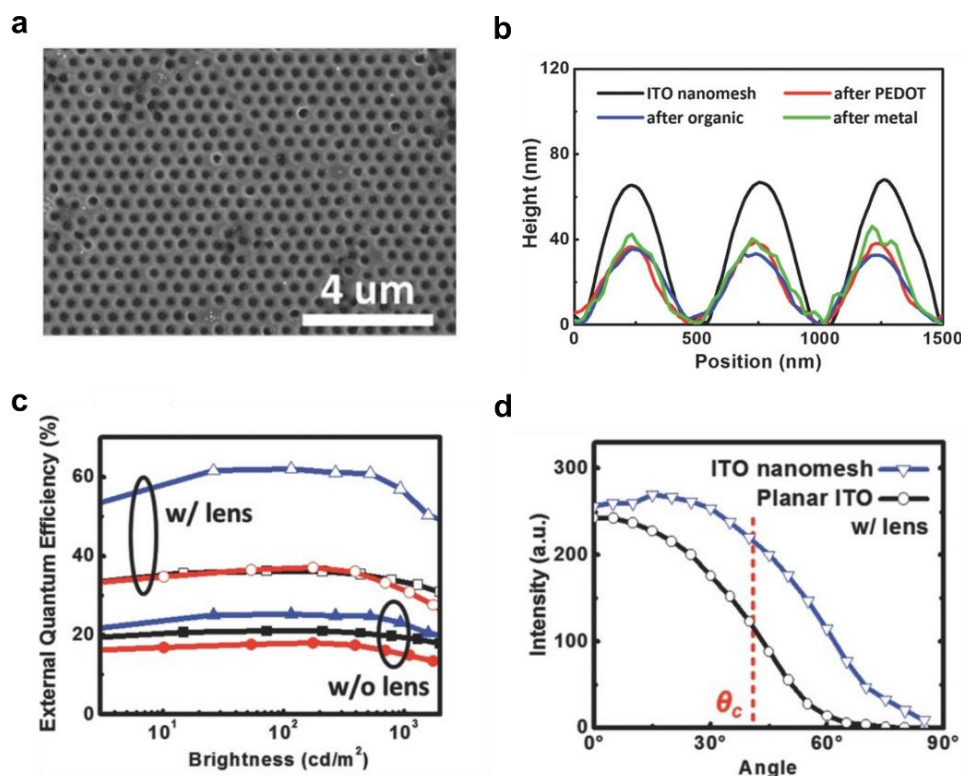


Figure 3.15. Corrugated nanopatterns formed by reactive ions etching the polystyrene nanosphere. (a) SEM image of the sputtered ITO nanomesh. (b) Surface profile for samples after ITO sputtering, after deposition of functional layers of OLEDs. (c) EQE of devices measured without and with half-sphere lens. The black represents the device based on planar ITO; the red is the device based on planar ITO/PEDOT:PSS and the blue is the device based on ITO nanomesh with PEDOT:PSS. (d) The angular spectral radiance for the planar device and the ITO nanomesh device with half-sphere lens attached. Reproduced from reference [180] with permission.

In the work from C. Chen *et al.*, ITO nanomesh was fabricated by etching the self-assembly monolayer of polystyrene nanospheres with an average diameter of 500 nm, followed by sputtering the ITO layer and lift-off of polystyrene nanospheres. As shown in Figure 3.15b, the spin-coating of PEDOT:PSS can slightly planarize the ITO nanomesh, while a corrugation height of about 35-40 nm was retained after the device fabrication. The EQE and luminous efficacy of green bottom OLEDs increased from (21.0%, 73.2 lm/W) to (25.3%, 107.9 lm/W) without external outcoupling strategy. With an extraction lens, planar ITO and ITO nanomesh devices exhibited EQE and luminous efficacy of (36.2%, 126.0 lm/W) and (61.9%, 264.3 lm/W), giving an EQE enhancement factor of 1.7. These results indicate that the ITO nanomesh indeed significantly enhances the coupling of internally generated photons into the substrate, but a large fraction of photons were still beyond the critical angle to the air cone. The angular spectral radiant intensity for devices based on ITO nanomesh and planar ITO indicated a significant enhanced irradiance beyond the critical angle of the glass substrate-air interface.

W. Koo *et al.* reported a method to extract trapped photons as waveguide modes and SPP modes by using spontaneously generated buckling for green fluorescent OLEDs.[170] Buckling structures were realized by cooling the bilayer system with a bottom elastic PDMS layer and a top stiff aluminum layer. Because of the different thermal expansion coefficient of these two layers, corrugated buckling structures form, to release the compressive stress after the external heating. The detailed generation theory will be discussed in Section 3.10.3. Short periodicity and proper depth is needed to efficiently diffract trapped photons into the air zone for the green OLED.

As shown in Figure 3.16, the atomic force microscope (AFM) measurements indicate that the buckling nanostructure has no directional preference. To obtain deeper nanostructures for efficient light outcoupling, further deposition of a 10 nm aluminum layer on a PDMS replica was needed. The buckling depth can reach 40-70 nm and 50-70 nm for two times and three times generation, respectively. The multiple generation has little influence on the peak periodicity, while a broader periodicity distribution can be obtained, as shown in Figure 3.16d. When using these nanostructures in OLEDs, the current density of these devices was increased under the same driving voltage compared to the reference device without nanostructure, resulting from a stronger electric field induced by the distance decrease between the top cathode and ITO anode on corrugated nanostructures. To exclude the influence of the electrical efficiency change, devices without buckling and with the decreased thickness of organic layers were fabricated and compared. Though the driving voltage is lower, the current efficiency for the device with 20% reduced thickness was comparable to the planar reference device. Further decrease of the organic layer thickness to 40% can dramatically reduce the device efficiency. With this, the current efficiency enhancement came from the optical effect, not the change of IQE. The current efficiency at 2000 cd/m² was enhanced by a factor of 1.8 and 2.2 with two times and three times generated buckling, respectively. No pronounced spectral change was noted after burying these nanostructures into OLEDs.

In work from C. Peng *et al.*, corrugations were generated with two ETLs with different glass transition temperatures.[172] Because of the difference in thermal and mechanical properties of the two electron transport materials with the high T_g material deposited on a lower T_g material, a buckled surface was spontaneously formed after thermal annealing above T_g . With TPD as the low T_g material ($\sim 60^\circ\text{C}$) fixed at 40 nm and Alq₃ as the high T_g material ($\sim 172^\circ\text{C}$), a well-defined corrugated structure can only form with a narrow range of the top Alq₃ thickness. The OLED showed an enhancement of 20% in EQE compared with the planar control device from 10% to 12% at 100 cd/m². However, the efficiency of the control device was quite low because of using PBD as ETL. The outcoupling strategy is limited by material combinations, making it difficult for getting highly efficient and stable OLEDs.

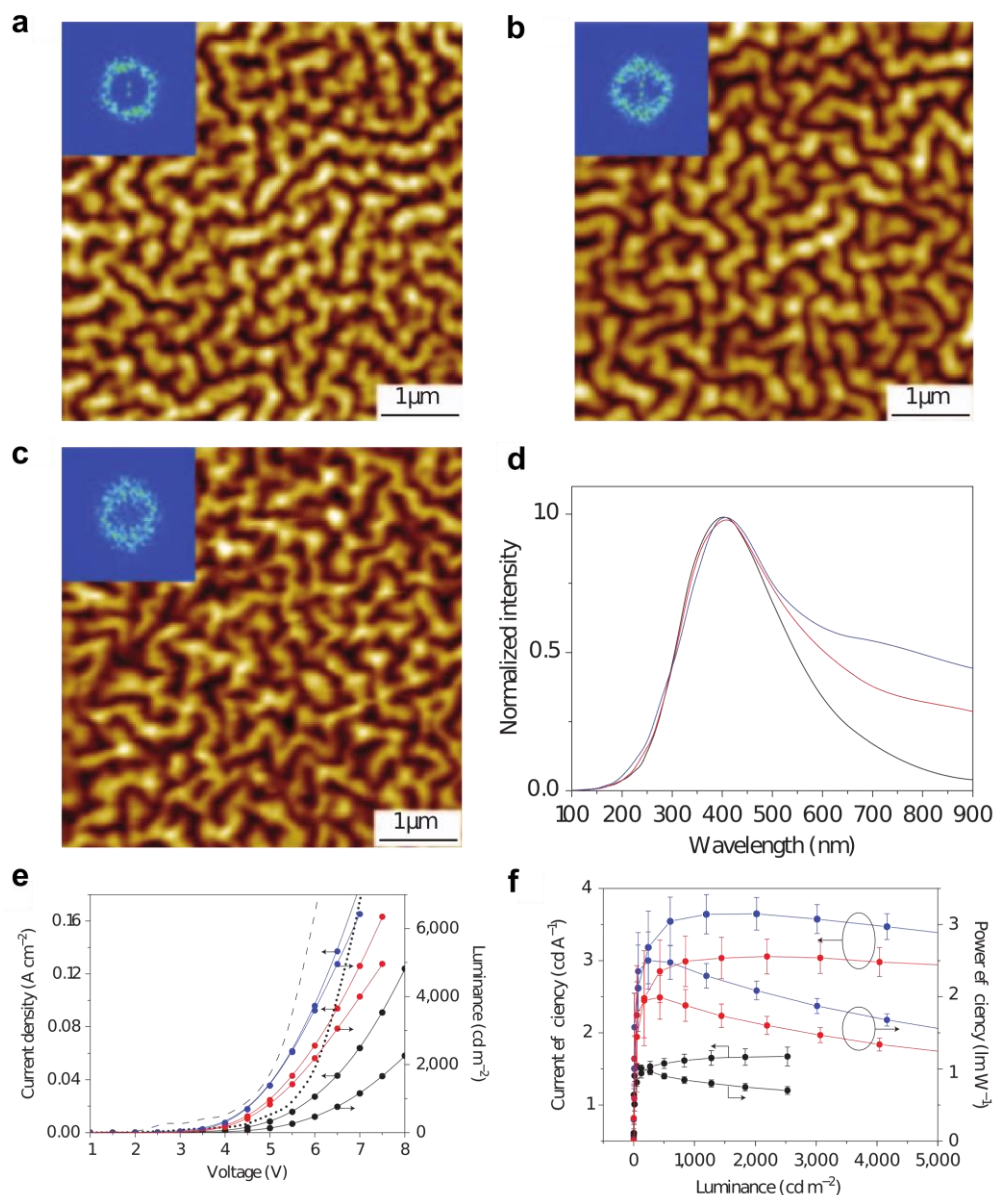


Figure 3.16. Spontaneously formed buckles for light extraction from bottom emitting OLEDs based on conventional fluorescent emitters. (a) buckles formed by a 10 nm thick aluminum layer on the soft PDMS. (b) (c) buckled nanostructures formed by deposition of a 10 nm aluminum layer twice and three times on a buckled PDMS replica, respectively. Inset: fast Fourier transfer (FFT) pattern for each AFM measurement. The ring shape of FFT patterns indicate the random distribution of these structures without preferential direction. (d) power spectra density function (PSDF) from FFTs as a function of wavelength for these nanostructures obtained by deposition of a 10 nm aluminum layer once (black line), twice (red line) and three times (blue line). (e) current density-luminance-voltage characteristic of the OLED without (black), with double times (red) and three times generated buckling (blue). The dotted and dashed lines denote the current density of OLEDs without nanostructure but with the organic layer thickness decreased by 20% and 40%, respectively. (f) current efficiency-luminance, power efficiency-luminance characteristics of OLEDs without (black), with double times (red) and three times generated buckling (blue). Error bars represent standard deviation of values from several devices. Reproduced from reference [170] with permission.

In general, the optical effect on OLED performance with gratings or corrugated nanostructures can be partially explained by Bragg diffraction. An appropriate periodicity is needed to meet the Bragg scattering by diffracting the waveguided light into the forward direction. For the trapped SPP modes at the interface between the cathode and organic functional layers, the integration of micro/nano patterns with the appropriate size is crucial for the outcoupling of trapped photons. There are reports where the implementation of nanostructures can decrease the device EQE, since the outcoupled electromagnetic waves interact with air modes by destructive interference, leading to a decrease of the entire EQE while an enhancement of luminance in the forward direction.[173,174]

The momentum shift of waveguide modes and SPP modes with the additional wave vector of gratings with a periodicity of Λ , can be described as:

$$k_x = k_{x0} \pm \frac{2\pi m}{\Lambda} \quad (3.40)$$

where k_x denotes the absolute wave vector in-plane component, k_{x0} denotes the parallel component of the wave vectors of waveguide modes or SPP modes without grating, m is an integer of the diffraction order based on a grating with a periodicity of Λ .

Equation (3.40) indicates that it is possible to shift the parallel wave vector of waveguide modes and SPP modes to smaller or even higher region with the additional wave vector from the grating nanostructures. According to previous analysis in Section 3.6, the energy of electromagnetic wave dissipated in different region is a function of the in-plane wave vector k_x . The wave vector for the electromagnetic wave in air zone is smaller compared that at the position of emissive layer. With grating nanostructures, there is the possibility that the device performance gets worse by adding further momentum from grating vectors. Meanwhile, it is difficult to simulate or predict the device performance with an unknown diffraction order m . Nevertheless, the theory of Bragg scattering shown in Equation (3.40) can give a rough estimation about finding proper grating structures before implementing in a device.

Micro/nano patterns internally extracting photons can bring electrical defects into the device, leading to a higher leakage current compared to planar devices or even electrical shorts. Based on this fact, non-intrusive strategies to extract or reduce the trapped photons as waveguide modes or SPP modes have been developed, without disturbing the geometry of organic function layers. For non-intrusive structures in bottom OLEDs, the nanostructure is a part of the substrate, but it is further planarized by another layer with different refractive index. By doing this, the scattering effect of nanostructures is maintained while the effect of changing the geometry of functional layers inside the device is reduced.

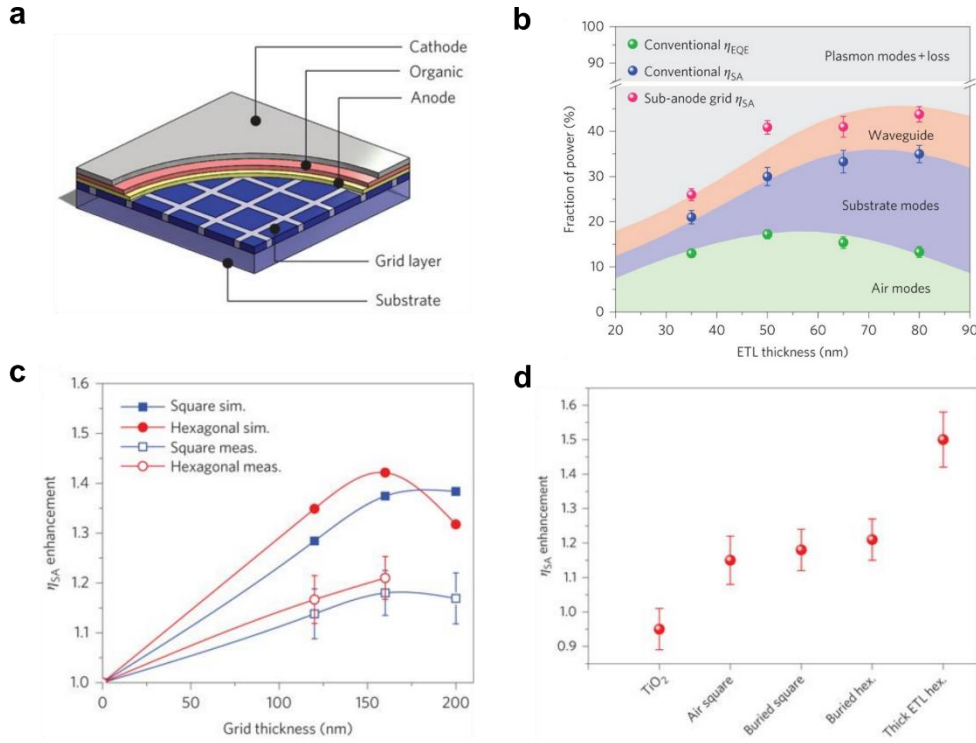


Figure 3.17. Light extraction from bottom OLEDs with a sub-anode grid. (a) a schematic cut-away view of an OLED with a sub-anode grid between the substrate and ITO anode. (b) simulated and experimental results about the dependence of outcoupling enhancement based on sub-anode grid. Simulated (sim.) and measured (meas.) enhancement factor of η_{SA} of square and hexagonal sub-grids vs grid thickness. (c) proportion of power coupled into various optical modes as a function of ETL thickness of the phosphorescent OLEDs. The η_{SA} and η_{EQE} of OLEDs with sub-anode grid and reference devices (symbols) are compared to the simulated power distribution of conventional devices (curves). (d) the enhancement factor of η_{SA} compared with a conventional device without sub-anode grid at the current density of 1 mA/cm^2 . Reproduced from reference [175] with permission.

The work of Y. Qu *et al.* reported a non-intrusive method by using a non-diffractive dielectric grid layer between the transparent ITO anode and the substrate, to efficiently extract the trapped photons as waveguide modes.[175] As shown in Figure 3.17a, the sub-anode grid layer was buried between the anode ITO layer and the glass substrate, which is composed with the grid and host materials. The shape of the grid, the thickness and the refractive index of the grid and host material can influence the outcoupling efficiency. The quantum efficiency of substrate and air mode, namely η_{SA} , has the possibility to be enhanced with an enhancement factor of 1.4 from the simulation. With the optimized grid structure, it is possible to fully extract the trapped photons in the waveguide modes. However, OLEDs based on thin ETL layer still showed a high leakage current, because of the introduction of protrusions during the lithography and pattern transferring process. For devices based on a thick ETL layer, it was possible to increase η_{SA} from $12 \pm 1\%$ for the controlled device to $18 \pm 1\%$ for devices with sub-anode grid, corresponding to an enhancement factor of 1.50 ± 0.08 .

The non-intrusive nanostructures, in principle, should not bring the problem of high leakage current or electrical defects. However, the multiple lithography and nanoimprinting processes can potentially induce defects into the device. Hence, a polishing process or a planarization layer is needed. Other non-intrusive nanostructures including microlens arrays with high refractive index inside the glass substrate[176], micro/nano patterns smoothed with another polymer layer with high refractive index have been introduced[177]. However, it should be noted that the fabrication of grids, microlens or micro/nano patterns involve complex lithography processes, which may hinder the practical utilization for either lighting or display applications.

According to Equation (3.20) and (3.32), the generation of waveguide modes results from the mismatch of refractive index, while SPP modes can be suppressed by matching the refractive index of the dielectric layer close to the metal. The idea to obtain efficient OLEDs by choosing functional materials inside the device to mitigate waveguide or SPP losses can be potentially useful, since there is no need to introduce nanostructures, while optically enhancing the outcoupling efficiency of planar OLEDs.

C. Fuchs *et al.* reported that, by using PEDOT:PSS as the HTL material with a low refractive index (~ 1.52), EQE enhancement by a factor of 1.2 compared to a reference sample for top emitting OLEDs was achieved.[178] The low refractive index PEDOT:PSS decreased the in-plane wave vector of the SPP excited at the interface between the bottom metallic anode and the HTL. The shift of SPP modes reduced the energy dissipated into evanescent loss modes, giving rise to an increase of the outcoupling efficiency. A. Salehi *et al.* reported a method by using the low refractive index ETL material tris-[3-(3-pyridyl)mesityl]borane (3TPYMB) (1.65, 550 nm) to effectively enhance the outcoupling efficiency for solution processed bottom emitting OLEDs.[179] The OLED showed 76% enhancement in EQE, with 59% of the enhancement from the mitigation of SPP modes and the remaining 17% from the change in charge balance. In the end, the OLED based on 3TPYMB as ETL and a TADF emitter showed a maximum EQE of 21.0%. However, since the refractive index of organic materials is related to their chemical structures and film morphology, it is challenging to match the refractive index and electrical properties at the same time as a functional layer, as discussed in Section 2.2.2 and 3.1.[16]

Strategies to outcouple substrate modes, waveguide modes and SPP modes may be combined together, to achieve highly efficient OLEDs. For example, external microlens foils or half-sphere lens were used to extract substrate modes while internal corrugated nanostructures were used to scatter waveguide modes and SPP modes.[180] Scattering nanoparticles were buried into high refractive polymer substrate to extract waveguide modes and substrate modes at the same time.[181] By combining different outcoupling strategies, it is possible to get a high enhancement factor compared to the controlled

device, together with a very high value of the absolute efficiency.

The outcoupling techniques to extract waveguide modes and SPP modes for top emitting OLEDs are somehow similar with these for bottom emitting OLEDs. Microlens array foil directly attaching to the capping layer[182], a reflective sub-electrode grid [183] and nano-sized texture surface[174] have been demonstrated. Compared to bottom OLEDs, there are only limited outcoupling strategies for top emitting devices and further exploration is needed, since the top emitting configuration is now widely used for display purposes.

3.9.3 Anisotropy factor

According to the electromagnetic model summarized in Section 3.5, the anisotropy factor a of organic emitters within devices can make an effect on the outcoupling efficiency. For highly efficient OLEDs, the transition dipole moment vectors should preferentially align in the horizontal orientation with respect to the substrate plane, since the horizontal alignment can facilitate the light outcoupling efficiency. According to Equation (3.18), only TM modes of vertical dipoles can escape the device. Hence, the preference in horizontal orientation of organic emitters can potentially increase the outcoupling efficiency. The dipole orientation of organic materials is highly related to the intrinsic permanent dipole moment and molecular shape, while it can also be influenced by the deposition temperature of substrates and the processing method.[81] For isotropic emitters such as Ir(ppy)₃, the anisotropy factor is 0.333, an average value in a three dimension space.[184] The red emitter Ir(MDQ)₂(acac) shows a slightly horizontal orientation, with an anisotropy factor of 0.24.[185]

3.9.4 Cavity resonance

As shown in Figure 3.2, the basic structure of OLEDs is in a form of an optical cavity. For devices with highly reflective electrodes, the cavity resonance formed between the bottom and top electrode can significantly affect the device performance including the device EQE and angular emission pattern. According to the theory of Fabry–Pérot cavity and two beam interference, the spectral intensity $I(\lambda)$ can be written as:[186][187]

$$I(\lambda) = Q \cdot I_0(\lambda) = \frac{(1 - R_{\text{top}})[1 + R_{\text{top}} + 2\sqrt{R_{\text{top}}}\cos(4\pi n_{\text{org},i}z_0/\lambda)]}{1 + R_{\text{top}}R_{\text{bot}} - 2\sqrt{R_{\text{top}}R_{\text{bot}}}\cos(4\pi L_{\text{cav}}/\lambda)} I_0(\lambda) \quad (3.41)$$

$$L_{\text{cav}} = \sum_i^n n_{\text{org},i} \cdot d_i \quad (3.42)$$

where the R_{top} and R_{bot} refer to reflectance of top cathode and bottom anode and $n_{\text{org},i}$ is the refractive index of the organic material $i = \{1, 2, \dots, n\}$, z_0 is the distance from the emitter to the top highly reflecting cathode, L_{cav} is the length of the cavity, d_i is the thickness for each organic layer i , λ is the wavelength and I_0 is the spectral intensity in the absence of a cavity. Here, the quality factor Q represents the multiple interactions of cavity resonance and beam interference.

It is possible to increase the spectral intensity by using a cavity with the quality factor Q larger than 1. According to Equation (3.41) and (3.42), the quality factor Q is related to the distance between the emissive layer to the top reflective electrode, the emissive spectrum as well as the reflectivity of bottom and top electrodes. As an estimation, by considering a simplified system consisting of an ideal metallic conductor and organic materials with a refractive index of $n_{\text{org}}(\lambda)$ and a glass substrate, the constructive interference orthogonal to the planar cavity at a wavelength of λ is determined by the emitter-to metal distance l_1 and the emitter-to substrate distance l_2 : [61]

$$\frac{4\pi}{\lambda} n_{\text{org}}(\lambda) l_1 - \pi = 2\pi m_1 \quad (3.43)$$

$$\frac{4\pi}{\lambda} n_{\text{org}}(\lambda) l_2 = 2\pi m_2 \quad (3.44)$$

where m_1 and $m_2 = \{0, 1, 2, \dots, n\}$ represent the resonance order. In Equation (3.43) and (3.44), a phase rotation angle is π at the organic/metal interface and 0 at the organic/glass interface. The cavity length L_{cav} in this case, can be simplified as:

$$n_{\text{org}}(\lambda) L_{\text{cav}} = \frac{\lambda}{4} (2m_1 + 2m_2 + 1) \quad (3.45)$$

For a typical device with fixed $l_2 = \lambda/2$ and $m_2 = 0$, the first constructive resonance can be obtained with cavity length of $L_{\text{cav}} = 3\lambda/4$ and the second constructive resonance of $L_{\text{cav}} = 5\lambda/4$. For a destructive interference, it can be achieved with $L_{\text{cav}} = \lambda$, while fixing $l_2 = \lambda/2$ and $m_2 = 0$.

For top emitting OLEDs, both the bottom and top electrodes are reflective metals. The precise design of cavity resonance can even give slightly higher EQE compared to the bottom emitting counterpart. For bottom emitting OLEDs with ITO anode, the

deposition of a thin reflective silver layer on top of it, could also lead to higher EQE by using the constructive resonance.[188]

The utilization of cavity to enhance the efficiency of OLEDs, however, can bring the disadvantage of strong angular dependent emission, which needs to be avoided for most applications. Meanwhile, the cavity resonance can also impact the radiative rate of excitons with a reduced exciton lifetime, which can mitigate the efficiency roll-off for devices operating under high current density.[189]

3.10 Micro/nano pattern fabrication

Even though tuning the anisotropy factor of emitting molecules and the cavity resonance can somehow enhance the device performance, the excitation of SPP modes, waveguide modes and substrate modes can still give rise to significant photon trapping in OLEDs. As discussed in previous sections, the application of micro/nano structures in OLEDs to extract trapped photons for both top and bottom emitting OLEDs is needed. In this section, the attention is paid on the fabrication technique and/or mechanism, to realize simple, scalable and cost-effective manufacturing techniques for outcoupling in OLEDs based on the mechanism introduced in previous sections.

3.10.1 Photolithography and laser interference

Photolithography, a widely used technology in chip industry, can be applied to fabricate predefined structures by transferring the geometric pattern from a photomask to light-sensitive photoresists via photon exposure. The photoresist-coated substrate is exposed to electron or light beams with a pre-defined pattern for conventional photolithography. The limited size of the structure, is defined by the light source, the lens system and the photoresist. It is possible to fabricate periodic structures from micrometers to several hundreds of nanometers by deep-UV radiation with an advanced mask/resist system.[190] Other photolithography techniques, such as electron-beam lithography (EBL) or interference lithography, possess the ability to directly pattern the photoresist without the need of mask to pre-define the pattern. The exposed area (positive photoresist) or the unexposed area (negative photoresist) is removed in the development solvents. The patterned photoresist can be then used as an etching mask during the following chemical or physical etching treatment.

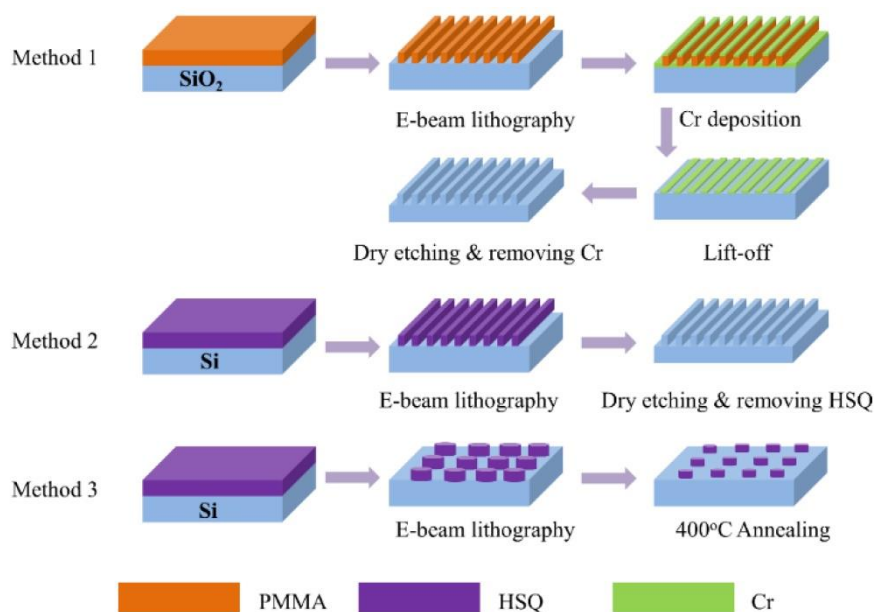


Figure 3.18. Typical procedures for making nanostructures by EBL. Method 1: dry etching with Cr as the etching mask following the lithography with positive resist PMMA. Method 2: dry etching with HSQ as the mask, based on negative resist HSQ. Method 3: with an EBL lithography process and an annealing treatment, with resist HSQ. Reproduced with permission from reference [191].

To schematically illustrate the procedures of fabricating periodic patterns by photolithography, as an example, typical methods based on EBL technique with either positive photoresist or negative photoresist are presented in Figure 3.18.[191] Since the EBL is directly radiated on the photoresist with electron beams, it is possible to obtain pillar or grating patterns with sizes from hundreds of nanometer down to about 20 nm by tuning the exposure dose. There is a minor difference for the fabrication procedures for silicon dioxide substrate or silicon wafer, based on positive photoresist PMMA and/or negative photoresist hydrogen silsesquioxane (HSQ). In method 1 (Figure 3.18), the fabrication of nanostructures on silicon dioxide (SiO_2) wafer was done by patterning soft PMMA resist, followed with a lift-off process. The chromium (Cr) layer was used as the etching mask for the reactive ion etching (RIE) process (dry etching), since the PMMA can be easily removed during the RIE process, giving shallow patterns in the SiO_2 wafer. The Cr layer possesses the durability to achieve grating patterns with depth to ~ 100 nm in the SiO_2 wafer. In method 2, the nano-pattern is fabricated on silicon wafer, where the organic photoresist HSQ is resistant to reactive ions during the RIE etching process, without the need of Cr layer. In the final method 3, pillar patterns with size down to sub-20 nm was obtained without the etching process, where the patterned resist HSQ was annealed at high temperature and turned to silica-like material. The pillar pattern of the HSQ resist can be used as master mold directly for nanoimprinting.

Even though EBL can fabricate patterns down to sub-20 nm, it is time-consuming and expensive technology compared to the interference lithography. Müller-Meskamp *et al.* demonstrated the possibility to structure thin metal films by direct ablation using laser interference patterning.[192] Hexagonally periodic array with different sizes can be achieved by setting the laser power density and the pulse numbers as a fast and simple method. Y Jin *et al.* demonstrated the feasibility of using periodic nanostructures generated by laser beam interference to extract trapped photons in top OLEDs.[193]

On one hand, as discussed in Section 3.9, when integrating periodic nanostructures into OLEDs, it is possible to raise the problem of wavelength or angular dependent enhancement behavior, which is unwanted for neither display or lighting purposes. It is therefore needed to seek for techniques to fabricate structures with a distribution of periodicity. On the other hand, photolithography techniques in general are expensive, involving multiple steps and different facilities, possessing the difficulty to fabricate 3-dimensional patterns on curved surfaces. Lithography-free and cost-effective technology is needed to fabricate micro/nano patterns for OLEDs.

3.10.2 Soft lithography

Soft lithography is a family of technologies involving of elastomeric stamps and/or modes as key elements to transfer the patterns to substrates. For soft lithography techniques, the manufacturing of micro/nano structures is realized by photolithography-free methods, such as self-assembly of organic materials, replica molding from structures fabricated beforehand by photolithography with a following contact printing, selective wet etching and so on.[194] For outcoupling purposes, it is definitely possible to fabricate micro/nano structures in the silicon wafer by photolithography, while the pattern can be used as a master mold and replicated as PDMS stamps. The replica PDMS modes can be used as stamps to transfer the structures into OLEDs. However, the photolithography process is still needed. The idea for lithography-free methods are originating from the replacement of photomasks in lithography. In other words, the substitution of photomask with a medium which can be used as a mask during the etching process, but it has the suitable size for outcoupling purposes at the same time.

Among lithography-free methods, the self-assembled monolayer of polystyrene (PS) nanospheres has been used to fabricate nanostructures for successful extraction of trapped photons in OLEDs, as discussed in Section 3.9.2.[180] Here, the detailed fabrication processes are introduced, including the patterning, etching, lift-off and anode deposition.

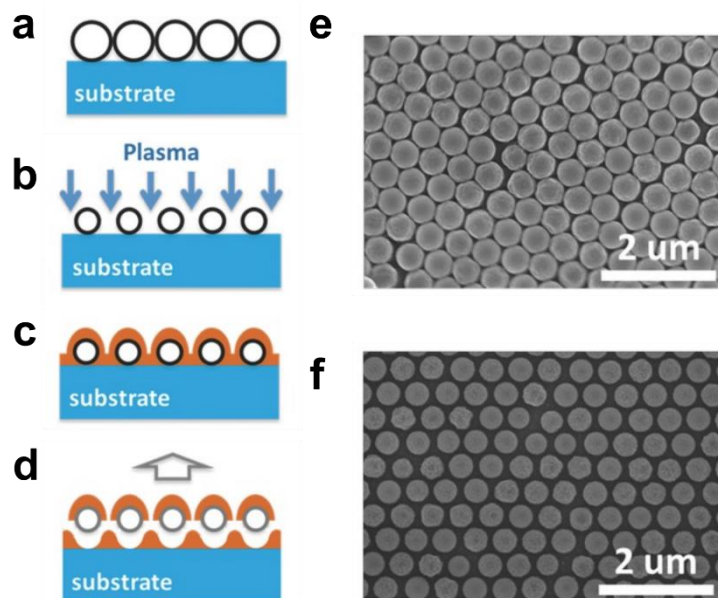


Figure 3.19. Soft lithography process by using PS nanospheres for outcoupling in OLEDs. (a) PS nanospheres assembly on the surface of substrates. (b) RIE etching. (c) ITO sputtering. (d) lift-off process. (e) SEM image of the self-assembled monolayer of PS nanospheres on the substrate before the RIE treatment. (f) SEM image of PS nanospheres after the RIE treatment. A shrink of the nanosphere is noted. Reproduced with permission from reference [180].

As shown in Figure 3.19, a close-packed PS nanosphere monolayer was obtained by spin-coating with the combination of water. Before the RIE etching with oxygen, the average diameter of the nanosphere was about 500 nm. The diameter was shrunk to about 270 nm after the RIE etching with oxygen, as shown in Figure 3.19b and f. The conductive oxide ITO layer was then deposited on the RIE treated nanosphere (Figure 3.19c). The structured ITO layer can be obtained by a lift-off process. It should be noted that the geometric pattern of ITO nanostructure in this case is dependent on the diameter and the distance between nanospheres after RIE etching.

It is possible to structure the commercial ITO substrate by soft lithography, followed by RIE etching and another wet etching processes, as shown in Figure 3.20. [195] After the generation of monolayer of PS nanospheres, a layer of tetraethyl orthosilicate sol-gel was spin-coated. The sol-gel can be converted to SiO_2 film via a hydrolysis reaction by thermal treatment in air. Because of the durability difference between PS nanosphere and the SiO_2 film, the RIE treatment will generate a nano-bowl pattern within the SiO_2 layer, as shown in Figure 3.20c. Further chemical etching with the piranha solution (concentrated sulfuric acid and hydrogen peroxide with a volume ratio of 7:3) on the ITO anode by using the nano-bowl geometry as a template, giving the final structured ITO with a similar nano-bowl appearance, as shown in Figure 3.20d.

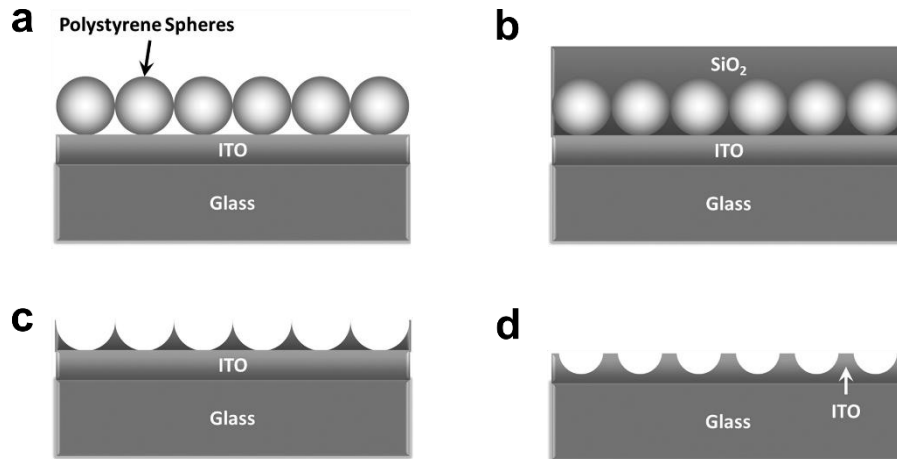


Figure 3.20. Structuring the commercial ITO substrate by soft lithography. (a) self-assembled monolayer of PS nanospheres on the surface of ITO. (b) PS nanospheres covered by a layer of spin-coated tetraethyl orthosilicate sol-gel, which can be converted to SiO₂ by a hydrolysis reaction. (c) RIE treatment to remove partial of the SiO₂ film and the PS nanospheres. (d) Chemical etching the ITO and remove of the residual SiO₂ by controlling chemical etching via the perforate SiO₂ film. Reproduced with permission from reference [195].

Since PS nanospheres with different diameters are commercial available, the soft lithography method to structure the TIO electrode can be used to fabricate nanostructures with a wide range of periodicities and depths.

3.10.3 Stress release

Structures with a wide scope of sizes such as wrinkles on aging human skin, folds on dried fruits and buckling on the engineering systems by compressing stiff films on soft substrates, are geometrical deformations which are theoretically induced by compressive or stretched stress in a multi-layer systems. Such systems give the impression of the wrinkle/buckling patterns with rich morphologies with a large scale scope. Even though it is possible to obtain structures with similar appearance to buckling/wrinkles on curved surfaces, the discussion here is focusing on a flat surface induced by compress or strain stress, since the aim of nanostructure generation is the application into flat OLEDs, while structures on curved surfaces are not compatible.[196]

Young's modulus E is a mechanical property that describes the stiffness/elasticity of a solid material. It is defined as the ratio between the applied stress (force per unit area) and proportional deformation of a uniaxial deformation in the linear elasticity regime:

$$E = \frac{F/A}{\Delta L/L} \quad (3.46)$$

where F is the applied force on the area A , ΔL is the deformation in one direction and L is the original length.

As the proportional deformation is a dimensionless term, the Young's modulus has a unit of Pa from the numerator of Equation (3.46). According to Equation (3.46), it is clear that the Young's modulus E is larger for stiff materials than that for soft elastic materials. For example, the Young's modulus is about 70 GPa for aluminum (Al), while it is only several MPa for PDMS, a widely used rubber-like polymer.

Possion's ratio ν is a parameter defined as the ratio of transformation in the axial and transverse direction under compressive or stretched tension. The plane-strain modulus \bar{E} can be defined as:

$$\bar{E} = \frac{E}{1 - \nu^2} \quad (3.47)$$

For the simple 2-dimensional case, upon loading the compressive stress σ , a buckling-like instability pattern can be found in a bi-layer system with a soft base and stiff surface layer with a thickness of t_s , as shown in Figure 3.21. The appearance of the buckling can be treated as a sinusoidal function with the periodicity p and depth h (2 times of the amplitude of a sinusoidal function). Since there is no need of photolithograph or etching processes, a further detailed discussion on generation mechanism is meaningful.

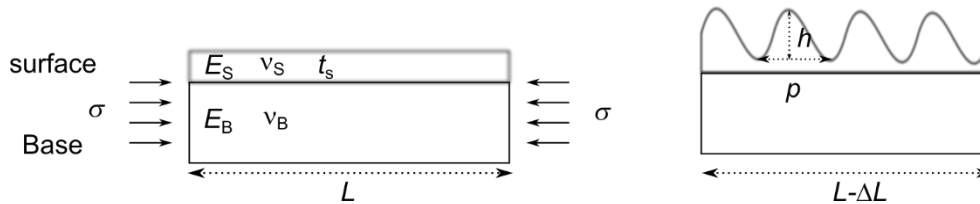


Figure 3.21. schematic illustration of buckling patterns upon compressive stress in a bi-layer system. The system forms a buckling pattern upon the compressive stress from the initial length L to a shorter length $(L - \Delta L)$. The subscript s denotes the surface stiff layer and b is the soft base.

Here, the plane of the soft base and the stiff surface is regarded as x - y plane, while the z -axis is perpendicular to the surface. The axis of the compressive force is defined as x -axis. The sinusoidal geometry of the buckling pattern can then be described as:

$$z = \frac{h}{2} \sin(2\pi x/p) \quad (3.48)$$

When compress a semi-infinite substrate with a stiff surface layer, the deformation of the system is determined by:[197]

$$\overline{E}_S I \frac{d^4 z}{dx^4} + F \frac{d^2 z}{dx^2} + kz = 0 \quad (3.49)$$

where $I = wt_S^3/12$, $k = \overline{E}_B w \pi / p$, F is the applied force and w is the width. Substituting Equation (3.48) into (3.49) gives:

$$16\overline{E}_S I \left(\frac{\pi}{p}\right)^4 - 4F \left(\frac{\pi}{p}\right)^2 + k = 0 \quad (3.50)$$

Solving Equation (3.50), the relationship of sinusoidal pattern and the applied force F can be written as:

$$F = 4\overline{E}_S I \left(\frac{\pi}{p}\right)^2 + \frac{\overline{E}_B w p}{4\pi} \quad (3.51)$$

Whenever the energy balanced ($\partial F / \partial p = 0$) is met, the periodicity p of the sinusoidal pattern can be deduced from Equation (3.51):

$$p = 2\pi t_S \left(\frac{\overline{E}_S}{3\overline{E}_B}\right)^{1/3} \quad (3.52)$$

Substituting Equation (3.47) into (3.52) gives

$$p = 2\pi t_S \left(\frac{E_S}{1 - \nu_S^2}\right)^{1/3} \left(\frac{3E_B}{1 - \nu_B^2}\right)^{-1/3} \quad (3.53)$$

According to Equation (3.53), it is clear that the periodicity p is dependent on the Young's modulus, Poisson's ratio for both the surface layer and bottom base. Moreover, the periodicity is linear with the thickness of the top stiff layer t_S .

The critical stress (σ_c) needed to initialize the buckling process can be calculated by dividing the applied force F to the cross-sectional area of the stiff film:

$$\sigma_c = \frac{F}{wt_S} = \frac{1}{4} \left(9\overline{E}_S \cdot \overline{E}_B^2\right)^{1/3} \quad (3.54)$$

Accordingly, the critical strain ε_c can be calculated by:

$$\varepsilon_c = \frac{\sigma_c}{E_S} = \frac{1}{4} \left(\frac{3\overline{E_B}}{\overline{E_S}} \right)^{\frac{2}{3}} \quad (3.55)$$

Mathematically, according to Equation (3.52) and (3.55), the relation between ε_c and p can be written as:

$$p = \frac{\pi t_S}{\sqrt{\varepsilon_c}} \quad (3.56)$$

Once the applied stress exceeds the threshold, the system forms sinusoidal buckling patterns. However, further increase the stress, the periodicity is theoretically constant, according to Equation (3.53). The depth of the sinusoidal structure should be then responsive to the increased stress. The expression of the depth h for the sinusoidal structure can be derived, by assuming that the release of strain in forms of deformation is equal to the overstrain ($\varepsilon - \varepsilon_c$) upon the onset of the geometrical instability. The relationship between the applied strain ε and the ε_c is written as:[197]

$$\varepsilon - \varepsilon_c = \frac{1}{p} \int_0^p \sqrt{1 + \left(\frac{dz}{dx} \right)^2} dx - 1 \quad (3.57)$$

The integral in Equation (3.57) denotes the contour length of the buckling within one period. When considering:

$$\sqrt{1 + \left(\frac{dz}{dx} \right)^2} \approx 1 + \frac{1}{2} \left(\frac{dz}{dx} \right)^2 \quad (3.58)$$

one can obtain the relation between parameters of sinusoidal pattern and the overstrain by substituting Equation (3.57) with (3.58) and (3.48):

$$\varepsilon - \varepsilon_c = \frac{\pi^2 h^2}{4p^2} \quad (3.59)$$

Combining Equation (3.59) and (3.56), the relation between the depth of the sinusoidal pattern and the overloading of the strain can be written as:

$$h = 2t_S \sqrt{\frac{\varepsilon - \varepsilon_c}{\varepsilon_c}} \quad (3.60)$$

Whenever the strain is much larger than the critical strain ε_c , Equation (3.60) can be further simplified as:

$$h \approx 2t_S\sqrt{\varepsilon} \quad (3.61)$$

According to Equation (3.54) and (3.61), in cases when the strain is much larger than the critical strain, the depth of the sinusoidal structure is linear with the thickness of the top stiff layer and the square root of the applied force F . Since the periodicity of the sinusoidal pattern is independent on the applied force, it is then possible to independently tune the periodicity and depth in a bi-layer system, by fixing the thickness of the top stiff layer with a soft base (E_B, ν_B) and stiff surface (E_S, ν_S) and optimizing the applied strain. It is reliable to obtain sinusoidal structures with sizes ranging from centimeter to nanometers scale by optimization of material composition and/or the thickness, which can be used for many applications including outcoupling purposes in OLEDs.[198] However, further increase of the applied force can destroy the continuous geometry, giving rise to new morphology such as cracks.[199]

Considering the previous analysis that the periodicity of sinusoidal pattern merely depends on the intrinsic properties of materials, it is accessible to measure the Young's modulus of some special materials such some 2D materials with only several atomic layers, by using the buckling generation method, where other general measurement strategies is not possible.[200] In some cases, when the Young's modulus is tunable by light or heat, the size of the sinusoidal pattern is changing with the variation of external environments, giving the possibility to fabricate sensors for various purposes.[201,202]

Even though sinusoidal patterns generated by mechanical forces have been widely used for flexible/stretchable optoelectronic devices, compressive stress induced by thermal radiation possesses vital importance, since the ease of fabricate without the need of direct contact. When metal films are deposited on the top of a flat soft based (for example, a layer of PDMS) with external heating, disordered buckling patterns can be noted on the surface when the system is cool down to room temperature.[203] If the soft base is perfectly smooth, while the substrate temperature is T_D during the deposition before cooling to T afterwards, the biaxial compressive force is given by:[204]

$$F = \frac{w(\alpha_B - \alpha_S)(T_D - T)}{\frac{1 - \nu_S}{t_S E_S} + \frac{1 - \nu_B}{t_B E_B}} \quad (3.62)$$

Here α refer to coefficient of thermal expansion (CTE).

The compressive stress can be further calculated as:

$$\sigma = \frac{F}{wt_S} = \frac{(\alpha_B - \alpha_S)(T_D - T)}{\frac{1 - \nu_S}{E_S} + \frac{t_S(1 - \nu_B)}{t_B E_B}} \quad (3.63)$$

Since $t_S(1 - \nu_B) \ll t_B E_B$, Equation (3.63) can be simplified as:

$$\sigma = \frac{E_S(\alpha_B - \alpha_S)(T_D - T)}{1 - \nu_S} \quad (3.64)$$

According to Equation (3.64), the compressive stress is linear with the difference of the CTE between the base and surface materials, the temperature difference and the Young's modulus of the surface layer.

The generation of nanostructures in the bi-layer system consisting of aluminum layer as top stiff surface and PDMS as the bottom soft base is discussed as a demonstration. The critical stress to form buckling can be obtained according to Equation (3.55). In this case, with the physical parameters $E_S = 70$ GPa, $E_B = 20$ MPa, $\nu_S = 0.35$ and $\nu_B = 0.48$, one can obtain the σ_c as 1.96×10^8 Pa. With $\alpha_S = 960 \times 10^{-6}$ K⁻¹ and $\alpha_B = 23.1 \times 10^{-6}$ K⁻¹, according to Equation (3.64), it is then possible to deduce that the system starts to form buckling patterns when the temperature difference is higher than 2 K. Such a small temperature difference can be easily reached in a vacuum chamber by the thermal energy during deposition of aluminum. According to Equation (3.53), to achieve a pattern with the periodicity of 500 nm, the thickness of deposited aluminum layer is about 7.9 nm.

Even though previous analysis demonstrates the facile access of buckling/wrinkle pattern by thermal introduction in a bi-layer system, one should note that it is difficult to independently control the periodicity and depth. This can be easily deduced by comparing Equation (3.53) and (3.56), since both the periodicity and depth are linear with the thickness of the top stiff layer. In other words, when increasing the thickness of the top layer, the periodicity and depth will increase at the same time. It is still technically possible to independently tune the periodicity and depth of micro/nano structures generated by thermal heating, since all these analyses are based on the assumption of flat substrates for a single generation. Multiple generation runs can in principle tune the periodicity and depth independently, as shown in Figure 3.16. Moreover, when the soft base is pre-defined with some geometrical patterns, the release of compressive stress is then confined with the pre-defined geometry, giving rise to much ordered pattern compared to buckling/wrinkles with directional randomness.[203]

Compared to methods involving photolithography and soft lithography, the generation of micro/nanostructures by compressive stress release with an appearance

of buckling/wrinkle is a facile, easy-access approach, without the need of expensive facilities for lithography or etching. Moreover, it is possible to fabricate structures with sizes from centimeters to nanometer regime as well, which is needed for external outcoupling and internal outcoupling for OLEDs, as discussed in Section 3.9. By using organic materials as the soft base, the generation of controllable nanostructures is possible in vacuum, compatible with the fabrication process of OLEDs.

3.11 Chapter summary

According to the description in this chapter, it is clear that many factors should be taken into account to obtain highly efficient OLEDs: the conversion efficiency of charges to excitons including singlets and triplets, the radiative efficiency within the device and the outcoupling efficiency from the multilayer microcavity structure. The final device performance is a sum of the intrinsic properties of functional materials, the device configuration as well as the outcoupling techniques.

Even though the mitigation of SPP modes and tuning the cavity resonance can somehow enhance the device efficiency, micro/nano structures are needed to extract photon from loss channels of substrate modes, waveguide modes and SPP modes. Extraction strategies for enhancing the EQE are still needed. The application of micro/nano patterns can mitigate the energy loss for state-of-the-art OLEDs with unity IQE. Even though nanostructures can be fabricated by lithography and etching processes with a precise control, complicated fabrication processes and high-costs can hinder their practical application. Structures generated by soft lithography and compressive stress release hold advantages of easy fabrication and pronounced enhancement without side-effects of periodic patterns such as wavelength and/or angular dependent emission. To compare the extraction efficiency between different strategies, the extraction efficiency is more meaningful compared to the enhancement factor. However, the introduction of nanostructure into a functional device can also harm the operation stability by altering the electrical property. Hence, the fabrication complexity, the device stability and the absolute efficiency with extraction structures should be emphasized.

4 Experimental and methods

In this chapter, the related materials used in this thesis are introduced, including materials for fabricating nanostructures, substrate and OLEDs. The device fabrication, encapsulation and evaluation are explained. A brief introduction to supplementary measurements including X-ray photoelectron spectroscopy and dynamic mechanical analysis are given. Furthermore, important measurements and characterization details of the nanostructures and photophysical properties are described. In the end, the device modeling details for both planar and structured OLEDs are specified.

4.1 Materials

The majority of materials are commercially purchased from different suppliers as stated below, while the TADF polymer is synthesized by Leibniz Institute of Polymer Research Dresden (IPF). The organic materials for Chapter 5 and Chapter 6 consist of small molecules, which are purified twice by vacuum gradient sublimation prior to device fabrication, except for the dopants for transport layer, which are used as received. For OLEDs based on TADF polymer emitter P1, the HTL, EBL and EML are prepared by spin-coating, while the remaining layers of HBL, ETL and cathode are fabricated by thermal evaporation.

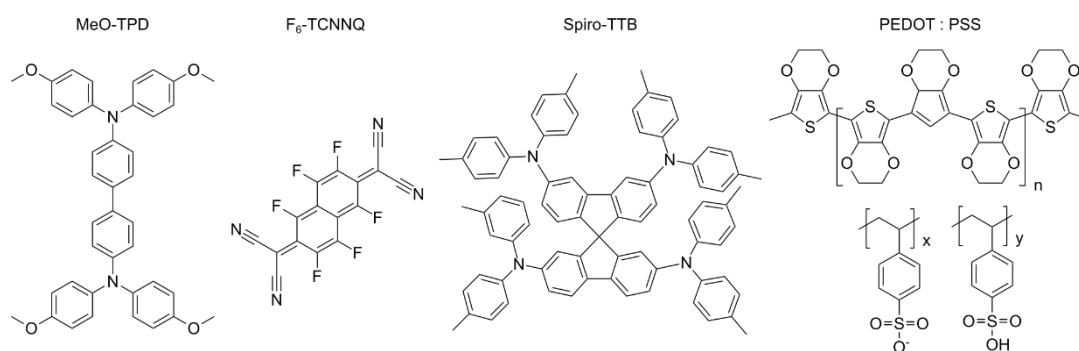


Figure 4.1. The chemical structure of HIL and HTL. MeO-TPD and Spiro-TTB layer doped with p-dopant F₆-TCNNQ can be used as HIL and HTL. PEDOT:PSS is used as solution-processed HTL.

Hole injection and transport layer (HIL and HTL): For thermal deposited devices, N,N,N',N'-tetrakis(4-methoxyphenyl)-benzidine (MeO-TPD, Lumtec), spiro-tetra(p-methyl-phenyl)-benzidine (Spiro-TTB, Lumtec) with small amount (2-4 mol%) of 2,2'-(perfluoro-naphthalene-2,6-diylidene) dimalononitrile (F₆-TCNNQ, Novaled)

doped films are used as HIL and HTL. For solution processed TADF devices, the well-known poly(3,4-ethylenedioxythiophene) polystyrene sulfonate (PEDOT: PSS, AI 4083, Heraeus Clevios™) are used as HTL. Chemical structures are shown in Figure 4.1.

Hole and electron blocking layer (HBL and EBL): The 2,2',7,7'-tetrakis-(N,N'-diphenylamino)-9,9'-spirobifluorene (Spiro-TAD, Lumtec) and/or N,N-di(naphthalen-1-yl)-N,N-diphenyl-benzidine (NPB) can be used as electron blocking layer for thermal evaporated OLEDs, while the bis(2-,ethyl-8-quinolinolato)-4-(phenyl-phenolato) aluminum-(III) (BAIq₂, Lumtec) and/or 4,7-diphenyl-1,10-phenanthroline (BPhen, Lumtec) is used as hole blocking layer. For solution-processed OLEDs based on TADF polymer P1, the poly(9-vinylcarbazole) (PVK, Mw ~1,100,000, Sigma-Aldrich) are used as EBL, while different materials are tested as HBL, including 2,4,6-tris[3-(diphenylphosphinyl)phenyl]-1,3,5-triazine (PO-T2T, Lumtec), bis[2-(diphenylphosphino)phenyl] ether oxide (DPEPO, Lumtec), BPhen (Lumtec), 2,2''-(1,3,5-benzenetriyl)-tris[1-phenyl-1H-benzimidazole] (TPBi, Lumtec) and 1,3,5-tri(m-pyridin-3-ylphenyl)benzene (TmPyPB, Lumtec). Their chemical configurations are shown in Figure 4.2.

Electron transport layer (ETL): BPhen doped with Cesium (Cs) are used as electron transport materials. For OLEDs based on the solution process, TPBi and BPhen doped with Cs are tested as ETL.

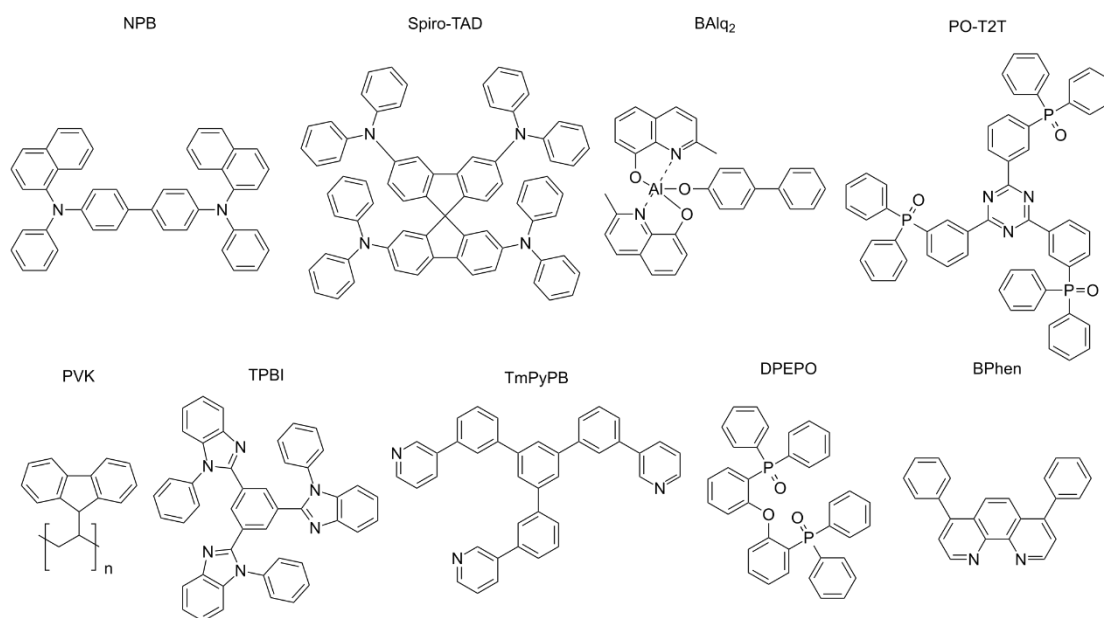


Figure 4.2. The chemical structure for HBL and EBL materials. NPB, Spiro-TAD and PVK (solution-processed) can be used as EBL, while BAIq₂, PO-T2T, TPBi, TmPyPB, DPEPO and BPhen can be used as HBL.

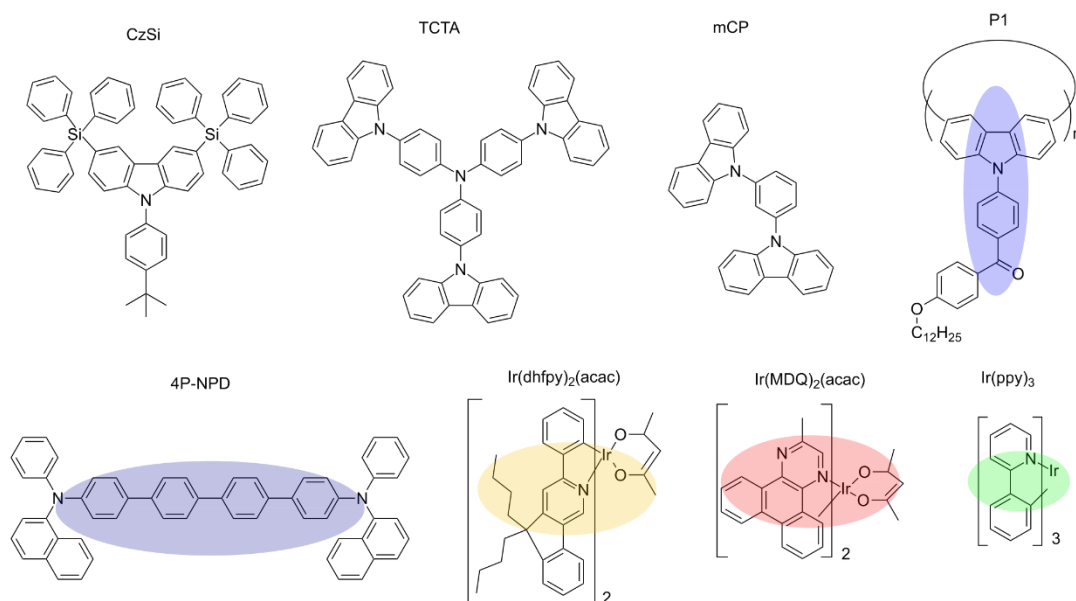


Figure 4.3. The chemical structure of hosts and different emitters. The pinned colorful ellipsoids indicate the emitting color of these organic emitters.

Emission layer (EML): Host materials including *N,N'*-di-1-naphthalenyl-*N,N'*-diphenyl-[1,1':4',1'':4'',1''':4''',1''''-quaterphenyl]-4,4''-diamine (4P-NPD), 4,4',4''-tris(*N*-carbazolyl)-triphenylamine (TCTA, Lumtec), NPB and TPBi are involved for OLEDs based on small molecules. For solution-processed OLEDs based on TADF emitter P1, several host materials including 1,3-Bis(*N*-carbazolyl)benzene (mCP, Lumtec), 9-(4-*tert*-butylphenyl)-3,6-bis(triphenylsilyl)-9H-carbazole (CzSi, Lumtec) and 2,4,6-tris[3-(diphenylphosphinyl)phenyl]-1,3,5-triazine (PO-T2T, Lumtec) are tested.

The conventional blue emitter 4P-NPD is used as the triplet harvesting blue emitter for the tandem white OLEDs. For phosphorescent emitters, the iridium(III)bis(2-methyldibenzo-[*f,h*]chinoxalin)(acetylacetonate) [Ir(MDQ)₂(acac), Lumtec], fac-tris(2-phenylpyridine) iridium(III) [Ir(ppy)₃, Lumtec], bis(2-(9,9-dihexylfluorenyl)-1-pyridine) (acetylacetonate) iridium(III) [Ir(dhfpv)₂(acac), Lumtec] are involved. The chemical structures for these emitters together with the TADF polymer P1 is shown in Figure 4.3.

Nanostructure generation and transfer: To reduce the error of mixing the base and curing agent, poly(dimethylsiloxane) (PDMS, SYLGARD® 184, Sigma-Aldrich) with a fixed base and curing agent ratio of 10:1 is purchased. To investigate the ratio influence and the pattern copy, PDMS (SYLGARD® 184) is bought from Dow Corning, where the ratio of the base to curing agent can be varied manually. NOA 63 glue is purchased from Norland Products Inc. The surface treatment material Perfluorodecyltrichlorosilane (FDTS) is bought from Alfa Aesar.

4.2 Nanostructure generation with PDMS

The base and curing agent are mixed manually and then degassed under vacuum for ca. 10 minutes. The mixture is then casted on pre-cleaned glass substrates at a speed of 1000 rpm. PDMS coated glass substrates are heated in an oven at different temperatures for different heating time. After the pretreatment, substrates with PDMS are transferred to the reactive ion etching (RIE) instrument (Oxford Plasmalab 80 Plus). After RIE treatment, samples are removed to a clean room environment with a humidity of 55% and then stored in the lab at room temperature.

The RIE treated PDMS are modified by FDTS vapor for one day in a closed container in a glovebox under nitrogen atmosphere. The PDMS mixture is used as replica material to reproduce patterns on the RIE treated PDMS. After mixing and degassing, the PDMS mixture with a ratio of 10: 1 of the base to curing agent is carefully poured onto FDTS treated samples and then treated in an oven at 80°C for 60 min. The stamped PDMS can be peeled off and used as nanoimprinting stamps. Diluted NOA 63 by mixing with acetone at a weight ratio of 1:1 is spin-coated on cleaned glass substrates with a speed of 8000 rpm. The PDMS stamp is pressed into NOA 63 resist by a nano-imprinter and cross-linked under UV radiation for 10 min.

4.3 Thin metal electrode fabrication and characterization

Quartz substrates (size 25 mm × 25 mm) are sequentially cleaned with isopropanol, acetone and DI water. After drying at 110 °C in an oven, the surface of the substrates are treated with oxygen plasma for 10 min. Molybdenum oxide (MoO₃) is deposited at a rate of 0.1 Å/s in a vacuum chamber under a pressure of ~10⁻⁷ mbar. The substrates are then moved to another metal chamber to deposit the Au and Ag films. The Au layers are thermally deposited at a rate of 0.3 Å/s. After this, a 7 nm Ag layer is fabricated. A four-point probe system is utilized to measure the sheet resistance. The morphology of the thin metal electrodes is detected by AFM. The complex permittivity of each material is measured by an EP4 imaging ellipsometer (Accurion GmbH). The transmission in the forward direction is confirmed with a Shimadzu UV-3100 UV-VIS-NIR spectrophotometer. With an integrating sphere, the light scattered to all direction is collected to measure the total transmittance.

4.4 Topography measurement

The pattern on NOA 63 resist is measured by SEM (DSM 982, Carl Zeiss), to measure the general appearance of the nanostructures. A high scanning resolution of AFM measurement (1024 by 1024) is done to determine the periodicity distribution, in an area of 10 μm by 10 μm . Another two measurements with a lower scanning resolution of 256 by 256 are carried out to get the average depth information. The periodicity distribution described in this thesis is coming from the high-resolution scan, while the average depth is obtained from all these measurements by averaging the results.

4.5 Device fabrication

Solution-processed OLEDs: The PEDOT:PSS are filtered and then spin-coated with a speed of 1000 rpm on the cleaned ITO substrates. An annealing process is done at 120°C for 30 min in ambient atmosphere before the following spin-coating processes. The other spin-coated layers are done inside a glovebox under nitrogen atmosphere and low water concentration. The PVK with a concentration of 10 mg/ml dissolved in 1,2-dichlorobenzene is coated with a speed of 2000 rpm. The film is annealed at 150°C for 10 min and cooled down to room temperature before casting the emissive layer. The P1 neat film is about 30 nm at a speed of 1000 rpm with a concentration of 5 mg/ml in toluene. For host-guest films, a thickness of about 50 nm can be obtained by spin-coating at a speed of 1000 rpm with a concentration of 7.5 mg/ml in toluene. The emissive layer is annealed at 40°C for 20 min in a glovebox. The following organic and cathode layers are fabricated in Lesker facilities from Kurt J. Lesker Co., under the vacuum of ca. 10^{-7} to 10^{-8} mbar. Deposition rates are monitored during material evaporation via quartz crystals.

OLEDs based on thin metal electrodes: Eagle XG glass substrates are cleaned and dried at 110 °C. The substrates are treated with oxygen plasma for 10 min. The OLEDs are fabricated in a Lesker facility as described above.

OLEDs on sputtered ITO with nanostructures: Glass substrates with nanoimprinted NOA 63 are degassed at 70°C under vacuum for 5 hours. The ITO anode is patterned as a four finger structure with a metal mask cut by laser. The ITO anodes are sputtered by sheet-to-sheet processing in the pilot scale in-line sputter coater. A conventional planar single magnetron system with oxide targets driven in direct current (DC) sputtering mode is applied. The cathode length is 75 cm. The sputtering is processed with a power of 3 kW and an oxygen gas flow of 6 sccm under a pressure of

0.3 Pa. After sputtering, the ITO samples are heated at 70°C for 1 hour in vacuum. The layer thickness of the ITO film is ca. 90 nm with a sheet resistance of 67 Ω . The ITO sputtering process is done in Fraunhofer Institute for Organic Electronics.

After the ITO sputtering, glass substrates are used without any further cleaning process. Substrates are heated under vacuum at 70°C for 1 hour to get rid of moisture during transfer. Devices are made in a Lesker tool (see above). The pixel size of OLED devices is calibrated, with a slight size variation (from 6.7 to 8.2 mm²) originating from difference of mask opening for the ITO sputtering.

Device encapsulation: All OLEDs are encapsulated in a glovebox under nitrogen atmosphere after fabrication. The encapsulation glass lid has a small area to host the getter material and make sure that no contact is made to the active area of the OLED pixels. The encapsulation lid is glued to the substrate by using an epoxy resin (XNR5516Z-L and XNR5590, Nagase Europa GmbH).

Device evaluation: The current density-voltage-luminance characteristics are recorded with a KEITHLEY SMU2400 and a calibrated silicon photodiode at the same time. Electroluminescence spectra under different driven voltages are measured by a calibrated spectrometer (CAS 140 CT, Instrument Systems). The EQE and luminous efficacy are further confirmed with a calibrated integrating sphere (LABSPHERE), with a SMU2400 and a calibrated spectrometer (CAS 140 CT). The angular dependent emission characteristic is obtained by a goniometer with a calibrated spectrometer and a rotatory stage in a step resolution of 1°.

4.6 XPS measurement

The chemical bonding energy and atomic concentration are measured by a XPS instrument (PHI 5600-CI, Physical Electronics, USA) with non-monochromatic Mg-K α (1253.6 eV, 400 W), at the incident angle of 54°. The atomic concentration of PDMS surface before and after RIE treatment is calculated with standard single element sensitivity factors.

4.7 Dynamic mechanical analysis (DMA)

DMA test is done to measure the Young's modulus by ARES2 (TA Instruments, USA). The PDMS samples are cured in petri dish and cut into a bar shape. The size is calibrated by a micrometer, with a small size variation from 4 cm \times 1 cm \times 1 cm. The measurement is carried out in a single-frequency scanning mode at the frequency of 1 Hz, with a heating rate of 10°C min⁻¹.

4.8 Device modeling

To numerically simulate the loss channels for the planar tandem white device, it is divided into two units and each unit is calculated independently, while keeping the other unit as passive layers present. The efficiency for air modes, substrate modes, waveguide modes and evanescent modes of each unit are summed up, to get the fraction of photons in each mode for the tandem device, of which the total assumed IQE is 200%. The theory is summarized in Section 3.5 and the tool is based on Mauro Furno's tool.[61] The layer thicknesses with corresponding complex refractive indices are used according to the device architecture. Other optical data, such as the anisotropy factor, the effective radiative efficiency and the electrical efficiency are obtained from literatures.

Optical simulations of corrugated devices are done with a commercial tool (Comsol Multiphysics 5.3) based on the finite element method (FEM).[205] The emitting dipoles and nanostructures are treated as 2D species to reduce the computing load. The simulated device architecture is following the experimental device, in which thin layers ($d \leq 10$ nm) sandwiching emission dipoles are treated as a single layer, to avoid the need for very small mesh elements in these layers. The optical indices for each layer are set according to the measured values. Sine nanostructures is used with various periodicities and amplitudes to simulate light outcoupling to the glass medium, where the glass substrate is treated as a half-infinite medium. Emission sources in simulations are treated as differently oriented point dipoles located at the corresponding emission interface since their much smaller size compared to the emitting wavelength. The model area is set to a lateral size of 20 μm around the emitting dipole, while the entire model is covered by a perfectly matching layer (PML) as the boundary condition, to avoid any reflection at the boundaries. Collection of the radiated light is at least one wavelength away (skin depth) from the film structure (planar and textured) to avoid the influence from coupling of evanescent waves to the PML.

The simulation is sweeping in 10 nm wavelength steps within the range from 400 to 800 nm, for sinusoidal textures with periodicities from 300 nm to 2000 nm and different depths. A flat structure is simulated as a comparison, in which internal efficiencies are set to match experimental results.

4.9 Photophysical properties measurement

Cleaned quartz substrates are treated with oxygen plasma for 10 min. The host-guest films are prepared by spin-coating in a glove box. For detailed time-dependent measurements, the time-correlated-single-photon-counting (TCSPC) technique is used. After exciting the sample with a laser at 373 nm with pulse width of 44 ps, the emitted photons are detected by a photomultiplier tube (PicoQuant PMA Hybrid) and the data is collected by a TCSPC module (PicoQuant TimeHarp 260). The PLQY of these films is confirmed by using a calibrated integrating sphere in nitrogen flow, with the CAS 140 CT spectrometer and a UV-LED (Thorlabs, 340 nm). The methodology of PLQY confirmation is following the method released by Friend *et al.*[206] The steady-state photoluminescence (PL) spectrum is obtained during the PLQY measurement. The UV-absorption measurement for materials for TADF devices is done with Shimadzu MPC 3100.

5 Improved optics by ultrathin MoO₃ layer for efficient OLEDs

Molybdenum trioxide (MoO₃) has been used as a wetting and energy-level modification layer in OLEDs and organic solar cells.[207–210] However, the optical effect has not been addressed and fully understood. In this chapter, the optical effect of the thin MoO₃ layer for bottom emitting tandem white and red OLEDs is thoroughly investigated. It is observed that a thin MoO₃ layer has a pronounced influence on the device performance. A systematic investigation is done on the device performance and the physical properties of thin films. Based on the theory of SPP modes and the dielectric constant measurements, the SPP mode is suppressed in the range from 400 nm to 520 nm with the presence of MoO₃ layer. Moreover, introducing a thin MoO₃ layer mitigates the reflectance of the composite Au/Ag electrode, resulting in a decreased destructive resonance within the device, confirmed by transfer matrix simulation and experiments. The synergistic effect enables to achieve efficient two-unit stacked white OLEDs, with the EQE and luminous efficacy of 38.8% and 53.9 lm/W at 1,000 cd/m², when substrate and air modes are included, making the EQE about 1.9 times higher compared to the reference without MoO₃ layer. The result is published in reference [187] and this chapter is based on this publication with permission.

5.1 Tandem white OLEDs

White OLEDs in a stacked architecture comprising the thin metal electrode are prepared without or with a 3 nm, 6 nm and 10 nm MoO₃ layer. The OLED structure is shown in Figure 5.1a, with a triplet harvesting blue-red unit (unit 1) and a green-yellow unit (unit 2), which has shown high efficiencies for devices with an ITO or PEDOT:PSS anode.[90,211] The full name and chemical structure of these materials can be found in Chapter 4. Samples with 0, 3, 6 and 10 nm MoO₃, are named as D0, D3, D6 and D10 in the following discussion.

The current-voltage and luminance-voltage characteristics for D0, D3, D6 and D10 are shown in Figure 5.1b. The leakage current for samples with MoO₃ is higher than those without MoO₃. According to Figure 5.1b, it is clear that the leakage current is gradually increased when rising the thickness of MoO₃ from 0 nm to 3 nm, 6 nm and 10 nm. The difference of leakage current in the low driving voltage range could result from the different roughness. However, at high voltages, the transport and recombination behavior of these devices is almost identically while the luminance for D0 is lower compared to D3, D6 and D10.

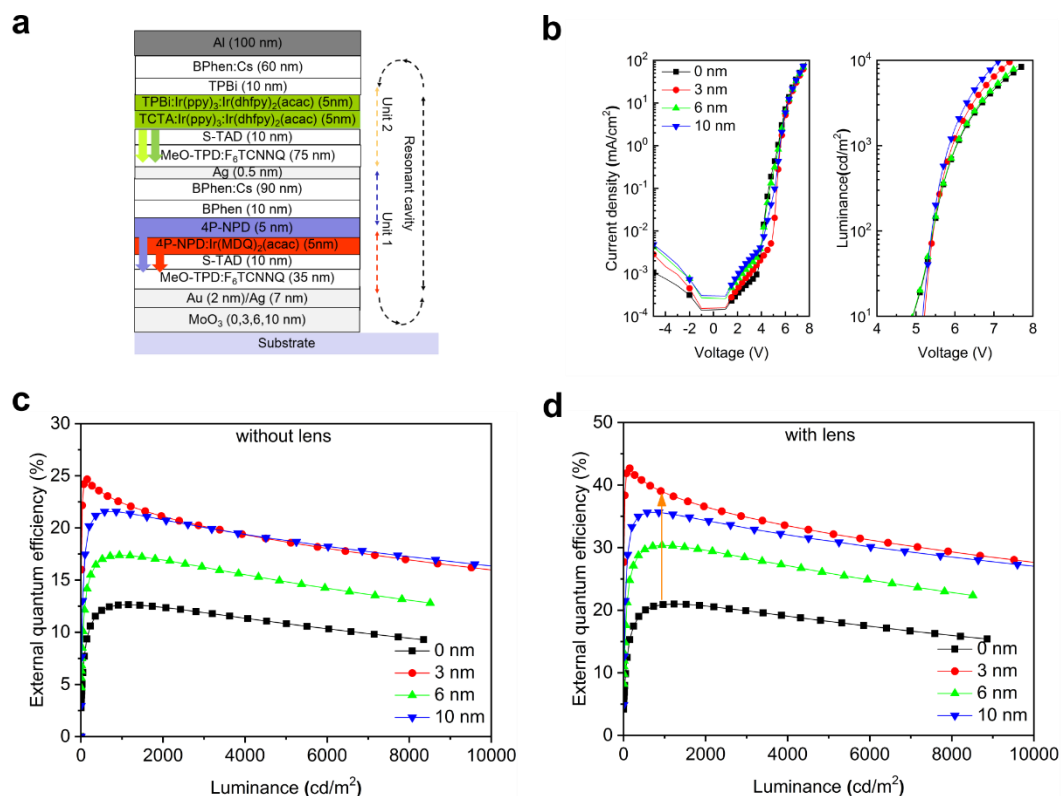


Figure 5.1. (a) Device architecture of white OLEDs based on a thin metal electrode. (b) Voltage-current density and voltage-luminance curves for samples with increasing thickness of MoO₃ (0 -10 nm). (c) EQE without half-sphere lens. (d) EQE obtained with attached half-sphere lens to extract photons trapped as substrate modes.

Compared to D0, the EQE of devices D3, D6 and D10 is much higher. As shown in Figure 5.1c, the EQE of D3 reaches over 22.5 % compared to 12.6 % for D0 at a luminance of 1,000 cd/m², corresponding to an enhancement factor of 1.8. To further extract trapped photons from the substrate, a half-sphere lens is attached to the planar substrate. In this measurement configuration, the EQE of D3 reaches 38.8% at a luminance of 1,000 cd/m², while the EQE for D0 is only 20.9%, which corresponds to an enhancement factor of 1.9. Compared to the device without MoO₃, the insertion of 3 or 10 nm MoO₃ can significantly improve the EQE. The device efficiency of D3 is comparable to white OLEDs based on ITO electrode, which can reach 26.8% at 1000 cd/m², while it is 22.5% with the MoO₃ composite electrode in the present work.[90]

The leakage current is slightly higher compared to the ITO-based OLEDs. It is interesting to note that the device with 6 nm MoO₃ (D6) shows slightly lower EQE compared to D3 or D10, but still higher than D0. The EQE of D6 is about 1.5 times higher than D0 at 1000 cd/m². The reason is not fully understood, but most probably related to a slight cavity change, since the angular dependent emission of D6 deviates more strongly from the Lambertian distribution compared to D3 or D10, as shown in Figure 5.2b. Compared to D3, the angular dependent EL change is larger for D0, as shown in Figure 5.2c and Figure 5.2d. The irradiance distribution for D3 is closer to the Lambertian emission compared to D0, indicating a better angular emission. Also, D0 gives the largest change of Commission Internationale de L'Eclairage (CIE) coordinates from 0° to 75°, with ($\Delta\text{CIE}_x, \Delta\text{CIE}_y$) of (-0.01, 0.1) for D3 and (-0.10, 0.16) for D0, as shown in Figure 5.2a. Moreover, as shown in Figure 5.3, the integrated EL spectrum of D6 is slightly different from D3 and 10, which may also contribute to the weaker enhancement of EQE.

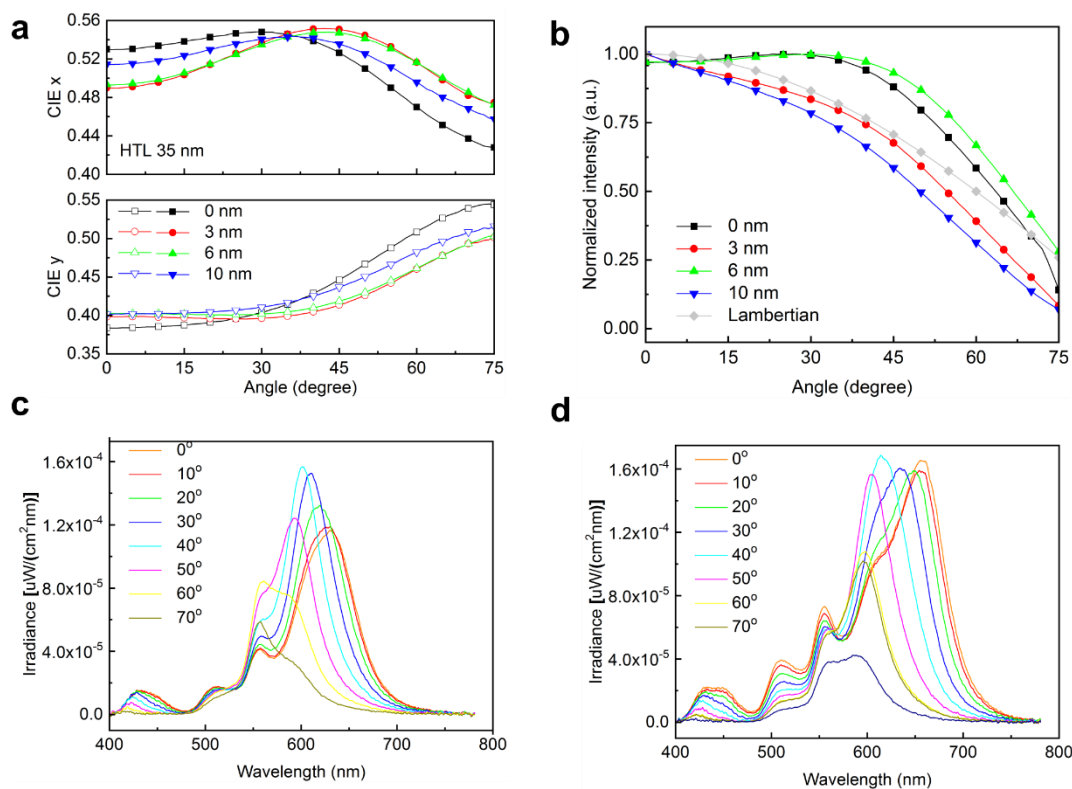


Figure 5.2. Angular emission properties for white devices. (a) Angular dependent CIE for devices for D0, D3, D6 and D10. (b) Normalized spectral radiant intensity for D0, D3, D6 and D10. (c) Angular dependent EL spectra for D0. (d) Angular dependent EL spectra for D3.

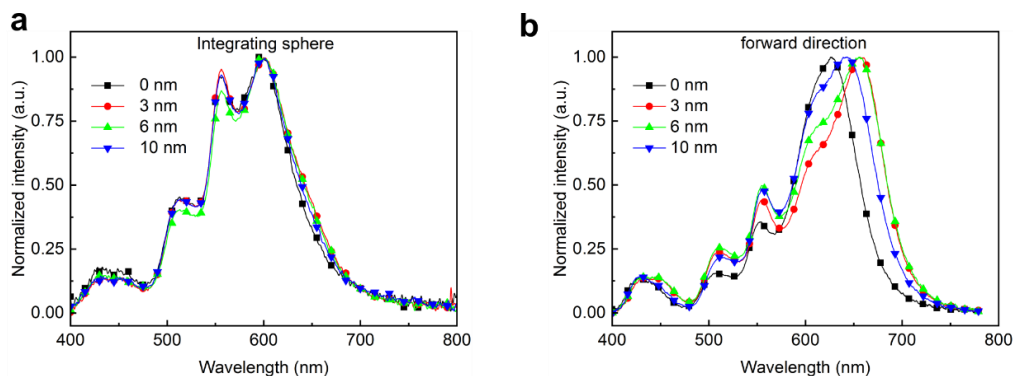


Figure 5.3. EL spectra of white devices. (a) From the integrating sphere; (b) In the forward direction.

5.2 Enhancement mechanism investigation

5.2.1 Minor influence on the electrical efficiency

According to Equation (3.25), the EQE of OLEDs is determined by the electrical efficiency γ , the normalized internally generated EL spectrum $S_{el}(\lambda)$, the effective radiative efficiency $\eta_{rad}(\lambda)$ and the outcoupling efficiency $\eta_{out}(\lambda)$. In the following, it is discussed which of these four factors is responsible for the observed EQE improvement.

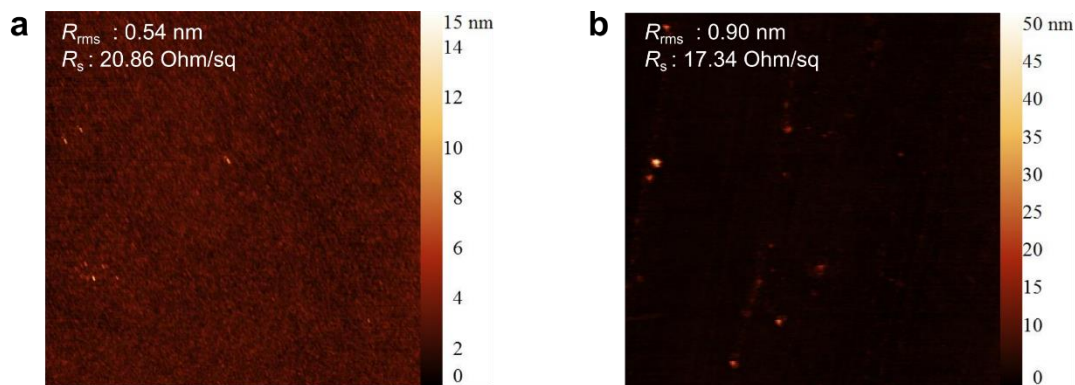


Figure 5.4. Morphology of thin metal electrodes Au (2 nm)/Ag (7 nm). (a) Without MoO₃ layer. (b) With 10 nm MoO₃ under the Au layer.

One possibility is that the electrical efficiency is enhanced because of a better film morphology with MoO₃ as a wetting layer, leading to an altered hole injection impacting on the charge balance. However, the morphology of thin metal electrodes without or with 10 nm MoO₃ is very similar, as shown in Figure 5.4. The root mean square roughness (R_{rms}) from AFM measurements of both electrodes is reasonably good with $R_{rms} < 1$ nm. It is interesting to note that the roughness of the electrode with 10 nm MoO₃ with $R_{rms} = 0.90$ nm is even slightly higher compared to the electrode without

MoO₃ with $R_{\text{rms}} = 0.54$ nm. This could result from the crystal nature of MoO₃, which gives slightly higher roughness compared to the flat electrode.[212] The results of AFM measurements are consistent with the observed leakage current increase for D10 and D0. Furthermore, the sheet resistances of these two electrodes are very similar. The Au (2nm)/Ag (7 nm) electrode without MoO₃ shows a resistance of 21 Ohm/sq, while for the electrode with 10 nm MoO₃, the resistance slightly decreases to 17 Ohm/sq. Hence, inserting the MoO₃ layer shouldn't cause a significantly better carrier injection. The similarity of voltage-current density characteristics of all electrode configurations at high driving voltages ($U > 6$ V) where devices are usually operated, support that the electrical efficiency γ is not the cause of EQE differences of these devices.

Because the devices are electrically identical with respect to the functional organic semiconductors and their layer sequence, neither the intrinsic emission spectra of the different emitters nor the energy transfer processes between them within the emission layers should change under the variation of the MoO₃ layer. Based on these considerations, the overall internal EL spectrum S_{el} should be the identical for all these devices and, hence, be considered as an unaltered source for the efficiency discussion. Thus, the increase of the device performance should originate from a pronounced enhancement of the outcoupling efficiency $\eta_{\text{out}}(\lambda)$ and/or the effective radiative efficiency $\eta_{\text{rad}}(\lambda)$.

5.2.2 The suppression of SPP modes

The dispersion relation of a SPP mode can be obtained by solving the Maxwell's Equations, as described in Section 3.6. Since the real part of the permittivity ϵ'_{met} is negative and the dielectric constant of the dielectric medium ϵ_{diel} is positive, the SPP dispersion can only exist when the absolute value of ϵ'_{met} is larger than ϵ_{diel} . In this case, a SPP mode propagates along the interface between the metal and the dielectric medium. Because the wave vector of the SPP is larger than the wave vector in free space ω/c , or within the dielectric medium $\omega/c\sqrt{\epsilon_{\text{diel}}}$, the SPP is intrinsically non-radiative.[145] The electromagnetic field exerts a force on the electron gas in the metal, driving a collective electron oscillation.[213] According to this analysis, the SPP cannot be excited when $\epsilon_{\text{diel}} > |\epsilon'_{\text{met}}|$. Therefore, it is possible to suppress the SPP loss channel in bottom OLEDs by tuning ϵ_{diel} to be larger than $|\epsilon'_{\text{met}}|$. [179,214,215]

As shown in Figure 5.5, the dielectric constant of MoO₃ is almost constant in the visible wavelength range. However, the real part of the Au permittivity is highly wavelength dependent. It is found that between 400 and about 520 nm (λ_2), the permittivity of MoO₃ is larger than $|\epsilon'_{\text{met}}|$ of Au. Also, in range of 400 to 485 nm (λ_1), the permittivity of SiO₂ is larger than the corresponding $|\epsilon'_{\text{met}}|$ of Au. According to the theory, the thin MoO₃ layer at the interface can suppress the SPP mode in the wavelength range from 400 to 520 nm. Compared to devices without MoO₃, the difference is relevant in the range from 485 to 520 nm. Experimentally, however, as shown in Figure 5.3, no significant change is noted between the normalized electroluminescence spectra for D0 and D3 or D10 in this range. The reason is unclear, but it could be that there is a coupling of SPP modes on both sides of the thin metal layer, making the energy dissipation mixed with another SPP mode along with interface of the electrode and hole transport layer.[216]

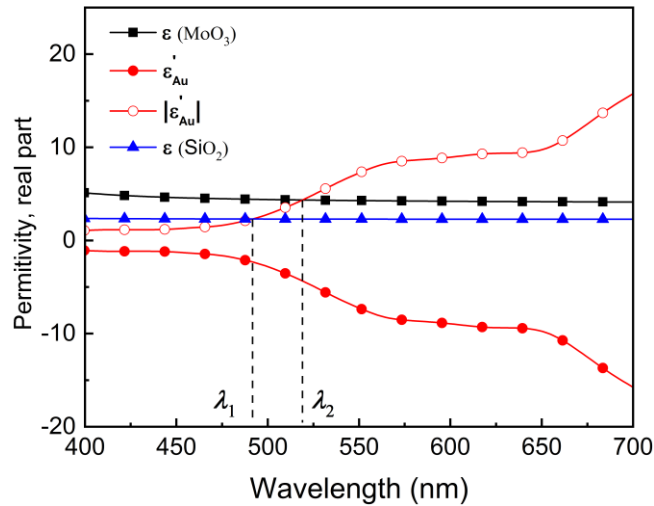


Figure 5.5. The measured permittivity of SiO₂, MoO₃ and Au (real part). Within the range from 400 to λ_1 , the permittivity of SiO₂ is larger than the permittivity (real part) of Au, while it is 400 nm to λ_2 for MoO₃.

5.2.3 Cavity resonance

Further investigation reveals that the other factor influencing on the EQE of white OLEDs is related to the cavity resonance. The bottom semi-transparent anode and the highly reflective top cathode form a Fabry-Pérot cavity in these devices. By considering the effect of a Fabry-Pérot cavity and two beam interference, the spectral intensity $I(\lambda)$ can be written as Equation (3.41).

Since the organic functional layers between the bottom thin metal electrode and top reflecting cathode is the same for devices with or with MoO₃ layer, according to Equation (3.41) and (3.42), the distance from the emitting interface to the top reflecting

cathode is important to achieve efficient devices. Assuming the refractive index of organic materials to be 1.7 at $\lambda = 610$ nm, the term $\cos(4\pi n_{\text{org},i} z_0/\lambda)$ is about $\cos(3\pi)$ for the white OLED structure, corresponding to a minimum value for the cosine function. This indicates that the red part of the white device emission is close to the destructive interference. A decrease of the reflectance of the bottom thin metal electrode could reduce the destructive interference. Therefore, it can increase the device performance. This is validated with help of transfer matrix simulations.

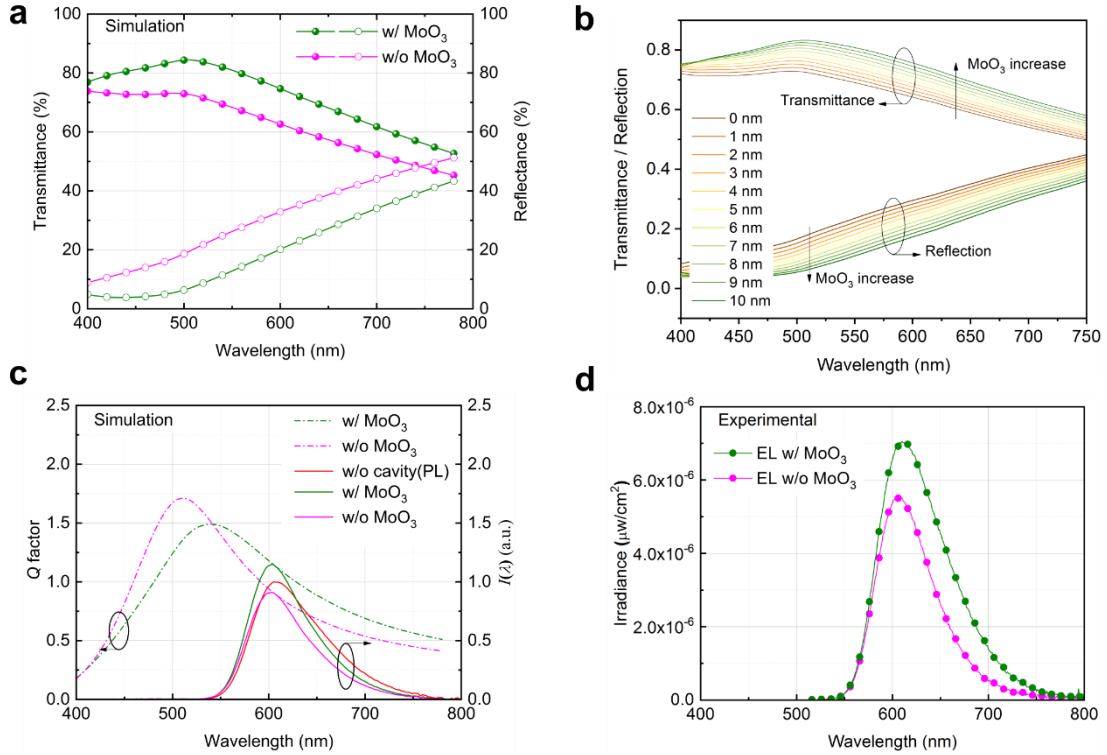


Figure 5.6. (a) Calculated transmittance and reflectance of the Au (2 nm)/Ag (7 nm) electrode without MoO₃ or with 10 nm MoO₃. Solid: transmittance; open: reflectance. (b) Calculated transmittance and reflectance of the electrode in a configuration of MoO₃ (x nm)/Au (2 nm)/Ag (7 nm). (c) Calculated Q factor for red OLEDs. PL spectrum of red emitter is plotted as EL spectrum in the absence of cavity. (d) Experimental spectral radiant intensity for red OLEDs with or without 10 nm MoO₃.

As shown in Figure 5.6a, the transmittance of the composite electrode with MoO₃ is about 10% higher compared to the one without MoO₃. Moreover, the reflectance of the electrode without MoO₃ is about 10% higher compared to the one with MoO₃. The more detailed simulations, shown in Figure 5.6b, indicate the increase of the MoO₃ thickness from 0 - 10 nm can gradually increase transmittance and reduce the reflection, with a film configuration of MoO₃ (x nm)/Au (2 nm)/Ag (7 nm). Since the red part of the white device is close to the destructive interference, a decrease of the reflectance of the bottom thin metal electrode by increasing the MoO₃ thickness from 0 to 10 nm can reduce the destructive interference, giving a higher device performance. Combing the effect of SPP mode suppression, we therefore anticipate a higher device efficiency for

the white devices with 5, 7, 8 nm MoO₃, compared to D0. This is also demonstrated by the EL spectra in the forward direction for these white devices, as shown in Figure 5.3b. A slight change of the MoO₃ thickness can modulate the cavity resonance, leading to a significant peak shift in the red region.

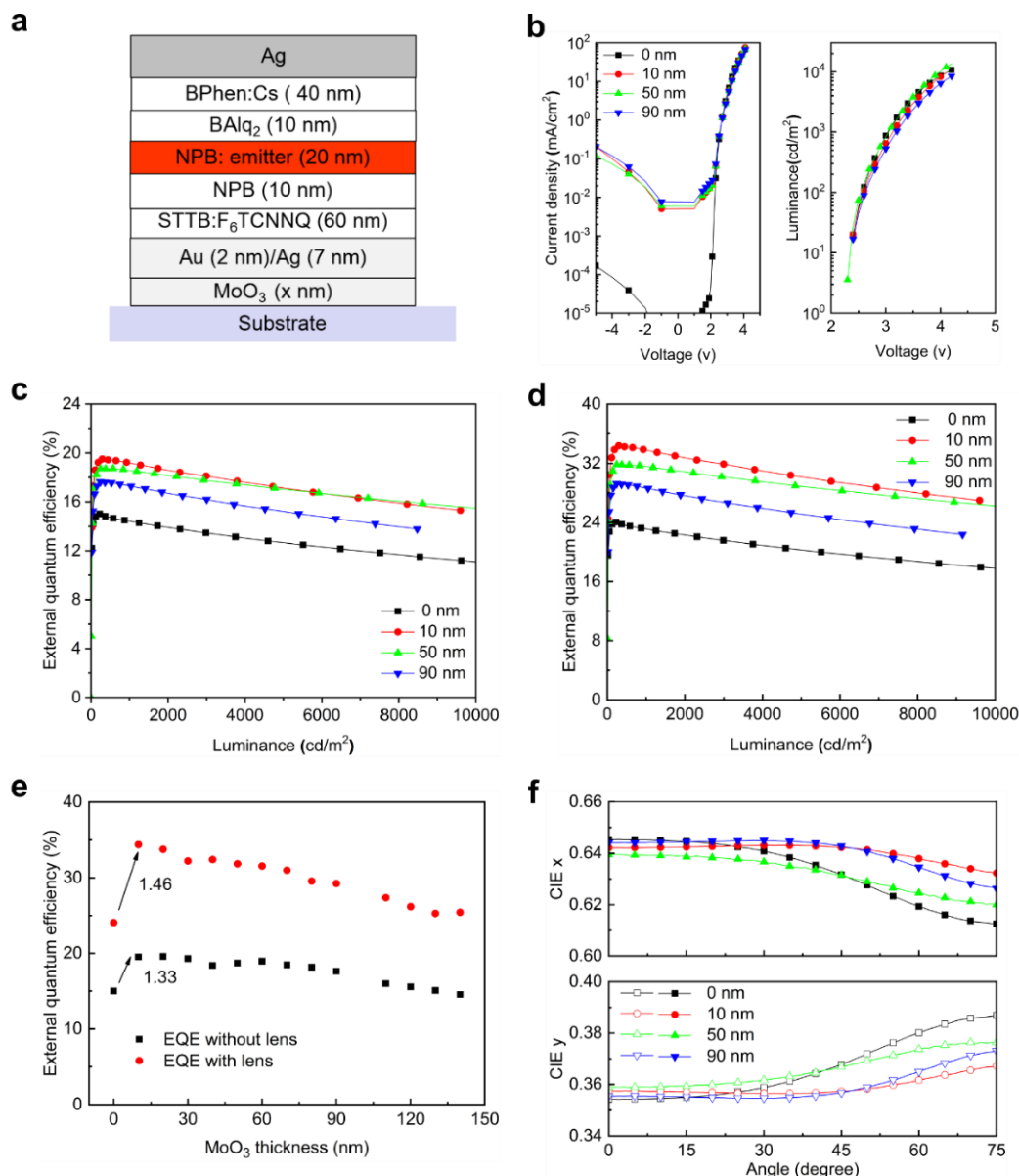


Figure 5.7. (a) Device architecture of bottom emitting red OLEDs based on a thin metal electrode. The red emitter is Ir(MDQ)₂(acac). (b) Voltage-current density and voltage-luminance characteristics. (c) EQE without half-sphere lens. (d) EQE with half-sphere lens. (e) The dependence of EQE on MoO₃ layer thickness. (f) The dependence of CIE coordinate as a function of emission angles from 0° to 75°.

To further analyze the cavity effect, red OLEDs are built based on thin metal electrodes with the thickness of MoO₃ varied from 0 nm to 140 nm with a step width of 10 nm. The device structure and performance are summarized in Figure 5.7. A similar phenomenon compared to white devices can be found in red ones. The voltage-current

density characteristics is almost the same, with higher leakage current for devices with the MoO₃ layer. Also, the EQE measured with a half-sphere lens at 1,000 cd/m² is increased from 24.1% to 34.4% by inserting 10 nm MoO₃ beneath the composite electrode Au (2 nm)/Ag (7 nm). Moreover, a significant CIE change for devices without MoO₃ at different emission angles in the range from 0° to 75° indicates pronounced cavity effects. The lowest CIE change is noticed for red OLEDs with 10 nm MoO₃ beneath the Au/Ag electrode.

Numerical simulations for red devices are conducted to investigate the influence of the cavity resonance on the spectral radiant intensity $I(\lambda)$. The transmittance and reflectance of these two electrodes are calculated based on a transfer matrix algorithm. The Q factor is then calculated according to Equation (3.41) and plotted in Figure 5.6c. It is wavelength dependent, and the maximum value can be obtained at $\lambda \approx 510$ nm for electrodes without MoO₃ and at $\lambda \approx 540$ nm for electrodes with 10 nm MoO₃ layer. Based on this, the spectral radiant intensity $I(\lambda)$ with the cavity can be calculated by multiplying the Q factor with the spectrum in absence of the cavity (photoluminescence spectrum), leading to a narrowing of the spectrum with cavity, as shown in Figure 5.6c. Furthermore, the intensity $I(\lambda)$ for devices with MoO₃ is higher compared to the one without this interlayer, indicating a higher device efficiency. High intensities $I(\lambda)$ can be obtained if the Q factor is larger than 1 and the shape of Q factor is close to the intrinsic emission spectrum. The calculated spectra are in good agreement with the experimentally obtained irradiance, which are depicted in Figure 5.6d. The numerical simulation of red devices shows that the presence of MoO₃ can tune transmittance and reflectance of the metal electrode and strongly influence the device performance.

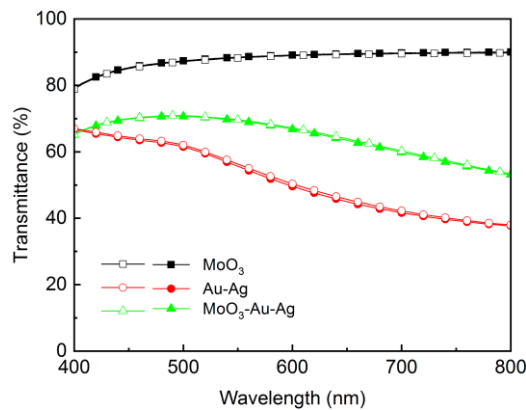


Figure 5.8. The influence of the MoO₃ layer on transmittance. Solid: the total transmittance; Open: the forward transmittance.

We should also note that the roughness of the electrode with 10 nm MoO₃ is not large enough to induce significant light scattering, which is found by transmittance measurements, shown in Figure 5.8. The transmittance in forward direction is almost identical with the total transmittance, indicating negligible light scattering effect.

5.2.4 Finite element analysis

To further explore the energy trapping mechanism, a simulation is done based on finite element analysis (FEA) with COMSOL multiphysics. The device structure is set for the bottom red OLEDs. Parameters for COMSOL simulations are summarized the Table 5.1. Wavelengths of 450 nm, 510 nm and 610 nm are chosen to analyze the relation between emitting wavelength and trapping mechanism. The simulation details can be found in the Section 4.8.

As shown in Figure 5.9 for each wavelength, 10 nm MoO₃ has only a minor influence on the energy dissipation of horizontal dipoles. However, energy trapping is more pronounced for vertical dipoles. At the wavelength of 450 nm, there is no significant energy trapping on the bottom anode for devices with or without MoO₃. This is consistent with the previous analysis because there is no SPP mode on the interface between Au and the substrate at 450 nm for both cases. At 510 nm, more energy is distributed near the bottom thin metal electrodes for the vertical dipole in devices without MoO₃, indicating less energy trapping for devices with MoO₃. This is in good agreement with the previous analysis, because the SPP mode between Au and the substrate is suppressed for devices with MoO₃ and the non-radiative SPP mode is present for devices without MoO₃ between $\lambda_1 = 485$ nm and $\lambda_2 = 520$ nm in Figure 5.5.

Table 5.1. COMSOL simulation parameters

	450 nm		510 nm		610 nm	
	<i>n</i>	<i>k</i>	<i>n</i>	<i>k</i>	<i>n</i>	<i>k</i>
Ag	0.04	2.648	0.05	3.223	0.058	4.094
Organic	1.7	0.001	1.7	0.001	1.7	0.001
Au	1.508	1.878	0.702	2.007	0.205	3.036
Glass	1.524	0.001	1.517	0.001	1.512	0
Al	0.633	5.454	1.015	6.627	1.314	7.296
MoO ₃	2.146	0.001	2.091	0	2.050	0

The lateral dimension of model is set to 5 μ m.

For both cases, there is a coupling of SPP modes between Au and the substrate at a wavelength of 610 nm. However, the cavity effect in the device with a thin MoO₃ layer can enhance the irradiance, while the emission is suppressed when there is no MoO₃. As a result, less energy trapping is noted for vertical dipoles in the device with 10 nm MoO₃ layer at $\lambda = 610$ nm. Since most of the energy losses result from vertical dipoles, emitters with a preferentially horizontal dipole orientation could increase the device efficiency.[80,217,218]

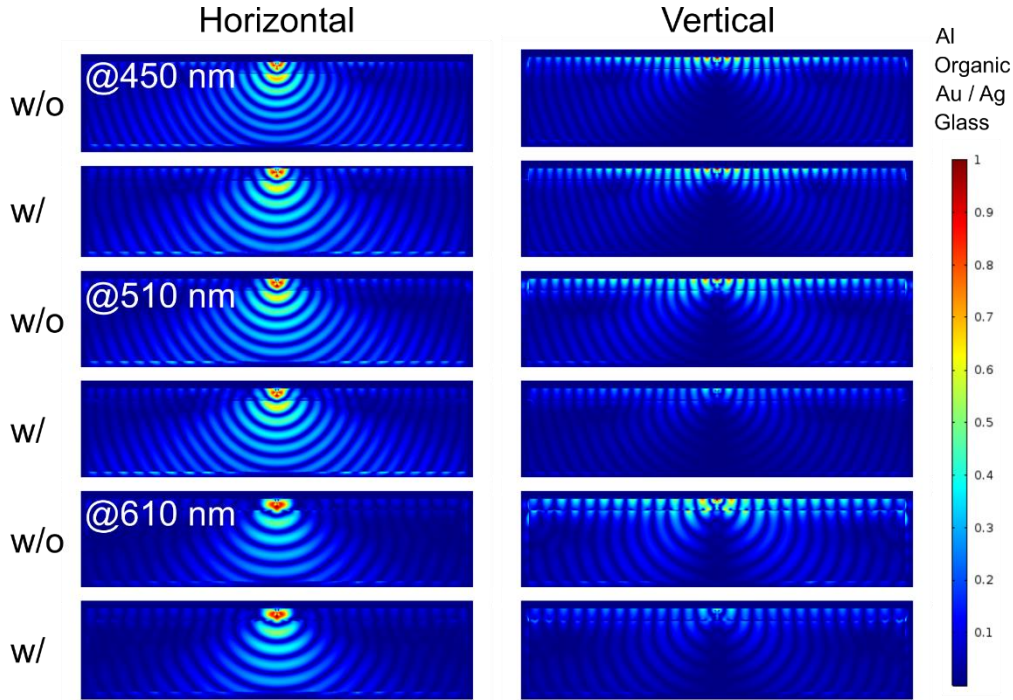


Figure 5.9. COMSOL simulation on the normalized power ($|E^2|$) intensity of horizontal and vertical dipoles at wavelength of 450 nm, 510 nm and 610 nm for devices w/ or w/o 10 nm MoO₃ layer. The top layer is Al and the bottom layer is glass, sandwiching organic layers and thin metal electrodes. The light line between glass and organic layer represents the composite electrode.

5.3 Chapter summary

In this chapter, the OLED efficiency is significantly enhanced by inserting a thin MoO₃ layer beneath a metal bilayer electrode composed of 2nm Au and 7 nm Ag. For white (red) OLEDs, the quantum efficiency with air and substrate modes is increased from 20.9% (24.1%) to 38.8% (34.4%) at 1,000 cd/m², leading to device performance comparable to ITO-based devices. At the same time, close to Lambertian emission can be obtained for devices with MoO₃. The improved device efficiency and the better angular emission properties are ascribed to a synergetic effect of suppressed non-radiative SPP modes and an enhanced cavity resonance. The results show that the application of MoO₃ is an elegant and simple method to control the non-radiative SPP mode and the cavity resonance in OLEDs with a thin metal electrode. Hence, this method suggests a way to convert photons trapped by SPP modes into radiative modes in OLEDs. Finally, by carefully designing the cavity, highly efficient monochrome OLEDs are built, showing a smaller full width at half maximum (FWHM). This could be a powerful strategy to tune the color purity for emitters with a large FWHM, for instance emitters relying on TADF emitters.[33,38,219]

6 *Tailor-made nanostructures for highly efficient white OLEDs*

OLEDs suffer from a significant share of trapped photons in a form of waveguide and SPP modes, leading to only moderate efficiencies. In this chapter, the results of an easy, scalable and cost-effective method to generate quasi-periodic nanostructures bridging chaotic and ordered systems, and its application for white OLEDs are summarized. Mechanical deformations with random orientation are generated on the surface of PDMS in response to stress release, initialized by RIE through external stimuli of physical bombardments, chemical reactions and elastic modulus mismatch between the top silica-like skin layer and the bottom elastic PDMS. These quasi-periodic nanostructures with periodicity and depth distribution from dozens of nanometer to micrometer range are induced by RIE treatment on PDMS for merely tens to hundreds of seconds. It is possible to independently tune the average depth from ~10 to 200 nm and the dominant periodicity from ~200 to 800 nm. Integrating these nanostructures into a two-unit tandem white OLED to extract trapped photons, a maximum EQE of 76.3% and a luminous efficacy of 95.7 lm/W are obtained with extracted substrate modes. The enhancement factor of 1.56 ± 0.12 at 10,000 cd/m² is achieved with a more homogeneous radiance distribution and a reduced color shift over observing angles, proving excellent potential for lighting applications. Furthermore, an optical model is built with consideration of the dipole orientation, emitting frequency (wavelength) and the dipole position on the sinusoidal texture. The results are published in reference [265] and this chapter is based on this publication.

6.1 Nanostructure generation and control

6.1.1 Basic information of RIE induced nanostructures

The fabrication of the nanostructures is schematically shown in Figure 6.1a. Undulations with dimensions from nanometer to micrometer range are found on the entire surface of the PDMS after a short duration of RIE treatment with oxygen and/or argon flow, as shown in Figure 6.1b. The appearance of these patterns is similar with mechanical instabilities, such as creases, folding or wrinkles induced by non-equilibrium on multilayered surfaces.[201,220–222]

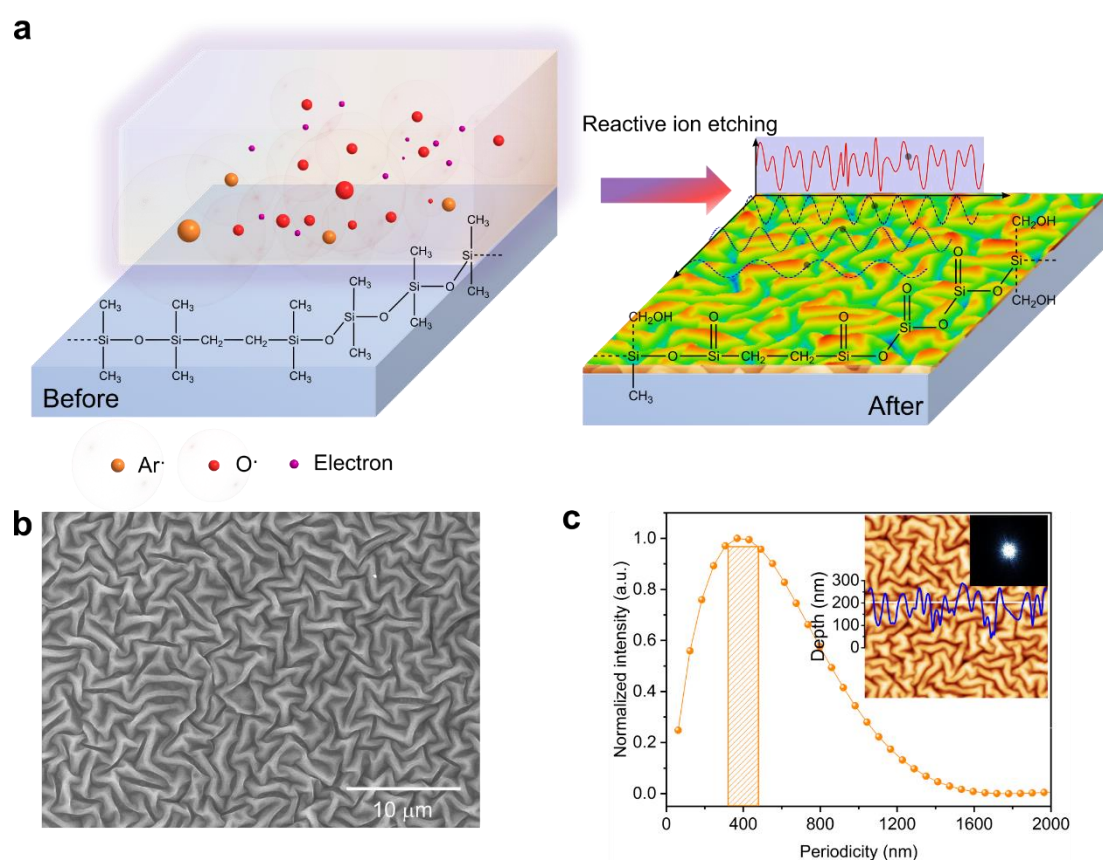


Figure 6.1. Schematic illustrations of RIE-induced nanostructures on the PDMS surface. (a) Thermally pretreated PDMS is modified by RIE with Ar, O₂ ions and electrons via physical bombardments and chemical reactions. After the treatment, the PDMS surface is turned to silica-like layer with a topography of sinusoidal undulations. The presented chemical structure of PDMS after the RIE treatment is one of the possible configurations. (b) SEM image. The nanostructure is widely and homogeneously distributed on the entire surface. (c) The periodicity distribution of the RIE-induced nanostructure. The orange bar indicates the dominant periodicity. Inset: AFM image with a size of $10 \mu\text{m} \times 10 \mu\text{m}$. The white line is chosen at a random position, showing a wavy profile (blue line). The ring shape of the inset FFT pattern indicates the nanostructure is orientated without directional preference. The nanostructures can be simplified to a sum of sinusoidal functions with different periodicities and amplitudes.

As shown in Figure 6.1, cross-section profiles of these nanostructures with sinusoidal shape can be found, with amplitudes ranging from tens to hundreds of nanometers. The ring shape of the FFT pattern (inset of Figure 6.1c) from AFM measurements indicates a random distribution in all directions. The radial power spectral density function (PSDF) from AFM measurements indicates widely distributed periodicities from less than 100 nm to more than 1,000 nm with a dominant periodicity for each individual nanostructure, as shown in Figure 6.1c. There is also a depth distribution with a dominant depth (Figure 6.2). The average depth of sinusoidal structure can be described as $D = 2R_a$, where R_a refers to the average roughness obtained from the AFM measurement.[160] It should be noted the average depth is different from the maximum of the depth distribution (the dominant depth p).

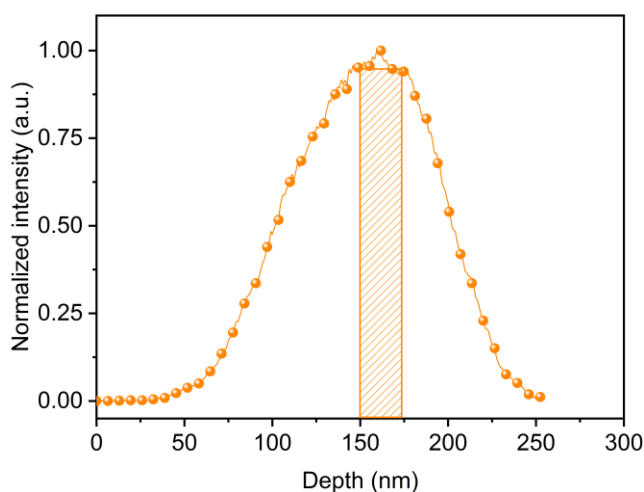


Figure 6.2. The depth (height) distribution of the nanostructure with a dominant depth.

6.1.2 Nanostructure uniformity

The nanostructures generated on the PDMS surface is uniform. The general appearance of the nanostructure can be measured by SEM, as shown in Figure 6.1b. The numerical quantification of the nanostructures is done by AFM measurements on different positions (at least four positions) randomly chosen for each sample, followed with a statistical analysis to check the deviation from each position.

As shown in Figure 6.3, the periodicity distribution of a specific structure (named as N1) is almost the same for all these measurements, where the periodicity distribution is obtained by AFM measurement. The dominant periodicity for N1 is 245.5 nm. There is only a slight deviation of the average depth at different positions, resulting from the intrinsic difference and the experimental deviation for each AFM measurement.

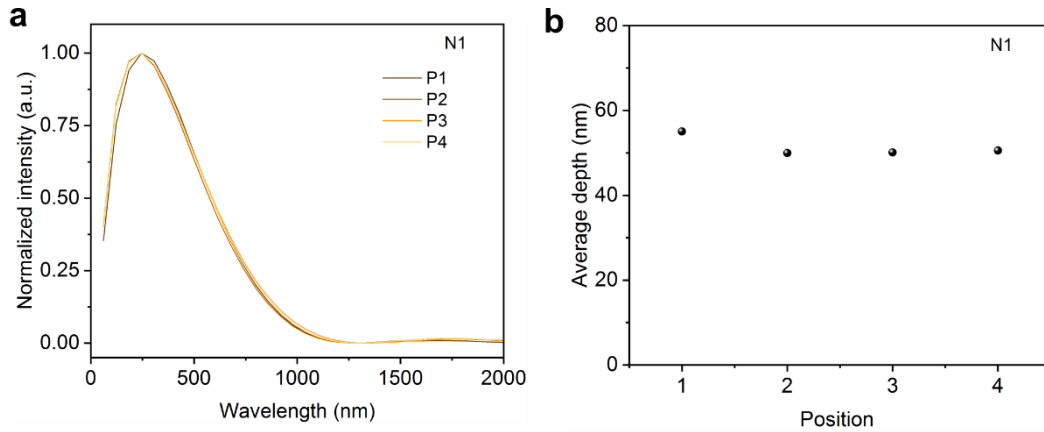


Figure 6.3. Uniformity investigation on sample N1 as a representative nanostructure generated by RIE treatment on PDMS. The structure is investigated with AFM at different local positions (P1 – P4) on sample N1. (a) Periodicity distribution. (b) Average depth. AFM measurements done with a resolution of 1024×1024.

The statistical parameters, including the FWHM and the dominant depth among the depth distribution of all investigated nanostructures at different positions, are summarized in Table 6.1 and Table 6.2. According to the statistical analysis, the deviation of the proposed aspect ratio (AR, $AR = \text{depth} / \text{periodicity}$) for the nanostructures at different position is very tiny, indicating that the nanostructures is uniform at different positions among the entire surface.

Table 6.1. The deviation of AR for each AFM measurement. The dominant periodicity are obtained from AFM measurements with a resolution of 1024×1024. The proposed AR is calculated as FWHM / dominant periodicity.

Sample	FWHM of depth distribution (nm)						Dominant periodicity (nm)	Mean of AR	Standard deviation
	256×256		1024×1024						
N1	73.6	73.7	90.3	81	77.8	84.1	245.5	0.326	0.026
N2	90.9	91.6	-	99.9	96.1	95.6	449.9	0.211	0.008
N3	83.7	89	-	92	82.9	-	245.5	0.354	0.018
N4	128.1	141.5	-	159.9	132	-	337.5	0.416	0.042
N5	149	149	-	155.8	150.8	-	1043	0.145	0.003

Table 6.2. The deviation of AR for each AFM measurement. The dominant periodicity is obtained from AFM measurements with a resolution of 1024×1024. The proposed AR is calculated as dominant depth / dominant periodicity.

Sample	Dominant depth of depth distribution (nm)						Dominant periodicity (nm)	Mean of AR	Standard deviation
	256×256		1024×1024						
N1	123.4	110	142.9	137.8	126.2	136.1	245.5	0.527	0.049
N2	148.4	155.5	-	161.7	134	158.3	449.9	0.337	0.024
N3	141	122.8	-	149.8	140.3	-	245.5	0.564	0.046
N4	184.9	209.4	-	263.4	216.5	-	337.5	0.648	0.097
N5	213.5	157.5	-	202	175	-	1043	0.179	0.024

6.1.3 Nanostructure reproducibility

As presented in Figure 6.1, the nanostructure is randomly orientated on the surface of PDMS after RIE treatment, but statistically, there is a distribution of the periodicity and depth for each nanostructure. The nanostructure is a system bridging chaos and order as a quasi-periodic pattern. According to AFM measurements, one can obtain the statistical properties including the periodicity, depth distribution and average depth. The experimental repeatability is monitored by measuring the quantitative parameters of periodicity and depth for the nanostructure generated in different batches with the same recipe.

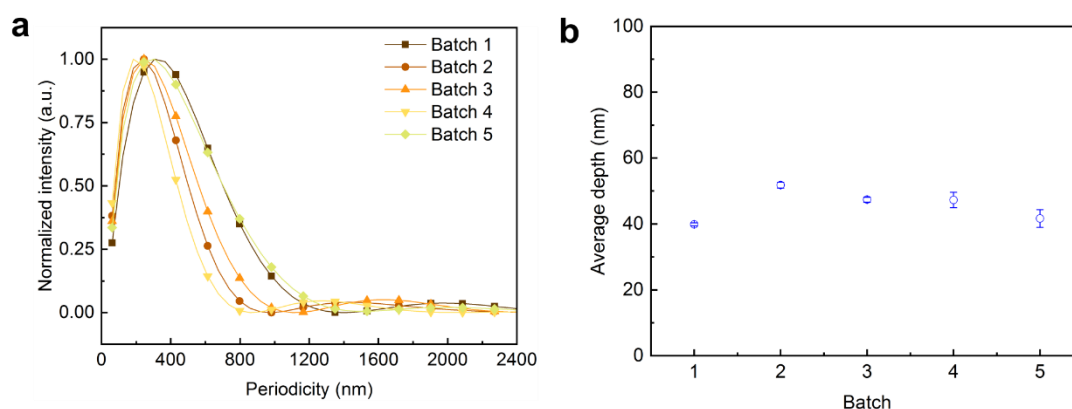


Figure 6.4. Experimental deviation from multiple runs for the nanostructures prepared with the same recipe. (a) Periodicity distribution. (b) The average depth. The error bar is the standard deviation from three AFM measurements at different positions for each sample. The PDMS preparation recipe: PDMS from Sigma-Aldrich, 1000 rpm, 80°C, 80 min. The RIE recipe: 50 sccm O₂, 50 W, 60 s.

As shown in Figure 6.4, for nanostructures generated in multiple runs, the periodicity is peaking ~ 350 nm. Only very small deviation of the average depth can be noted, as shown in Figure 6.4b. Therefore, the generation of nanostructures by RIE treatment on PDMS surface is controllable with good repeatability.

6.1.4 Nanostructure control

It is possible to maintain the shape of the periodicity distribution without significant shift of the dominant periodicity while tuning the average depth D by changing the RIE treatment power and duration time. As depicted in Figure 6.5a, the dominant periodicity is ~ 350 nm. There is only a slightly difference in the large periodicity range, when the RIE power is increased from 20 to 200 W, while the PDMS preparation condition is the same and RIE treatment time is constant at 60 s. However, the average depth increases from 20 to 120 nm in a linear form (Figure 6.5b).

A similar behavior is noted between the RIE duration time and the average depth. As shown in Figure 6.6, the prolongation of RIE treatment time from 60 to 210 s varies the dominant periodicity slightly, while the average depth increases linearly from 20 to 50 nm. These results indicate that the RIE treatment energy by either increasing the power or the time of the RIE treatment influences the depth of the nanostructure without significantly changing the periodicity distribution.

It is worth noting that a slight variation of the heating time of the PDMS layer can significantly affect the periodicity distribution, as shown in Figure 6.5c. The shorter the pretreatment time, the larger the dominant periodicity. Under the same RIE recipe, the dominant periodicity shifts from 610 nm for PDMS cured for 40 min, to 490 nm for samples pretreated for 60 min and further decreases to 180 nm for samples heated for 80 min or longer. In addition, samples thermally pretreated for 40 and 60 min give a wider periodicity distribution than these with thermal pretreatment for 120 min or 160 min. The main difference is in the range of large periodicities. However, the average depth corresponds to 200 nm for PDMS cured for 40 min, which is about 6 times larger than the PDMS cured for 160 min (35 nm), as depicted in Figure 6.5d. These results demonstrate the possibility to manipulate the periodicity distribution and average depth simultaneously by optimizing the pretreatment time of the PDMS layer.

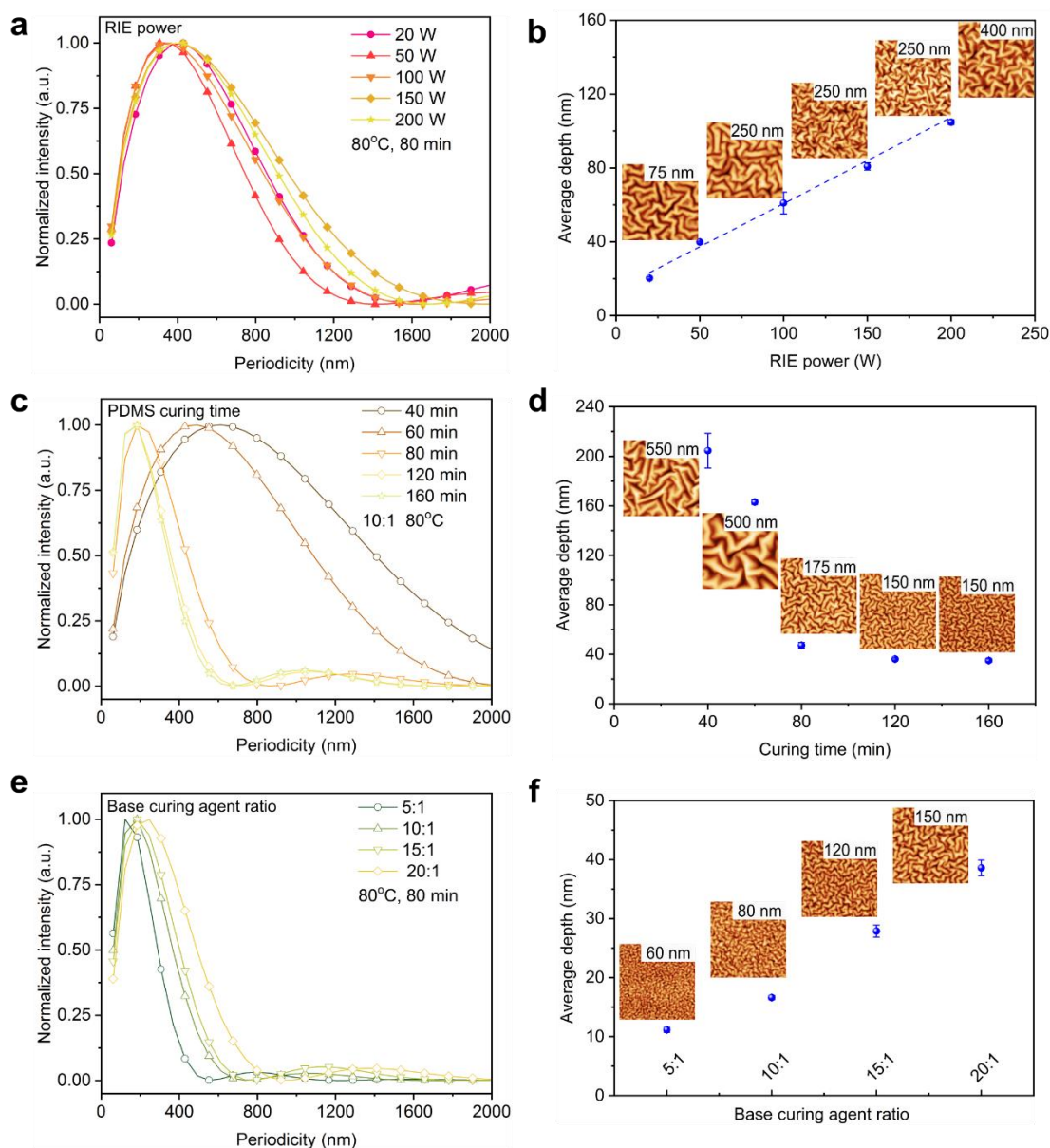


Figure 6.5. The control of RIE-induced nanostructures. The influence of the RIE power (a, b), the PDMS pretreatment time (c, d) and the weight ratio of the base and curing agent (e, f) on the periodicity distribution (a, c, e) and the average depth (b, d, f). The inset AFM figures are shown with a size of $5 \mu\text{m} \times 5 \mu\text{m}$, with different color scale from 0 nm to the maximum height marked for each figure. Error bar: the standard deviation from at least 3 AFM measurements on different sites.

Further investigations indicate that the weight ratio of the base to the curing agent of PDMS can also tune the periodicity distribution and the average depth. As depicted in Figure 6.5e, the dominant periodicity increases from 120 to 250 nm when the weight ratio of the base to the curing agent raises from 5:1 to 20:1. Meanwhile, the average depth raises when the ratio is increasing, as shown in Figure 6.5f. The average depth is 40 nm for the sample with a ratio of 20:1, which is about 3 times larger compared to the PDMS with a ratio of 5:1 (12 nm).

As shown in Figure 6.6, when fixing the RIE treatment power and time, the variation of gas species can affect the periodicity distribution and the average depth substantially. In general, samples treated with mere argon give larger nanostructures compared to samples treated with O₂ only. The Ar flow with a rate of 10 sccm leads to nanostructures with a dominant periodicity of 730 nm and an average depth of 140 nm, while a 10 sccm O₂ flow can only induce a pattern with a dominant periodicity of 300 nm and an average depth of 90 nm. Varying the ratio of O₂ and Ar can slightly tune the periodicity distribution and average depth. The increase of the oxygen flow in the mixed gas can slightly decrease the average depth of the nanostructure.

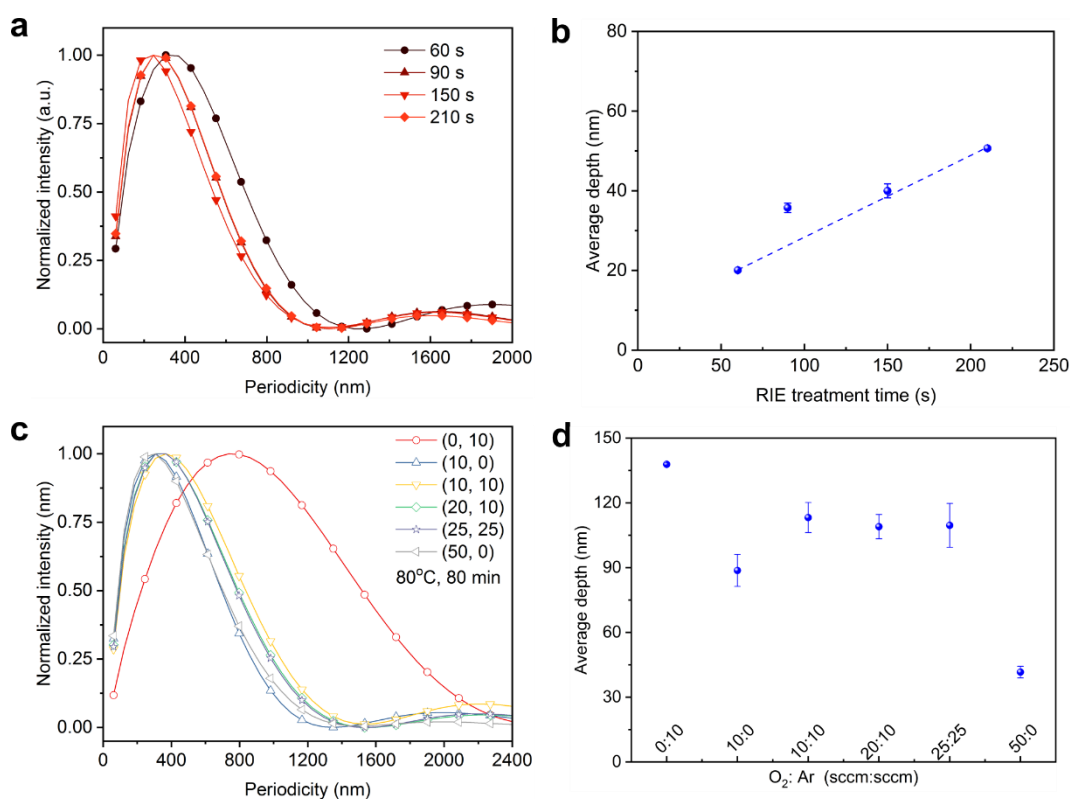


Figure 6.6. The control of the periodicity distribution and average depth. The influence of the RIE treatment duration time (a and b) and the influence of the gas flow during RIE treatment (c and d), on the periodicity distribution a, c and average depth b, d. For a and b, the PDMS is consisted of a weight ratio of the base to curing agent of PDMS at 10:1 and cured at 80 °C for 80 min. RIE recipe: 20 W, 50 sccm O₂ for varied duration time. For c and d, PDMS is pretreated at 80 °C for 80 min, with a weight ratio of the base to curing agent at 10:1. RIE recipe: 50 W, 60 s, with various gas flow rates.

In summary, the various options to control the deformation of PDMS by RIE conditions significantly increase the design freedom of photonic nanostructures for OLED light outcoupling compared to the lithography, molding or nanoimprinting techniques. Only this control makes it possible to tailor-make such structures for a given OLED architecture, which is of key importance, as the latter can vary strongly depending on their application.[88]

From all these observations, it is possible to tune the average depth from ~10 to ~140 nm and the dominant periodicity from ~200 nm to ~800 nm, simultaneously or independently. This is realized by controlling the PDMS pretreatment time, the weight ratio between the base and curing agent of PDMS, the gas flow, the power and the duration time of the RIE treatment. According to these results, we anticipate that the characteristic nanostructure parameters can be extended beyond the explored limits with a broader variation of those parameters.

6.1.5 Mechanism of nanostructure control

As a next step, mechanism behind the nanostructure generation and controllability is investigated. To detect the chemical composition of the PDMS surface after the RIE treatment, an X-ray photoelectron spectroscopy (XPS) measurement is conducted and the result is shown in Figure 6.7a. For the as-prepared PDMS before the RIE treatment, the Si 2p binding energy is 102.5 eV, which is in agreement with the previously reported value for PDMS.[223] After the RIE treatment, the Si 2p peak shifts to 103.1 eV. Here, the XPS spectra can be fitted with three different components, representing possible chemical structures (Si-O binding) of the surface layer. According to previous reports, the peak at ~102.2 eV represents the chemical configuration of $[(CH_3)_2SiO_{2/2}]$, ~103.2 eV $[(CH_3)SiO_{3/2}]$ and ~104.0 eV $[SiO_{4/2}]$. [223–225] For the as-prepared PDMS, the majority component is $[(CH_3)_2SiO_{2/2}]$, which is consistent with chemical configuration of PDMS. After the RIE treatment, the ratio of $[(CH_3)_2SiO_{2/2}]$ decreases, while the proportion of $[(CH_3)SiO_{3/2}]$ and $[SiO_{4/2}]$ increases.

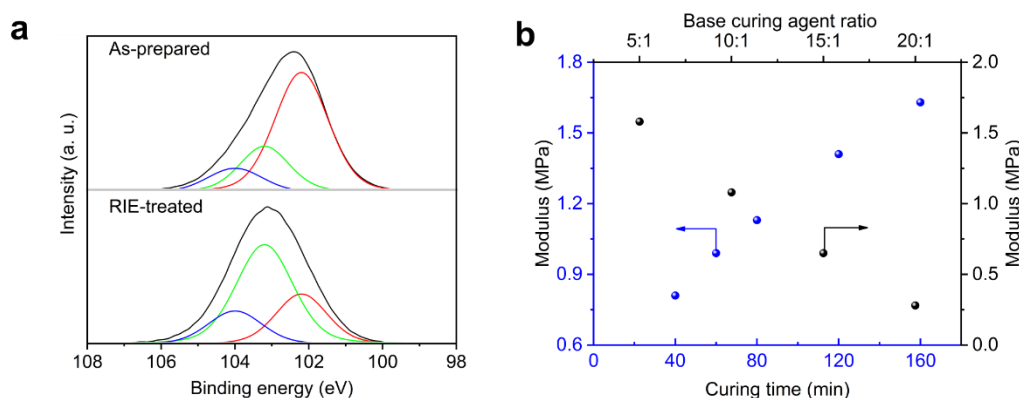


Figure 6.7. Mechanism investigation on the generation and control of RIE-induced nanostructures. (a) The binding energy of the Si 2p peak and fitted components. (b) The storage modulus of PDMS after the thermal pretreatment. The pretreatment condition for PDMS with different weight ratio of the base to the curing agent: 80 °C, 80 min. The thermal pretreatment condition for PDMS with a 10:1 weight ratio: 80 °C and varied time.

The atomic concentration (at%) of the as-prepared and RIE-treated PDMS is summarized in Table 6.3. The as-prepared PDMS at the surface is composed of 27.8 at% oxygen and 46.2 at% carbon. However, the concentration of oxygen increases to more than 40 at% and the concentration of carbon decreases to less than 30 at% after the RIE treatment. The atomic concentration of silicon is almost the same after the RIE treatment. From these observations, it is reasonable to deduce that the surface of PDMS is turned to a silica-like layer.

Table 6.3. The atomic concentration for the as-prepared and RIE treated PDMS.

	C	O	Si	O : Si ratio
As-prepared	46.2%	27.8%	26.0%	1.07
RIE treated	28.0%	46.4%	25.6%	1.81

Identical XPS spectra are obtained for samples being treated with different RIE recipes, including various values of treatment power or gas flow rate, as summarized in Table 6.4. The composition of the surface layer is independent from the treatment power when only oxygen is used as treatment gas. Moreover, different gas flow rates result in identical XPS spectra, indicating the composition of the top silica-layer does not change with different gas flows. This should be attributed to the fact that the silica-like layer on the PDMS generated by the RIE treatment hinders further treatment of the deeper layer of PDMS[225], and thus, gives the composition of the top layer of RIE-treated PDMS identical in the first several or dozens of nanometers. However, the real thickness of this silica-like top layer cannot directly be measured, because of the wavy geometry and the strong adhesion to the soft PDMS base without a clear boundary.

To investigate the change of the modulus of the as-prepared PDMS with different heating time and weight ratio, the DMA measurement is done. Here, the storage modulus is regarded as Young's modulus in the stressing measurement mode.[226] As depicted in Figure 6.7b, the extension of pretreatment time can increase the modulus, whenever the weight ratio of base to the curing agent is the same. It is 0.8 MPa for PDMS cured for 40 min and further increases to 1.6 MPa when extending the curing time to 160 min, while keeping the weight ratio at 10:1. The modulus also raises when the weight of curing agent in the mixture is increased. It changes from about 0.3 MPa to 1.6 MPa, when the weight ratio of the base to the curing agent varies from 20:1 to 5:1. This result can be ascribed to the fact that extending the curing time or increasing the weight ratio of curing agent of PDMS leads to a higher cross-link level, which gives rise to a higher modulus.

Since the chemical composition of the silica-like layer is between the intrinsic PDMS and silica, it is reasonable to deduce that the Young's modulus of this layer ranges from MPa to GPa (modulus of intrinsic silica), which should be higher compared to the as-prepared PDMS and lower than that for pure silica. However, the exact value of the Young's modulus of the top silica-like layer can not be measured directly due to the influence of the bottom soft PDMS.[227] Nevertheless, the silica-like layer generated on the surface can be regarded as a stiff layer in this bilayer system.

Table 6.4. The RIE treated PDMS with identical XPS spectra.

Pretreatment condition	O ₂ (sccm)	Ar (sccm)	Power (W)	RIE duration time (s)
80 °C, 80 min	10	0	50	60
80 °C, 80 min	10	10	50	60
80 °C, 80 min	20	10	50	60
80 °C, 80 min	50	10	150	60

Based on these results, the generation and controllability of RIE-induced nanostructures can be explained by the theory of thin-film deformation in a planar bilayer system. Layered thin materials generate mechanical deformations such as creases, wrinkles and undulations on the surface in response to small compressive stress release between the top stiff layer and the bottom soft base, induced by thermal, light, mechanical or osmotic stimuli.[196,201,221,228,229] Deformations arrange randomly in directions and amplitude, accompanied with in-plane stress release on the entire surface. Therefore, the generated pattern depends on the distribution of the stress field, mechanical properties of the top stiff film and the elastic soft base, as well as the geometry of substrates.[196] Moreover, the further increase of the compressive stress leads to new morphological phases such as folds or even cracks.[199,230]

Oxygen or argon flow can turn to be reactive species such as radicals, ions and electrons by the interaction between the glow discharge and undissociated gases during RIE treatment.[231] These highly reactive species can modify the PDMS surface by chemical reactions and physical bombardments. The components of PDMS can be oxidized to volatile gases, which are removed by the vacuum pumping system during RIE treatment, transforming the surface into a form of silica-like composition. Deformation starts to minimize the total energy of the bilayer system, when the compressive stress σ exceeds the critical level σ_c , induced by the stimuli of RIE treatment and the modulus mismatch between the top stiff silica-like layer and the bottom soft PDMS. The dominant periodicity p can be influenced by the thickness of

the top silica-like layer t_s , the modulus of the silica-like layer E_s and the modulus of the PDMS E_{PDMS} . According to Equation (3.53), the dominant periodicity p drops to a shorter range, when the modulus of PDMS (E_{PDMS}) is increased by extending the pretreatment time or increasing the weight ratio of the curing agent, which is confirmed by the DMA (see Figure 6.7b). In cases of the RIE treatment with only oxygen gas, increasing the RIE power or time has little impact on E_{PDMS} , E_s or t_s , as revealed by XPS and DMA measurement. The dominant periodicity p of the RIE-induced nanostructures can be maintained without pronounced shift. However, the depth of these nanostructures can be tuned by increasing the compressive stress through channels of physical bombardment and heat leakage from chemical oxidization, according to Equation (3.61). Similar linear relationships between the roughness of polymer surface and the plasma treatment power or time have been reported during plasma treatment of other polymer systems.[232,233] For RIE treatments with argon flow, it could be that the thickness of the top stiff layer t_s and the compressive stress σ are changed at the same time, leading to a variation of the periodicity distribution and depth simultaneously.

6.2 Optical modeling of planar white OLEDs

The application of quasi-periodic nanostructures in white OLEDs is investigated using optical modelling. First, planar white tandem devices are numerically evaluated using an in-house developed simulation tool, which is based on the classical electromagnetic theory and considering the Purcell factor, the transition dipole moment orientation of the emitter molecules as well as the absorption and non-radiative losses over the entire emission spectrum.[61] The model previously showed a good agreement with experimental results for planar monochromatic OLEDs,[178,234] as well as for tandem white devices.[235] This model enables a detailed analysis of the light distribution over different loss channels and is used as a starting point for further simulations of nanostructured devices.

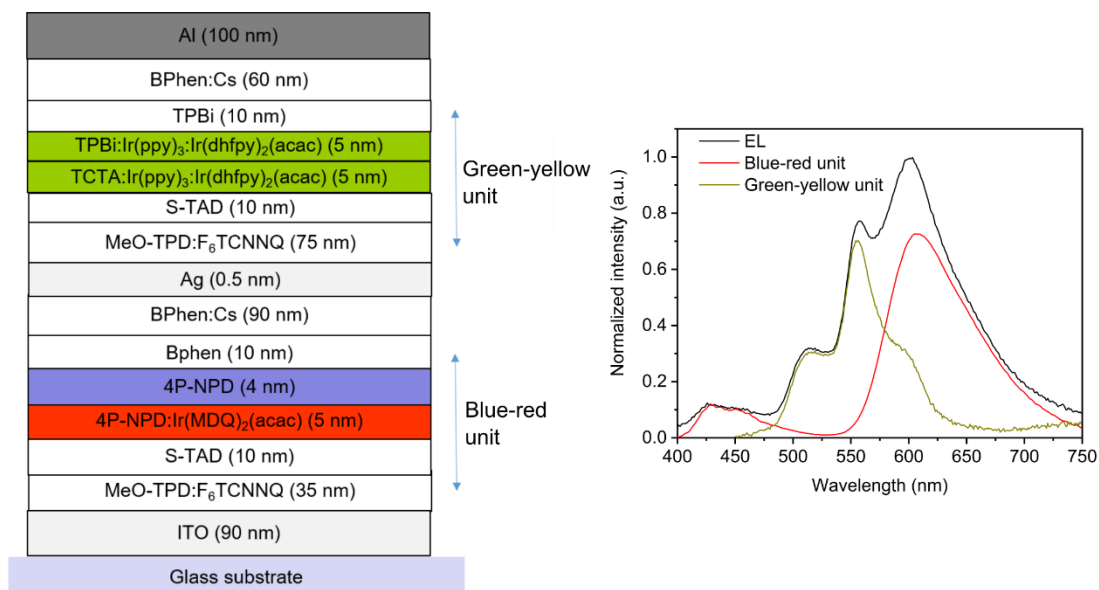


Figure 6.8. The EL spectrum fitting for the planar white tandem OLED. The spectrum is split into two parts according to the device structure: blue-red unit and green-yellow unit.

To numerically simulate the loss channels, the planar tandem device is divided into two units, and each unit is simulated separately, while still having the other unit as passive layers present. The quantum efficiency for air modes, substrate modes, waveguide modes and evanescent modes are summed up respectively, to get the fraction of photons in each mode for the tandem device, of which the ideal EQE would be 200%. As input data, layer thicknesses with corresponding complex refractive indices are used. Other data, like the anisotropy factor, the radiative efficiency and the electrical efficiency are taken from the literature.[61,235] We here calculate the loss channels for each of the units separately,[235] where the electroluminescent spectrum $S_{el}(\lambda)$ for each unit is fitted from the emission spectrum obtained in the integrating sphere measurement, as shown in Figure 6.8. To calculate the energy losses for each unit, the other unit is treated as functional organic layers without emission. The effective radiative quantum yield η_{rad} , the anisotropy factor a , the electrical efficiency γ for each emitter are obtained from literatures, as summarized in Table 6.5.

Table 6.5. The summary of parameters for optical analysis of planar white OLEDs.

	Emitter	η_{rad}	a	γ
Blue-red unit	4P-NPD	0.92[133]	0.33	0.73[168]
	Ir(MDQ) ₂ (acac)[185]	0.7	0.24	1
Green-yellow unit	Ir(ppy) ₃ [61]	0.76	0.31[184]	0.9
	Ir(dhfp) ₂ (acac)[236]	0.7	0.25[184]	1

As shown in the Table 6.6, the majority of non-radiative losses is coming from a medium effective radiative efficiency and the electrical efficiency, giving the IQE for the planar tandem white OLED about 125%, which is very close to the previously reported tandem white OLEDs based on 4P-NPD system.[133,168]

Table 6.6. The fraction of power for each unit of the planar white OLED.

	χ_{air} (%)	χ_{sub} (%)	χ_{wav} (%)	χ_{SPP} (%)	absorption (%)	non-radiative loss (%)
Blue-red unit	9.8	7.0	27.4	11.9	11.2	32.7
Green-yellow unit	10.2	12.0	10.0	15.6	8.8	43.4

6.3 Optical modeling of structured white OLEDs

The quasi-periodic nanostructures can be simplified to a sum of sinusoidal functions with different periodicities and heights and their effect on optical properties in OLEDs is evaluated using the finite element method (FEM).[237] Optical simulations of corrugated devices are performed using a commercially available simulation tool, Comsol Multiphysics. Dipoles and nanostructures are treated with the 2D model to reduce the computing load. The simulated device architecture is very similar to experimental devices with the same total thickness, in which thin layers sandwiching emission dipoles are treated as a single emission layer, to avoid the need for very small mesh elements in very thin layers ($d \leq 10$ nm). The optical indices (n, k) for each layer are set according to the experimental measured results. A sine structure with various periodicities and heights is used to simulate light outcoupling to the glass substrate, where the glass substrate is treated as a half-infinite medium. Organic emitting molecules are much smaller than emitting wavelength, thus emission sources in simulations can be treated as differently oriented point dipoles positioned at the corresponding emission interface. The simulated area in the model is set to a lateral size of 20 μm around the dipole, and the entire structure is surrounded by a perfectly matching layer (PML) as the absorbing boundary condition, to suppress any reflections at the boundaries. Collection of the emitted light is at least one wavelength away from the thin film structure (flat and textured) to avoid coupling of evanescent waves to the PML. The simulation is done in 10 nm wavelength steps from 400 to 800 nm, for sine textures with periodicities ranging from 300 nm to 2000 nm and different heights. For comparison, a flat structure is simulated, and internal efficiencies are set to match experimental results. Parameters in simulations are held constant during all simulations for nanostructured devices, with only varied values of p and h of the sinusoidal texture.

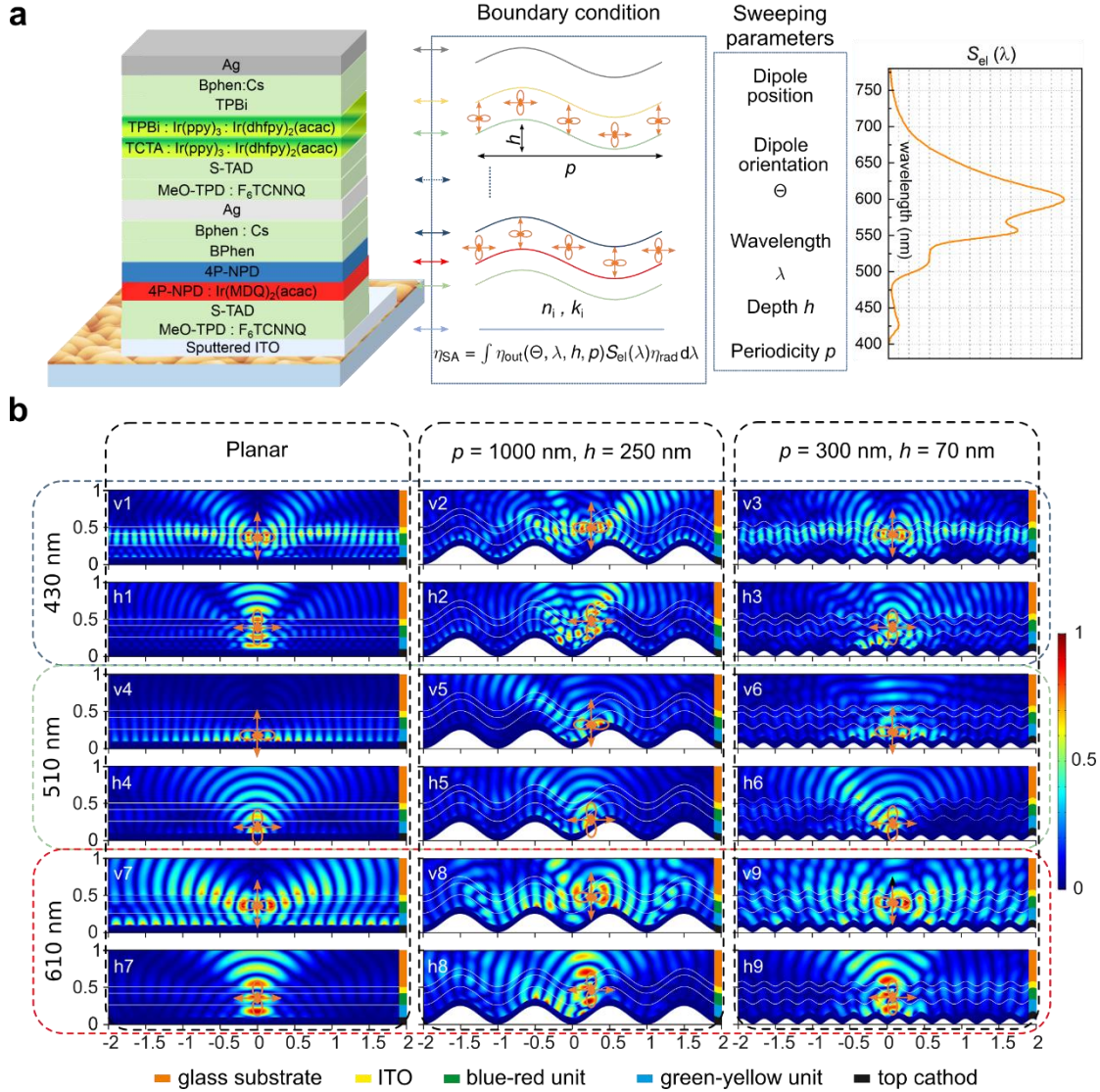


Figure 6.9. Schematic diagrams of the proposed optical modeling and power dissipation for emitting dipoles on nanostructures. (a) The device architecture and schematic illustration of the simulation model. The outcoupling efficiency η_{out} is dependent on the dipole orientation Θ and the position on the sinusoidal interface, emitting wavelength λ , periodicity p and depth h of the sinusoidal nanostructures. (b) Normalized steady state electric field for vertical and horizontal dipoles. At wavelengths 430 nm for vertical dipoles (v1 - v3) and horizontal dipoles (h1 - h3), 510 nm for vertical dipoles (v4 - v6) and horizontal dipoles (h4 - h6), 610 nm for vertical dipoles (v7 - v9) and horizontal dipoles (h7 - h9). Three different configurations are presented – flat (first column), nanostructured devices with $p = 1000$ nm, $h = 250$ nm (second column) and $p = 300$ nm, $h = 70$ nm (third column). Dipoles are located in the middle - between minima and maxima of the sine texture inside corresponding emission layers. All dimensions are in μm .

As shown in Figure 6.9a, using 2D simulations, each single sine nanotexture with periodicity p and height h at the specific wavelength is modeled separately. The emission interface follows the shape of the sine texture, thus five different dipole positions on a single period, e.g. dipole in valley, on and between hills are simulated. The device configuration is following the one used in experiments. Optical modeling is done in the wavelength range from 400 to 800 nm with a step width of 10 nm. When focusing on extracting waveguide and SPP modes only, the outcoupling efficiency η_{out}

to the substrate is simulated. The simulated η_{SA} can be obtained by weighting the outcoupling efficiency with the normalized electroluminescent spectrum $S_{el}(\lambda)$ and multiplying with the effective radiative efficiency η_{rad} of the planar white device, corresponding to experimental measurements of η_{SA} . The final η_{SA} is calculated as an averaged result over five different dipole positions within one periodicity of sine texture for both horizontal and vertical dipoles [217,238] (Figure 6.9a). In principle, the final outcoupling performance of each random nanostructure is the sum of different periodicities and heights, corresponding to the periodicity and depth distribution for each of the nanostructure detected by the AFM measurements. As a first estimation, a sinusoidal texture with the dominant periodicity and dominant depth given by measured distributions can be representative for the final device performance based on quasi-periodic nanostructures.

To illustrate the light distribution inside the device, the color maps of the normalized electric field for the planar device is depicted in Figure 6.9b. It shows that most photons emitted from the vertical dipoles are trapped in organic layers and at the surface of the metal cathodes. On the other hand, energy trapping for horizontal dipoles is less pronounced. Hence, the enhancement caused by the nanostructure is expected to be more significant for vertical dipoles compared to the horizontal ones. Moreover, the light distribution depends strongly on the position of the emitting dipoles in the stack, as we can see that the main losses for the blue/red are due to waveguiding, since the emitting layers are close to the ITO and far from the top metal cathode. However, for the green/yellow emitting dipoles, which are much closer to the metal cathode, the main losses arise from the coupling of light to SPP modes.

Figure 6.9b shows the normalized electric field of horizontal and vertical dipoles at three representative wavelengths (emission peaks), on two nanostructures with periodicity of 1000 nm and height of 250 nm, and with periodicity of 300 nm and height of 70 nm, respectively. It should be noted that the dipole position on the nanostructure strongly influences on the outcoupling efficiency η_{out} . For example, the vertical dipole located at the bottom of the sine texture with a wavelength of 510 nm exhibits a value η_{out} of 37.5% while at the middle of the sine texture it can reach up to 52.8%. Similarly, for the horizontal dipole, it reaches 55.5% and 71.7% at the bottom and middle of the sine texture, respectively. As there can be more than 15% absolute difference in η_{out} between different dipole positions on the nanostructure, five different positions (a higher number of dipoles makes only small difference) are taken into account, allowing to simulate an uniform distribution of emitting molecules on the textured surface.

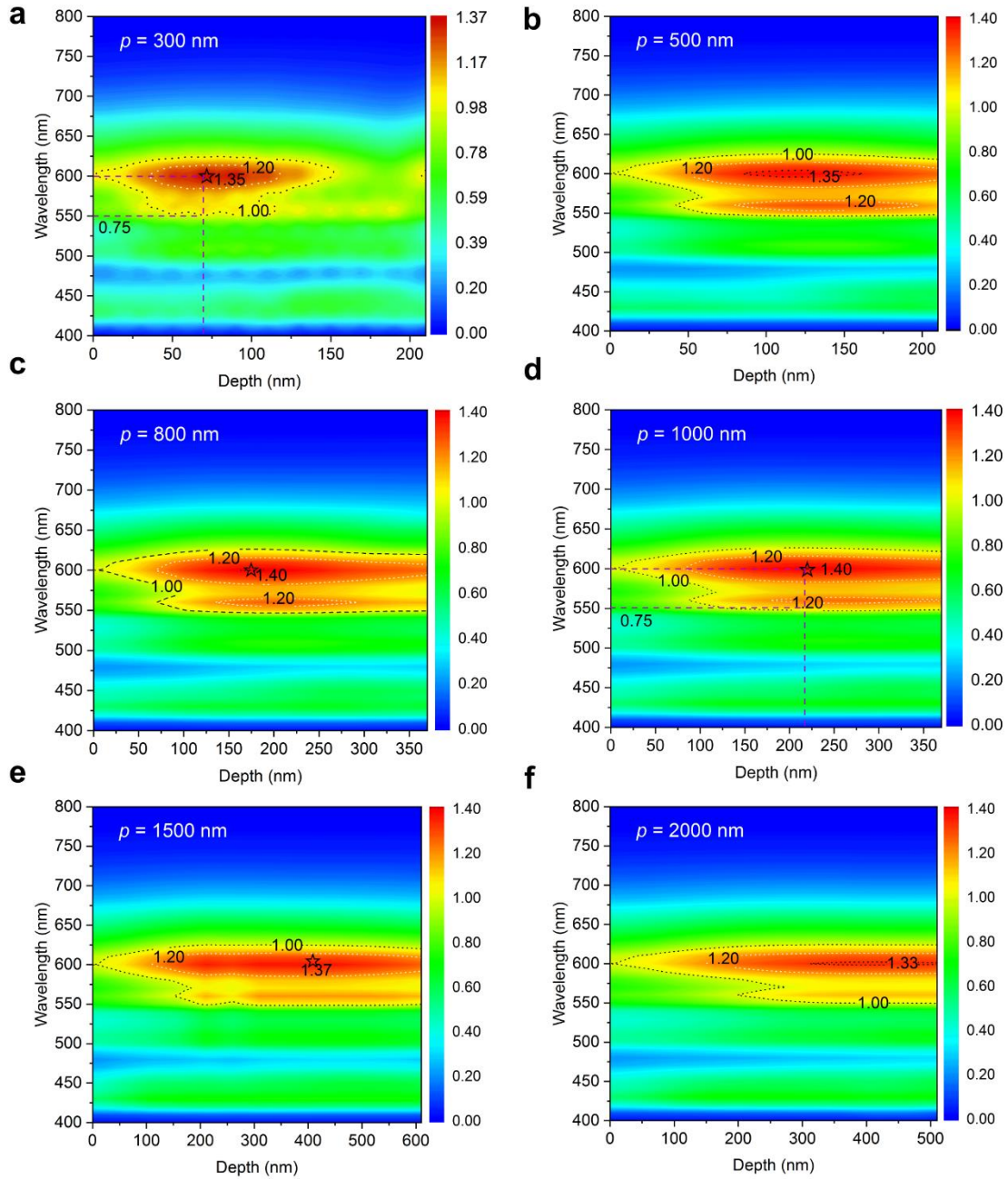


Figure 6.10. Numerical simulation of the enhancement for white OLEDs. The depth of 0 nm indicates flat devices. The spectra for flat devices are normalized as [0, 1]. The simulated intensity for devices on nanostructures at different wavelength is then normalized to the maximum intensity of the flat device. (a) White OLEDs on nanostructures with periodicity $p = 300$ nm. (b) $p = 500$ nm. (c) $p = 500$ nm. (d) $p = 500$ nm. (e) $p = 500$ nm and (f) $p = 500$ nm with different depth are presented.

Numerically, the enhancement of η_{SA} is dependent on the dipole orientation, the size of the nanostructure, the position of dipoles on the nanostructure and the radiated frequency and emitting spectrum. The enhancement factors are shown in Figure 6.10, in which the intensity is normalized to the peak intensity of the flat device, for textures with different periodicities. For the white OLEDs based on nanostructures with periodicity $p = 300$ nm, the highest enhancement factor of ~ 1.35 can be obtained at a

wavelength 600 nm, with a texture depth of about 70 nm. At 550 nm, the intensity of the planar device is reduced by a factor of about 0.75, while the intensity of the device on a sinusoidal nanostructure can still reach up to 1.0. Thus, it is also possible to obtain similar enhancement factor ($1.0 / 0.75 = 1.33$) at 550 nm. When increasing the periodicity to 1000 nm, shown in Figure 6.10d, maximum enhancement factor of 1.40 at 600 nm can be realized with a sine texture depth of 220 nm. An even slightly higher enhancement factor can be achieved at 550 nm ($1.20 / 0.75 = 1.6$). The change of periodicity and depth at each wavelength can influence on the enhancement factor. This is consistent with the general idea that the device efficiency depends on the geometry of the nanostructure and the emitting wavelength. Moreover, a sinusoidal nanostructure with only one fixed periodicity can already induce a wavelength-dependent enhancement. This shows the advantage of using textures with a periodicity and depth distribution for white OLEDs, as these can contain a wider range of periods and heights and thus provide a more uniform enhancement over the entire emission wavelength.

In Figure 6.11, it is demonstrated that the simulated enhancement factor is highly dependent on the aspect ratio (AR, $AR = \text{depth} / \text{periodicity}$) of sinusoidal textures. Rigorous simulations show a distinct trend of improving device efficiency by increasing the AR up to ~ 0.25 , where a maximum improvement of ~ 1.45 is predicted. Increasing the AR further decreases the efficiency. Moreover, higher efficiencies are predicted by using periodicities in the range between 500 nm and 1000 nm, while for a sine texture with a periodicity smaller than 300 nm (dimensions near subwavelength range) or larger than 1500 nm (structures are becoming flat in the dipole vicinity), improvements are less pronounced.

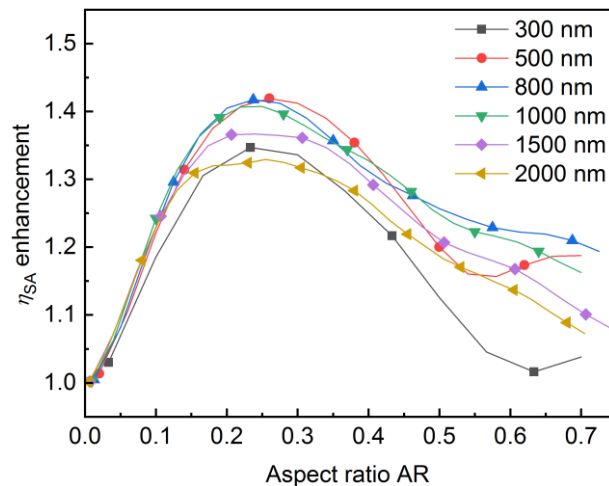


Figure 6.11. Numerical simulation results of η_{SA} enhancement factor dependent on the aspect ratio of sinusoidal nanostructures with different periodicities.

6.4 White OLEDs with nanostructures

RIE-induced nanostructures are applied for extracting trapped photons from bottom-emitting white OLEDs. The layer sequence of the highly optimized two-unit tandem white OLED based on a p-i-n structure is shown in Figure 6.8. It consists of a triplet harvesting blue-red unit and double emission architecture of a green-yellow unit connected by a thin charge generation layer. Although these devices can in principle directly be fabricated directly on the PDMS surface, here replicas are used for different measurements and device fabrication. The average transmittance of the sputtered ITO on the optical resin within the visible wavelength is about 76% (Figure 6.12a), which is slightly lower compared to the commercial one, but it is still sufficient to make efficient OLEDs. Here, five different nanostructures named N1-N5 with varied periodicity distribution and depth distribution is used (Figure 6.12c). Identical flat devices are fabricated on the same sputtered ITO for comparison.

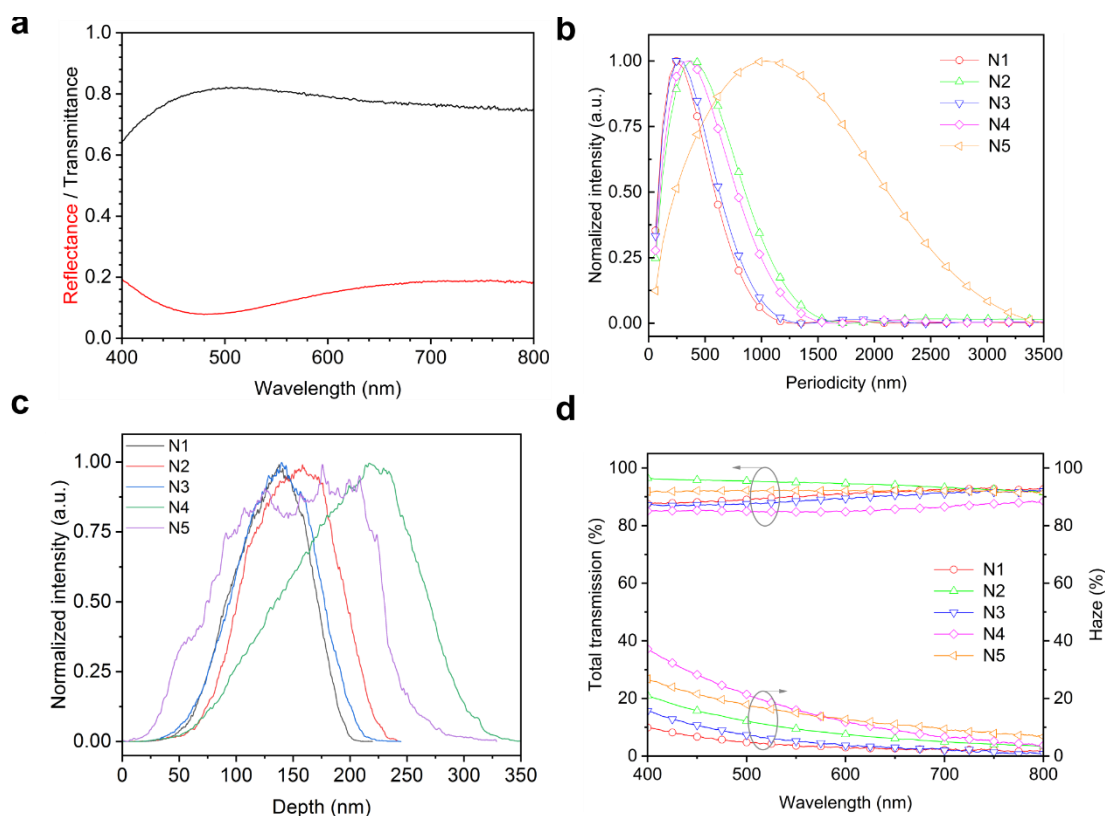


Figure 6.12. Basic properties of ITO anode and nanostructures used for white OLEDs. **a**, The transmission and reflectance of the sputtered ITO. Thickness: 90 nm. **b**, The periodicity distribution. **c**, The depth distribution. **d**, The total transmission and haze factor

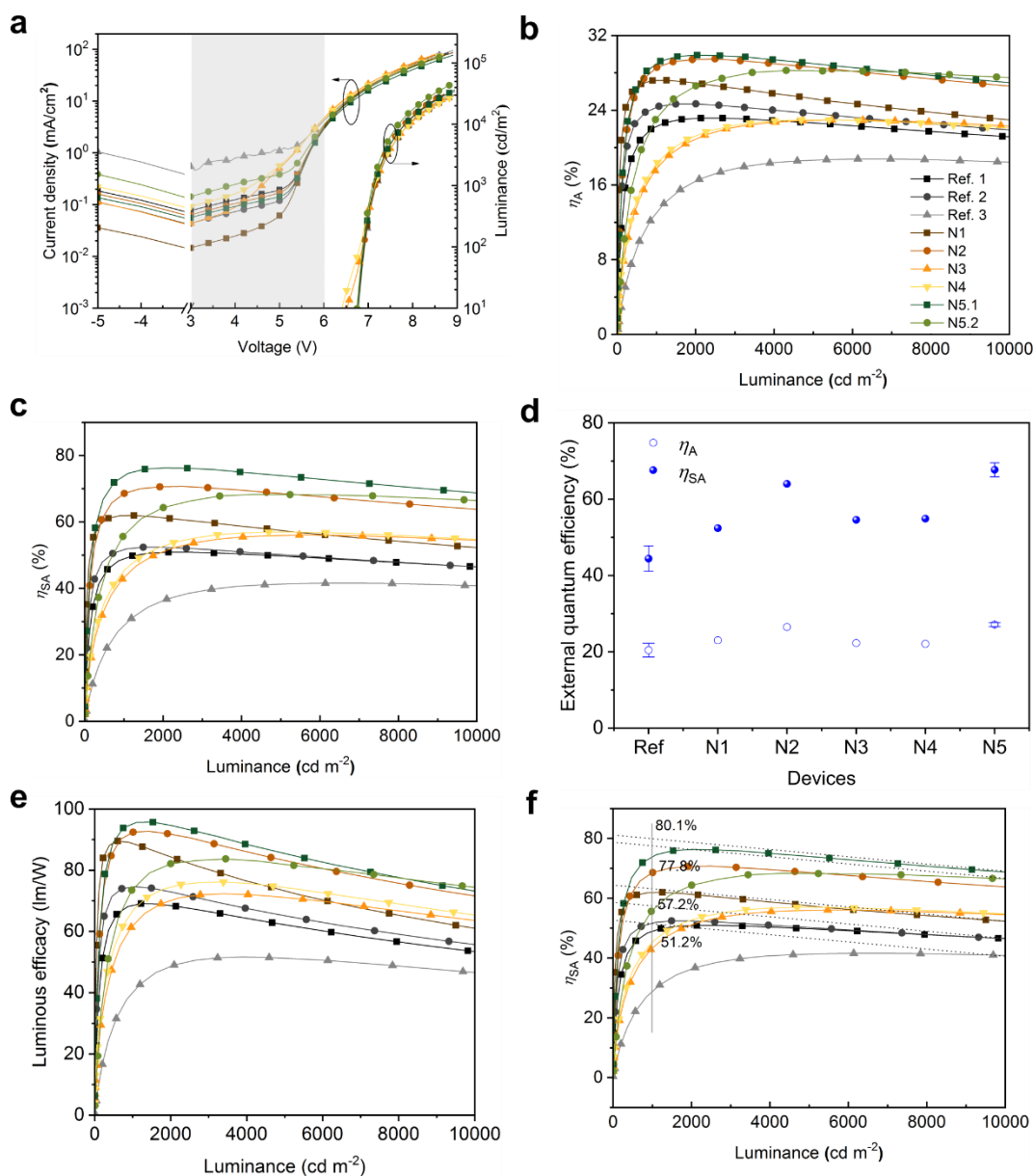


Figure 6.13. OLED performance based on RIE-induced nanostructures. (a) The current density – voltage – luminance characteristics of investigated devices. The gray area indicates the pronounced influence of leakage current during that voltage range. (b) Luminance - η_A characteristics for all devices. (c) Luminance - η_A characteristics for all devices. (d) The η_A and η_{SA} at the luminance of 10000 cd/m^2 . (e) Luminance - luminous efficacy with a hemisphere lens. (f) Recalculate the “real” maximum η_{SA} with consideration of different leakage current.

As shown in Figure 6.13a, under low driving voltage, the difference of voltage-current density curves mainly arises from the leakage current. The leakage current for all devices is in the range from 0.02 to 0.4 mA/cm^2 under reverse voltage of 4 V, resulting from the perturbation of the nanostructure beneath the ITO and the intrinsically higher roughness of ITO films without annealing process.[239] Compared to previously reported OLEDs with the same stack on the commercial ITO, the leakage current is about 1-2 orders of magnitude higher.[90] In present investigation, the

voltage-current density characteristics for all devices is identical for voltages larger than 6 V, since the influence from the leakage current is not significant in this range.

Previously reported nanostructured OLEDs show higher current density under the same driving voltage compared to the planar device, because of the partially reduced distance between the peak and valley of the nanostructured bottom and top electrode.[170,240] However, this is not observed in this investigations, which might result from the utilization of p- and n-doped transport layers as they possess much higher charge carrier mobility compared to the intrinsic transport materials.[78] The thickness reduction of the doped transport layers has little influence on the carrier transport and recombination processes.[76,78] Therefore, the efficiency enhancement at high luminance arises from the optical effect of the nanostructure and not from the thickness reduction of functional layers or change of the electrical efficiency.

To verify the influence of different nanostructures on the device performance, quantum efficiency η_A and η_{SA} are measured by a calibrated integrating sphere for all devices, presented in Figure 6.13b and Figure 6.13c. The planar device shows a maximum η_A of $22.2 \pm 3.1\%$. For devices with nanostructures, a maximum η_A of $29.1 \pm 1.1\%$ can be obtained. The shape of the EQE versus luminance characteristics is influenced by the leakage current for these samples, which mainly influences the maximum value of η_A , rendering a comparison at low to medium luminance levels improper. At a luminance of $10,000 \text{ cd/m}^2$, where the influence of leakage current is negligible, the η_A of the planar device slightly drops to $20.4 \pm 1.8\%$, while it remains $27.3 \pm 0.3\%$ for the textured device N5. For the other textured devices, the η_A can stay as high as 23% - 27% at $10,000 \text{ cd/m}^2$, as summarized in Figure 6.13d.

The maximum η_{SA} of $48.3 \pm 5.8\%$ can be obtained for the planar device and it rolls-off to $44.4 \pm 3.3\%$ at $10,000 \text{ cd/m}^2$. For textured samples based on nanostructures, a maximum η_{SA} of 76.3 % and luminous efficacy of 95.7 lm/W is achieved and it rolls-off to 69.0 % and 73.9 lm/W at $10,000 \text{ cd m}^{-2}$, as shown in Figure 6.13e. It demonstrates an enhancement factor of 1.53 ± 0.12 at $10,000 \text{ cd/m}^2$.

The extraction efficiency η_{EE} , which is defined according to Equation (3.39), can be calculated with the “real” maximum η_{SA} with consideration of different leakage current. As shown in Figure 6.13f, to get the “real” η_{SA} maxima without the influence of leakage current, we choose the device with the minimum leakage current as a reference and assume all these devices have the same roll-off. With the simulated energy loss fractions in Table 6.6, the extraction efficiency η_{EE} for devices based on N5 can be calculated. For example,

$$\eta_{EE,1} = \frac{\eta_{SA}^{w/} - \eta_{SA}^{w/o}}{\chi_{wav.} + \chi_{SPP}} = \frac{80.1\% - 51.2\%}{27.4\% + 11.9\% + 10.0\% + 15.6\%} = 44.5\% \quad (6.1)$$

Furthermore, with different references and devices performance based on N5 in this study, an extraction efficiency of 36.6% is demonstrated for a highly optimized white OLEDs based on N5.

It is interesting to note that the ratio of η_{SA} to η_A is higher for textured devices compared to planar devices, as summarized in Table 6.7. For example, the ratio of η_{SA} / η_A at 10,000 cd/m² for the planar device is 2.18 compared to 2.47 for device N5 with the nanostructure. This result indicates that the nanostructures couple more photons to the substrate which are then extracted by the attached hemisphere. The wavy profile of nanostructures can indeed guide the photons trapped as waveguide modes by reducing the incident angle to the substrate. However, because of the intrinsically flat geometry of these nanostructures (low AR), the incident angle is still high when transmitted to the interface of the glass substrate and air zone, leading to a situation where some of the extracted photons from waveguide modes or SPP modes are still in the substrate. Those photons can be rather easily extracted from the substrate with common external outcoupling structures. A similar phenomenon has been reported when using an ITO nanomesh for improved outcoupling from bottom green OLEDs.[180]

Table 6.7. The ratio of η_{SA} / η_A for devices with or without nanostructures.

	Planar ref.	N1	N2	N3	N4	N5
η_{SA} / η_A^*	2.18	2.29	2.41	2.45	2.48	2.47

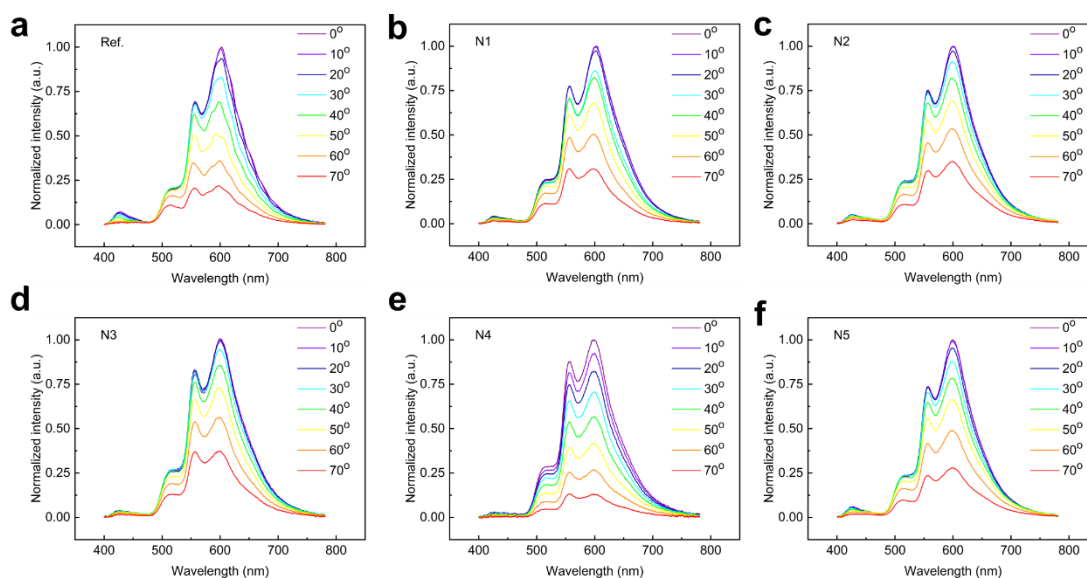


Figure 6.14. Angular dependent EL spectra for different devices. The change of EL spectra for samples with or without nanostructure from 0° (forward direction) to 70°.

As shown in Figure 6.14, there is no significant spectral change at different angles for devices with or without nanostructures. The shift of CIE coordinates for different angles is depicted in Figure 6.15a. A more pronounced CIE shift is noted for the planar device at different observation angles, while there is no significant CIE shift for the textured device, demonstrating that the incorporation of nanostructures into the white OLEDs improves the color stability.

Figure 6.15b shows the angular dependent radiant intensity for these devices with or without nanostructures. The emission profile is tuned from slightly less-Lambertian for the planar device to super-Lambertian emission for nanostructured devices. The angular and wavelength independent emission behavior demonstrates that the presence of quasi-periodic nanostructures can reduce the microcavity effect and increase the homogeneity of the energy distribution in the forward radiated hemisphere. RIE-induced nanostructures with a dominant periodicity reported in the present work, bring none of the drawbacks such as wavelength or angular dependent emission behavior compared to 1D or 2D grating structures, which is important for lighting applications.[171]

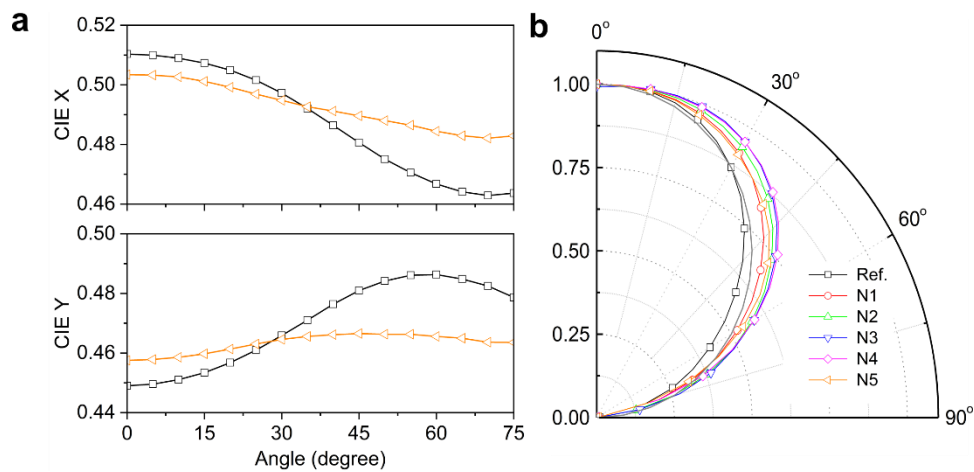


Figure 6.15. (a) The angular dependence of CIE. (b) The angular radiant intensity. The gray line is the Lambertian distribution.

6.5 Complexity of experimental aspect ratio

We have seen an increased η_{SA} for nanostructured white OLEDs compared to flat devices. For nanostructure N1 to N4, the periodicity distribution ranges from less than 100 nm to more than 1000 nm, while N5 has a broader periodicity distribution to more than 3000 nm, peaking at about 1000 nm, as shown in Figure 6.12. There are several possibilities to define the experimental AR for these nanostructures, which are

dependent on the different definition of the actual depth – none of them seem to resemble the complex corrugations perfectly. A detailed analysis is needed to compare three cases: $2R_a$, FWHM and dominant depth h among the depth distribution. For such complicated nanostructure system containing chaotic and ordered features, these possibilities allow to get a deeper understanding of the optical influence of these nanostructures.

As shown in Figure 6.12, the depth of these quasi-periodic nanostructures is widely distributed from 0 nm to more than 300 nm. The average roughness R_a , which has been widely used for describing the depth of nanostructures,[160] is mathematically defined as:[241]

$$R_a = \frac{1}{N} \sum_1^N (h_n - \bar{h}) \quad (6.2)$$

where N represents the total data points of AFM measurements, h_n is the height for a specific point n and \bar{h} is the average height for all positions.

For the nanostructure generation mechanism investigated in this work, it is more reasonable to treat the average depth as $2R_a$, since the generation of nanostructures is in response to the compressive stress release among the entire PDMS surface, as discussed in the main text, while the average roughness is taking all the position into account.

However, for outcoupling trapped photos in OLEDs, it is that the real geometry of the nanostructures makes the optical influence, not the mathematically averaged depth. Therefore, a definition of the depth close to the real geometry would be better for outcoupling purposes.

The area normalized density function of the depth distribution in the AFM measurement is defined as:[241]

$$\int_{-\infty}^{\infty} \rho(h) dh = 1 \quad (6.3)$$

where the $\rho(h)$ is the density function for all depth. The dominant depth of the density function $\rho(h)$ represents the depth with the highest density among all the depth measured. In this point of view, the dominant depth can represent the optical effects from the real nanostructures.

It should be noted that the experimental error can influence the absolute value of the dominant depth h among a specific depth distribution, resulting from the shift of the lowest depth (0 nm) in AFM measurements. Averaging dominant depth among different

high-resolution AFM measurements at a low noise level can statistically reduce the error.

For periodic 2D grating or pillar structures, the relative difference of the peaks of the depth density function $\rho(h)$ can represent the real depth for these structures.[151] For complicated nanostructures with a broad depth distribution in this work, there are hardly two peaks in the density function of depth distribution, shown in Figure 6.12. A compromised way is using the FWHM of the density function. However, there is a lack of clear physical meaning for the FWHM for these nanostructures.

It is noted that technically, when treating the dominant depth h as the depth to calculate the AR of the physical samples prepared in this study, a good match between experimental and simulation results of the enhancement factor can be obtained, even though the AR may vary in a broad range because of the broad depth distribution, as shown in Figure 6.16. In this case (depth = dominant depth h), an AR around 0.2 shows the best device performance. When the AR is 0.60 (N4), the enhancement factor is 1.24 ± 0.10 , growing towards an enhancement factor of 1.45 ± 0.12 obtained for a reduced AR of 0.41 (N2). The enhancement factor can be further increased to 1.53 ± 0.12 when AR drops to 0.19 (N5). These results indicate that the final enhancement is a synergistic effect from the periodicity and depth distribution of the nanostructures.

For the other two cases, as discussed previously, because of the weakness of physical meaning for the FWHM and the improper description for the outcoupling effect with $2R_a$, they both give larger deviation from the simulation results. However, for such a nanostructure system bridging chaos and order, the evaluation of the depth by the dominant depth h among the density function can also bring some system errors, e.g. the determination of the ‘zero’ depth cannot be given with absolute certainty.

The enhancement factor obtained from experimental results is slightly higher than in the numerical simulations, such differences can be assigned to the simplification of the simulation model to only two spatial dimensions without the consideration of the nanostructure directional arrangement because of a limited computing capacity, while texture and dipole are both 3D objects. Nonetheless, the similarity of simulation and experimental trends reveals the rationality of simplifying quasi-periodic nanostructures to sinusoidal textures to estimate their optical performances and understand such a complicated system by using the proposed optical model. We anticipate that it is also possible to use this model to understand the optical effect of nanostructures on the device efficiency of perovskite light-emitting diodes.[242]

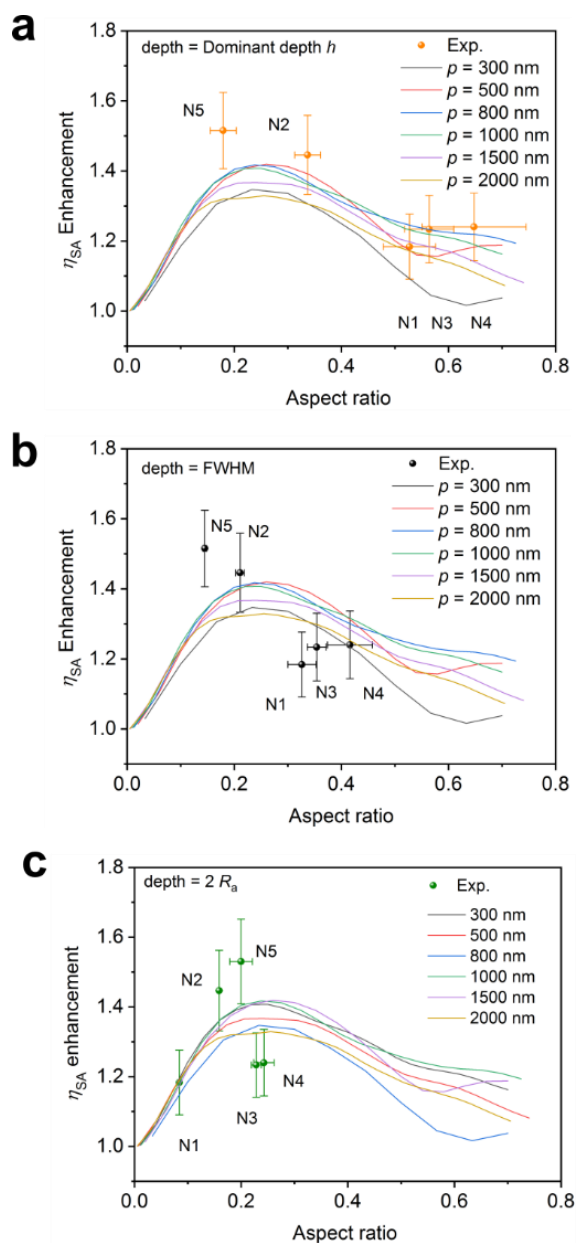


Figure 6.16. The different definition of depth (dots) for these nanostructures with simulated results (curves). (a) Depth = dominant depth; (b) Depth = FWHM; and (c) Depth = $2R_a$. The error bar is the standard deviation of at least 3 AFM measurements with high quality at different positions.

6.6 Comparison with literatures

To compare the EQE of white OLEDs and the enhancement factor from different studies about outcoupling with internal strategies, a literature summary is shown in Table 6.8. For both the absolute EQE and the enhancement factor, devices with the RIE-induced nanostructures in this thesis are among the top values compared to the reported results in the literatures, demonstrating the efficiency of these nanostructure to outcouple trapped photons from white OLEDs.

Table 6.8. Comparison of internal outcoupling structures for white OLEDs, based on EQE of white OLEDs without any outcoupling strategy (w/o), with only internal outcoupling strategy (w/in), with only external outcoupling strategy (w/ex) and with both internal and external outcoupling strategy (w/w) reported in literatures. The enhancement factor is calculated in three different cases I: EQE(w/w) / EQE (w/o), II: EQE (w/in) / EQE(w/o), III: EQE (w/w) / EQE (w/ex) in this summary, depending on the date availability.

Light extraction strategies		External quantum efficiency				Enhancement factor	Ref.
		(%)					
Internal	External	w/o	w/in	w/ex	w/w		
Low index grid ^{a,*}	Micro lens array	14.7	19	25	34	2.31 ^I , 1.29 ^{II} , 1.42 ^{III}	[243]
Deterministic aperiodic nanostructures (DANs) ^{a,*}	-	26	56	-	-	2.15 ^{II}	[244]
Vacuum nanohole array (VaNHA) ^{b,*}	Half-sphere lens	19.3	43.9	36.9	75.9	3.93 ^I , 2.27 ^{II} , 2.06 ^{III}	[167]
High index substrate ^{a,*}	Index-matched half-sphere lens	13.1	14.4	24	34	2.60 ^I , 1.10 ^{II} , 1.42 ^{III}	[152]
Nano-particle based scattering layers (NPSLs) ^{b,†}	Half-sphere lens	22	33	-	46	2.09 ^I , 1.5 ^{II}	[245]
Subelectrode micro lens array (SEMLA) ^{a,*}	Micro lens array	16	20		27	1.69 ^I , 1.25 ^{II}	[176]
Multifunctional Nanofunnel Arrays (NFAs) ^{b,*}	NFAs	12.7	20	19.6	29.4	2.31 ^I , 1.57 ^{II}	[246]
Metal oxide nanostructures ^{c,†}	Half-sphere lens	14.3	20.3	26.6	35.5	2.48 ^I , 1.42 ^{II} , 1.33 ^{III}	[247]
RIE-induced nanostructures ^{c,†}	Half-sphere lens	20.4	27.3	44.4	69.0	3.38 ^I , 1.34 ^{II} , 1.55 ^{III}	This work

a, averaged peak value, if available. b, at 1,000 cd/m². c, average value at 10,000 cd/m².

*, single-unit white OLEDs. †, double-unit tandem white OLEDs

6.7 Chapter summary

In this chapter, a new method is demonstrated for extracting trapped photons from white OLEDs, by implementing quasi-periodic nanostructures induced by RIE treatment on the PDMS surface. The topography of these nanostructures can be controlled by tuning the pretreatment conditions of the PDMS and the RIE recipes. The mechanism for the nanostructure generation and control is explained by mechanical deformation within a bilayer system on a planar surface, initialized by compressive stress release because of external stimuli from chemical reactions, physical bombardments and the modulus mismatch between the RIE-induced silica-like stiff top layer and elastic bottom PDMS. The utilization of RIE-induced nanostructures in white OLEDs has shown the capability to efficiently extract waveguide modes and SPP modes leading to a higher efficiency, together with improved color stability and more homogeneous radiance distribution. An optical model considering the dipole position and dipole orientation is proposed to simulate the device performance by dividing the nanostructures into sinusoidal textures with a dominant periodicity and height. Optical simulations indicate that the highest enhancement can be expected for an aspect ratio of $AR \approx 0.25$. Because nanostructures can be directly generated on the PDMS surface, they are compatible with emerging flexible devices. The controllable, facile and scalable method to fabricate these quasi-periodic nanostructures presents a powerful tool-set for generation and manipulation of complicated nanostructures, which also holds promising application potential in optical, biological and mechanical fields.

7 Concluding remarks and outlook

The following chapter summarizes the main results of this thesis. Based on these results in OLEDs, the possible expansion into other optoelectronic devices are presented. The scientific possibilities for further investigation based on these results are discussed.

7.1 Summary

In this thesis, different approaches for the light extraction in white OLEDs are investigated. Special focus was put on the photon generation and dissipation processes inside OLEDs. The outcoupling efficiency of OLEDs can be significantly enhanced by suppressing the surface plasmon-polariton mode, mitigating the destructive cavity resonance or extracting trapped photons.

The optical effect of a thin layer of MoO₃ has been systematically investigated for bottom emitting OLEDs. Previously, it is believed that the thin MoO₃ layer can enhance the adhesion of composed Au/Ag electrode as a seeding layer. This investigation demonstrates that actually, the deposition of 2 nm Au on glass substrates can already give a smooth surface with a low mean square roughness ($R_{\text{rms}} < 1$ nm). Meanwhile, a thin MoO₃ layer plays a substantial role for the device performance. Based on an electrode structure of MoO₃ (3 nm)/Au (2 nm)/Ag (7 nm), white tandem OLEDs can achieve 22.5% of EQE and 28.2 lm/W at 1,000 cd/m². After extraction of substrate modes by using a half-sphere lens, it can reach up to 38.8% of EQE and 53.9 lm/W of luminous efficacy. However, the EQE of the reference device without MoO₃ decreases to 12.6% (air modes) and 20.9% (substrate and air modes). Thus, by inserting the 3 nm MoO₃ layer, an efficiency enhancement factor of about 1.9 by is realized. Further device characterization demonstrates that devices with MoO₃ layer shows a better spectral stability and more homogeneous radiance distribution. The insertion of the thin MoO₃ layer under the composite electrode has a minor influence on the electrical property of the device, because the MoO₃ is located beneath the electrode, rather than being sandwiched between two electrodes.

Even though the suppressing of SPP modes has an influence in the range of 400 – 520 nm, the dielectric constant of MoO₃ is not high enough in wavelength longer than 520 nm. The replacement of MoO₃ by other optical materials with higher dielectric constant in this range can even enhance the performance further. The combination of SPP theory and different materials with various dielectric constant can expand the result

into other wavelength regime and many of other systems.

The modulation of reflection and transmission of the composite electrode by the thin layer of MoO₃, can be easily utilized for OLEDs based on emitters with a broad emission spectrum, such as many of TADF emitters. Since many of these emitters possess a wide emission spectrum with FWHM more than 100 nm, the comparably low color quality may jeopardize their practical application.[38] By controlling the cavity resonance, the FWHM of EL spectrum can be reduced with enhanced color purity. However, a strong cavity effect can also bring serious angular dependent emission. Tuning the cavity resonance by a thin layer of MoO₃ in this thesis, rather than changing the thickness of the semi-transparent metal electrode or charge transport layers, brings a smaller side-effect of angular dependent emission.[96]

Even though the MoO₃ layer can reduce SPP modes and enhance the device efficiency, the EQE of OLEDs based on MoO₃/Au/Ag electrode is only comparable to ITO-based devices. Photon trapping in forms of substrate modes, waveguide modes and SPP modes still make serious photon trapping in these devices. To reduce these losses, a facial and lithography-free method to fabricate controllable nanostructures is developed by modifying the surface of PDMS with RIE. These nanostructures possess directional randomness and dimensional order, while the dominant periodicity among the periodicity distribution and average depth can be manipulated simultaneously or independently, by varying the pretreatment condition of PDMS and/or the RIE treatment recipe. Experimentally, it is possible to tune the average depth from about 10 to 140 nm and the dominant periodicity from about 200 nm to 800 nm. The XPS measurement indicates that the surface of PDMS is converted to a silica-like layer. Together with the modulus measurement of PDMS before the RIE treatment, it suggests that the compressive stress release between the top stiff layer and the bottom soft base should contribute to the generation of quasi-periodic nanostructures. An enhancement factor of EQE 1.53 ± 0.12 at 10,000 cd/m² is achieved for a highly optimized white tandem OLEDs, with a maximum EQE as high as of 76.3% and a luminous efficacy of 95.7 lm/W with extracted substrate modes. Additionally, a reduced color shift over viewing angles can be obtained with a more homogeneous radiance distribution. However, it should be noted that a large fraction of outcoupled photons is still trapped as substrate modes, while external outcoupling strategies are still needed. We anticipate these nanostructures can not only be used for outcoupling purpose in OLEDs, but also for many of other potential areas such as sensors, flexible and stretchable devices. [248]

The nanostructures generated by RIE treatment on PDMS can be further tuned to a larger size shown in this thesis, which can also be promising as external outcoupling structures for bottom emitting OLEDs.

Even though an optical model for flat OLEDs has been reported in 2012, which has been successfully applied to understand the trapping mechanism of OLEDs, there is still no optical model to numerically simulate the optical behavior for devices based on nanostructures with a periodicity and depth distribution.[61] In this thesis, a 2D optical model based on finite element analysis is built, by treating the corrugated quasi-periodic nanostructures as sinusoidal nanotexture and considering the dipole orientation, emitting wavelength and the dipole position on the texture. The numerical simulation result indicates that the enhancement factor is highly dependent on the aspect ratio AR of sinusoidal textures. A maximum improvement of ~ 1.45 is predicted with the AR at about 0.25. A wavelength dependent enhancement behavior is noted for a single sinusoidal texture because of a fixed periodicity, which is consistent with previous results for OLEDs based on gratings.

Technically, there are three possible ways to define the depth of the nanostructure for the outcoupling purpose. Even though the dominant depth among the depth distribution gives a clear physical meaning, which nicely meets the intrinsic mechanism that the real geometrical structure affect the outcoupling efficiency, the lack of an absolute certainty of the zero depth during AFM measurements can potentially give an error of the value for each nanostructure. Based on the statistics of a series of high quality AFM measurements, it shows that the experimental AR calculated with the dominant depth among the depth distribution can nicely follow the simulation results.

Since there is a periodicity and depth distribution for nanostructures generated by RIE treatment on PDMS surface, the simulation in this thesis is only considering the dominant periodicity, giving rise to a system error without the consideration of the periodicities deviated from the dominant periodicity. The evaluation of multiple periodicities for the specific nanostructures and weighting their effect according to the periodicity density function can improve the accuracy of the optical modelling.

It should be noted that there is another system error of the simulation results, rising from the fact that emitting dipoles are physically 3D elements, while the simulation is only 2D. Further improvement of the optical model to 3D level should strengthen it with higher accuracy. Nevertheless, the idea of treating these nanostructures as sinusoidal texture to model the optical effect may facilitate the further development of optical outcoupling for quantum dot LEDs or perovskite LEDs.[242]

7.2 Outlook

The photon trapping in OLEDs, on one hand, leads to a significant energy loss for either display or lighting applications. On the other hand, because of the energy loss, a higher current density is needed to reach the practical luminance level at several thousand candela, leading to triplet-triplet or singlet-triplet annihilation processes. These bimolecular quenching processes not only reduce the IQE of OLEDs, but facilitate the device degradation at the same time.[60,249] In the ideal case, the enhancement of outcoupling efficiency should improve the device lifetime at the same luminance level. According to the empirical experience, the lifetime of an OLED is related to the luminance:

$$LT(L_1) = \frac{LT(L_0)}{(L_0/L_1)^n} \quad (7.1)$$

where n is an empirical number, defined by intrinsic device structure.[250]

Tremendous endeavor has been made to develop the new strategies to enhance the outcoupling efficiency or understand the optical effect from these nanostructures. At this stage, it is likely that more attention should be paid to reduce the side-effects such as the change of electrical property or complicated fabrication processes, which can move these outcoupling strategies from scientific concepts forward to practical application. Moreover, for display applications, in most cases, OLEDs are fabricated with a top-emitting configuration, but the investigation on outcoupling strategies for top emitting OLEDs is still limited.[97]

Cost-effective, scalable and compatible with the present fabrication processes of OLEDs are some of the basic requirements for outcoupling techniques. The development of outcoupling strategies for blue OLEDs is beneficial, which can enhance the device efficiency and further, hopefully extend the device lifetime. Fabricating outcoupling nanostructures during OLEDs deposition without breaking the vacuum (in-situ generation) is promising. The compressive stress release induced nanostructures by thermal treatment may facilitate the development of in-situ generated patterns for outcoupling purposes, but the control of the periodicity and depth independently needs further investigations.

8 Appendix

TADF emitters have been intensively investigated since their successful application for fully harvesting triplets in OLEDs. Remarkable research has been conducted on small molecules with TADF property, while the knowledge about TADF polymer emitters is still limited. In this appendix chapter, the investigation on the interactions between host materials and a guest TADF polymer P1 is summarized. It is noted that the host material has a substantial effect on the PLQY and the TADF characteristics. The chapter is based on the publication of reference [266].

8.1 Host influenced TADF

TADF devices based on dendrimers and/or polymers have gained huge attention, because of the possibility of easy fabrication by solution processes and high efficiency at the same time. Meanwhile, to achieve macromolecules with TADF property, there are in general two approaches: incorporating TADF monomers into polymer side chains while the main chain is not conjugated; polymerizing donor and acceptor parts to form the main chain where the charge transfer state emission has TADF character and each TADF unit is separated without conjugation.[39,251–253] Previously, a method to generate an efficient blue TADF polymer was reported from our institute by polymerizing a non-TADF monomer (4-(3,6-dibromo-carbazol-9-yl)phenyl)(4-(dodecyloxy) phenyl)methanone to conjugated polymer macrocycles. The appearance of the TADF polymer, named as P1 (Figure A. 1), is resulting from the conjugation-induced reduction of the effective energy splitting between the respective $^1,^3\text{CT}$ charge transfer states, while keeping a sufficient radiative decay rate.[254] The previous report on P1 was focusing on the synthesis and the origin of TADF property, without further investigation on the influence of host materials or OLED devices. Here, the research is focused on the interactions between the TADF polymer P1 and different host materials including 9-(4-tert-Butylphenyl)-3,6-bis(triphenylsilyl)-9H-carbazole (CzSi), 2,4,6-Tris[3-(diphenylphosphinyl)phenyl]-1,3,5-triazine (PO-T2T) and 1,3-Bis(N-carbazolyl)benzene (mCP). The chemical structures are shown in Figure A. 1.

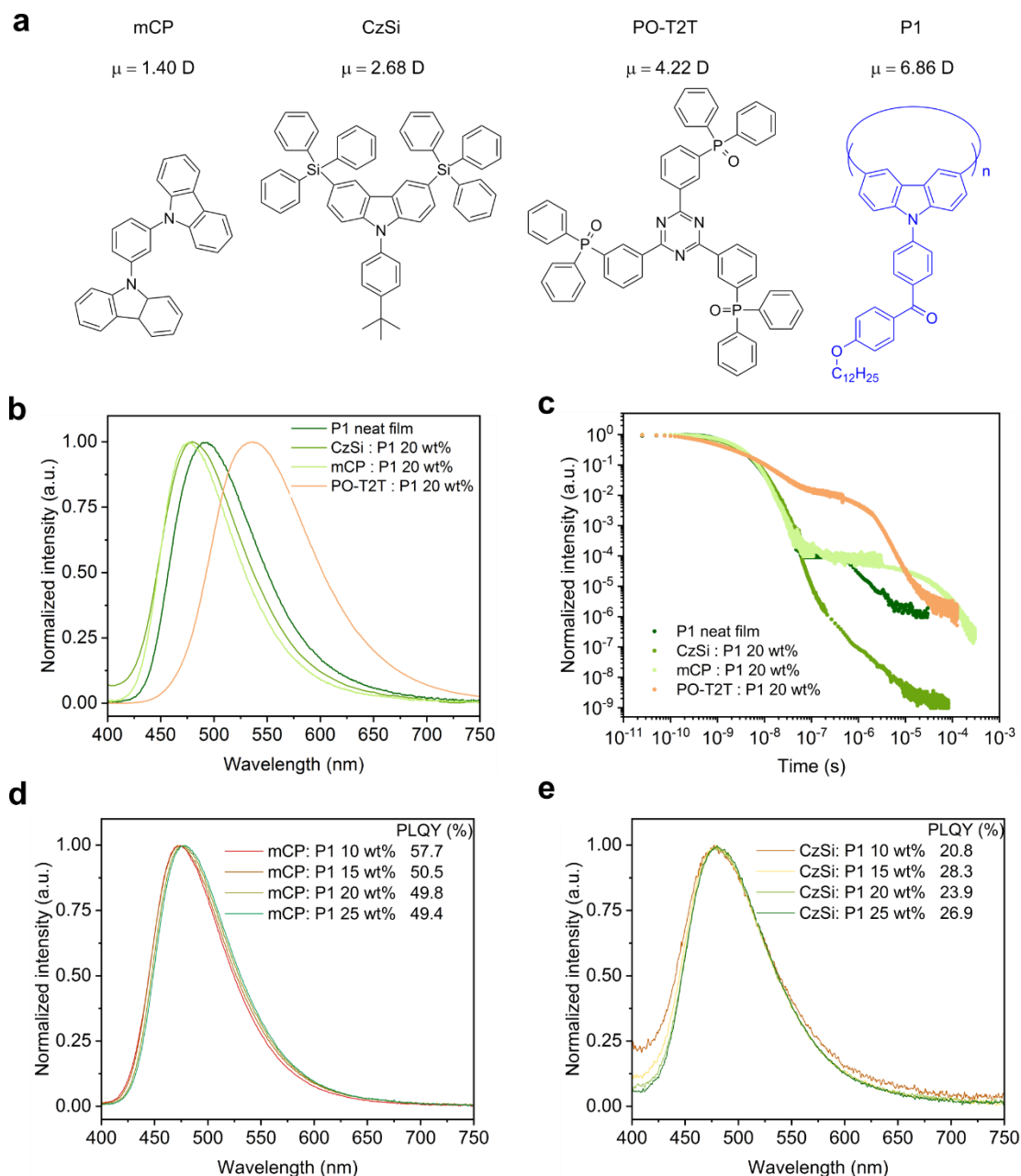


Figure A. 1. Photophysical property of P1 in different hosts. (a) Chemical structure of host materials and emitter P1, with calculated electrical dipole moment μ . The trimer of P1 is treated as the host for the P1 neat film for dipole moment calculation. The calculation is based on the density functional theory with molecules in the ground state, using the functional B3LYP and 6-31g(d) basis set. (b) PL spectra of different films with P1. (c) Transient PL decay measured at room temperature (ca. 297 K), detected at the peak wavelength in the steady state PL spectra, excited with a pulse laser at a wavelength of 373 nm. (d) PL spectra and the PLQY for P1 doped in mCP. (e) PL spectra and the PLQY for P1 doped in CzSi.

The PLQY and the delayed fluorescence for P1 is sensitive to the surrounding environment. The P1 neat film shows a moderate PLQY of 30.7%. The PL spectrum of the neat film is peaking at ~ 490 nm. When embedded in a host material (structures shown in Figure A. 1a) with a wide energy gap and high triplet energy (Figure A.6a), the PLQY for the mixed film also changes. Doped with a concentration of 20 wt% in

CzSi, a widely used host material for blue emitters with a wide bandgap,[255] a lower PLQY of 23.9 % can be realized. The PLQY in CzSi is slightly increased to around 30 %, with different P1 concentration from 10 wt% to 25 wt%, as shown in Figure A. 1e. For mCP: P1 films, the PLQY reaches 57.7 % with 10 wt% of P1. It decreases to 49.4 % when increasing the doping concentration of P1 to 25 wt%. The change of the doping concentration within the range of 10 wt% to 25 wt% has only a minor influence on the PL spectrum, as shown in Figure A. 1d. The PL spectrum of mCP: P1 20 wt% films peak at 477 nm, which is slightly blue-shifted compared to the P1 neat film, beneficial for achieving blue OLEDs.

The change of the emission spectrum of mCP, CzSi and non-doped film is likely due to the interaction with hosts with different dipole moments. As shown in Figure A. 1a, the dipole moment of the mCP is as small as 1.40 D, while it is 6.86 D for P1. Here, the trimer is treated as the host material for the P1 neat film in the density functional theory (DFT) calculation. It is interesting to note that the PL emission peak is red-shifted to 532 nm, indicating the possibility of a CT-emission between P1 and PO-T2T. Before systematically investigating the photophysical property of the PO-T2T and P1 mixture, the detailed influence of host materials mCP and CzSi on the TADF characteristics is analyzed.

Time-Correlated-Single-Photon-Counting (TCSPC) measurements done at the maximum PL wavelength show that the host molecule makes a substantial influence on the decay profile of the prompt and delayed fluorescence. The transient decay of the prompt and delayed fluorescence can be fitted by multi-exponential functions:

$$y = \sum_i A_i \exp\left(-\frac{x}{t_i}\right) \quad (\text{A. 1})$$

The averaged decay lifetime τ can be calculated with the fitting parameters by:

$$\tau = \frac{\sum_i A_i t_i^2}{\sum_i A_i t_i} \quad (\text{A. 2})$$

Thus, the lifetime of prompt fluorescence τ_{PF} and delayed fluorescence τ_{DF} can be fitted by Equation (A.1) and (A.2).

The intensity of prompt fluorescence I_{PF} and delayed fluorescence I_{DF} can be obtained by integrating the area of transient PL measurement shown in Figure A. 2. The quantum yield of prompt fluorescence (Φ_{PF}) and delayed fluorescence (Φ_{DF}) among the total PLQY can be calculated by:

$$\Phi_{\text{PF}} = \frac{I_{\text{PF}}}{I_{\text{PF}} + I_{\text{DF}}} \Phi_{\text{PLQY}} \quad (\text{A. 3})$$

$$\Phi_{\text{DF}} = \frac{I_{\text{DF}}}{I_{\text{PF}} + I_{\text{DF}}} \Phi_{\text{PLQY}} \quad (\text{A. 4})$$

For typical TADF emitters, the decay rate of the prompt fluorescence k_r is orders higher than the rate of RISC k_{RISC} . The quantum yield Φ_{PF} is kinetically determined by:

$$\Phi_{\text{PF}} = \frac{k_r}{k_r + k_{\text{nr}}^s + k_{\text{ISC}}} = k_r \tau_{\text{PF}} \quad (\text{A. 5})$$

Since Φ_{PF} and τ_{PF} can be obtained experimentally, the decay rate k_r can be obtained by:

$$k_r = \frac{\Phi_{\text{PF}}}{\tau_{\text{PF}}} \quad (\text{A. 6})$$

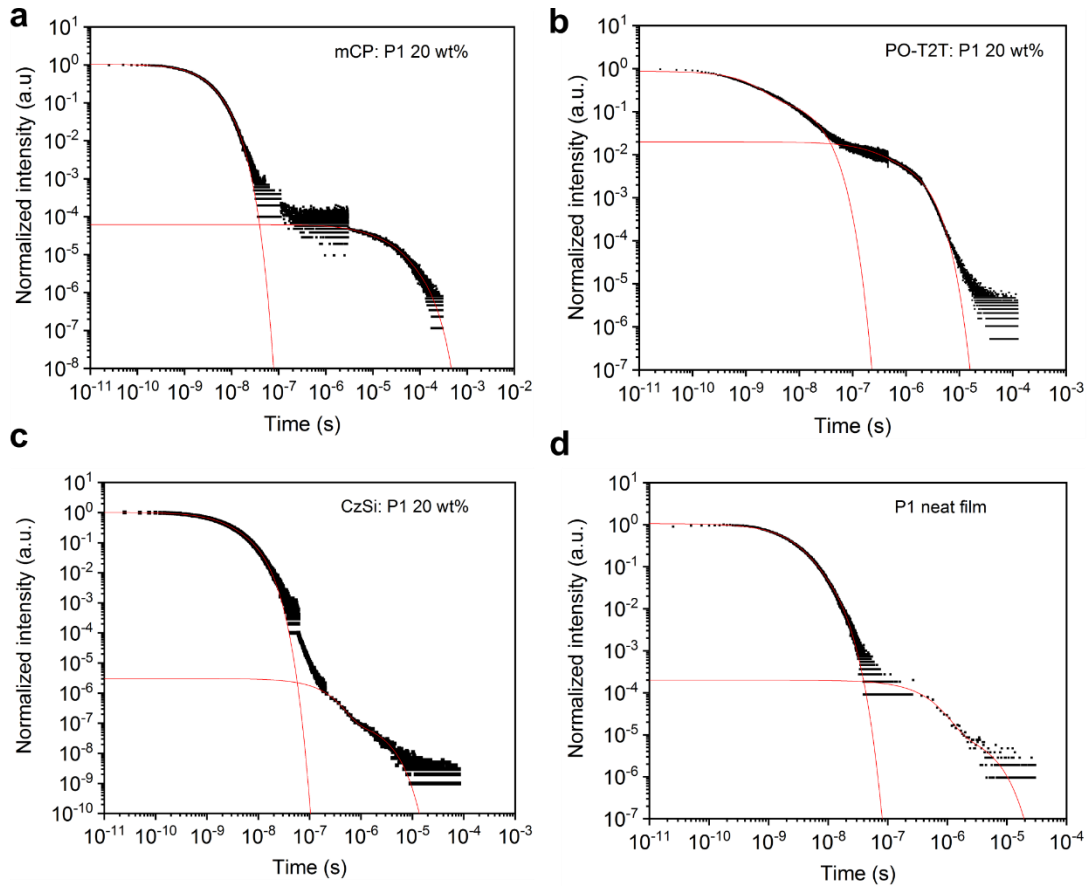


Figure A. 2. Transient PL decay profile fitting, measured at the peak wavelength for each film under the excitation of 375 nm laser. The red lines are fit curves. (a) mCP : P1 20 wt%, (b) PO-T2T : P1 20 wt%, (c) CzSi : P1 20 wt% and (d) P1 neat film.

According to Equation (A.3) – (A.6), the Φ_{PF} , Φ_{DF} and k_r can be obtained. Technically, as shown in Figure A. 2, the transient PL decay profile can be fitted for these emissive systems.

The detailed fitting parameters for prompt fluorescence and calculated τ_{PF} is summarized in Table A. 1, while the fitting parameter for delayed fluorescence and τ_{DF} is summarized in Table A. 2, respectively.

Table A. 1. Fitting details of the prompt fluorescence and intensity (I_{PF}).

	A_1	t_1	A_2	t_2	τ_{PF} (s)	I_{PF}
mCP: P1 20 wt%	0.63	2.04×10^{-9}	0.4	4.45×10^{-9}	3.44×10^{-9}	3.09×10^{-9}
PO-T2T: P1 20 wt%	0.66	1.22×10^{-9}	0.21	1.58×10^{-8}	1.30×10^{-8}	4.6×10^{-9}
CzSi: P1 20 wt%	0.53	1.46×10^{-9}	0.49	4.66×10^{-9}	3.85×10^{-9}	3.09×10^{-9}
P1 neat film	0.81	1.98×10^{-9}	0.25	5.49×10^{-9}	3.60×10^{-9}	2.97×10^{-9}

Table A. 2. Fitting details of the prompt fluorescence and intensity (I_{DF}).

	A_1	t_1	A_2	t_2	A_3	t_3	τ_{DF} (s)	I_{DF}
mCP: P1 20 wt%	1.26×10^{-5}	6.48×10^{-5}	3.04×10^{-5}	2.12×10^{-5}	1.88×10^{-5}	4.20×10^{-5}	4.43×10^{-5}	1.62×10^{-9}
PO-T2T: P1 20 wt%	0.01015	2.22×10^{-7}	0.00974	1.38×10^{-6}	0	0	1.21×10^{-6}	9.8×10^{-9}
CzSi: P1 20 wt%	2.93×10^{-6}	1.75×10^{-7}	1.22×10^{-7}	1.92×10^{-6}	0	0	7.21×10^{-7}	4.25×10^{-13}
P1 neat film	1.88×10^{-4}	4.26×10^{-7}	1.22×10^{-5}	4.05×10^{-6}	0	0	1.81×10^{-6}	9.02×10^{-11}

The photophysical properties of P1 in different hosts are summarized in Table A.3. The τ_{PF} is 3.60 ns for P1 neat film and it is slightly different for CzSi (3.85 ns) and mCP (3.44 ns). The τ_{DF} varies significantly for the neat film and doped films. The τ_{DF} is 1.81 μ s for P1 neat film, while it is 0.72 μ s in CzSi and 44.32 μ s in mCP. Moreover, big variations of the Φ_{PF} and Φ_{DF} , and further the ratio of Φ_{PF} / Φ_{DF} are noted. In the neat film, only a very small amount of delayed fluorescence ($\Phi_{DF} = 0.90$ %) is observed, with a ratio of Φ_{DF} / Φ_{PF} at 0.03. The delayed fluorescence in CzSi is negligible, with Φ_{DF} of only 0.0029 % and extremely low Φ_{DF} / Φ_{PF} (0.00014). The delayed fluorescence is much more pronounced in mCP, in which $\Phi_{DF} = 16.9$ % and $\Phi_{DF} / \Phi_{PF} = 0.52$ is obtained. Compared to CzSi, the Φ_{DF} in mCP host is more than 5900 times higher.

Table A.3. Photophysical properties of films with P1.

Film	Φ_{PLQY}	λ_{max} (nm)	Φ_{PF} (%)	Φ_{DF} (%)	$\Phi_{\text{DF}} / \Phi_{\text{PF}}$	τ_{PF} (ns)	τ_{DF} (μs)	$k_{\text{r}} (\times 10^7 \text{ s}^{-1})$
P1 neat	30.7 %	490	29.8	0.90	0.03	3.60	1.81	8.27
CzSi: P1 20 wt%	23.9 %	477	23.9	2.86×10^{-3}	1.20×10^{-4}	3.85	0.72	6.21
mCP: P1 20 wt%	49.8 %	476	32.9	16.9	0.52	3.44	44.32	9.50
PO-T2T: P1 20 wt%	8.1 %	532	2.6	5.5	2.13	13.00	1.21	0.20

A low value of $\Phi_{\text{DF}} / \Phi_{\text{PF}}$ can jeopardize the triplet harvesting in an electrical driving device, since triplets are generated in the first place, rather than from ISC from singlets under optical excitation. The extremely low value of $\Phi_{\text{DF}} / \Phi_{\text{PF}}$ in the CzSi host gives a hint that most of the generated triplets in the device cannot efficiently transfer to singlets, indicating the CzSi : P1 system improper for device applications.

8.2 Photophysical properties of PO-T2T : P1 mixture

The large shift of PL spectrum of the PO-T2T : P1 mixed film indicates a possible intermolecular CT-emission, which is typically referred to as ‘exciplex’ in the OLED community between small molecules.[79,256–258] As shown in Figure A.4, compared to the pure emission of PO-T2T and P1, the PL spectrum of the mixed film is red-shifted by ~ 170 nm and ~ 60 nm, respectively. According to previous reports, the LUMO level of the PO-T2T is about 3.5 eV and the HOMO level of P1 is 5.7 - 5.8 eV.[79] The PO-T2T as the donor and P1 as the acceptor can form a CT-state with an energy gap of about 2.2 - 2.3 eV, which is close to the emission energy of the PO-T2T : P1 mixture, indicating that the yellow emission in the PO-T2T : P1 blend is resulting from the charge transfer between PO-T2T and P1. As shown in Figure A.4b, when varying the P1 concentration in the PO-T2T and P1 mixture films from 20 wt% to 60 wt%, there is no significant change of the PL spectra measured under ambient condition, with the PL peak at about 540 nm. Increasing the concentration of P1 to 80 wt% can shift the PL maximum to 548 nm.

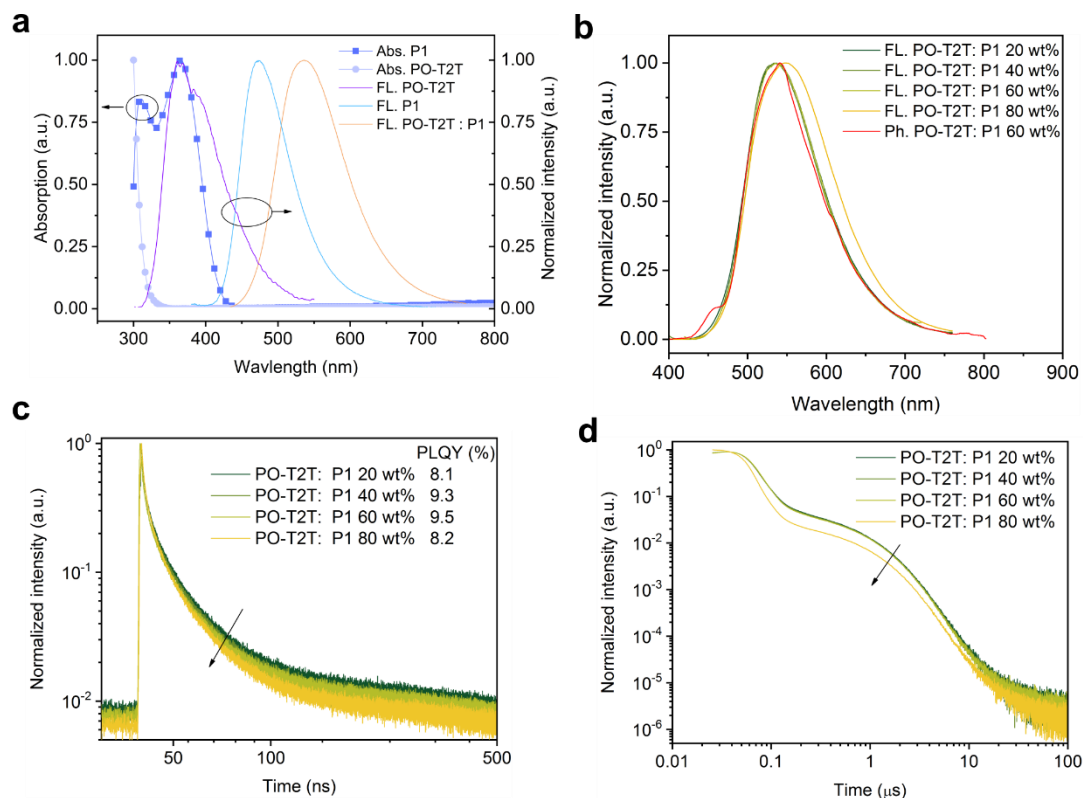


Figure A.4. The CT-emission between PO-T2T and P1 with TADF property. (a) Normalized absorption and fluorescence spectrum of P1, PO-T2T and the CT-emission of PO-T2T : P1. (b) Room temperature steady state fluorescence spectra with different doping concentration and the representative phosphorescent spectrum in liquid nitrogen. (c) The prompt fluorescence decay of CT-emission. The PLQY for the CT-emission with different P1 concentration is inset. (d) The delayed fluorescence decay of the CT-emission.

Further investigations demonstrate that the CT-emission has also the TADF property. The phosphorescence spectra measured under 77 K in liquid nitrogen, have only a small red-shift compared to the steady PL spectra, as shown in Figure A.4b and Figure A. 3.

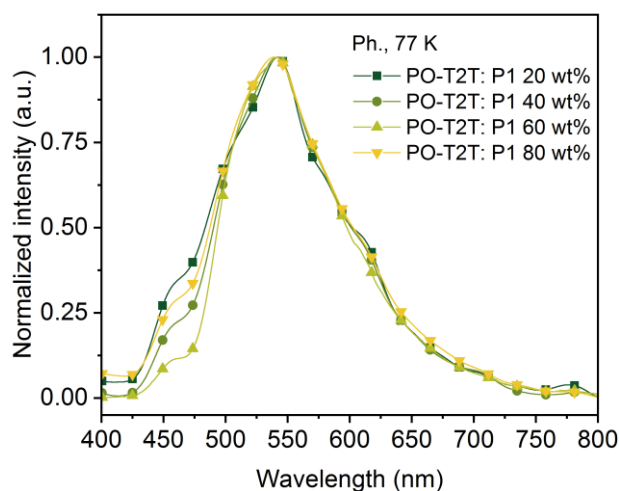


Figure A. 3. Phosphorescent spectra of PO-T2T : P1 films in liquid nitrogen (77 K).

The similarity of PL spectra at the room temperature and the phosphorescent spectra indicates a small ΔE_{ST} . The lineshape of normalized emissive spectrum can be fitted with a group of Gaussian functions:[259]

$$\begin{aligned} \frac{I(E)}{E^3} &= a_1 \sum_{n=0}^{\infty} \left(\frac{s^n}{n!} e^{-s} \right) G_n(x, \sigma_n, E_{\text{vert}}, E_{\text{vir}}) \\ &= a_1 \sum_{n=0}^{\infty} \left(\frac{s^n}{n!} e^{-s} \right) \left[\exp \left(-\frac{(x - (E_{\text{vert}} + s * E_{\text{vir}} - n * E_{\text{vir}}))^2}{2\sigma_n^2} \right) \frac{1}{\sigma_n \sqrt{2\pi}} \right] \end{aligned} \quad (\text{A.7})$$

where a_1 is a scale factor, E_{vert} is the vertical transition energy of the specific state, E_{vir} is the vibrational energy of the ground state. G_n is an individual line in a form of Gaussian function with a line-width σ_n .

As shown in Figure A. 5, by fitting the fluorescent and phosphorescent spectrum, both the singlet and triplet transition energy can be obtained. The singlet energy level is 2.162 eV, while the triplet energy level is 2.155 eV, giving the ΔE_{ST} as small as 7 meV. The detailed fitting parameters are summarized in Table A. 4.

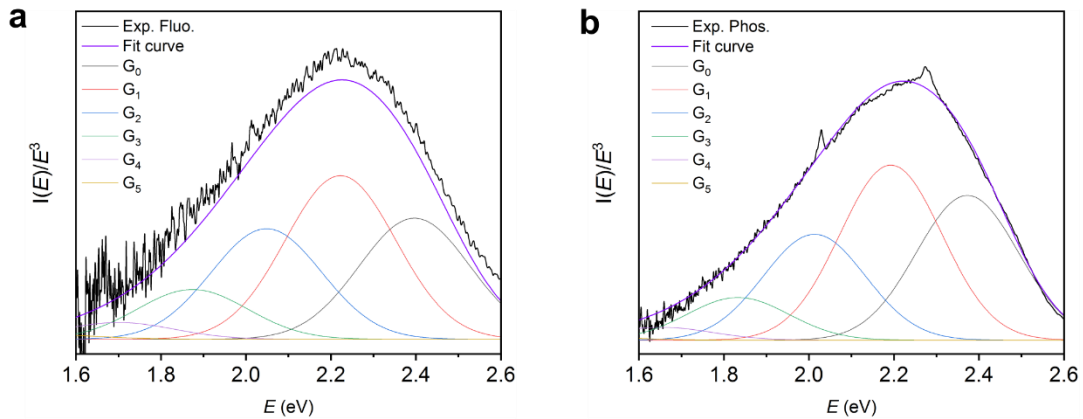


Figure A. 5. Lineshape fitting of CT-emission (a) Fluorescence. (b) Phosphorescence. For both spectra, it can be fitted with six Gaussian functions $G_n(x)$ in Equation (A.7).

Similar transient PL emission profiles have been obtained for the system with varied P1 concentration from 20 wt% to 80 wt%, as shown in Figure A. 2. The τ_{PF} is 13.0 ns for 20 wt% P1, while it only slightly decreases to 11.1 ns, 11.2 ns and 8.6 ns, for films with 40 wt%, 60 wt% and 80 wt% P1, respectively. The τ_{DF} is around 1.20 μ s, with a minor variation with different P1 concentrations from 20 wt% to 60 wt%. A more pronounced change for films with 80 wt% P1 is more likely raising from the red-shift of steady state PL emission, as shown in Figure A. 2b. The results shows that the ratio between the donor and acceptor has minor influence on the transient decay of the CT-emission, which is similar compared to the first reported CT-emission with TADF characteristics between small molecules and polymers.[260]

Table A. 4. Lineshape fitting parameters for both fluorescence and phosphorescence spectra with Equation (A.7).

	a_1	s	σ_0	σ_1	σ_2	σ_3	σ_4	σ_5	E_{vir}	E_{vert}
Fluo.	0.520104	1.35061	0.13	0.13	0.13	0.13	0.13	0.13	0.174178	2.1615
Phos.	0.532334	1.20916	0.12	0.12	0.12	0.12	0.12	0.12	0.180028	2.15524

The PLQY of the PO-T2T : P1 system is only 8 - 10% (Figure A. 2c), demonstrating that the non-radiative decay is the major relaxation process. Nevertheless, a significant delayed fluorescence is observed, with the ratio of $\Phi_{\text{DF}} / \Phi_{\text{PF}}$ larger than 2, indicating there are cycling processes from triplets and singlets.[254] The detailed photophysical properties of PO-T2T : 20 wt% P1 are also summarized in Table A.3.

It is interesting to observe that, even though the singlet state is decreasing by increasing the dipole moment of host materials (Figure A. 1a), the ratio $\Phi_{\text{DF}} / \Phi_{\text{PF}}$ is not fully following the trend. As we can see, the PL emission is red-shifted for the non-doped film compared to the mCP : P1 system, while the ratio $\Phi_{\text{DF}} / \Phi_{\text{PF}}$ is still much lower compared to the later. Thus, a deeper blue emission together with a higher fraction of delayed fluorescence are obtained at the same time in host mCP, which is beneficial for fabricating efficient blue OLEDs. According to the photophysical investigation and DFT analysis, factors including host-guest energy transfer, dipole moment of host materials and CT-state generation can contribute to different $\Phi_{\text{DF}} / \Phi_{\text{PF}}$ ratios for the TADF polymer in different hosts.

8.3 Monochrome OLEDs based on P1

Based on the photophysical investigations, we further explore monochrome OLEDs based on P1 with different device structures. The device structures and characteristics are summarized in Table A. 5. The energy diagram is shown in Figure A.6a. As depicted in Figure A.6b, for the monochrome devices D1 (PO-T2T : 20 wt% P1) and D2 (mCP : 20 wt% P1), the slight difference of the voltage-current density behavior is likely resulting from the different transport property of host materials. However, much difference of voltage-current density behavior is noted for D3 (P1 / PO-T2T) and D4 (P1 / 1,3,5-tri(m-pyridin-3-ylphenyl)benzene, TmPyPB), as shown in Figure A.6b. The reason can be ascribed to the difference of the LUMO level for PO-T2T and TmPyPB (Figure A.6a). A voltage larger than 6 V is needed to turn D1 - D4 on. Many reasons may contribute to the high turn-on voltage of D1 and D2, including limited transport mobility of the PVK and PEDOT:PSS layer.[260]

As shown in Figure A.6e and Table A. 5, the emission color for D2 and D4 is cyan blue, with the CIE coordinates (0.24, 0.37) for D2 and (0.20, 0.35) for D4. However, a very different emission color is noted for D1 (PO-T2T: 20 wt% P1) and D3 (P1 / PO-T2T). The EL spectra with a peak wavelength located at about 530 nm for D3 is very close to the PL spectrum of the CT-emission between PO-T2T and P1 (Figure A.6b). The device cavity and the emission from intrinsic P1 may contribute to the slight deviation of EL spectrum of D1 from the PL spectrum of PO-T2T and P1 CT-state.

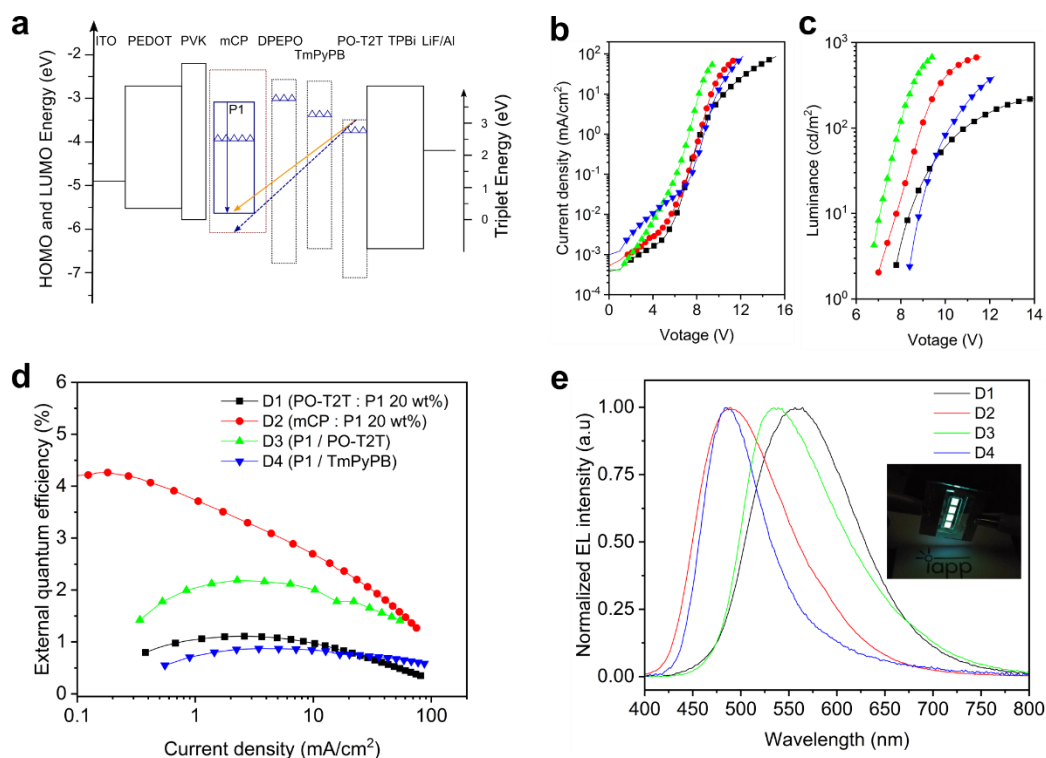


Figure A.6. Monochrome OLEDs based on P1. (a) Schematic diagram of energy levels of representative devices. The top line of the box indicating the LUMO and the bottom line refers to the HOMO level. The solid blue arrow represents the intrinsic emission from the TADF polymer P1, while the orange arrow represents the CT-emission between PO-T2T and P1, the dashed blue line represents the possible CT-emission between host mCP and PO-T2T. The triangles refer to the triplet energy level. (b) The voltage-current density characteristic. (c) The voltage-luminance characteristic. (d) Current density-EQE. (d) Normalized EL spectrum at 100 cd/m². The inset picture is a photo of the OLEDs with mCP as the host material.

For D4 with P1 neat film as emitting layer, as shown in Figure A.6d and Table A. 5, an EQE_{max} of 0.87% is obtained. The reason for such low device performance could be imbalanced charge carrier injection, intrinsic lower PLQY value and the inefficient RISC process. A further device optimization by insetting a PVK layer on top of PEDOT:PSS may enhance the charge balance and block the triplet diffusion to hole transport layer. A medium EQE of 4.26% can be obtained for D2 with 20 wt% P1 doped in mCP, as shown in Figure A.6d and Table A. 5. The EQE_{max} is 1.11% for D1 and 2.19% for D3, with the CT-emission between PO-T2T and P1.

Table A. 5. Summary of the device characteristics.

Device	Device structure ^a (EBL/ EML/ HBL)	EQE _{max} (%)	CE _{max} (cd/A)	LE _{max} (lm/W)	CIE (x, y)
D1	PVK (15 nm)/ PO-T2T : P1 20 wt% (50 nm)/ DPEPO (10 nm)/ TPBi (50 nm)/ LiF (1 nm)	1.11	0.92	0.91	(0.42, 0.52)
D2	PVK (15 nm)/ mCP : P1 20 wt% (50 nm)/ DPEPO (10 nm)/ TPBi (50 nm)/ LiF (1 nm)	4.26	3.03	2.46	(0.24, 0.37)
D3	P1 (30 nm)/ PO-T2T (10 nm)/ Bphen : Cs (50 nm)	2.19	1.93	1.90	(0.39, 0.54)
D4	P1 (30 nm)/ TmPyPB (10 nm)/ Bphen : Cs (50 nm)	0.87	0.69	0.44	(0.20, 0.35)
D5	PVK (15 nm)/PO-T2T : P1 99 wt% (50 nm)/ DPEPO (10 nm)/ TPBi (50 nm)/ LiF (1 nm)	1.74	1.81	1.84	(0.28, 0.40)
D6	PVK (15 nm)/ PO-T2T : P1 99.5 wt% (50 nm)/ DPEPO (10 nm)/ TPBi (50 nm)/ LiF (1 nm)	1.20	1.34	1.58	(0.31, 0.44)

a. The complete device is composed as ITO/ PEDOT : PSS (70 nm)/ EBL/ EML/ HBL/ Al (100 nm).

b. Simulation results. Details in experimental sections.

8.4 Polychrome OLEDs with dual emission from P1 and CT-state

OLEDs with polychromatic emission are constructed with a single emitting layer combining the blue emission from P1 and the yellow emission from the CT-emission between PO-T2T and P1. As shown in Figure A.9a, in such a mixed film, there are two TADF processes, including the TADF cycling within P1 itself and the CT-emission between PO-T2T and P1. Excitons generated in P1 can transfer to the CT-state by several different processes: FRET or Dexter energy transfer determined by the CT-state concentration;^[126] or even simple charge separation from local exciton to CT exciton as in solar cells.^[258] Since the increase of PO-T2T concentration in the mixed film can tune the emission to yellow (e.g. D1), the major part of the film should be P1 to achieve a double-color emission. Based on these analyses, we tested the P1 polymer film embedded with 0.5 wt% (device D6) and 1 wt% PO-T2T (device D6), to demonstrate double-color emission close to white spectrum in a single-EML architecture.

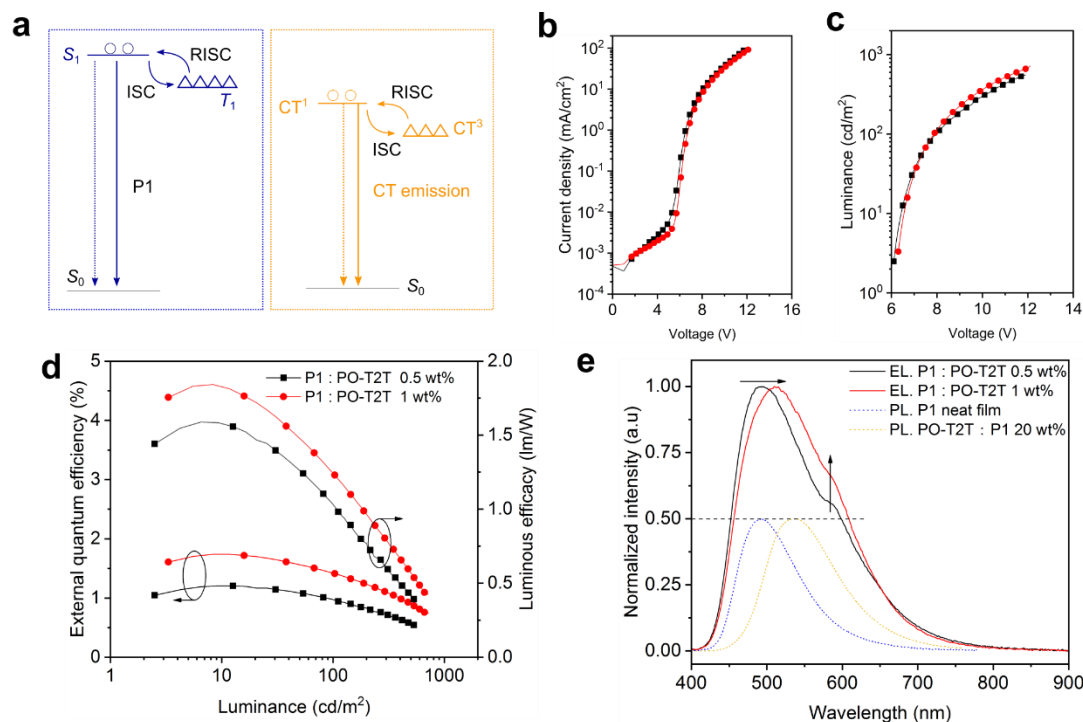


Figure A.7. Single layer OLEDs with dual emission from P1 and the CT-emission for D5 and D6. (a) Schematic illustration of the emission for the mixed film with P1 and PO-T2T. The solid lines represent the radiative relaxation, while dashed lines represent the non-radiative loss. (b) The voltage-current density characteristics. (c) The voltage-luminance characteristics. (d) EQE-luminance-luminous efficacy characteristics. (e) Normalized EL spectra in the forward direction at 100 cd/m^2 .

As shown in Figure A.7b and Table A. 5, the slight change of the PO-T2T concentration has little influence on the electrical property of D5 and D6. The luminance for D5 is slightly higher than D6, as shown in the Figure A.7c. A maximum EQE of 1.74 % and 1.20 % is achieved for D5 and D6 at around 10 cd/m^2 , as shown in Figure A.9d. The EQE slightly rolls off to 1.41 % at 100 cd/m^2 for D5 and 0.97 % at 100 cd/m^2 for D6. A maximum luminous efficacy of 1.84 lm/W for D5 and 1.59 lm/W for D6 can be realized.

The EL spectra are shown in Figure A.7e. The device D5 with 0.5 wt% PO-T2T shows two separate peaks, located at ~ 490 nm and ~ 570 nm, giving a CIE of (0.31, 0.43) with the FWHM of 146 nm. Slightly increasing the concentration of PO-T2T to 1 wt% can shift the first peak to about 510 nm, while the intensity of the shoulder peak is enhanced. In the end, D6 gives a final CIE of (0.28, 0.40) with the FWHM of 153 nm. As far as we know, this is the first demonstration of TADF CT-emission between polymer and small molecules for polychromatic OLEDs with a CIE close to a white color. It may be possible to further optimize to reach white OLEDs by further increasing the concentration of PO-T2T.

8.5 Summary

In this appendix chapter, the host material in the polymer OLEDs has been proved to play a vital role. The influence of different host materials on the photophysical property of a TADF polymer P1 and the device performance is investigated. Almost no delayed fluorescence is observed in the neat film or in host CzSi. The delayed fluorescence can be enhanced by thousands of times when using mCP as host materials compared to CzSi. Furthermore, a CT-emission between the PO-T2T and P1 is observed, which possesses a pronounced TADF property with a ΔE_{ST} as small as 7 meV and a ratio of 2.13 between delayed fluorescence to prompt fluorescence. When using the TADF polymer P1 to build monochrome OLEDs, cyan blue devices can be achieved for P1 neat film or embedded in mCP. A maximum EQE of 4.26% is achieved for devices with mCP as the host material, while it is only 0.87% for the device based on the P1 neat film.

Together with the yellow emission from the CT-emission between PO-T2T : P1 and the intrinsic blue emission from P1, OLEDs with polychromatic emission can be realized with a low doping concentration of PO-T2T, which can be a starting point for further investigation on high efficiency white OLEDs based on solution processes with purely organic TADF polymers. A maximum EQE of 1.74% and luminous efficacy of 1.84 lm/W is achieved.

References

- [1] C.W. Tang, S.A. VanSlyke, Organic electroluminescent diodes, *Appl. Phys. Lett.* 51 (1987) 913.
- [2] JOLED to Start Providing OLED Display Panel Samples to ASUS | JOLED Inc., (n.d.). <https://www.j-oled.com/news-eng/2018-1-5/> (accessed August 9, 2018).
- [3] OLED Microdisplays | OLED-Info, (n.d.). <https://www.oled-info.com/oled-microdisplays> (accessed August 9, 2018).
- [4] Mercedes to introduce OLED taillights in its upcoming S-Class Coupe and Cabriolet cars | OLED-Info, (n.d.). <https://www.oled-info.com/mercedes-introduce-oled-taillights-its-upcoming-s-class-coupe-and-cabriolet-cars> (accessed August 9, 2018).
- [5] G.L. Miessler, P.J. Fischer, D.A. Tarr, C.F. Macrae, I.J. Bruno, J.A. Chisholm, P.R. Edgington, P. McCabe, E. Pidcock, L. Rodriguez-Monge, R. Taylor, J. Van De Streek, P.A. Wood, *Inorganic Chemistry*, Fifth edition, Pearson Education, the United States of America, 2012.
- [6] R. V. Hoffman, *Organic Chemistry*, Second edition, John Wiley & Sons, New Jersey, 2004.
- [7] P. Atkins, J. de Paula, *Elements of Physical Chemistry*, Fifth edition, Oxford University Press, Great Britain, 2009.
- [8] Z.R. Grabowski, K. Rotkiewicz, W. Rettig, Structural Changes Accompanying Intramolecular Electron Transfer: Focus on Twisted Intramolecular Charge-Transfer States and Structures, *Chem. Rev.* 103 (2003) 3899–4031.
- [9] Y. Hong, J.W.Y. Lam, B.Z. Tang, Aggregation-induced emission, *Chem. Soc. Rev.* 40 (2011) 5361.
- [10] J.R. Lakowicz, *Principles of Fluorescence Spectroscopy*, Third edition, New York, 2006.

- [11] D. Harvey, *Modern Analytic Chemistry*, First edition, The McGraw-Hill Companies, the United States of America, 2000.
- [12] J. Peatross, W. Michael, *Physics of Light and Optics*, 2015 edition, Brigham Young University, 2015.
- [13] S.I. Hayek, *Mechanical Vibration and Damping*, in: *Encycl. Appl. Phys.*, John Wiley, New York, 2003: pp. 561–590.
- [14] T. Higashihara, M. Ueda, Recent progress in high refractive index polymers, *Macromolecules*. 48 (2015) 1915–1929.
- [15] B. Wang, G.L. Wilkes, J.C. Hedrick, S.C. Liptak, J.E. McGrath, New high-refractive-index organic/inorganic hybrid materials from sol-gel processing, *Macromolecules*. 24 (1991) 3449–3450.
- [16] A. Salehi, Y. Chen, X. Fu, C. Peng, F. So, Manipulating Refractive Index in Organic Light Emitting Diodes., *ACS Appl. Mater. Interfaces*. 10 (2018) 9595–9601.
- [17] Y.H. Huang, C.Y. Lu, S.T. Tsai, Y.T. Tsai, C.Y. Chen, W.L. Tsai, C.Y. Lin, H.W. Chang, W.K. Lee, M. Jiao, C.C. Wu, Enhancing light out-coupling of organic light-emitting devices using indium tin oxide-free low-index transparent electrodes, *Appl. Phys. Lett.* 104 (2014) 183302.
- [18] B. Cai, O. Sugihara, H.I. Elim, T. Adschiri, T. Kaino, A novel preparation of high-refractive-index and highly transparent polymer nanohybrid composites, *Appl. Phys. Express*. 4 (2011) 092601.
- [19] Q. Wei, R. Pötzsch, X. Liu, H. Komber, A. Kiriy, B. Voit, P.A. Will, S. Lenk, S. Reineke, Hyperbranched Polymers with High Transparency and Inherent High Refractive Index for Application in Organic Light-Emitting Diodes, *Adv. Funct. Mater.* 26 (2016) 2545–2553.
- [20] Q. Wei, X. Zan, X. Qiu, G. Öktem, K. Sahre, A. Kiriy, B. Voit, High Refractive Index Hyperbranched Polymers Prepared by Two Naphthalene-Bearing Monomers via Thiol-Yne Reaction, *Macromol. Chem. Phys.* 217 (2016) 1977–

- 1984.
- [21] K. Nakabayashi, T. Imai, M.C. Fu, S. Ando, T. Higashihara, M. Ueda, Synthesis and characterization of poly(phenylene thioether)s containing pyrimidine units exhibiting high transparency, high refractive indices, and low birefringence, *J. Mater. Chem. C*. 3 (2015) 7081–7087.
- [22] K. Nakabayashi, T. Imai, M.C. Fu, S. Ando, T. Higashihara, M. Ueda, Poly(phenylene thioether)s with Fluorene-Based Cardo Structure toward High Transparency, High Refractive Index, and Low Birefringence, *Macromolecules*. 49 (2016) 5849–5856.
- [23] J. Mei, N.L.C. Leung, R.T.K. Kwok, J.W.Y. Lam, B.Z. Tang, Aggregation-Induced Emission: Together We Shine, United We Soar!, *Chem. Rev.* 115 (2015) 11718–11940.
- [24] C.T. Chen, Evolution of red organic light-emitting diodes: Materials and devices, *Chem. Mater.* 16 (2004) 4389–4400.
- [25] S. Schmidbauer, A. Hohenleutner, B. König, Chemical degradation in organic light-emitting devices: Mechanisms and implications for the design of new materials, *Adv. Mater.* 25 (2013) 2114–2129.
- [26] M.A. Baldo, M.E. Thompson, S.R. Forrest, High-efficiency fluorescent organic light-emitting devices using a phosphorescent sensitizer, *Nature*. 403 (2000) 750–753.
- [27] K. Schmidt, S. Brovelli, V. Coropceanu, D. Beljonne, J. Cornil, C. Bazzini, T. Caronna, R. Tubino, F. Meinardi, Z. Shuai, J.L. Brédas, Intersystem crossing processes in nonplanar aromatic heterocyclic molecules, *J. Phys. Chem. A*. 111 (2007) 10490–10499.
- [28] S. Hirata, Recent Advances in Materials with Room-Temperature Phosphorescence: Photophysics for Triplet Exciton Stabilization, *Adv. Opt. Mater.* 5 (2017) 1–50.
- [29] M.A. Baldo, D. O'brien, Y. You, A. Shoustikov, Highly efficient phosphorescent

- emission from organic electroluminescent devices, *Nature*. 395 (1998) 151–154.
- [30] M. Thompson, The Evolution of Organometallic Complexes in Organic Light-Emitting Devices, *MRS Bull.* 32 (2007) 694–701.
- [31] D. Di, A.S. Romanov, L. Yang, J.M. Richter, J.P.H. Rivett, S. Jones, T.H. Thomas, M.A. Jalebi, R.H. Friend, M. Linnolahti, M. Bochmann, D. Credgington, High-performance light-emitting diodes based on carbene-metal-amides, *Science*. 163 (2017) 159–163.
- [32] M. Thompson, The Evolution of Organometallic Complexes in Organic Light-Emitting Devices, *MRS Bull.* 32 (2007) 694–701.
- [33] H. Uoyama, K. Goushi, K. Shizu, H. Nomura, C. Adachi, Highly efficient organic light-emitting diodes from delayed fluorescence., *Nature*. 492 (2012) 234–8.
- [34] B.L. Brand, B. Witholt, Fluorescence Measurements, *Methods Enzym.* 11 (n.d.) 776–856.
- [35] C. Baleizão, M.N. Berberan-Santos, External heavy-atom effect on the prompt and delayed fluorescence of [70]fullerenes, *ChemPhysChem*. 11 (2010) 3133–3140.
- [36] A. Endo, K. Sato, K. Yoshimura, T. Kai, A. Kawada, H. Miyazaki, C. Adachi, Efficient up-conversion of triplet excitons into a singlet state and its application for organic light emitting diodes, *Appl. Phys. Lett.* 98 (2011) 2009–2012.
- [37] Q. Zhang, H. Kuwabara, W.J. Potscavage, S. Huang, Y. Hatae, T. Shibata, C. Adachi, Anthraquinone-based intramolecular charge-transfer compounds: Computational molecular design, thermally activated delayed fluorescence, and highly efficient red electroluminescence, *J. Am. Chem. Soc.* 136 (2014) 18070–18081.
- [38] M.Y. Wong, E. Zysman-Colman, Purely Organic Thermally Activated Delayed Fluorescence Materials for Organic Light-Emitting Diodes, *Adv. Mater.* 29 (2017).

- [39] T. Huang, W. Jiang, L. Duan, Recent Progress in Solution Processable TADF Materials for Organic Light-Emitting Diodes, *J. Mater. Chem. C* 6 (2018) 5577–5596.
- [40] Z. Liu, M.F. Qayyum, C. Wu, M.T. Whited, P.I. Djurovich, K.O. Hodgson, B. Hedman, E.I. Solomon, M.E. Thompson, A codeposition route to CuI-pyridine coordination complexes for organic light-emitting diodes, *J. Am. Chem. Soc.* 133 (2011) 3700–3703.
- [41] Y. Gong, L. Zhao, Q. Peng, D. Fan, W.Z. Yuan, Y. Zhang, B.Z. Tang, Crystallization-induced dual emission from metal- and heavy atom-free aromatic acids and esters, *Chem. Sci.* 6 (2015) 4438–4444.
- [42] Y.M. Cheng, Y.S. Yeh, M.L. Ho, P.T. Chou, P.S. Chen, Y. Chi, Dual room-temperature fluorescent and phosphorescent emission in 8-quinolinolate osmium(II) carbonyl complexes: Rationalization and generalization of Intersystem crossing dynamics, *Inorg. Chem.* 44 (2005) 4594–4603.
- [43] W. Zhao, Z. He, J.W.Y. Lam, Q. Peng, H. Ma, Z. Shuai, G. Bai, J. Hao, B.Z. Tang, Rational Molecular Design for Achieving Persistent and Efficient Pure Organic Room-Temperature Phosphorescence, *Chem.* 1 (2016) 592–602.
- [44] Y. Su, S.Z.F. Phua, Y. Li, X. Zhou, D. Jana, G. Liu, W.Q. Lim, W.K. Ong, C. Yang, Y. Zhao, Ultralong room temperature phosphorescence from amorphous organic materials toward confidential information encryption and decryption, *Sci. Adv.* 4 (2018) 1–12.
- [45] Y. Liu, G. Zhan, Z.W. Liu, Z.Q. Bian, C.H. Huang, Room-temperature phosphorescence from purely organic materials, *Chinese Chem. Lett.* 27 (2016) 1231–1240.
- [46] O. Bolton, D. Lee, J. Jung, J. Kim, Tuning the photophysical properties of metal-free room temperature organic phosphors via compositional variations in bromobenzaldehyde/dibromobenzene mixed crystals, *Chem. Mater.* 26 (2014) 6644–6649.

- [47] Y. Tao, R. Chen, H. Li, J. Yuan, Y. Wan, H. Jiang, C. Chen, Y. Si, C. Zheng, B. Yang, G. Xing, W. Huang, Resonance-Activated Spin-Flipping for Efficient Organic Ultralong Room-Temperature Phosphorescence, *Adv. Mater.* 1803856 (2018) 1–8.
- [48] A. Segura-Carretero, C. Cruces-Blanco, B. Cañabate-Díaz, J.F. Fernández-Sánchez, A. Fernández-Gutiérrez, Heavy-atom induced room-temperature phosphorescence: A straightforward methodology for the determination of organic compounds in solution, *Anal. Chim. Acta.* 417 (2000) 19–30.
- [49] J. Xu, A. Takai, Y. Kobayashi, M. Takeuchi, Phosphorescence from a pure organic fluorene derivative in solution at room temperature, *Chem. Commun.* 49 (2013) 8447–8449.
- [50] S. Reineke, M.A. Baldo, Room temperature triplet state spectroscopy of organic semiconductors, *Sci. Rep.* 4 (2015) 3797.
- [51] C. Salas Redondo, P. Kleine, K. Roszeitis, T. Achenbach, M. Kroll, M. Thomschke, S. Reineke, Interplay of Fluorescence and Phosphorescence in Organic Biluminescent Emitters, *J. Phys. Chem. C.* 121 (2017) 14946–14953.
- [52] R. Kabe, C. Adachi, Organic long persistent luminescence, *Nature.* 550 (2017) 384–387.
- [53] Y. Xie, Y. Ge, Q. Peng, C. Li, Q. Li, Z. Li, How the Molecular Packing Affects the Room Temperature Phosphorescence in Pure Organic Compounds: Ingenious Molecular Design, Detailed Crystal Analysis, and Rational Theoretical Calculations, *Adv. Mater.* 29 (2017).
- [54] V. Gohri, S. Hofmann, S. Reineke, T. Rosenow, M. Thomschke, M. Levichkova, B. Lüssem, K. Leo, White top-emitting organic light-emitting diodes employing a heterostructure of down-conversion layers, *Org. Electron. Physics, Mater. Appl.* 12 (2011) 2126–2130.
- [55] J. Lee, N. Chopra, D. Bera, S. Maslov, S.H. Eom, Y. Zheng, P. Holloway, J. Xue, F. So, Down-conversion white organic light-emitting diodes using microcavity

- structure, *Adv. Energy Mater.* 1 (2011) 174–178.
- [56] D.L. Dexter, A theory of sensitized luminescence in solids, *J. Chem. Phys.* 21 (1953) 836–850.
- [57] S. Reineke, K. Walzer, K. Leo, Triplet-exciton quenching in organic phosphorescent light-emitting diodes with Ir-based emitters, *Phys. Rev. B - Condens. Matter Mater. Phys.* 75 (2007) 1–13.
- [58] S. Reineke, G. Schwartz, K. Walzer, K. Leo, Direct observation of host-guest triplet-triplet annihilation in phosphorescent solid mixed films, *Phys. Status Solidi - Rapid Res. Lett.* 3 (2009) 67–69.
- [59] D.Y. Kondakov, T.D. Pawlik, T.K. Hatwar, J.P. Spindler, Triplet annihilation exceeding spin statistical limit in highly efficient fluorescent organic light-emitting diodes, *J. Appl. Phys.* 106 (2009).
- [60] J. Lee, C. Jeong, T. Batagoda, C. Coburn, M.E. Thompson, S.R. Forrest, Hot excited state management for long-lived blue phosphorescent organic light-emitting diodes, *Nat. Commun.* 8 (2017) 1–9.
- [61] M. Furno, R. Meerheim, S. Hofmann, B. Lüssem, K. Leo, Efficiency and rate of spontaneous emission in organic electroluminescent devices, *Phys. Rev. B.* 85 (2012) 1–21.
- [62] S. Hofmann, T.C. Rosenow, M.C. Gather, B. Lüssem, K. Leo, Singlet exciton diffusion length in organic light-emitting diodes, *Phys. Rev. B - Condens. Matter Mater. Phys.* 85 (2012) 1–8.
- [63] K. Narushima, Y. Kiyota, T. Mori, S. Hirata, M. Vacha, Suppressed Triplet Exciton Diffusion Due to Small Orbital Overlap as a Key Design Factor for Ultralong-Lived Room-Temperature Phosphorescence in Molecular Crystals, *Adv. Mater.* (2019) 1807268.
- [64] H. Bässler, Charge Transport in Disordered Organic Photoconductors a Monte Carlo Simulation Study, *Phys. Status Solidi.* 175 (1993) 15–56.
- [65] M.A. Lampert, R.B. Schilling, *Current Injection in Solids: The Regional*

- Approximation Method, *Semicond. Semimetals*. 6 (1970) 1–96.
- [66] V. Coropceanu, J. Cornil, D. Silva, D. A. Y. Olivier, R. Silbey, J.L. Bredas, D.A. da Silva Filho, J.-L.J.-L. Brédas, Y. Olivier, R. Silbey, J.-L.J.-L. Brédas, Charge transport in organic semiconductors., *Chem. Rev.* 107 (2007) 926–52.
- [67] S. Tiwari, N.C. Greenham, Charge mobility measurement techniques in organic semiconductors, *Opt. Quantum Electron.* 41 (2009) 69–89.
- [68] A.P. Kulkarni, C.J. Tonzola, A. Babel, S.A. Jenekhe, Electron transport materials for organic light-emitting diodes, *Chem. Mater.* 16 (2004) 4556–4573.
- [69] S. Jhulki, J.N. Moorthy, Small Molecular Hole-Transporting Materials (HTMs) in Organic Light-Emitting Diodes (OLEDs): Structural Diversity and Classification, *J. Mater. Chem. C*. 6 (2018) 8280–8325.
- [70] D. Zhang, X. Song, H. Li, M. Cai, Z. Bin, T. Huang, L. Duan, High-Performance Fluorescent Organic Light-Emitting Diodes Utilizing an Asymmetric Anthracene Derivative as an Electron-Transporting Material, *Adv. Mater.* 1707590 (2018) 1–8.
- [71] B. Lüssem, C.M. Keum, D. Kasemann, B. Naab, Z. Bao, K. Leo, Doped Organic Transistors, *Chem. Rev.* 116 (2016) 13714–13751.
- [72] M. Schwarze, B.D. Naab, M.L. Tietze, R. Scholz, P. Pahner, F. Bussolotti, S. Kera, D. Kasemann, Z. Bao, K. Leo, Analyzing the n-Doping Mechanism of an Air-Stable Small-Molecule Precursor, *ACS Appl. Mater. Interfaces*. 10 (2018) 1340–1346.
- [73] C. Gaul, S. Hutsch, M. Schwarze, K.S. Schellhammer, F. Bussolotti, S. Kera, G. Cuniberti, K. Leo, F. Ortman, Insight into doping efficiency of organic semiconductors from the analysis of the density of states in n-doped C60 and ZnPc, *Nat. Mater.* 17 (2018).
- [74] M.L. Tietze, J. Benduhn, P. Pahner, B. Nell, M. Schwarze, H. Kleemann, M. Krammer, K. Zojer, K. Vandewal, K. Leo, Elementary steps in electrical doping of organic semiconductors, *Nat. Commun.* 9 (2018) 1–8.

- [75] J.M. Bharathan, Y. Yang, Polymer/metal interfaces and the performance of polymer light-emitting diodes, *J. Appl. Phys.* 84 (1998) 3207–3211.
- [76] R. Meerheim, B. Lüssem, K. Leo, Efficiency and Stability of p-i-n Type Organic Light Emitting Diodes for Display and Lighting Applications, *Proc. IEEE.* 97 (2009) 1606–1626.
- [77] B. Lüssem, M. Riede, K. Leo, Doping of organic semiconductors, *Phys. Status Solidi Appl. Mater. Sci.* 210 (2013) 9–43.
- [78] K. Walzer, B. Maennig, M. Pfeiffer, K. Leo, Highly efficient organic devices based on electrically doped transport layers, *Chem. Rev.* 107 (2007) 1233–1271.
- [79] Z. Wu, L. Yu, F. Zhao, X. Qiao, J. Chen, F. Ni, C. Yang, T. Ahamad, S.M. Alshehri, D. Ma, Precise Exciton Allocation for Highly Efficient White Organic Light-Emitting Diodes with Low Efficiency Roll-Off Based on Blue Thermally Activated Delayed Fluorescent Exciplex Emission, *Adv. Opt. Mater.* (2017) 1700415.
- [80] D. Yokoyama, Molecular orientation in small-molecule organic light-emitting diodes, *J. Mater. Chem.* 21 (2011) 19187.
- [81] T.D. Schmidt, T. Lampe, M.R. Daniel Sylvinson, P.I. Djurovich, M.E. Thompson, W. Brütting, Emitter Orientation as a Key Parameter in Organic Light-Emitting Diodes, *Phys. Rev. Appl.* 8 (2017) 1–28.
- [82] A. Fischer, P. Pahnner, B. Luessem, K. Leo, R. Scholz, T. Koprucki, K. Gaertner, A. Glitzky, Self-heating, bistability, and thermal switching in organic semiconductors, *Phys. Rev. Lett.* 110 (2013) 1–5.
- [83] A. Fischer, T. Koprucki, K. Gaertner, M.L. Tietze, J. Brueckner, B. Luessem, K. Leo, A. Glitzky, R. Scholz, Feel the heat: Nonlinear electrothermal feedback in organic LEDs, *Adv. Funct. Mater.* 24 (2014) 3367–3374.
- [84] Y. Qiu, L.W. Antony, J.J. De Pablo, M.D. Ediger, Photostability Can Be Significantly Modulated by Molecular Packing in Glasses, *J. Am. Chem. Soc.* 138 (2016) 11282–11289.

- [85] Y. Esaki, T. Komino, T. Matsushima, C. Adachi, Enhanced Electrical Properties and Air Stability of Amorphous Organic Thin Films by Engineering Film Density, *J. Phys. Chem. Lett.* 8 (2017) 5891–5897.
- [86] J. Ràfols-Ribé, P.A. Will, C. Hänisch, M. Gonzalez-Silveira, S. Lenk, J. Rodríguez-Viejo, S. Reineke, High-performance organic light-emitting diodes comprising ultrastable glass layers, *Sci. Adv.* 4 (2018) 1–10.
- [87] M. Pope, H.P. Kallmann, P. Magnante, Electroluminescence in organic crystals, *J. Chem. Phys.* 38 (1963) 2042–2043.
- [88] S. Reineke, M. Thomschke, B. Lüssem, K. Leo, White organic light-emitting diodes: Status and perspective, *Rev. Mod. Phys.* 85 (2013) 1245–1293.
- [89] I.N. Kholmanov, S.H. Domingues, H. Chou, X. Wang, C. Tan, J.Y. Kim, H. Li, R. Piner, A.J.G. Zarbin, R.S. Ruoff, Reduced graphene oxide/copper nanowire hybrid films as high-performance transparent electrodes, *ACS Nano.* 7 (2013) 1811–1816.
- [90] W. Gaynor, S. Hofmann, M.G. Christoforo, C. Sachse, S. Mehra, A. Salleo, M.D. McGehee, M.C. Gather, B. Lüssem, L. Müller-Meskamp, P. Peumans, K. Leo, Color in the corners: ITO-free white OLEDs with angular color stability, *Adv. Mater.* 25 (2013) 4006–4013.
- [91] S. Kee, N. Kim, B. Park, B.S. Kim, S. Hong, J.H. Lee, S. Jeong, A. Kim, S.Y. Jang, K. Lee, Highly Deformable and See-Through Polymer Light-Emitting Diodes with All-Conducting-Polymer Electrodes, *Adv. Mater.* 30 (2018) 1–7.
- [92] N. Li, S. Oida, G.S. Tulevski, S.-J. Han, J.B. Hannon, D.K. Sadana, T.-C. Chen, Efficient and bright organic light-emitting diodes on single-layer graphene electrodes., *Nat. Commun.* 4 (2013) 2294.
- [93] D.L. Mathine, H.S. Woo, W. He, T.W. Kim, B. Kippelen, N. Peyghambarian, Heterogeneously integrated organic light-emitting diodes with complementary metal–oxide–silicon circuitry, *Appl. Phys. Lett.* 76 (2000) 3849–3851.
- [94] Y. Kajiyama, K. Joseph, K. Kajiyama, S. Kudo, H. Aziz, Small feature sizes and

- high aperture ratio organic light-emitting diodes by using laser-patterned polyimide shadow masks, *Appl. Phys. Lett.* 104 (2014) 53303.
- [95] J. Zou, K. Zhang, J. Li, Y. Zhao, Y. Wang, S.K.R. Pillai, H. Volkan Demir, X. Sun, M.B. Chan-Park, Q. Zhang, Carbon Nanotube Driver Circuit for 6×6 Organic Light Emitting Diode Display, *Sci. Rep.* 5 (2015) 11755.
- [96] S. Hofmann, M. Thomschke, P. Freitag, M. Furno, B. Lüssem, K. Leo, Top-emitting organic light-emitting diodes: Influence of cavity design, *Appl. Phys. Lett.* 97 (2010) 2008–2011.
- [97] S. Hofmann, M. Thomschke, K. Leo, Top-emitting organic light-emitting diodes, *Opt. Express.* 19 (2011) 1143–1147.
- [98] X.-D. Zhao, Y.-Q. Li, H.-Y. Xiang, Y.-B. Zhang, J.-D. Chen, L.-H. Xu, J.-X. Tang, Efficient Color-Stable Inverted White Organic Light-Emitting Diodes with Outcoupling-Enhanced ZnO Layer, *ACS Appl. Mater. Interfaces.* 9 (2017) 2767–2775.
- [99] M. Thomschke, S. Hofmann, S. Olthof, M. Anderson, H. Kleemann, M. Schober, B. Lüssem, K. Leo, Improvement of voltage and charge balance in inverted top-emitting organic electroluminescent diodes comprising doped transport layers by thermal annealing, *Appl. Phys. Lett.* 98 (2011) 2011–2014.
- [100] L.S. Liao, K.P. Klubek, C.W. Tang, High-efficiency tandem organic light-emitting diodes, *Appl. Phys. Lett.* 84 (2004) 167–169.
- [101] M. Fung, Y. Li, L. Liao, Tandem Organic Light-Emitting Diodes, *Adv. Mater.* 28 (2016) 10381–10408.
- [102] F. Guo, D. Ma, White organic light-emitting diodes based on tandem structures, *Appl. Phys. Lett.* 87 (2005) 1–3.
- [103] T.C. Rosenow, M. Furno, S. Reineke, S. Olthof, B. Lüssem, K. Leo, Highly efficient white organic light-emitting diodes based on fluorescent blue emitters, *J. Appl. Phys.* 108 (2010) 1–6.
- [104] Z. Zhang, K. Guo, Y. Li, X. Li, G. Guan, H. Li, Y. Luo, F. Zhao, Q. Zhang, B.

- Wei, Q. Pei, H. Peng, A colour-tunable, weavable fibre-shaped polymer light-emitting electrochemical cell, *Nat. Photonics*. 9 (2015) 233–238.
- [105] L. Derue, S. Olivier, D. Tondelier, T. Maindron, B. Geffroy, E. Ishow, All-Solution-Processed Organic Light-Emitting Diodes Based on Photostable Photocross-linkable Fluorescent Small Molecules, *ACS Appl. Mater. Interfaces*. 8 (2016) 16207–16217.
- [106] T. Chiba, Y.-J. Pu, J. Kido, Solution-Processed White Phosphorescent Tandem Organic Light-Emitting Devices, *Adv. Mater.* 27 (2015) 4681–4687.
- [107] M. Godumala, S. Choi, H.J. Kim, C. Lee, S. Park, J.S. Moon, K. Si Woo, J.H. Kwon, M.J. Cho, D.H. Choi, Novel dendritic large molecules as solution-processable thermally activated delayed fluorescent emitters for simple structured non-doped organic light emitting diodes, *J. Mater. Chem. C*. 6 (2018) 1160–1170.
- [108] J. Song, J. Li, J. Xu, H. Zeng, Superstable Transparent Conductive Cu@Cu₄Ni Nanowire Elastomer Composites against Oxidation, Bending, Stretching, and Twisting for Flexible and Stretchable Optoelectronics., *Nano Lett.* 14 (2014) 6298–305.
- [109] NTSC, (n.d.). <https://en.wikipedia.org/wiki/NTSC> (accessed March 26, 2019).
- [110] F. Fries, M. Fröbel, P.Y. Ang, S. Lenk, S. Reineke, Real-time beam-shaping without additional optical elements, *Light Sci. Appl.* (2017) 18.
- [111] S. Reineke, Controlling Excitons : Concepts for Phosphorescent Organic LEDs at High Brightness Sebastian Reineke, 2009.
- [112] L.-S. Cui, S.-B. Ruan, F. Bencheikh, R. Nagata, L. Zhang, K. Inada, H. Nakanotani, L.-S. Liao, C. Adachi, Long-lived efficient delayed fluorescence organic light-emitting diodes using n-type hosts, *Nat. Commun.* 8 (2017) 2250.
- [113] Y. Wang, Y. Zhu, G. Xie, H. Zhan, C. Yang, Y. Cheng, Bright white electroluminescence from a single polymer containing a thermally activated delayed fluorescence unit and a solution-processed orange OLED approaching

- 20% external quantum efficiency, *J. Mater. Chem. C.* 5 (2017) 10715–10720.
- [114] C.-Y. Chan, L.-S. Cui, J.U. Kim, H. Nakanotani, C. Adachi, Rational Molecular Design for Deep-Blue Thermally Activated Delayed Fluorescence Emitters, *Adv. Funct. Mater.* (2018) 1706023.
- [115] H. Choukri, A. Fischer, S. Forget, S. Chnais, M.C. Castex, D. Ads, A. Siove, B. Geffroy, White organic light-emitting diodes with fine chromaticity tuning via ultrathin layer position shifting, *Appl. Phys. Lett.* 89 (2006) 1–4.
- [116] Y. Duan, M. Mazzeo, V. Maiorano, F. Mariano, D. Qin, R. Cingolani, G. Gigli, Extremely low voltage and high bright p-i-n fluorescent white organic light-emitting diodes, *Appl. Phys. Lett.* 92 (2008) 1–4.
- [117] C.H. Kim, J. Shinar, Bright small molecular white organic light-emitting devices with two emission zones, *Appl. Phys. Lett.* 80 (2002) 2201–2203.
- [118] Z.Y. Xie, J.S. Huang, C.N. Li, S.Y. Liu, Y. Wang, Y.Q. Li, J.C. Shen, White light emission induced by confinement in organic multiheterostructures, *Appl. Phys. Lett.* 74 (1999) 641–643.
- [119] Y.S. Huang, J.H. Jou, W.K. Weng, J.M. Liu, High-efficiency white organic light-emitting devices with dual doped structure, *Appl. Phys. Lett.* 80 (2002) 2782–2784.
- [120] C.H. Chuen, Y.T. Tao, Highly-bright white organic light-emitting diodes based on a single emission layer, *Appl. Phys. Lett.* 81 (2002) 4499–4501.
- [121] J.H. Jou, Y.S. Chiu, C.P. Wang, R.Y. Wang, H.C. Hu, Efficient, color-stable fluorescent white organic light-emitting diodes with single emission layer by vapor deposition from solvent premixed deposition source, *Appl. Phys. Lett.* 88 (2006) 2004–2007.
- [122] Y. Yang, T. Peng, K. Ye, Y. Wu, Y. Liu, Y. Wang, High-efficiency and high-quality white organic light-emitting diode employing fluorescent emitters, *Org. Electron. Physics, Mater. Appl.* 12 (2011) 29–33.
- [123] Y.C. Tsai, J.H. Jou, Long-lifetime, high-efficiency white organic light-emitting

- diodes with mixed host composing double emission layers, *Appl. Phys. Lett.* 89 (2006) 2004–2007.
- [124] L. Zong, Y. Xie, C. Wang, J.-R. Li, Q. Li, Z. Li, From ACQ to AIE: the suppression of the strong π - π interaction of naphthalene diimide derivatives through the adjustment of their flexible chains, *Chem. Commun.* 52 (2016) 11496–11499.
- [125] B. Liu, L. Wang, M. Xu, H. Tao, J. Zou, D. Gao, L. Lan, H. Ning, J. Peng, Y. Cao, Efficient hybrid white organic light-emitting diodes with extremely long lifetime: the effect of n-type interlayer., *Sci. Rep.* 4 (2014) 7198.
- [126] T. Higuchi, H. Nakanotani, C. Adachi, High-Efficiency White Organic Light-Emitting Diodes Based on a Blue Thermally Activated Delayed Fluorescent Emitter Combined with Green and Red Fluorescent Emitters, *Adv. Mater.* 27 (2015) 2019–2023.
- [127] Z. Wu, D. Ma, Recent advances in white organic light-emitting diodes, *Mater. Sci. Eng. R Reports.* 107 (2016) 1–42.
- [128] Z. Wu, J. Luo, N. Sun, L. Zhu, H. Sun, L. Yu, D. Yang, X. Qiao, J. Chen, C. Yang, D. Ma, High-Performance Hybrid White Organic Light-Emitting Diodes with Superior Efficiency/Color Rendering Index/Color Stability and Low Efficiency Roll-Off Based on a Blue Thermally Activated Delayed Fluorescent Emitter, *Adv. Funct. Mater.* 26 (2016) 3306–3313.
- [129] D. Zhang, L. Duan, Y. Li, D. Zhang, Y. Qiu, Highly efficient and color-stable hybrid warm white organic light-emitting diodes using a blue material with thermally activated delayed fluorescence, *J. Mater. Chem. C.* 2 (2014) 8191–8197.
- [130] J. Zhao, X. Chen, Z. Yang, Z. Chi, Z. Yang, Y. Zhang, J. Xu, Z. Chi, M.P. Aldred, Highly-efficient fully non-doped white organic light-emitting diodes consisting entirely of thermally activated delayed fluorescence emitters, *J. Mater. Chem. C.* 6 (2018) 3226–3232.

- [131] D. Zhang, X. Cao, Q. Wu, M. Zhang, N. Sun, X. Zhang, Y. Tao, Purely organic materials for extremely simple all-TADF white OLEDs: A new carbazole/oxadiazole hybrid material as a dual-role non-doped light blue emitter and highly efficient orange host, *J. Mater. Chem. C* 6 (2018) 3675–3682.
- [132] S. Hofmann, M. Hummert, R. Scholz, R. Luschtinetz, C. Murawski, P.A. Will, S.I. Hintschich, J. Alex, V. Jankus, A.P. Monkman, B. Lüssem, K. Leo, M.C. Gather, Engineering blue fluorescent bulk emitters for OLEDs: Triplet harvesting by green phosphors, *Chem. Mater.* 26 (2014) 2414–2426.
- [133] G. Schwartz, M. Pfeiffer, S. Reineke, K. Walzer, K. Leo, Harvesting triplet excitons from fluorescent blue emitters in white organic light-emitting diodes, *Adv. Mater.* 19 (2007) 3672–3676.
- [134] G. Schwartz, S. Reineke, T.C. Rosenow, K. Walzer, K. Leo, Triplet Harvesting in Hybrid White Organic Light-Emitting Diodes, *Adv. Funct. Mater.* 19 (2009) 1319–1333.
- [135] L. Zhu, Y. Zhao, H. Zhang, J. Chen, D. Ma, Using an ultra-thin non-doped orange emission layer to realize high efficiency white organic light-emitting diodes with low efficiency roll-off, *J. Appl. Phys.* 115 (2014).
- [136] Y. Yin, J. Yu, H. Cao, L. Zhang, H. Sun, W. Xie, Efficient non-doped phosphorescent orange, blue and white organic light-emitting devices, *Sci. Rep.* 4 (2014).
- [137] Y. Zhao, J. Chen, D. Ma, Ultrathin nondoped emissive layers for efficient and simple monochrome and white organic light-emitting diodes, *ACS Appl. Mater. Interfaces.* 5 (2013) 965–971.
- [138] R. Sheng, L. Zuo, K. Xue, Y. Duan, P. Chen, G. Cheng, Y. Zhao, Efficient white phosphorescent organic light-emitting diodes consisting of orange ultrathin and blue mixed host emission layers, *J. Phys. D: Appl. Phys.* 49 (2016).
- [139] J.Y. Lee, Mixed-host-emitting layer for high-efficiency organic light-emitting diodes, *J. Inf. Disp.* 15 (2014) 139–144.

- [140] Q. Fu, J. Chen, C. Shi, D. Ma, Solution-processed small molecules as mixed host for highly efficient blue and white phosphorescent organic light-emitting diodes, *ACS Appl. Mater. Interfaces*. 4 (2012) 6579–6586.
- [141] C.-C. Lin, M.-J. Huang, M.-J. Chiu, M.-P. Huang, C.-C. Chang, C.-Y. Liao, K.-M. Chiang, Y.-J. Shiau, T.-Y. Chou, L.-K. Chu, H.-W. Lin, C.-H. Cheng, Molecular Design of Highly Efficient Thermally Activated Delayed Fluorescence Hosts for Blue Phosphorescent and Fluorescent Organic Light-Emitting Diodes, *Chem. Mater.* 29 (2017) 1527–1537.
- [142] J.S. Kim, P.K.H. Ho, N.C. Greenham, R.H. Friend, Electroluminescence emission pattern of organic light-emitting diodes: Implications for device efficiency calculations, *J. Appl. Phys.* 88 (2000) 1073–1081.
- [143] R.H. Ritchie, Plasma Losses by Fast Electrons in Thin Films, *Phys. Rev.* 106 (1957) 874–881.
- [144] C.J. Powell, J.B. Swan, Effect of Oxidation on the Characteristic Loss Spectra of Aluminum and Magnesium, *Phys. Rev.* 118 (1960) 640–643.
- [145] H. Raether, Surface plasmons on smooth and rough surfaces and on gratings, Springer-Verlag, New York. (1988) 136.
- [146] P.B. Johnson, R.W. Christy, Optical constants of the noble metals, *Phys. Rev. B.* 6 (1972) 4370–4379.
- [147] X.C. Ma, Y. Dai, L. Yu, B.B. Huang, Energy transfer in plasmonic photocatalytic composites, *Light Sci. Appl.* 5 (2016) e16017.
- [148] X.T. Geng, B.J. Chun, J.H. Seo, K. Seo, H. Yoon, D.E. Kim, Y.J. Kim, S. Kim, Frequency comb transferred by surface plasmon resonance, *Nat. Commun.* 7 (2016) 1–7.
- [149] R. Sundararaman, P. Narang, A.S. Jermyn, W.A. Goddard, H.A. Atwater, Theoretical predictions for hot-carrier generation from surface plasmon decay, *Nat. Commun.* 5 (2014) 1–8.
- [150] X. Dai, A. Messanvi, H. Zhang, C. Durand, J. Eymery, C. Bougerol, F.H. Julien,

- M. Tchernycheva, Flexible Light-Emitting Diodes Based on Vertical Nitride Nanowires, *Nano Lett.* 15 (2015) 6958–6964.
- [151] P. Will, E.B. Schwarz, C. Fuchs, R. Scholz, S. Lenk, S. Reineke, Scattering quantified: Evaluation of corrugation induced outcoupling concepts in organic light-emitting diodes, *Org. Electron.* 58 (2018) 250–256.
- [152] S. Reineke, F. Lindner, G. Schwartz, N. Seidler, K. Walzer, B. Lussem, K. Leo, White organic light-emitting diodes with fluorescent tube efficiency, *Nature.* 459 (2009) 234–238.
- [153] S. Möller, S.R. Forrest, Improved light out-coupling in organic light emitting diodes employing ordered microlens arrays, *J. Appl. Phys.* 91 (2002) 3324–3327.
- [154] Y. Sun, S.R. Forrest, Organic light emitting devices with enhanced outcoupling via microlenses fabricated by imprint lithography, *J. Appl. Phys.* 100 (2006) 1–7.
- [155] M. Kovačič, P.-A. Will, B. Lipovsek, M. Topič, S. Lenk, S. Reineke, J. Krč, Coupled optical modelling for optimization of organic light-emitting diodes with external outcoupling structures, *ACS Photonics.* 5 (2017) 422–430.
- [156] J.W. Shin, D.H. Cho, J. Moon, C.W. Joo, S.K. Park, J. Lee, J.H. Han, N.S. Cho, J. Hwang, J.W. Huh, H.Y. Chu, J.I. Lee, Random nano-structures as light extraction functionals for organic light-emitting diode applications, *Org. Electron. Physics, Mater. Appl.* 15 (2014) 196–202.
- [157] Y.C. Leem, J.S. Park, J.H. Kim, N.S. Myoung, S.Y. Yim, S. Jeong, W. Lim, S.T. Kim, S.J. Park, Light-Emitting Diodes with Hierarchical and Multifunctional Surface Structures for High Light Extraction and an Antifouling Effect, *Small.* 12 (2016) 161–168.
- [158] J.-J. Kim, J. Lee, S.-P. Yang, H.G. Kim, H.-S. Kweon, S. Yoo, K.-H. Jeong, Biologically Inspired Organic Light-Emitting Diodes, *Nano Lett.* 16 (2016) 2994–3000.
- [159] J. Moon, E. Kim, S. Koo, K. Lee, J. Shin, D. Cho, J. Lee, C. Woong, N. Sung, J.

- Han, B. Yu, S. Yoo, J. Lee, Organic wrinkles for energy efficient organic light emitting diodes, *Org. Electron.* 26 (2015) 273–278.
- [160] I. Lee, J.Y. Park, S. Gim, J. Ham, J.H. Son, J.-L. Lee, Spontaneously Formed Nanopatterns on Polymer Films for Flexible Organic Light-Emitting Diodes, *Small.* 11 (2015) 4480–4484.
- [161] Y.-S. Park, K.-H. Han, J. Kim, D.-H. Cho, J. Lee, Y. Han, J.T. Lim, N.S. Cho, B. Yu, J.-I. Lee, J.-J. Kim, Crystallization-assisted nano-lens array fabrication for highly efficient and color stable organic light emitting diodes, *Nanoscale.* 9 (2017) 230–236.
- [162] S. Chen, H.S. Kwok, Light extraction from organic light-emitting diodes for lighting applications by sand-blasting substrates., *Opt. Express.* 18 (2010) 37–42.
- [163] C. Bohren, D. Huffman, Absorption and Scattering of Light by Small Particles
Absorption and Scattering of Light by Small Particles, John Wiley & Sons: New York, 1983.
- [164] J. Shen, F. Li, Z. Cao, D. Barat, G. Tu, Light Scattering in Nanoparticle Doped Transparent Polyimide Substrates, *ACS Appl. Mater. Interfaces.* 9 (2017) 14990–14997.
- [165] T.W. Koh, J.A. Spechler, K.M. Lee, C.B. Arnold, B.P. Rand, Enhanced Outcoupling in Organic Light-Emitting Diodes via a High-Index Contrast Scattering Layer, *ACS Photonics.* 2 (2015) 1366–1372.
- [166] Y.-W. Lim, O. Eun Kwon, S.-M. Kang, H. Cho, J. Lee, Y.-S. Park, N. Sung Cho, W.-Y. Jin, J. Lee, H. Lee, J.-W. Kang, S. Yoo, J. Moon, B.-S. Bae, Y. Lim, S. Kang, H. Lee, B. Bae, O.E. Kwon, H. Cho, J. Lee, Y. Park, N.S. Cho, J. Moon, W. Jin, J. Kang, S. Yoo, Built-In Haze Glass-Fabric Reinforced Siloxane Hybrid Film for Efficient Organic Light-Emitting Diodes (OLEDs), *Adv. Funct. Mater.* (2018) 1802944.
- [167] S. Jeon, S. Lee, K.-H. Han, H. Shin, K.-H. Kim, J.-H. Jeong, J.-J. Kim, High-

- Quality White OLEDs with Comparable Efficiencies to LEDs, *Adv. Opt. Mater.* 17013491 (2018) 1–8.
- [168] T.C. Rosenow, M. Furno, S. Reineke, S. Olthof, B. Lüssem, K. Leo, Highly efficient white organic light-emitting diodes based on fluorescent blue emitters, *J. Appl. Phys.* 108 (2010).
- [169] K. Tong, X. Liu, F. Zhao, D. Chen, Q. Pei, Efficient Light Extraction of Organic Light-Emitting Diodes on a Fully Solution-Processed Flexible Substrate, *Adv. Opt. Mater.* (2017) 1700307.
- [170] W.H. Koo, S.M. Jeong, F. Araoka, K. Ishikawa, S. Nishimura, T. Toyooka, H. Takezoe, Light extraction from organic light-emitting diodes enhanced by spontaneously formed buckles, *Nat. Photonics.* 4 (2010) 222–226.
- [171] Y.R. Do, Y.C. Kim, Y.-W. Song, C.-O. Cho, H. Jeon, Y.-J. Lee, S.-H. Kim, Y.-H. Lee, Enhanced Light Extraction from Organic Light-Emitting Diodes with 2D SiO₂/SiN_x Photonic Crystals, *Adv. Mater.* 15 (2003) 1214–1218.
- [172] C. Peng, S. Liu, X. Fu, Z. Pan, Y. Chen, F. So, K.S. Schanze, Corrugated Organic Light Emitting Diodes Using Low T_g Electron Transporting Materials, *ACS Appl. Mater. Interfaces.* 8 (2016) 16192–16199.
- [173] C. Fuchs, T. Schwab, T. Roch, S. Eckardt, A. Lasagni, S. Hofmann, B. Lüssem, L. Müller-Meskamp, K. Leo, M.C. Gather, R. Scholz, Quantitative allocation of Bragg scattering effects in highly efficient OLEDs fabricated on periodically corrugated substrates, *Opt. Express.* 21 (2013) 16319.
- [174] T. Schwab, C. Fuchs, R. Scholz, A. Zakhidov, K. Leo, M.C. Gather, Coherent mode coupling in highly efficient top-emitting OLEDs on periodically corrugated substrates, *Opt. Express.* 22 (2014) 7524.
- [175] Y. Qu, M. Slocsky, S.R. Forrest, Enhanced light extraction from organic light-emitting devices using a sub-anode grid, *Nat. Photonics.* 9 (2015) 758–763.
- [176] Y. Qu, J. Kim, C. Coburn, S.R. Forrest, Efficient, Non-Intrusive Outcoupling in Organic Light Emitting Devices Using Embedded Microlens Arrays, *ACS*

- Photonics. 5 (2018) 2453–2458.
- [177] J.B. Preinfalk, T. Eiselt, T. Wehlius, V. Rohnacher, T. Hanemann, G. Gomard, U. Lemmer, Large-Area Screen-Printed Internal Extraction Layers for Organic Light-Emitting Diodes, *ACS Photonics*. 4 (2017) 928–933.
- [178] C. Fuchs, P.-A. Will, M. Wiczorek, M.C. Gather, S. Hofmann, S. Reineke, K. Leo, R. Scholz, Enhanced light emission from top-emitting organic light-emitting diodes by optimizing surface plasmon polariton losses, *Phys. Rev. B*. 245306 (2015) 11.
- [179] A. Salehi, S. Ho, Y. Chen, C. Peng, H. Yersin, F. So, Highly Efficient Organic Light-Emitting Diode Using A Low Refractive Index Electron Transport Layer, *Adv. Opt. Mater.* 5 (2017) 1–7.
- [180] C.-Y. Chen, W.-K. Lee, Y.-J. Chen, C.-Y. Lu, H.Y. Lin, C.-C. Wu, Enhancing Optical Out-Coupling of Organic Light-Emitting Devices with Nanostructured Composite Electrodes Consisting of Indium Tin Oxide Nanomesh and Conducting Polymer, *Adv. Mater.* 27 (2015) 4883–4888.
- [181] E. Kim, H. Cho, K. Kim, T.-W. Koh, J. Chung, J. Lee, Y. Park, S. Yoo, A Facile Route to Efficient, Low-Cost Flexible Organic Light-Emitting Diodes: Utilizing the High Refractive Index and Built-In Scattering Properties of Industrial-Grade PEN Substrates, *Adv. Mater.* 27 (2015) 1624–1631.
- [182] M. Thomschke, S. Reineke, B. Lüssem, K. Leo, Highly efficient white top-emitting organic light-emitting diodes comprising laminated microlens films, *Nano Lett.* 12 (2012) 424–428.
- [183] Y. Qu, C. Coburn, D. Fan, S.R. Forrest, Elimination of Plasmon Losses and Enhanced Light Extraction of Top-Emitting Organic Light-Emitting Devices Using a Reflective Subelectrode Grid, *ACS Photonics*. 4 (2017) 363–368.
- [184] A. Graf, P. Liehm, C. Murawski, S. Hofmann, K. Leo, M.C. Gather, Correlating the transition dipole moment orientation of phosphorescent emitter molecules in OLEDs with basic material properties, *J. Mater. Chem. C*. 2 (2014) 10298–10304.

- [185] T.D. Schmidt, D.S. Setz, M. Flämmich, J. Frischeisen, D. Michaelis, B.C. Krummacher, N. Danz, W. Brütting, Evidence for non-isotropic emitter orientation in a red phosphorescent organic light-emitting diode and its implications for determining the emitter's radiative quantum efficiency, *Appl. Phys. Lett.* 99 (2011) 2012–2015.
- [186] D.G. Deppe, C. Lei, C.C. Lin, D.L. Huffaker, Spontaneous emission from planar microstructures, *J. Mod. Opt.* 41 (1994) 325–344.
- [187] Y. Li, Z. Tang, C. Hänisch, P.-A. Will, M. Kovačič, J.-L. Hou, R. Scholz, K. Leo, S. Lenk, S. Reineke, Ultrathin MoO₃ Layers in Composite Metal Electrodes: Improved Optics Allow Highly Efficient Organic Light-Emitting Diodes, *Adv. Opt. Mater.* (2018) 1801262.
- [188] R. Meerheim, R. Nitsche, K. Leo, High-efficiency monochrome organic light emitting diodes employing enhanced microcavities, *Appl. Phys. Lett.* 93 (2008) 10–13.
- [189] C. Murawski, P. Liehm, K. Leo, M.C. Gather, Influence of cavity thickness and emitter orientation on the efficiency roll-off of phosphorescent organic light-emitting diodes, *Adv. Funct. Mater.* 24 (2014) 1117–1124.
- [190] A. Pimpin, W. Srituravanich, Reviews on micro- and nanolithography techniques and their applications, *Eng. J.* 16 (2012) 37–55.
- [191] Y. Li, T. Shi, X. Gao, G. Tu, The fabrication of nanostructures with a large range of dimensions and the potential application for light outcoupling in organic light-emitting diodes, *J. Micromechanics Microengineering.* 29 (2018) 035007.
- [192] L. Muller-Meskamp, S. Schubert, T. Roch, S. Eckhardt, A.F. Lasagni, K. Leo, Transparent Conductive Metal Thin-Film Electrodes Structured by Direct Laser Interference Patterning, *Adv. Eng. Mater.* 17 (2015) 1215–1219.
- [193] Y. Jin, J. Feng, X.L. Zhang, Y.G. Bi, Y. Bai, L. Chen, T. Lan, Y.F. Liu, Q.D. Chen, H.B. Sun, Solving efficiency-stability tradeoff in top-emitting organic light-emitting devices by employing periodically corrugated metallic cathode, *Adv.*

- Mater. 24 (2012) 1187–1191.
- [194] Y. Xia, G.M. Whitesides, Soft Lithography, *Angew. Chemie - Int. Ed.* 37 (1998) 550–575.
- [195] X.-B. Shi, M. Qian, Z.-K. Wang, L.-S. Liao, Nano-honeycomb structured transparent electrode for enhanced light extraction from organic light-emitting diodes, *Appl. Phys. Lett.* 106 (2015) 223301.
- [196] N. Stoop, R. Lagrange, D. Terwagne, P.M. Reis, J. Dunkel, Curvature-induced symmetry breaking determines elastic surface patterns., *Nat. Mater.* 14 (2015) 337–42.
- [197] J.Y. Chung, A.J. Nolte, C.M. Stafford, Surface wrinkling: A versatile platform for measuring thin-film properties, *Adv. Mater.* 23 (2011) 349–368.
- [198] E.P. Chan, A.J. Crosby, Fabricating microlens arrays by surface wrinkling, *Adv. Mater.* 18 (2006) 3238–3242.
- [199] R. Seghir, S. Arscott, Controlled mud-crack patterning and self-organized cracking of polydimethylsiloxane elastomer surfaces, *Sci. Rep.* 5 (2015) 14787.
- [200] N. Iguñiz, R. Frisenda, R. Bratschitsch, A. Castellanos-gomez, Revisiting the Buckling Metrology Method to Determine the Young's Modulus of 2D Materials, *Adv. Mater.* (2019) 1807150.
- [201] F. Li, H. Hou, J. Yin, X. Jiang, Near-infrared light-responsive dynamic wrinkle patterns, *Sci. Adv.* 4 (2018) eaar5762.
- [202] H. Hou, J. Yin, X. Jiang, Reversible Diels-Alder Reaction To Control Wrinkle Patterns: From Dynamic Chemistry to Dynamic Patterns, *Adv. Mater.* (2016). doi:10.1002/adma.201602105.
- [203] N. Bowden, S. Brittain, A. Evans, Spontaneous formation of ordered structures in thin films of metals supported on an elastomeric polymer, *Nature.* 393 (1998) 146–149.
- [204] D.B.H. Chua, H.T. Ng, S.F.Y. Li, Spontaneous formation of complex and ordered structures on oxygen-plasma-treated elastomeric polydimethylsiloxane, *Appl.*

- Phys. Lett. 76 (2000) 721.
- [205] COMSOL Multiphysics® Modeling Software, (n.d.). <https://www.comsol.com/> (accessed August 27, 2018).
- [206] J.C. de Mello, H.F. Wittmann, R.H. Friend, An Improved Experimental Determination of External Photoluminescence Quantum Efficiency, *Adv. Mater.* 9 (1997) 230–232.
- [207] S. Schubert, J. Meiss, L. Müller-Meskamp, K. Leo, Improvement of transparent metal top electrodes for organic solar cells by introducing a high surface energy seed layer, *Adv. Energy Mater.* 3 (2013) 438–443.
- [208] T. Schwab, S. Schubert, S. Hofmann, M. Fröbel, C. Fuchs, M. Thomschke, L. Müller-Meskamp, K. Leo, M.C. Gather, Highly Efficient Color Stable Inverted White Top-Emitting OLEDs with Ultra-Thin Wetting Layer Top Electrodes, *Adv. Opt. Mater.* 1 (2013) 707–713.
- [209] T. Schwab, S. Schubert, L. Müller-Meskamp, K. Leo, M.C. Gather, Eliminating Micro-Cavity Effects in White Top-Emitting OLEDs by Ultra-Thin Metallic Top Electrodes, *Adv. Opt. Mater.* 1 (2013) 921–925.
- [210] S. Lenk, T. Schwab, S. Schubert, L. Müller-Meskamp, K. Leo, M.C. Gather, S. Reineke, White organic light-emitting diodes with 4 nm metal electrode, *Appl. Phys. Lett.* 107 (2015) 163302.
- [211] Y.H. Kim, J. Lee, W.M. Kim, C. Fuchs, S. Hofmann, H.W. Chang, M.C. Gather, L. Müller-Meskamp, K. Leo, We want our photons back: Simple nanostructures for white organic light-emitting diode outcoupling, *Adv. Funct. Mater.* 24 (2014) 2553–2559.
- [212] I. Hancox, K. V. Chauhan, P. Sullivan, R.A. Hatton, A. Moshar, C.P.A. Mulcahy, T.S. Jones, Increased efficiency of small molecule photovoltaic cells by insertion of a MoO₃ hole-extracting layer, *Energy Environ. Sci.* 3 (2010) 107–110.
- [213] W.L. Barnes, A. Dereux, T.W. Ebbesen, Surface plasmon subwavelength optics, *Nature.* 424 (2003) 824–30.

- [214] S. Kim, J.-L. Lee, Design of dielectric/metal/dielectric transparent electrodes for flexible electronics, *J. Photonics Energy*. 2 (2012) 021215.
- [215] K. Hong, J.H. Son, S. Kim, B.H. Koo, J.-L. Lee, Design rules for highly transparent electrodes using dielectric constant matching of metal oxide with Ag film in optoelectronic devices, *Chem. Commun.* 48 (2012) 10606.
- [216] P. Andrew, W.L. Barnes, Energy transfer across a metal film mediated by surface plasmon polaritons., *Science*. 306 (2004) 1002–1005.
- [217] M.J. Jurow, C. Mayr, T.D. Schmidt, T. Lampe, P.I. Djurovich, W. Brütting, M.E. Thompson, Understanding and predicting the orientation of heteroleptic phosphors in organic light-emitting materials, *Nat. Mater.* 15 (2016) 85–91.
- [218] T.D. Schmidt, D.S. Setz, M. Flämmich, J. Frischeisen, D. Michaelis, B.C. Krummacher, N. Danz, W. Brütting, Evidence for non-isotropic emitter orientation in a red phosphorescent organic light-emitting diode and its implications for determining the emitter's radiative quantum efficiency, *Appl. Phys. Lett.* 99 (2011) 1–4.
- [219] Q. Zhang, B. Li, S. Huang, H. Nomura, H. Tanaka, C. Adachi, Efficient blue organic light-emitting diodes employing thermally activated delayed fluorescence, *Nat. Photonics*. 8 (2014) 326–332.
- [220] H. Jiang, D.-Y. Khang, J. Song, Y. Sun, Y. Huang, J. a Rogers, Finite deformation mechanics in buckled thin films on compliant supports, *Proc. Natl. Acad. Sci.* 104 (2007) 15607–15612.
- [221] D.J. Schunter, M. Brandenbourger, S. Perriseau, D.P. Holmes, Elastogranular Mechanics: Buckling, Jamming, and Structure Formation, *Phys. Rev. Lett.* 120 (2018) 78002.
- [222] P. Kim, M. Abkarian, H. a. Stone, Hierarchical folding of elastic membranes under biaxial compressive stress, *Nat. Mater.* 10 (2011) 952–957.
- [223] M.R. Alexander, R.D. Short, F.R. Jones, M. Stollenwerk, J. Zabold, W. Michaeli, An X-ray photoelectron spectroscopic investigation into the chemical structure

- of deposits formed from hexamethyldisiloxane/ oxygen plasmas, *J. Mater. Sci.* 31 (1996) 1879–1885.
- [224] D.F. Mitchell, K.B. Clark, J.A. Bardwell, W.N. Lennard, G.R. Massoumi, I. V Mitchell, Film Thickness Measurements of SiO₂ by XPS, *Surf. Interface Anal.* 21 (1994) 44–50.
- [225] C. Logofatu, C.C. Negri, R. V Ghita, F. Ungureanu, C. Cotirlan, C.G.A.S.M. and M.F. Lazarescu, Study of SiO₂/Si Interface by Surface Techniques, 2011.
- [226] H.-G. Park, H.-C. Jeong, Y.H. Jung, D.-S. Seo, Control of the wrinkle structure on surface-reformed poly(dimethylsiloxane) via ion-beam bombardment., *Sci. Rep.* 5 (2015) 12356.
- [227] C. Lee, X. Wei, J.W. Kysar, J. Hone, Measurement of the Elastic Properties and Intrinsic Strength of Monolayer Graphene, *Science* (80-.). 321 (2008) 385–388.
- [228] G. Cao, X. Chen, C. Li, A. Ji, Z. Cao, Self-assembled triangular and labyrinth buckling patterns of thin films on spherical substrates, *Phys. Rev. Lett.* 100 (2008) 1–4.
- [229] Q. Wang, L. Zhang, X. Zhao, Creasing to cratering instability in polymers under ultrahigh electric fields, *Phys. Rev. Lett.* 106 (2011) 1–4.
- [230] J.B. Kim, P. Kim, N.C. Pégard, S.J. Oh, C.R. Kagan, J.W. Fleischer, H. a. Stone, Y.-L. Loo, Wrinkles and deep folds as photonic structures in photovoltaics, *Nat. Photonics.* 6 (2012) 327–332.
- [231] J.W. Coburn, H.F. Winters, Plasma etching—A discussion of mechanisms, *J. Vac. Sci. Technol.* 16 (1979) 391–403.
- [232] C. Zong, Y. Zhao, H. Ji, X. Han, J. Xie, J. Wang, Y. Cao, S. Jiang, C. Lu, Tuning and Erasing Surface Wrinkles by Reversible Visible-Light-Induced Photoisomerization, *Angew. Chemie - Int. Ed.* 55 (2016) 3931–3935.
- [233] R.L. Bruce, F. Weilnboeck, T. Lin, R.J. Phaneuf, G.S. Oehrlein, B.K. Long, C.G. Willson, J.J. Vegh, D. Nest, D.B. Graves, Relationship between nanoscale roughness and ion-damaged layer in argon plasma exposed polystyrene films, *J.*

- Appl. Phys. 107 (2010).
- [234] J. Lee, T.-H. Han, M.-H. Park, D.Y. Jung, J. Seo, H.-K. Seo, H. Cho, E. Kim, J. Chung, S.-Y. Choi, T.-S. Kim, T.-W. Lee, S. Yoo, Synergetic electrode architecture for efficient graphene-based flexible organic light-emitting diodes, *Nat. Commun.* 7 (2016) 11791.
- [235] M. Furno, T.C. Rosenow, M.C. Gather, B. Lüssem, K. Leo, Analysis of the external and internal quantum efficiency of multi-emitter, white organic light emitting diodes, *Appl. Phys. Lett.* 101 (2012).
- [236] S. Hofmann, M. Furno, B. Lüssem, K. Leo, M.C. Gather, Investigation of triplet harvesting and outcoupling efficiency in highly efficient two-color hybrid white organic light-emitting diodes, *Phys. Status Solidi Appl. Mater. Sci.* 210 (2013) 1467–1475.
- [237] J. Jin, *The Finite Element Method in Electromagnetics*, 3rd editio, John Wiley & Sons, Inc., 2014.
- [238] J. Song, K.H. Kim, E. Kim, C.K. Moon, Y.H. Kim, J.J. Kim, S. Yoo, Lensfree OLEDs with over 50% external quantum efficiency via external scattering and horizontally oriented emitters, *Nat. Commun.* 9 (2018).
- [239] M. Gulen, G. Yildirim, S. Bal, A. Varilci, I. Belenli, M. Oz, Role of annealing temperature on microstructural and electro-optical properties of ITO films produced by sputtering, *J. Mater. Sci. Mater. Electron.* 24 (2013) 467–474.
- [240] M. Fujita, T. Ueno, K. Ishihara, T. Asano, S. Noda, H. Ohata, T. Tsuji, H. Nakada, N. Shimoji, Reduction of operating voltage in organic light-emitting diode by corrugated photonic crystal structure, *Appl. Phys. Lett.* 85 (2004) 5769–5771.
- [241] Statistical Analysis, (n.d.). <http://gwyddion.net/documentation/user-guide-en/statistical-analysis.html> (accessed February 4, 2019).
- [242] Y. Cao, N. Wang, H. Tian, J. Guo, Y. Wei, H. Chen, Y. Miao, W. Zou, K. Pan, Y. He, H. Cao, Y. Ke, M. Xu, Y. Wang, M. Yang, K. Du, Z. Fu, D. Kong, D. Dai, Y. Jin, G. Li, H. Li, Q. Peng, J. Wang, W. Huang, Perovskite light-emitting diodes

- based on spontaneously formed submicrometre-scale structures, *Nature*. 562 (2018) 249–253.
- [243] Y. Sun, S.R. Forrest, Enhanced light out-coupling of organic light-emitting devices using embedded low-index grids, *Nat Phot.* 2 (2008) 483–487.
- [244] Q.-D. Ou, L. Zhou, Y.-Q. Li, S. Shen, J.-D. Chen, C. Li, Q.-K. Wang, S.-T. Lee, J.-X. Tang, Extremely Efficient White Organic Light-Emitting Diodes for General Lighting, *Adv. Funct. Mater.* 24 (2014) 7249–7256.
- [245] H.W. Chang, J. Lee, S. Hofmann, Y. Hyun Kim, L. Müller-Meskamp, B. Lüssem, C.C. Wu, K. Leo, M.C. Gather, Nano-particle based scattering layers for optical efficiency enhancement of organic light-emitting diodes and organic solar cells, *J. Appl. Phys.* 113 (2013).
- [246] L. Zhou, Q.-D. Ou, Y.-Q. Li, H.-Y. Xiang, L.-H. Xu, J.-D. Chen, C. Li, S. Shen, S.-T. Lee, J.-X. Tang, Efficiently Releasing the Trapped Energy Flow in White Organic Light-Emitting Diodes with Multifunctional Nanofunnel Arrays, 25 (2015) 2660–2668.
- [247] Y.H. Kim, J. Lee, W.M. Kim, C. Fuchs, S. Hofmann, H.-W. Chang, M.C. Gather, L. Müller-Meskamp, K. Leo, We Want Our Photons Back: Simple Nanostructures for White Organic Light-Emitting Diode Outcoupling, *Adv. Funct. Mater.* 24 (2014) 2553–2559.
- [248] D.-Y. Khang, J.A. Rogers, H.H. Lee, Mechanical Buckling: Mechanics, Metrology, and Stretchable Electronics, *Adv. Funct. Mater.* 19 (2009) 1526–1536.
- [249] S. Kim, H.J. Bae, S. Park, W. Kim, J. Kim, J.S. Kim, Y. Jung, S. Sul, S.-G. Ihn, C. Noh, S. Kim, Y. You, Degradation of blue-phosphorescent organic light-emitting devices involves exciton-induced generation of polaron pair within emitting layers, *Nat. Commun.* 9 (2018) 1211.
- [250] S. Scholz, D. Kondakov, B. Luesem, K. Leo, Degradation mechanisms and reactions in organic light-emitting devices, *Chem. Rev.* 115 (2015) 8449–8503.
- [251] X. Lin, Y. Zhu, B. Zhang, X. Zhao, B. Yao, Y. Cheng, Z. Li, Y. Qu, Z. Xie, Highly

- Efficient TADF Polymer Electroluminescence with Reduced Efficiency Roll-off via Interfacial Exciplex Host Strategy, *ACS Appl. Mater. Interfaces*. 10 (2018) 47–52.
- [252] Y. Li, G. Xie, S. Gong, K. Wu, C. Yang, Dendronized delayed fluorescence emitters for non-doped, solution-processed organic light-emitting diodes with high efficiency and low efficiency roll-off simultaneously: Two parallel emissive channels, *Chem. Sci.* 7 (2016) 5441–5447.
- [253] Q. Wei, Z. Ge, B. Voit, Thermally Activated Delayed Fluorescent Polymers: Structures, Properties, and Applications in OLED Devices, *Macromol. Rapid Commun.* 1800570 (2018) 1–19.
- [254] Q. Wei, P. Kleine, Y. Karpov, X. Qiu, H. Komber, K. Sahre, A. Kiriy, R. Lygaitis, S. Lenk, S. Reineke, B. Voit, Conjugation-Induced Thermally Activated Delayed Fluorescence (TADF): From Conventional Non-TADF Units to TADF-Active Polymers, *Adv. Funct. Mater.* 27 (2017) 1–11.
- [255] Y.J. Cho, K.S. Yook, J.Y. Lee, High efficiency in a solution-processed thermally activated delayed-fluorescence device using a delayed-fluorescence emitting material with improved solubility, *Adv. Mater.* (2014) 6642–6646.
- [256] K. Goushi, K. Yoshida, K. Sato, C. Adachi, Organic light-emitting diodes employing efficient reverse intersystem crossing for triplet-to-singlet state conversion, *Nat. Photonics*. 6 (2012) 253–258.
- [257] X.K. Liu, Z. Chen, J. Qing, W.J. Zhang, B. Wu, H.L. Tam, F. Zhu, X.H. Zhang, C.S. Lee, Remanagement of Singlet and Triplet Excitons in Single-Emissive-Layer Hybrid White Organic Light-Emitting Devices Using Thermally Activated Delayed Fluorescent Blue Exciplex, *Adv. Mater.* 27 (2015) 7079–7085.
- [258] S. Ullbrich, J. Benduhn, X. Jia, V.C. Nikolis, K. Tvingstedt, F. Piersimoni, S. Roland, Y. Liu, J. Wu, A. Fischer, D. Neher, S. Reineke, D. Spoltore, K. Vandewal, Emissive and charge-generating donor – acceptor interfaces for organic optoelectronics with low voltage losses, *Nat. Mater.* (2019) 1–6.

- [259] M. De Jong, L. Seijo, A. Meijerink, F.T. Rabouw, Resolving the ambiguity in the relation between Stokes shift and Huang-Rhys parameter, *Phys. Chem. Chem. Phys.* 17 (2015) 16959–16969.
- [260] P.H. Pander, S. Gogoc, M. Colella, P. Data, F.B. Dias, Thermally-Activated Delayed Fluorescence in Polymer-Small Molecule Exciplex Blends for Solution-Processed Organic Light-Emitting Diodes, *ACS Appl. Mater. Interfaces.* 10 (2018) 28796–28802.
- [261] K. Harada, M. Riede, K. Leo, O.R. Hild, C.M. Elliott, Pentacene homojunctions: Electron and hole transport properties and related photovoltaic responses, *Phys. Rev. B - Condens. Matter Mater. Phys.* 77 (2008) 1–9.
- [262] J.L. Brédas, G.A.H. Wetzelaer, M. Kuik, P.W.M. Blom, B. de Boer, C. Risko, C. Campbell, H.T. Nicolai, Unification of trap-limited electron transport in semiconducting polymers, *Nat. Mater.* 11 (2012) 882–887. doi:10.1038/nmat3384.
- [263] R. Meerheim, M. Furno, S. Hofmann, B. Lüssem, K. Leo, Quantification of energy loss mechanisms in organic light-emitting diodes, *Appl. Phys. Lett.* 97 (2010).
- [264] J.J. Shiang, T.J. Faircloth, A.R. Duggal, Experimental demonstration of increased organic light emitting device output via volumetric light scattering, *J. Appl. Phys.* 95 (2004) 2889–2895.
- [265] Y. Li, M. Kovačič, J. Westphalen, S. Oswald, Z. Ma, C. Hänisch, P. Will, L. Jiang, M. Junghaehnel, R. Scholz, S. Lenk, and S. Reineke. Bridging Chaos and Order: Tailor-Made Nanostructures for Highly Efficient White Organic Light-Emitting Diodes. (submitted)
- [266] Y. Li, Q. Wei, L. Cao, F. Fries, M. Cucchi, Z. Wu, R. Scholz, S. Lenk, B. Voit, Z. Ge, and S. Reineke. Organic light-emitting diodes based on conjugation-induced thermally activated delayed fluorescence polymers: Interplay between intra- and intermolecular charge transfer states. (in preparation)

List of Abbreviations

2D	2-dimensional
3D	3-dimensional
ACQ	Aggregation caused quenching
AEE	Aggregation enhanced emission
AFM	Atomic force microscope
AR	Aspect ratio
CGL	Charge generation layer
CIE	Commission Internationale de L'Eclairage
CRI	Color rendering index
CTE	Coefficient of thermal expansion
DMA	Dynamic mechanical analysis
DSC	Differential scanning calorimetry
EBL	Electron blocking layer
E_g	Energy gap
EIL	Electron injection layer
EL	Electroluminescence
EML	Emission layer
EQE	External quantum efficiency
ETL	Electron transport layer
FEM	Finite element method
FFT	Fast Fourier transfer
FRET	Förster resonance energy transfer
FWHM	Full width at half maximum
HBL	Hole blocking layer
HIL	Hole injection layer
HOMO	Highest occupied molecular orbital
HTL	Hole transport layer
IC	Internal conversion
IQE	Internal quantum efficiency

ISC	Intersystem crossing
ITO	Indium tin oxide
LIV	Luminance-current density-voltage
LUMO	Lowest unoccupied molecular orbital
NTSC	National Television System Committee in North America
OLED	Organic light-emitting diodes
PDMS	Polydimethylsiloxane
PEDOT:PSS	Poly(3,4-ethylenedioxythiophene)-poly(styrenesulfonate)
PLQY	Photoluminescence quantum yield
PML	Perfect matching layer
PMMA	Poly(methyl methacrylate)
PSDF	Power spectral density function
RIE	Reactive ion etching
R_{rms}	Mean square roughness
SCLC	Space-charge limited current
SEM	Scanning electron microscope
SPP	Surface plasmon polariton
TADF	Thermally activated delayed fluorescence
TCSPC	Time-correlated single photon counting
TE	Transverse electric
T_g	Glass transition temperature
TGA	Thermogravimetric analysis
TIR	Total internal reflection
TM	Transverse magnetic
XPS	X-ray photoelectron spectroscopy
ΔE_{ST}	Singlet-triplet splitting
η_{CE}	Current efficiency
η_{EE}	Extraction efficiency
η_{LE}	Luminous efficacy
η_{S}	Quantum efficiency of OLEDs with substrate modes
η_{SA}	Quantum efficiency of OLEDs with substrate and air modes

Acknowledgement

I am very thankful for many people for their great support to finish my PhD thesis during my stay in Dresden Integrated Center for Applied Physics and Photonic Materials (IAPP). Coworkers in IAPP are always open for beneficial discussions and kind for help. There are so many people I own them my appreciation, but I cannot list all of them here because of limited space. Without their help, I cannot finish this thesis successfully. Thanks the Chinese Scholarship Council and GA funding at TU Dresden for financial support.

Firstly, I would like to acknowledge Prof. Karl Leo and Prof. Sebastian Reineke for giving me the opportunity to work at IAPP rather than working in a company. I am deeply indebted to my supervisor Prof. Sebastian Reineke for his continuous support and academic instruction. I am very grateful for giving me a large scientific freedom during my PhD and helping me whenever I need. Furthermore, I would like to thank Prof. Sebastian Reineke and Prof. Karl Leo for reviewing of my thesis.

I would like to acknowledge Prof. Dr. Guoli Tu (Huazhong university of Science and Technology) for his expertise in preparing the third review of this thesis.

I would like to thank Dr. Simone Lenk as my group leader for her great support and instruction during my entire PhD time. Without her kind help, I cannot get used to the scientific life at IAPP so fast and finish my PhD on time. Thank you for all your supervision, suggestion and patience.

I would like to thank Dr. Reinhard Scholz for his expertise and help in theory and simulation. Thanks for leading me to a deeper physical world.

I would like to thank all my collaborators during my PhD time, especially Dr. Kovačič, Milan, Jasper Westphalen, Dr. Steffen Oswald and Dr. Manuela Junghaehnel.

I would like to thank Dr. Angelika Wolf for her kind help for GA funding application.

I would like to thank the Lesker team: Tobias Günther, Andreas Wendel and

Caroline Walde for their continuous support of making lesker samples.

I would like to thank the engineer team: Sven Kunze, Daniel Dietrich and previous engineer Andreas Büst for technical support.

I would like to thank Tina Träger for purifying materials.

I would like to thank Prof. Zheng Tang for his kind help for the transmission and reflectance simulation.

I would like to thank Prof. Zaifei Ma for her instructions on AFM measurements and also for giving me nice and kind suggestions on how to organize my entire PhD topic. Thanks for giving very thoughtful comments on this thesis.

I would like to thank Dr. Lihui Jiang for inspiring discussions on chemical reactions and mechanisms. I am thankful for his kind suggestions on the career development.

I would like to thank Dr. Tian-yi Li, Dr. Ji-ling Hou and Dr. Xiuling Yu for helping me to adjust the new lifestyle in Dresden during my early stage of PhD.

I would like to thank my officemates Irma Slowik and Tim Wagner for joyful discussions and encouragement during the writing time.

I would like to thank Dr. Axel Fischer, Paul-Anton Will, Christian Hänisch, Yuan Liu, Jinhan Wu and Dr. Zhongbin Wu for beneficial discussions on OLEDs and so on.

I am sincerely thankful for my wife Jinxiu for her love, sacrifice and understanding. Thank my parents, uncle, my brother and the other family members. Without your support and understanding, I could not have completed my PhD.

Erklärung

Diese Dissertation wurde am Institut für Angewandte Physik der Fakultät Mathematik und Naturwissenschaften an der Technischen Universität Dresden unter wissenschaftlicher Betreuung von Prof. Dr. Sebastian Reineke angefertigt.

Hiermit versichere ich, dass ich die vorliegende Arbeit ohne unzulässige Hilfe Dritter und ohne Benutzung anderer als der angegebenen Hilfsmittel angefertigt habe. Die aus fremden Quellen direkt oder indirekt übernommenen Gedanken sind als solche kenntlich gemacht. Die Arbeit wurde bisher weder im Inland noch im Ausland in gleicher oder ähnlicher Form einer anderen Prüfungsbehörde vorgelegt.

Weiterhin versichere ich, dass bisher keine Promotionsverfahren stattgefunden haben. Ich erkenne die Promotionsordnung der Fakultät Mathematik und Naturwissenschaften an der Technischen Universität Dresden vom 15.10.2015 an.

Dresden, 3. May 2019

Yungui Li